Role of mechanical forces in mitosis and heart muscle

By

Nilay Taneja

Dissertation

Submitted to the Faculty of the

Graduate School of Vanderbilt University

in partial fulfillment of the requirements

for the degree of

DOCTOR OF PHILOSOPHY

In

Cell and Developmental Biology

September 30, 2020

Nashville, Tennessee

Approved:

Dylan T. Burnette, Ph. D., Advisor

Ryoma Ohi, Ph.D., Committee Chair

Alissa M. Weaver, M.D., Ph.D.

Vivian Gama, Ph. D.

Christopher S. Williams, M.D., Ph. D

DEDICATION

I dedicate this thesis to my grandfather,

Brij Kishore Taneja,

without whom I would not have a love for nature, science, discipline, perseverance,

and above all,

the need to question everything.

ACKNOWLEDGEMENTS

I would first like to thank my advisor, Dr. Dylan Burnette, for his incredible mentoring during my years in graduate school. Indeed, I would not be writing this thesis if not for his guidance that has shaped nearly every aspect of my graduate school training. Dylan's infectious enthusiasm for science, his creativity, his skills as an experimentalist and talent for microscopy have all contributed to my development as a scientist. He has also inspired my pursuit of artistically displaying microscopy data. Above all, however, Dylan has been patient, kind and very supportive as a mentor. He has been always been ready to help if I have been stuck, but also always willing to let me pursue my "cowboy" experiment ideas. His constant advocacy for my career advancement, whether it is opportunities to form new collaborations, or presenting my work at meetings, has given me the perfect start to my career in science. I am excited to see Dylan advance in his own career, and I hope we will continue to have a long and fruitful professional and personal relationship. I surely will strive to carry forward Dylan's scientific and mentoring legacy in my future endeavors.

In addition to Dylan, I would like to extend a big thanks to the past and present members of the laboratory who greatly enriched my graduate school experience. When I joined the laboratory, Aidan Fenix was the only other graduate student in the lab. His passion for science, willingness to help, and be a good lab mate was a major contributing factor to my joining the lab. He also laid a great roadmap for any graduate student to follow to have a successful graduate career. Subsequently, Abigail Neininger joined our group, and greatly added to both the expertise of the lab in data quantification, as well as infusing fresh life into the lab. Indeed, we have collaborated extensively over the last few years and my work has greatly benefitted from her contribution, both in our initial joint project as well as future projects. I would also like to thank our research specialist, Karren Hyde, for her help and support in keeping the lab running as well as many discussions on molecular biology. I would also like to extend my thanks to Sophie Baillargeon, who brought in her engineering expertise into the lab and spearheaded the development of micropipette aspiration in the lab. It has been a great pleasure collaborating with Sophie and she has had a big impact on bringing new insight into my work. I would finally like to thank the latest addition to our lab, James Hayes. I wish our overlap had been longer, but I am excited to see him carry forward the research program in our laboratory. I feel fortunate to have had great colleagues and friends during these years.

Scientific research has rarely been as collaborative as it is today, and my own research could not have been completed without collaborations inside and outside Vanderbilt. I would like to thank Dr. Lindsay Rathbun from Dr. Heidi Hehnly's lab, Syracuse University, who were great collaborators on the cell shape during cytokinesis study. They helped expand my horizons and think more about the centrosome, which I admit until that point I shied away from. I would like to thank Caleb Snyder and Dr. Matthew Bersi from Dr. David Merryman's lab, Vanderbilt University, for our long and fruitful collaboration. I have leaned heavily on Matt for his expertise on cell mechanics and our countless conversations have greatly advanced my knowledge and skills in that area. I would like to thank Megan Rasmussen from Dr. Vivian Gama's lab, with whom I have also had a long and fruitful collaboration. Our collaboration on mitochondrial dynamics in cardiac myocytes was a rewarding experience and greatly added to the repertoire of concepts and techniques I was exposed to.

I have been fortunate to have an extended mentor network at Vanderbilt University. It would be impossible to articulate every little conversation that has shaped my career development in significant ways. I would like to thank my committee chair, Dr. Ryoma (Puck) Ohi for his continued support, even after he left Vanderbilt. Our conversations about science have been invaluable to me, and the many letters he had to write for me greatly helped me figure out the next steps in my career. I would also like to thank Dr. Vivian Gama, who apart from being a helpful committee member and collaborator, has been incredibly supportive during my graduate school years with her countless letters of recommendation. I would also like to thank Dr. Alissa Weaver and Dr. Christopher Williams for also being helpful members of my thesis committee, and for helping me thinking about my research from every perspective. I would also like to thank other faculty members in the department, Dr. Matt Tyska, Dr. Marija Zanic, Dr. Kris Burkewitz, Dr. Andrea Page McCaw, Dr. David Miller, Dr. Irina Kaverina, Dr. David Cortez, and Dr. Ian Macara, for great scientific advice and help with reagents over the years. I would also like to thank the amazing community of fellow graduate students and postdocs, who have made the Cell and Developmental Biology department fun, vibrant and intellectual.

I would like to extend a special thanks to Dr. Chris Wright. His leadership at the Program in Developmental Biology has greatly enriched my thinking as a scientist. Besides getting exposed to a plethora of developmental biology literature, his passion for thinking deeply about science has been very inspiring to me and had a large impact on the scientific directions I have taken for my postdoctoral career. He went above and beyond in helping me find the right

postdoctoral lab and connected me with people in the field. I would similarly like to extend a big thanks to Dr. Robert (Bob) Coffey. Early in graduate school, the Epithelial Pathobiology course was my favorite course and his leadership made this course a great tool to enhance scientific networking and critical thinking. He was also enthusiastic in his willingness to help me when I asked for his guidance in thinking about the right postdoctoral lab.

I would also like to thank all the sources of funding that have facilitated my research. I would not have had the opportunity to work at Vanderbilt without the Vanderbilt International Scholars Program, led by Dr. Kathy Gould. This program provides the much-needed level playing field for international students by providing two years of dedicated funding. I am greatly indebted to the program for providing me the opportunity to come to the United States for my doctoral training. I would like to again thank my mentor for financially supporting my research. I would also like to thank the American Heart Association for supporting two years of my training. Finally, I would like to thank the Graduate School at Vanderbilt as well as the American Society for Cell Biology for supporting travel to meetings that are essential to the scientific development.

Vanderbilt University has been an incredible place to train as a scientist. I would like to acknowledge the countless support systems that have facilitated my research, especially the Nikon Centre for Excellence Cell Imaging Shared Resource, which has provided the microscopes and support without which almost none of this research would be possible. I would also like to thank all the core facilities at Vanderbilt University. I would like to thank Susan Walker, Kristi Hargrove and CDB POD members for ensuring the smooth running of the department.

I have also been very fortunate to have had an amazing support system in my personal life. I would like to thank my parents, Sanju and Sunil Taneja, for being pillars of support, encouragement, and love throughout these years. They have always been there to provide the much-needed perspective on life when stresses of graduate school loomed large. I would like to thank my grandparents, Prem and Kishore Taneja, for their love and support. I would also like to thank my sister, Gauri, for her constant support and cheering me on for every little accomplishment. I would like to thank the remarkable individuals I get to call my friends-Kalen Petersen, Ankit Kushwaha, Kristin Kwakwa-Petersen, Andrea Cuentas, Oscar Ortega, Tessa Popay, Rafael Folkes-Perez, Oakleigh Folkes-Perez, Amanda Erwin, Brian Gitschlag, Ben Kesler and Maria Fomicheva for making these six years effortless and enjoyable. As an

international student with my family on another continent, my friends have been a great support system.

Finally, I would like to thank my amazing wife, Aichurok Kamalova, for making this whole journey worth it. I am incredibly fortunate to have met Aichurok on the first day of my graduate school as a fellow member of the Vanderbilt International Scholars Program. She has embodied countless roles in this short span of six years, being first my best friend, then my girlfriend and now my family. It is difficult to overstate how lucky I have been to have had a partner during this graduate school journey, especially someone going through her own graduate school journey. I would like to thank Aichurok for her love, understanding, support, and patience during these years. As with any Ph.D. experience, mine has been full of ups and downs, with long hours, failed experiments, the difficulty of publishing papers and finding jobs. I am thankful to Aichurok for keeping me grounded and always reminding to not lose sight of not only my goals, but also the important things in life and being happy. A talented scientist herself, she has also been amazing at helping me with countless aspects of science, whether it is bouncing ideas, preparing for talks, or experimental troubles. I eagerly look to the future for our next phases of life full of love and more exciting science. I could not ask for more.

TABLE OF CONTENTS

LIST OF TABLES

LIST OF FIGURES

LIST OF ABBREVIATIONS

PALM	Photo-activated Localization Microscopy
STORM	Stochastic Optical Reconstruction Microscopy
MII	Non-muscle myosin II
CMII	Cardiac myosin II
FAK	Focal adhesion kinase
hiCM	Human induced pluripotent stem cell derived cardiomyocyte
MSF	Muscle Stress Fiber
ECM	Extracellular matrix
SIM	Structured Illumination Microscopy
RLC	Regulatory Light Chain
FA	Focal adhesion
FN	Fibronectin
ERM	Ezrin Radixin Moesin
NRK	Normal Rat Kidney
TIRF	Total Internal Reflection Fluorescence
mEGFP	Monomeric Enhanced Green Fluorescent Protein
siRNA	Small interfering Ribose Nucleic Acid
iPSC	Induced Pluripotent Stem Cell
STED	Stimulated Emission Depletion Microscopy
SEM	Scanning Electron Microscopy
ATP	Adenosine triphosphate
DSF	Dorsal Stress Fiber
CRISPR	Clustered Regularly Interspaced Palindromic Repeats
MDCK	Madin Darby Canine Kidney
ERM	Ezrin Radixin Moesin
FRAP	Fluorescence Recovery after Photobleaching
KO	Knockout

Chapter 1- Introduction

The ability to interconvert mechanical and biochemical signals is the fundamental property of every living organism, from single cells to complex multi-cellular organisms. Cells harness chemical energy obtained from ATP hydrolysis to generate mechanical forces, which drive a rich repertoire of cellular processes, from intracellular transport, cell migration, cell division, and muscle contraction to tissue morphogenesis. These vastly diverse processes are all driven by interplay between the three primary cytoskeletal systems present in most mammalian cells- actin filaments, microtubules, and intermediate filaments. Intrinsically and extrinsically generated mechanical forces can then act as stimuli, creating biochemical signals that can alter cell fate and behavior. The broad discipline investigating these processes from the molecular to the organism scale is termed mechanotransduction (Wozniak and Chen, 2009). Defects in different aspects of mechanotransduction underlie hundreds of human pathologies such as cancer, cardiomyopathies, muscular dystrophy, blood disorders and hearing loss.

Decades of intense investigation have revealed insights into how molecular motors generate force at the molecular scale. The molecular motor myosin-II is one of the earliest molecular motors to be characterized biochemically. Classic *in vitro* studies have established the mechanochemical cycle of myosin-II binding to actin filaments (O'Connell et al., 2007) (Figure 1-1). This cycle powers processes such as muscle contraction and cell division. Recent advances in cryo-electron microscopy and tomography have revealed the atomic scale structures of molecular motors or assemblies (Mentes et al., 2018; Stepanek and Pigino, 2016). This structural information combined with light microscopy-based reconstitution assays has revealed how motors such as dyneins generate motion (Cianfrocco et al., 2015). These results have furthered our understanding of intracellular transport on microtubules, chromosome segregation by the mitotic spindle, and ciliary motion. While large leaps have been made using reductionist approaches, it is well appreciated that living cells are vastly more complex. For instance, kinesins and dyneins can compete for microtubule track occupancy, activating upstream kinases can compete for myosin motors, and extracellular cues such as substrate stiffness provide mechanical inputs to cytoskeletal networks. Furthermore, extensive crosstalk exists between the actin, microtubule, and intermediate filament cytoskeletons. Therefore, there is a large gap in knowledge that exists between

understanding the biophysical properties of motors and their tracks *in vitro* versus their function and regulation in cells and tissues.

The development of super-resolution light microscopy techniques has begun to bridge the gap between molecular scale information obtained *in vitro*, and observing the behavior of cytoskeletal networks in intact, living cells. Single molecule techniques such as Photo-activated Localization Microscopy (PALM) and Stochastic Optical Reconstruction Microscopy (STORM) have revealed nanoscale architecture of cellular structures such as focal adhesions (Kanchanawong et al., 2010), adherens junctions (Bertocchi et al., 2017), and the actin cortex (Xia et al., 2019). These single-molecule localization techniques allow not only to observe the intact architecture of the cytoskeleton, but also offer insight into how these might be regulated. However, these techniques largely remain limited to fixed cells, and therefore lack dynamic information. On the other hand, techniques such as Structured Illumination Microscopy (SIM), which allows a doubling of the spatial resolution obtained via light microscopy to ~ 110 nm (Gustafsson, 2005; Schermelleh et al., 2008), have shown how myosin-II supramolecular assemblies called stacks assemble at the leading edge of living crawling cells (Fenix *et al.*, 2016).

In conjunction with super-resolution techniques, imaging techniques that allow the measurement of protein dynamics within cells are also essential to studying mechanotransduction. Notably, Fluorescence Recovery after Photobleaching (FRAP) can be used to infer the turnover and/or diffusion of cytoskeletal proteins in live cells, which again provides an additional layer of information about the behavior of these molecules in living cells. Conversely, the development of photo-activable proteins allows measurement of protein dynamics within the context of entire structures. For instance, photoactivation of mitochondrial matrix proteins can be used to measure mitochondrial fusion (Rasmussen et al., 2020). In another example, photoactivation of the Z-disc protein alpha-actinin was used to show how cardiac sarcomeres assemble (Fenix et al., 2018).

Biophysical approaches such as laser ablation, atomic force microscopy and optical tweezers can be used to directly measure forces or probe the material properties of living cells. Since the protein-protein interactions that drive the generation of cortex tension occur at the nanoscale, measurements such as cortex tension are useful emergent properties of these interactions that can be used to learn the basic principles of mechanotransduction. These measurements, combined with mathematical models have started to reveal the fundamental

principles of processes such as cell migration, morphogenesis, and muscle contraction. With the increase in large amounts of data as well as continued appreciation for quantitative approaches, cell biology has thus become an increasingly interdisciplinary field of investigation, combining the fields of biophysics, high-resolution microscopy, mathematical modeling, and biochemistry to study mechanotransduction. Therefore, we are at an exciting phase of cell biology, with many discoveries to be made on the function of cytoskeletal networks in living cells, combining quantitative microscopy and biophysical tools.

In the following sections, we will focus on select cytoskeletal structures that generate forces within living cells, as well as those that relay these forces to and from the extracellular environment. These concepts will be specifically discussed in the context of two myosin-II driven cellular processes, cell division driven by non-muscle myosin-II (referred throughout as MII), and heart muscle contraction driven by cardiac myosin-II (referred to as β-CMII). While these two processes differ greatly in the specific function achieved, studying them has revealed some unifying principles of cell shape regulation and contractile system assembly that appear conserved across cell types.

Figure 1-1

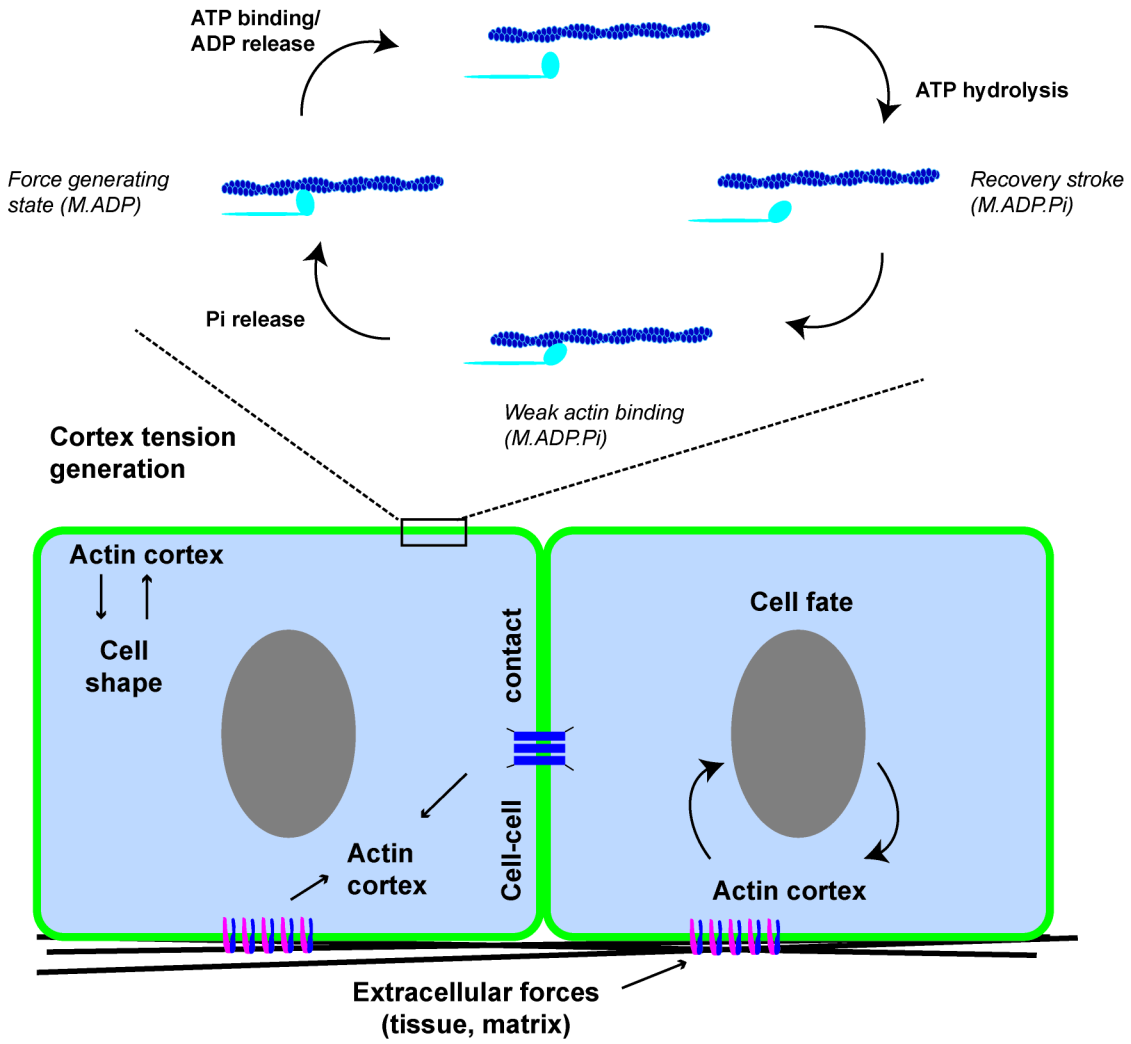

Figure 1-1- The basic principles of mechanotransduction

The actin cortex is a thin network of actin filaments underneath the plasma membrane responsible for generation of cortex tension through the action of myosin motors generating force on actin filaments using ATP hydrolysis. Cortex tension generated by the actin cortex is required for both maintaining and changing cell shape, which can feed-back on the actin cortex. Cell-cell and cell-matrix contacts link the actin cortex with the cortex of other cells and the extracellular matrix, respectively. These contacts form signaling centers that can then further drive changes in actin cortex mechanics. While initial views of cell mechanics proposed that cell fate drives the mechanical state of the cell, it is increasingly appreciated that forces generated by the actin cortex can alter cell fate by exerting forces on the nucleus.

Cell division

Cell division is a fundamental property of living cells. This process allows living organisms to perpetuate their genetic material to future generations. From its first ornate description in the late 1800s by Walther Flemming, cell division has fascinated biologists for more than a century. In mammalian cells, cell division, or the mitotic phase of the cell cycle, can be divided into two processes- karyokinesis and cytokinesis. Karyokinesis involves the distribution of the genetic material into the daughter cells, while cytokinesis allows the daughter cells to physically separate from each other following karyokinesis. While extensive crosstalk occurs between the two processes, these processes can also be completely uncoupled from each other. For instance, organisms such as fruit flies undergo multiple rounds of karyokinesis prior to cellularization during embryogenesis. In adult mammals, cells of the megakaryocyte lineage undergo karyokinesis followed by programmed cytokinetic failure to generate multiple nuclei (Lordier et al., 2012).

The faithful segregation of genetic material is achieved through a complex microtubule-based machine called the mitotic spindle. The cyclin/Cdk1 complex, also termed as mitosis promoting factor, is essential to coordinating key processes such as spindle assembly (Prosser and Pelletier, 2017) and cell rounding (Enserink and Kolodner, 2010) required for successful karyokinesis (Figure 1-2). Cell rounding is thought to be required for effective chromosome segregation in cell culture. It must be noted, however, that the precise contribution of cell rounding to chromosome segregation *in vivo* remains contentious, where interphase cells shape appears to control spindle orientation (Bosveld et al., 2016; Fink et al., 2011). Recent work has elucidated that the promiscuous Ser/Thr kinase Cdk1 is first activated by cyclin A2 during S-phase, where it promotes an increase in focal adhesion and stress fiber formation through activating the formin FMNL2 (Jones et al., 2018). During G2, Cdk1 is downregulated by association with cyclin B1, resulting in disassembly of focal adhesion complexes and initiation of cell de-adhesion and rounding (Jones et al., 2018). In parallel, cyclin B1/Cdk1 also initiate nuclear envelope breakdown (Hinchcliffe et al., 1999). During prometaphase, microtubules start to form attachments with condensed chromosomes at specialized structures called kinetochores. Opposing forces from kinetochore microtubules bound to kinetochores of sister chromatids gradually align the chromosomes to the “metaphase plate”, usually at the central plane of the spherical cell. A complex spindle assembly checkpoint mechanism occurs

to ensure that the chromosomes are tightly aligned at the metaphase plate (Prosser and Pelletier, 2017). The destruction of cyclin B initiates exit from metaphase, resulting in the separation of the sister chromatids by destruction of the cohesion complex. The separation of the sister chromosome marks the end of Anaphase A. During Anaphase B, signals from spindle midzone initiate the assembly of the actin filament based contractile ring (Green et al., 2012) (Figure 1-2).

Signals emanating from the spindle midzone activate the small GTPase RhoA that drives both the activation of non-muscle myosin-II and actin polymerization (Green et al., 2012). Non-muscle myosin-II activation is achieved by both activation of Rho-associated kinase (ROCK), which phosphorylates the regulatory light chain (RLC) of non-muscle myosin-II, as well as inactivates myosin phosphatase, resulting in synergistic RLC phosphorylation. In parallel, RhoA also activates the actin nucleator Dia1, which increases actin polymerization at the equatorial region of the cell. Work from the Wang (Fishkind and Wang, 1993) and Gerlich (Spira et al., 2017) labs has shown that the increase in myosin contractility precedes the increased ordering of actin filaments, ultimately giving the contractile apparatus a ring-like appearance. Ultimately, myosin-II contractility is the major driver of contractile ring ingression in mammalian cells. Indeed, most mammalian cells in culture are sensitive to the myosin-II ATPase inhibitor, blebbistatin (Straight et al., 2003). However, highly adhesive cells in culture, such as NRK cells, as well as the amoeba *Dictyostelium* can divide without a contractile ring, instead using the force generated by daughter cell migration for cytokinesis (Kanada et al., 2005; Neujahr et al., 1997). This suggests that cells have evolved multiple mechanisms to complete this fundamental process.

Cytokinesis is concluded when the two daughter cells physically separate, a process termed abscission (Green et al., 2012). Upon completion of cleavage furrow ingression, the spindle midzone matures into the spindle midbody. The spindle midbody acts a scaffold for the abscission machinery, which involves the ESCRT complex, myosin-IIB and microtubule associated proteins; the midbody is also an essential fate determinant and is often asymmetrically inherited between the two daughter cells. The completion of cytokinesis is also marked by the initiation of cell spreading of the two daughter cells and reassembly of stress fibers.

Cytokinesis is a widely studied process in the context of mechanotransduction, since it involves multiple dramatic force-driven events- mitotic spindle assembly, chromosome

segregation, mitotic spindle orientation, cell rounding, cell abscission and contractile ring ingression. Among the many fascinating future directions for the field is the cross-talk between actin, microtubule and intermediate filament cytoskeletons to regulate cell shape and spindle orientation (discussed in Chapter 2); regulation of the mechanical properties of the actin cortex (Chapters 3 and 4); mechanisms driving contractile ring ingression and organization (Chapter 4).

Figure 1-2

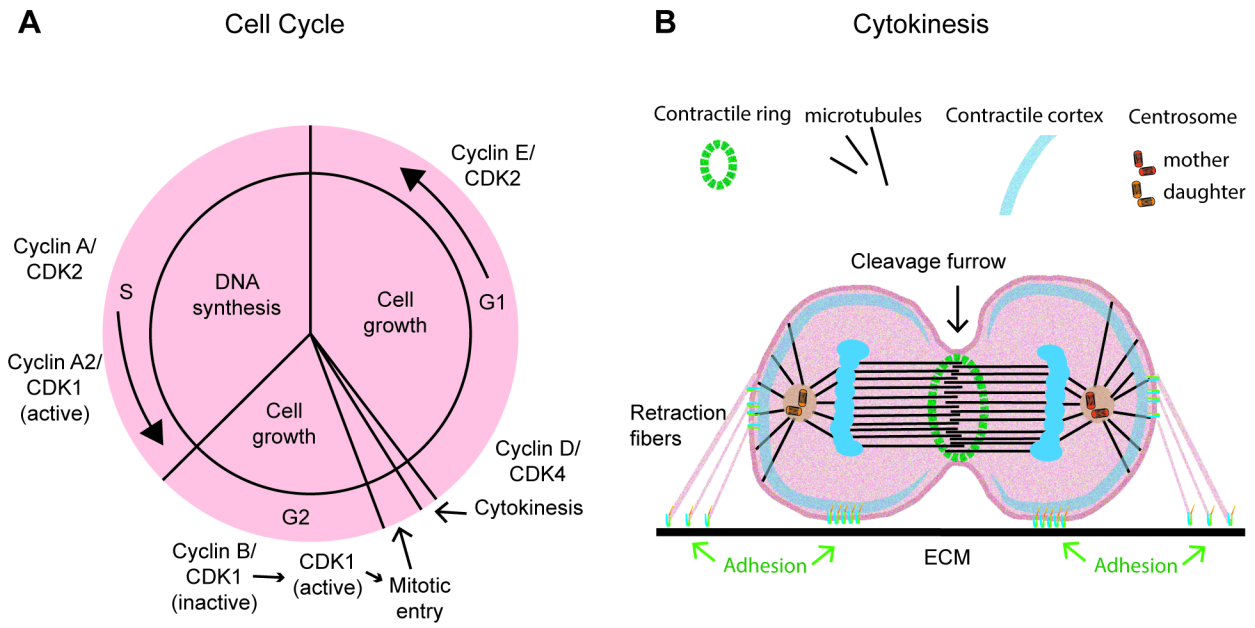

Figure 1-2- Cell cycle stages and cytokinesis

A) Overview of the cell cycle and important kinases and cyclins involved in each stage. The kinase Cdk1 has been shown to be a master regulator of cell adhesion during the cell cycle. During S-phase, association of Cdk1 with cyclin A2 results in increased Cdk1 in increased stress fiber assembly. Upon entry into G2, association of Cdk1 with cyclin B1 results in Cdk1 inactivation, resulting in the initiation of stress fiber disassembly. Activation of Cdk1 results in mitotic entry, which requires stress fiber disassembly. Upon mitotic exit, Cdk1 activity re-initiates the formation of focal adhesions. B) Side (XZ) view of a single cell undergoing cytokinesis.

Heart muscle contraction

The heart is a remarkable model system to study mechanotransduction since the primary function of this organ is to generate contractile force throughout the life of the organism. Individual cardiac myocytes within the heart must be able to both assemble contractile structures during development, and remodel and maintain these structures during adult function in response to physiological and pathological stress. The fundamental unit of contraction within cardiac myocytes is the myofibril, which is composed of a series of sarcomeres, highly organized structures comprising “thin” actin filaments and “thick” myosin-II filaments (Figure 1-3). Cardiac myosin-II filaments exert contractile force on antiparallel actin filaments to shorten the sarcomere. Actin filaments from adjacent sarcomeres are anchored at Z-discs by α-actinin mediated cross-linking, ultimately transmitting contractile force to neighboring sarcomeres (Knoll et al., 2011; Kovacic-Milivojevic et al., 2001). These forces are then relayed at the cellular, tissue, and organ levels to generate heartbeat. Hundreds of other proteins have been shown to localize to the sarcomere, and how this complex structure is assembled and maintained has fascinated cell biologists for decades (Sanger et al., 2005).

Decades of research have culminated in the understanding that myofibrils are built using a template comprising of mostly “non-muscle” components (Sanger et al., 2005). Specifically, muscle stress fibers (MSFs, also previously called “pre-myofibrils” by the Sanger lab or “non-muscle like stress fiber” by the Holtzer lab) serve as the precursors for myofibrils (Dlugosz et al., 1984; Fenix et al., 2018; Rhee et al., 1994). These stress fibers then form a template to incorporate muscle components. This transition presents itself with multiple unanswered questions- what regulates this transition during differentiation in early development? How does an MSF increase its force generating capacity? How are these increasing contractile forces balanced? These questions are equally relevant in the adult. The balance between contraction and adhesion must be maintained into adulthood since the heart is routinely exposed to increased load both during physiological and pathological stress. For instance, exercise leads to thickening of the myocardium and increased ejection fraction (Fernandes et al., 2015). On the other hand, during disease states such as cardiomyopathies, increased thickening of the myocardium is associated with reduced ejection fraction and heart function (Braunwald, 2017). Indeed, most causative mutations are present in genes encoding proteins involved in either in

sarcomere contraction (such as α-myosin-II, β-myosin-II, and titin) or cell adhesion (such as vinculin, kindlin, and laminin) (Hershberger et al., 2013).

While extensive work has been done on the organism level where these detrimental phenotypes have been linked to mutations in these genes, the cellular mechanisms underlying these changes remain less understood. On the other end of the spectrum, single molecule biophysical approaches have shown how proteins such as vinculin, talin and myosin-II respond to force, and how disease-causing mutations change these responses (Finer et al., 1994; Huang et al., 2017; Tapia-Rojo et al., 2020). Understanding how multiple mechano-sensory proteins act in concert, integrating extracellular and intracellular cues, and converting them to cellular responses that ultimately result in organ level responses during development and disease is an exciting new ground for studying basic cardiovascular cell biology.

We will now move on to providing an overview of the contractile actomyosin structures found in cells, followed by description of relevant structures that mediate cell adhesion that resists these contractile forces. The studies that follow will hopefully impress upon the reader the complex regulation of contractile function. These studies, I hope, will also reveal some unifying principles of contractile system assembly, where similar mechanical principles are used to build contractile networks to perform very different functions – cell division and muscle contraction.

Figure 1-3

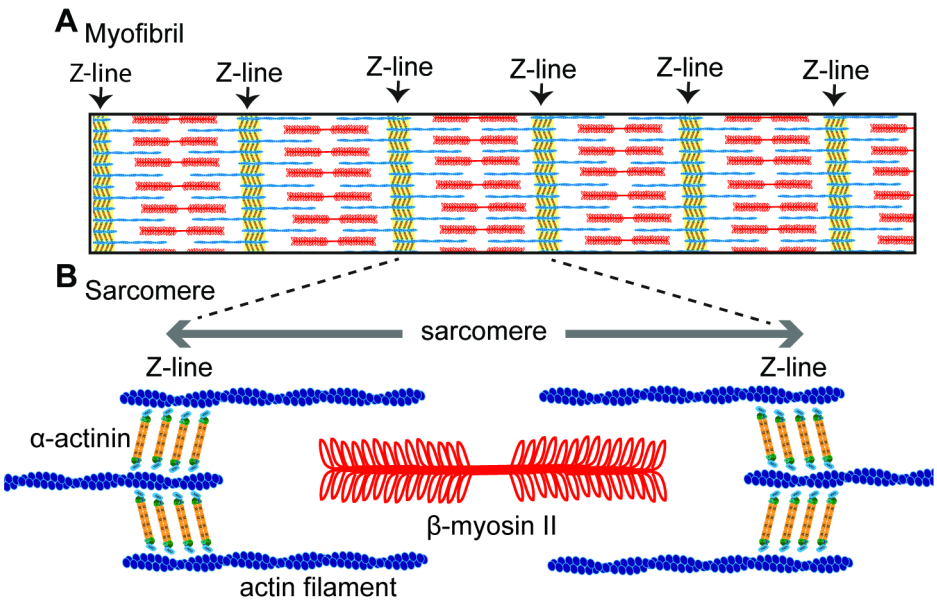

Figure 1-3- Myofibril organization and structure

The functional units of contraction within cardiac myocytes are myofibrils, which are composed of a series of sarcomeres. Coupling of myofibrils across multiple cells results in tissue level generation of contractile force that drives the pumping of blood out of the ventricle.

Force generating structures: Actin cortex

One of the most dramatic changes that occur in the actin cytoskeleton during cell division is the disassembly of stress fibers and the formation of an isotropic network of actin filaments called the actin cortex (Figure 1-4). While first studied in the context of cell division, the actin cortex is being appreciated as a universal structure that is involved in force generation in multiple cellular processes, such as cell migration and morphogenesis (Svitkina, 2020). While the existence of “surface activity” in migrating cells was first reported in 1973 (Trinkaus, 1973), a molecular understanding of the cortex has only emerged in the past two decades using quantitative microscopy, biophysics, and mathematical modeling. The actin cortex can be considered the fundamental “canvas” of contractile network associated with the plasma membrane which can then be remodeled and repurposed into different networks- lamellipodia, blebs, stress fibers, the metaphase cortex, filopodia, microvilli and the contractile ring (Salbreux *et al.*, 2012). How this control of network formation occurs, how the mechanical properties of these networks are determined and how these networks interact with one another and other filament systems are all open questions that will continue to interest cell biologists in the coming decades.

The actin cortex is also a challenging structure to study, since it requires nanometer resolution to elucidate its structure, comprises hundreds of proteins that constantly turn over at different rates and are regulated by different signaling pathways (Salbreux *et al.*, 2012). While single molecule imaging techniques have been used to elucidate the structure of the ventral surface of embryonic stem cells (Xia et al., 2019) and the axons of neurons (Xu et al., 2012), these techniques are still limited to fixed cells. Therefore, a more common approach has been to combine macroscopic biophysical properties such as cortex tension with molecular perturbations, and then conceptualize these into physical descriptions of the cortex. However, these models still tend to be very coarse grained, and make multiple assumptions on physical parameters of the cell that cannot be physically measured in live cells (Salbreux *et al.*, 2012). Nevertheless, exciting discoveries have been made on the factors that regulate cortex tension. Notably, regulation of actin filament length is essential to determining the mechanical properties of the cortex (Chugh et al., 2017).

The major source of force generation in the cortex, however, is myosin-II motors pulling on the actin network (Vicente-Manzanares *et al.*, 2009). However, multiple paralogs of myosin-II exist

at the cortex. They also vary in expression based on the tissue and developmental stage where they are expressed (Vicente-Manzanares *et al.*, 2009). For instance, myosin-IIC is expressed in the gut and inner ear (Donaudy et al., 2004; Golomb et al., 2004). Myosin-IIB is strongly expressed in the heart during development but its expression is reduced in the adult (Tullio et al., 1997). Myosin-IIB is also strongly enriched in the embryonic brain (Murakami et al., 1991). There are limited studies that determine the molecular mechanisms that regulate the tissue-specific expression of myosin-II paralogs. One of the best-known instances of active regulation of myosin-II paralog expression is during megakaryocyte differentiation (Lordier et al., 2012). Megakaryocytes are giant multinucleated cells that are the precursors of blood platelets. To facilitate multinucleation, myosin-IIB expression is repressed by RUNX1. Later during proplatelet formation, myosin-IIA is then upregulated to generate tension required to cleave proplatelets from the megakaryocyte.

Myosin-II paralogs have been shown to have distinct biophysical properties *in vitro*. For instance, myosin-IIA has been shown to have a higher ATPase activity, as well as a lower duty ratio, i.e., it spends a smaller proportion of its mechanochemical cycle bound to actin in the force generating state (Kovacs et al., 2003; Rosenfeld et al., 2003; Wang et al., 2003). On the other hand, myosin-IIB has been shown to have a lower ATPase activity and higher duty ratio (Kovacs et al., 2003; Rosenfeld et al., 2003; Wang et al., 2003). These studies were performed using purified S1 fragments, which comprise only the N-terminal motor domain. It was only recently that the behavior of full-length myosin-II paralogs was characterized *in vitro* (Melli et al., 2018). Myosin-IIB can undergo processive movement on actin filaments, while myosin-IIA is unable to do so. The contributions of these behaviors to force generation at the actin cortex of living cells remain to be elucidated.

Myosin-II paralogs can also co-assemble in the same myosin-II filament to form hetero-filaments (Beach et al., 2014; Shutova et al., 2014). The myosin-II bipolar filaments comprise ~30 motors (Billington et al., 2013). It was recently shown that addition of as little as 6 myosin-IIB filaments to a hetero-filament was sufficient to allow the hetero-filament to undergo processive movement on actin filaments (Melli et al., 2018). Hetero-filaments of myosin-II paralogs have been reported at the leading edge of migrating cells (Beach et al., 2014; Shutova et al., 2014), the spreading edge of developing cardiomyocytes (Fenix et al., 2018) as well as at the contractile ring during cytokinesis (Beach et al., 2014). Whether hetero-filament

formation is an actively regulated process, or simply a function of multiple paralogs present in the cell remains to be elucidated.

Figure 1-4

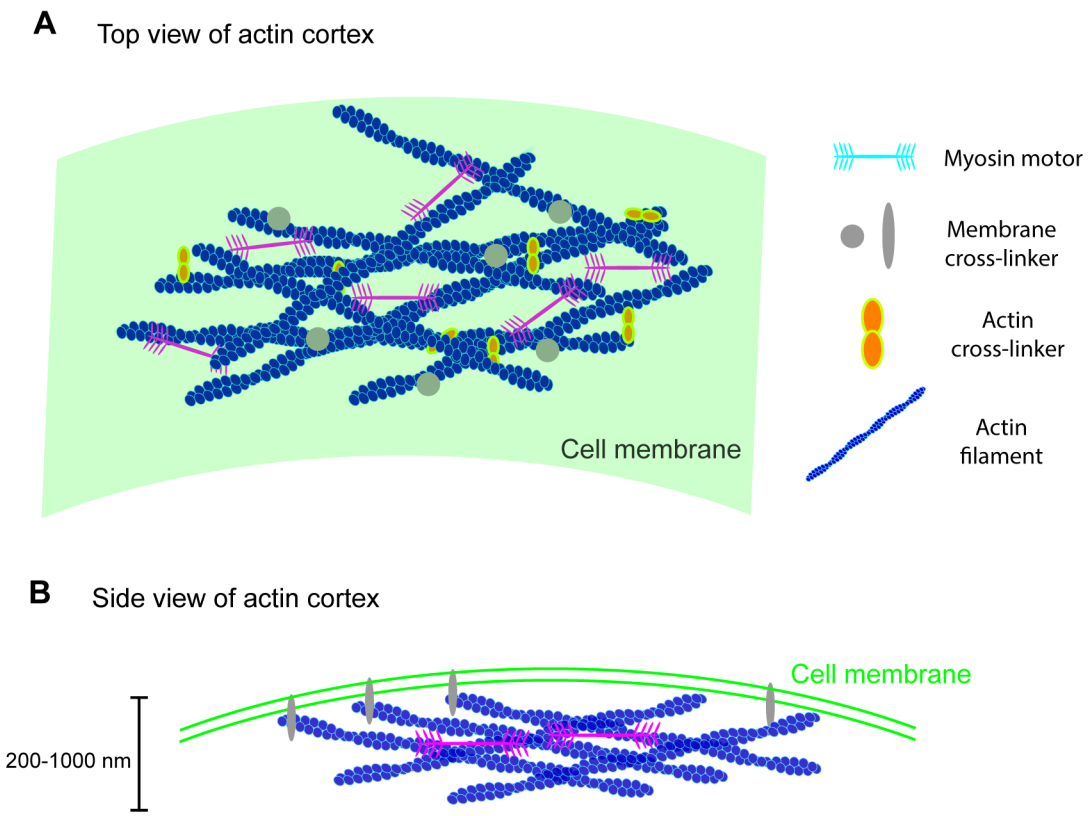

Figure 1-4- Structure and organization of the actomyosin cortex

A) Top view of the actomyosin cortex underneath the cell membrane (green). A simplified view of the cortex is shown here. Proteomic analysis of the cortex has suggested that it comprises ~150 proteins whose functions range from actin nucleation, cross-linking, bundling and turnover. B) Side view of the actin cortex showing its position with the respect to the cell membrane. Actin-membrane cross linkers such as the ERM (Ezrin, Radixin, Moesin) family of proteins link the actin cortex to the plasma membrane. The actin cortex is a very thin network and ranges from 200-1000 nm depending on the cell type.

Force generating structures: Stress fibers and myofibrils

The actin cortex of migrating cells is often organized as different types of stress fibers. These structures are assembled by cells in response to external physical or chemical cues, such as increased stiffness of the extracellular matrix or gradients of chemokines. The primary function of stress fibers is to exert forces upon the external environment, to achieve a wide array of cellular functions, such as cell migration, cell invasion and matrix organization (Tojkander et al., 2012).

The defining characteristic of stress fibers is that they are composed of 15-30 actin filaments bundled by the cross-linking protein α-actinin spaced at ~0.3 μm apart (Tojkander et al., 2012). Stress fibers, however, can vary widely in their components, mechanism of assembly, regulation, and cellular function. There are currently four classes of stress fibers: actin arcs (also called transverse arcs), ventral stress fibers, dorsal stress fibers and the perinuclear actin cap. These classifications are primarily made on the basis of cellular location, contractility, and the mode of connection of the stress fiber to the extracellular matrix (Figure 1-5).

Actin arcs are a widely observed contractile stress fiber characterized by myosin-II striations that alternate with α-actinin (Hotulainen and Lappalainen, 2006). These stress fibers are assembled at the leading edge and undergo rearward translocation on the dorsal surface of migrating cells where they ultimately re-integrate with the actin cortex at the top of the cell (Burnette et al, 2011). These stress fibers are characteristic of actively migrating cells such as keratocytes (Svitkina et al., 1997) and neuronal growth cones (Zhang et al., 2003), as well as of T-cells during immunological synapse formation (Murugesan et al., 2016). These stress fibers are not directly attached to the extracellular matrix (Hotulainen and Lappalainen, 2006). Another population of stress fibers, called dorsal stress fibers, connects actin arcs on the dorsal surface with the substrate on the ventral side via specialized attachments called focal adhesions (Hotulainen and Lappalainen, 2006), which we discuss in the next section. Importantly, dorsal stress fibers are non-contractile and lack myosin-II (Hotulainen and Lappalainen, 2006). Ventral stress fibers are similar in composition and organization to actin arcs but are present at the ventral surface of the cell and have focal adhesions on either end anchoring them to the substrate (Burnette et al., 2014; Hotulainen and Lappalainen, 2006). Ventral stress fibers are thought to assemble through different mechanisms than actin arcs, either through fusion of actin arcs with two dorsal stress fibers, or *de novo* from the actin cortex

on the ventral surface (Hotulainen and Lappalainen, 2006; Lehtimäki et al., 2020; Tojkander et al., 2015). Furthermore, ventral stress fibers are associated with cells that form more stable contacts with the extracellular matrix. These stress fibers have also been shown to exert the highest level of tension among the stress fiber populations (Lee et al., 2018). The perinuclear actin cap is a lesser-studied stress fiber but is known to transmit contractile force to the nucleus and is necessary for force-mediated changes in gene expression (Tojkander et al., 2012). The nesprin family of proteins forms a bridge between the actin cytoskeleton and lamin intermediate filaments that form the nuclear membrane. Elegant work over the last few years has shown that contractile force can directly alter chromatin structure through this mechanical network, revealing the long sought molecular link between mechanical force and gene expression (Graham and Burridge, 2016).

Myofibrils can be considered highly specialized stress fibers that are composed of muscle specific components. Much like a striated stress fiber, myofibrils are composed of actin filament bundles that are cross-linked by α-actinin (Figure 1-3). However, one of the key differences between a myofibril and non-muscle striated stress fiber is that the α-actinin cross-links are present ~1.8 μm to 2.2 μm apart. This spacing is primarily controlled by the presence of titin, often referred to as the “molecular ruler”. This giant protein spans half the length of the sarcomere, with its N-terminal domain binding α-actinin at the Z-disc and its C-terminus extending to the M-line (Maruyama, 1997). The other key difference between these two types of stress fibers is the presence of muscle specific myosin-II, namely α- and β-myosin-II. These myosins are characterized by a low duty ratio, that is, they are bound in actin filaments in the force generating state for a short proportion of their mechanochemical cycle (O'Connell et al., 2007). This allows the myofibril to undergo rapid contractions and actively pull on actin filaments. Non-muscle striated stress fibers, on the other hand, are comprised of slower of myosin-II motors, such as non-muscle myosin-IIA and non-muscle myosin-IIB. This allows stress fibers to generate and sustain tension at longer time scales.

Figure 1-5

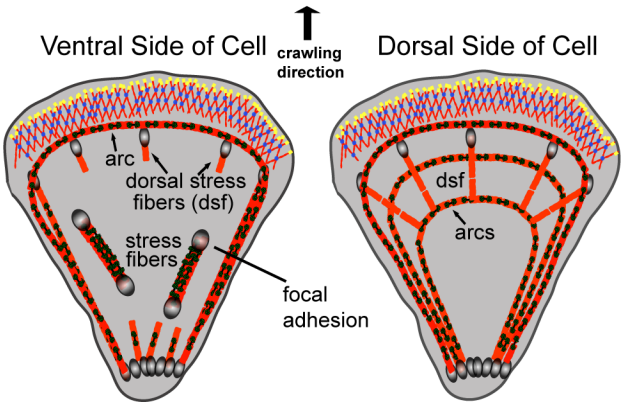

Figure 1-5- Stress fiber populations in a migrating cell

The leading edge of a migrating cells is comprised of a branched actin network called the lamellipodium. Towards the cell body, the lamellipodium transition into the contractile lamella comprised of actin arcs. Actin arcs are present on the dorsal surface of the cell and are contractile (contain myosin-II). Dorsal stress fibers span axially, connecting actin arcs with focal adhesion at cell-ECM contacts. Ventral stress fibers are anchored to the ECM on either end through focal adhesions and are present on the ventral surface of the cell.

Adhesive structures- Focal adhesions and adherens junctions

Resistive forces oppose contractile forces produced in cells, and this dynamic force balance is required to generate shape changes, or to transmit these forces to the extracellular environment and other cells. Cells have evolved a diverse array of specialized protein assemblies that mediate these connections. We will be discussing two primary structures- focal adhesions and adherens junctions.

Focal adhesions are highly specialized protein assemblies that mediate the coupling of the cell cytoskeleton to the extracellular matrix (Geiger et al., 2009). This coupling is essential for sensing both chemical and mechanical cues and drives a myriad of cellular responses, such as cell survival, proliferation, cell fate determination, cell shape changes, matrix degradation, and traction force generation (Geiger et al., 2009). Proteomic studies have estimated around 60 proteins to be present at cell-matrix attachment sites (Horton et al., 2016). We will be limiting our discussion to canonical integrin based focal adhesions.

Integrins are a large family of extracellular receptors that recognize extracellular matrix ligands, such as fibronectin, laminin, and collagen (Hynes, 2002). The ability to recognize different ECM ligands arises from the diversity in α and β subunits of integrin receptors. The reader is directed to excellent reviews on integrin receptor diversity and activation mechanisms (Hynes, 2002; Kim et al., 2011). Integrins can be activated through both “inside out” and “outside in” pathways (Kim et al., 2011). The “outside in” pathway is the classical mechanism of integrin activation. A super-resolution technique called interferometric PALM (iPALM) has revealed the nanoscale architecture of focal adhesions, offering an insight into understanding the pathways mediated focal adhesion assembly (Figure 1-6) (Kanchanawong et al., 2010). Binding to ECM ligands on the extracellular side induces integrin activation. This allows the binding of talin to the cytoplasmic tail of the β subunit, initiating a cascade of events resulting in recruitment of focal adhesion kinase (FAK), paxillin, α-actinin and vinculin. As a result, the layer of proteins associated with the β subunits of integrins is called the “signaling layer”. Subsequent integrin activation requires the presence of mechanical forces, which drive conformational changes in multiple molecules, notably talin and integrin. Mechanical forces increase clustering of integrins, which allows the formation of new focal adhesion complexes (Ciobanasu et al., 2014). Furthermore, mechanical forces cause additional vinculin binding sites to be revealed in the C-terminal region of talin (del Rio et al., 2009). Vinculin is known to be the key link between

focal adhesions and the actin cytoskeleton (Thievessen et al., 2013). This layer is thus called the “force transduction layer”. Greater coupling to the actin cytoskeleton results in generation of more tension, which then further activates the cascades that allow the growth of protein assemblies at focal adhesions. This force dependent process is called focal adhesion maturation. Actin nucleators such as Arp2/3 are activated by upstream activators, which were found to reside in the next layer called the “actin regulatory layer”. This leads to increase in actin polymerization, further strengthening the link between the ECM and the actin cytoskeleton. Alternatively, tension or intracellular signaling can also trigger integrin activation in a ligand independent manner (Kim et al., 2011). This “inside out” signaling mechanism has been shown to be mediated by the small GTPase, Rap1 in the latter case (Katagiri and Kinashi, 2012), or by pulling forces from retraction fibers at the metaphase cortex in the former case (Petridou and Skourides, 2016) (Figure 1-2).

Due to the presence of multiple mechanosensitive proteins within focal adhesions, these structures are adapted to both sense and respond to changes in the mechanical environment of cells. For instance, increased stiffness can activate integrins directly to initiate the formation of focal adhesions, which then allows cells to generate greater traction forces on stiffer substrates (Friedland et al., 2009; Wei et al., 2008). Focal adhesions also act as potent signaling centers, with kinases such as FAK, Integrin Linked Kinase and Src communicating with other signaling pathways that ultimately affect cell survival and proliferation. For instance, when anchorage-dependent cells detach from the ECM, they undergo a form of programmed cell death called anoikis (Paoli et al., 2013). This is mediated by a lack of pro-survival signaling such as Akt signaling. Signaling pathways connected to focal adhesions can also determine cell fate choice. For instance, in a now classic study, the stiffness of the extracellular matrix can affect the fate decisions made by mesenchymal stem cells (Engler et al., 2006). On stiffer substrates, these cells differentiated into bone progenitors, while on soft substrates they favor neuronal lineages. To summarize, focal adhesions play vital roles in almost every aspect of cellular physiology.

Super-resolution imaging approaches were subsequently applied to cell-cell adhesions and surprisingly, these connections also show a similar hierarchical organization, with some components in common (Bertocchi et al., 2017). The direct receptors for cell-cell adhesion are a large family of proteins called cadherins (Harris and Tepass, 2010). The catenin complex links the cadherins to the actin cytoskeleton, with the catenin complex playing an analogous

role to talin (Bays and DeMali, 2017). Similar to cell-ECM adhesions, vinculin is a vital link to the actin cytoskeleton and plays multiple roles in mechanotransduction (Bays and DeMali, 2017).

Cell-cell adhesion thus forms another mechanosensory structure that can integrate information from other cells and therefore through the entire tissue. Indeed, cell-cell adhesion has been shown to play vital roles in tissue morphogenesis, acting as a means to mechanically couple the cytoskeletons of thousands of cells to produce collective cell behaviors such as organ sculpting, cell sorting and collective cell migration (Harris and Tepass, 2010). It must be noted that cadherins only form one class of cell-cell adhesion molecule. Many other classes of cell-cell adhesion complexes play diverse roles such as epithelial barrier function, synapse formation and immune response generation. These will not be discussed further here.

Figure 1-6

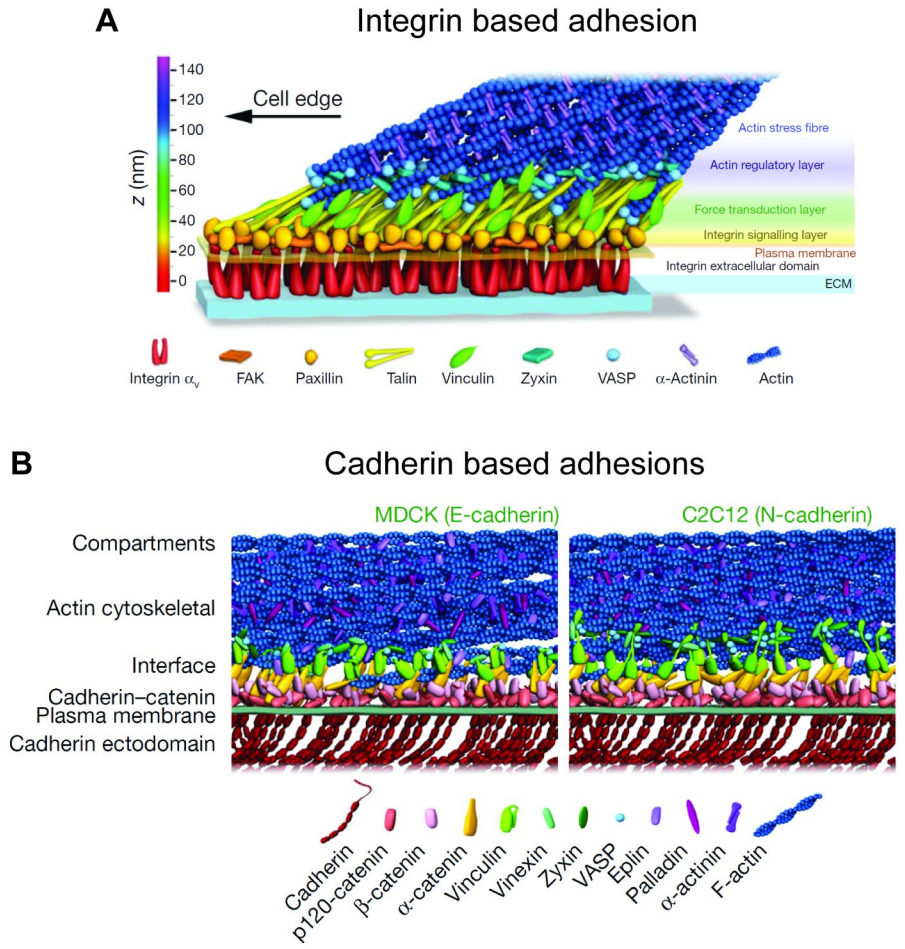

Figure 1-6- Nanoscale architecture of cell-ECM cell-cell adhesions

A super-resolution technique called interferometric Photoactivated Localization Microscopy (iPALM) can be used to obtain an axial resolution of ~10 nm. This technique has been used to reveal the nanoscale architecture of cell-ECM (A) and cell-cell (B) adhesions, showing that these are composed of different “layers”. For instance, in cell-ECM adhesions, the integrin extracellular layer binds ECM ligands, the intracellular domain of integrins that associates with talin and FAK forms the signaling layer, which recruits proteins such as vinculin that link to the actin cytoskeleton to form the force transduction layer. Actin regulating proteins such as VASP form the actin regulatory layer and activate actin nucleators such as Arp2/3. Actin nucleators further increase actin polymerization to strengthen the link between the ECM and the actin cytoskeleton. A similar organizational principle was discovered at cell-cell adhesions. The illustrations were obtained from- A)- (Kanchanawong et al., 2010), B)- (Bertocchi et al., 2017)

Chapter 2- The role of cell-substrate adhesion during cell division

Taneja, N., Fenix, AM., Rathbun, L., Millis, BA., Tyska, MJ., Hehnly, H., Burnette, DT. (2016). *Scientific Reports (6), 29846*

Taneja, N., Rathbun L., Hehnly, H., Burnette, DT. (2019). *Current Opinion in Cell Biology (56), 46-52*

Introduction

The ability to divide is a fundamental property of living cells. The 3D orientation of cell division is essential for embryogenesis, maintenance of tissue organization and architecture, as well as controlling cell fate. Recent studies on mitotic spindle orientation have focused on the role of microtubules in spindle placement. The mitotic spindle is a microtubule-based structure composed of both central spindle microtubules as well as astral microtubules that extend from the centrosomes and interact with the polar cortex (Figure 1-2). Pulling forces generated by astral microtubules contribute to the placement and subsequent separation of chromosomes from the metaphase plate. However, additional mechanisms are likely needed to position the spindle in three-dimensional space beyond that of astral microtubules. Some of the earliest studies of spindle orientation focused on cell shape as the major driver of spindle placement, where the mitotic spindle is preferentially placed along the longest axis of a cell, called Hertwig's rule. One key regulator in controlling cell shape is the actin cytoskeleton (Pollard and Cooper, 2009). Actin-dependent structures, such as the actin cortex (Bosveld et al., 2016; Fink et al., 2011) and sub-cortical actin clouds (Kwon et al., 2015) have been implicated in spindle positioning. Strikingly, many of the molecular players that regulate the actin cytoskeleton have been identified at the centrosome through proteomic analysis (Andersen et al., 2003). The centrosome is not only a microtubule organizing center but also nucleates actin filaments (Farina et al., 2016), suggesting that crosstalk likely exists between the actin and microtubule cytoskeletons. The crosstalk between these two elements is likely an essential mechanism for spindle placement. An understanding of how this crosstalk is coordinated in space and time requires better elucidation of the molecular nature of contractile and adhesive actin-based structures during mitosis and cytokinesis.

Upon mitotic entry, the actin cytoskeleton is re-organized to disassemble stress fibers to form an isotropic contractile cortical network, allowing the cell to increase surface tension and adopt a spherical shape (Ramanathan et al., 2015; Ramkumar and Baum, 2016). Upon completion of anaphase, accumulation of myosin II at the equator results in the formation of a contractile ring, the major contractile apparatus that drives cytokinesis (Barr and Gruneberg, 2007). This accumulation can occur through both spindle dependent and independent mechanisms. The former is mediated through the centralspindlin complex, while the latter occurs through polarity cues, such as those mediated by Protein Kinase N in *Drosophila* neuroblasts (Glotzer, 2017; Roth et al., 2015; Tsankova et al., 2017).

While the mechanisms generating contractility at the cleavage furrow have been intensively studied, a second actomyosin network exists at the polar ends of the cell. The polar cortex, which usually retains low contractility during cytokinesis, can generate substantial forces that can cause spindle oscillations (Burton and Taylor, 1997; Sedzinski et al., 2011). The adhesive actin structures that balance these contractile forces to modulate the final three-dimensional shape of the cell are less well understood.

The geometry of the cleavage furrow during mitosis is often asymmetric *in vivo* and plays a critical role in stem cell differentiation and the relative positioning of daughter cells during development (Das et al., 2003; Goulas et al., 2012; Guillot and Lecuit, 2013; Jinguji and Ishikawa, 1992; Kosodo et al., 2004). Early observations of adhesive cell lines revealed asymmetry in the shape of the cleavage furrow, where the bottom (i.e., substrate attached side) of the cleavage furrow ingressed less than the top (i.e., unattached side) (Fishkind and Wang, 1993). This data suggested substrate attachment could be regulating furrow ingression to determine cell shape, in turn affecting the final three-dimensional orientation of the mitotic spindle.

Results

We started our exploration of how adhesions shape the cleavage furrow using a classic model of mitosis: single cells dividing in culture. FAs are formed through binding of specific integrins to extracellular matrix (ECM) proteins. Therefore, we plated HeLa cells on coverslips coated with 10 µg/mL fibronectin (FN) (Figure 2-1) as previously used for studies of cell migration (Thievessen et al., 2013). After fixation, DNA was labeled with Hoechst and myosin IIA was labeled with fluorescent antibodies. Hoechst allowed us to identify cells in mitosis and myosin IIA labeling allowed us to visualize cell shape. 3D structured illumination microscopy (SIM) (Gustafsson, 2005; Schermelleh et al., 2008) of cells in anaphase B/telophase revealed the cleavage furrow was symmetrical in the XY plane, which indicated the cell had ingressed equally from either side (Figure 2-1). However, XZ projections revealed the cleavage furrow often ingressed further from the top of the cell than the bottom (Figure 2-1), consistent with previous findings using adhesive NRK cells (Fishkind and Wang, 1993). We next wanted to test if the geometry of the cleavage furrow was dependent on the extent of adhesion to the substrate.

Studies during interphase reported that cells make smaller and less stable FAs on coverslips coated with low densities of FN (i.e., <5 µg/mL) and larger and more stable FAs on substrates coated with high concentrations of FN (>30 µg/mL) (Gupton and Waterman-Storer, 2006). We predicted increasing adhesions with a “high” FN substrate would result in less ingression from the bottom of the cell and, thus, an asymmetrical cleavage furrow. Therefore, we plated cells on low (1 µg/mL FN) and high (50 µg/mL FN) adhesive substrates and then analyzed cell shape. Cells were grouped into three stages of anaphase (i.e., early, mid, and late) based on the axial diameter of the contractile ring (see Figure 2-S1 and Materials and Methods). We noted a ~4-fold and ~13-fold increase in ingression from the bottom on the low adhesive substrate compared to the high adhesive substrate during early and mid-anaphase, respectively (Figure 2-1). Notably, high bottom ingression was measured during late anaphase on both low and high FN. Midbody formation was observed at varying distances from the substrate, suggesting other mechanisms could be operating during the final stages of cytokinesis. Furthermore, we also calculated the aspect ratio of the contractile ring to test whether these resistive forces were transmitted to the ring. The contractile ring was significantly more circular on the low adhesive substrate (1 µg/mL FN, Figure 2-S1), while on the high adhesive substrate (50 µg/mL FN) the ring was flatter and had a significantly

increased aspect ratio (Figure 2-S1, 1.3 compared to 1). Together, these initial observations suggest that increasing adhesion to the substrate drives asymmetrical ring contraction by preventing ingression from the bottom of the cell.

We next wanted to understand the nature of the adhesive forces that control 3D shape of the cleavage furrow. A previously described mitotic population of adhesions can occur within retraction fibers (Mitchison, 1992; Sanger and Sanger, 1980). Retraction fibers form during mitotic entry and are thought to contribute to the XY orientation of the mitotic spindle during metaphase and further dictate the pattern of cell spreading after mitotic exit of the two daughter cells (Cramer and Mitchison, 1993; Thery et al., 2005). Each retraction fiber has a FA mediating attachment to the substrate. We hypothesized retraction fibers on high FN substrates would form larger/more stable FAs and these may be driving asymmetric furrow ingression. To test this hypothesis, we localized the FA protein, paxillin, in cells during anaphase. Surprisingly, we found no difference in the sizes of FAs at the ends of retraction fibers (Figure 2-1, white arrows in panel C). However, we did observe an additional population of adhesions distinct from retraction fibers, located directly underneath the cell body (Figure 2-1, green arrows in panel C). Consistent with reported data for interphase cells, mitotic cells assembled more adhesions and had a greater spread area on the high FN substrate compared to the low FN samples (Figure 2-1 and Figure 2-S2).

To understand the temporal dynamics of mitotic adhesions, we turned to live cell TIRF microscopy. HeLa cells expressing EGFP-Paxillin and H2B-mCherry were imaged starting at metaphase through anaphase and telophase. Small, but distinct and highly dynamic adhesions were observed underneath the cleavage furrow, undergoing continuous formation and turnover (Figure 2-1). Mitotic FAs underneath the furrow disappeared just prior to cleavage furrow ingression (Figure 2-1). This was followed by initiation of cell spreading (Figure 2-1). Therefore, mitotic FAs exist during the metaphase to anaphase transition and are spatially and temporally distinct from retraction fibers.

Figure 2-1

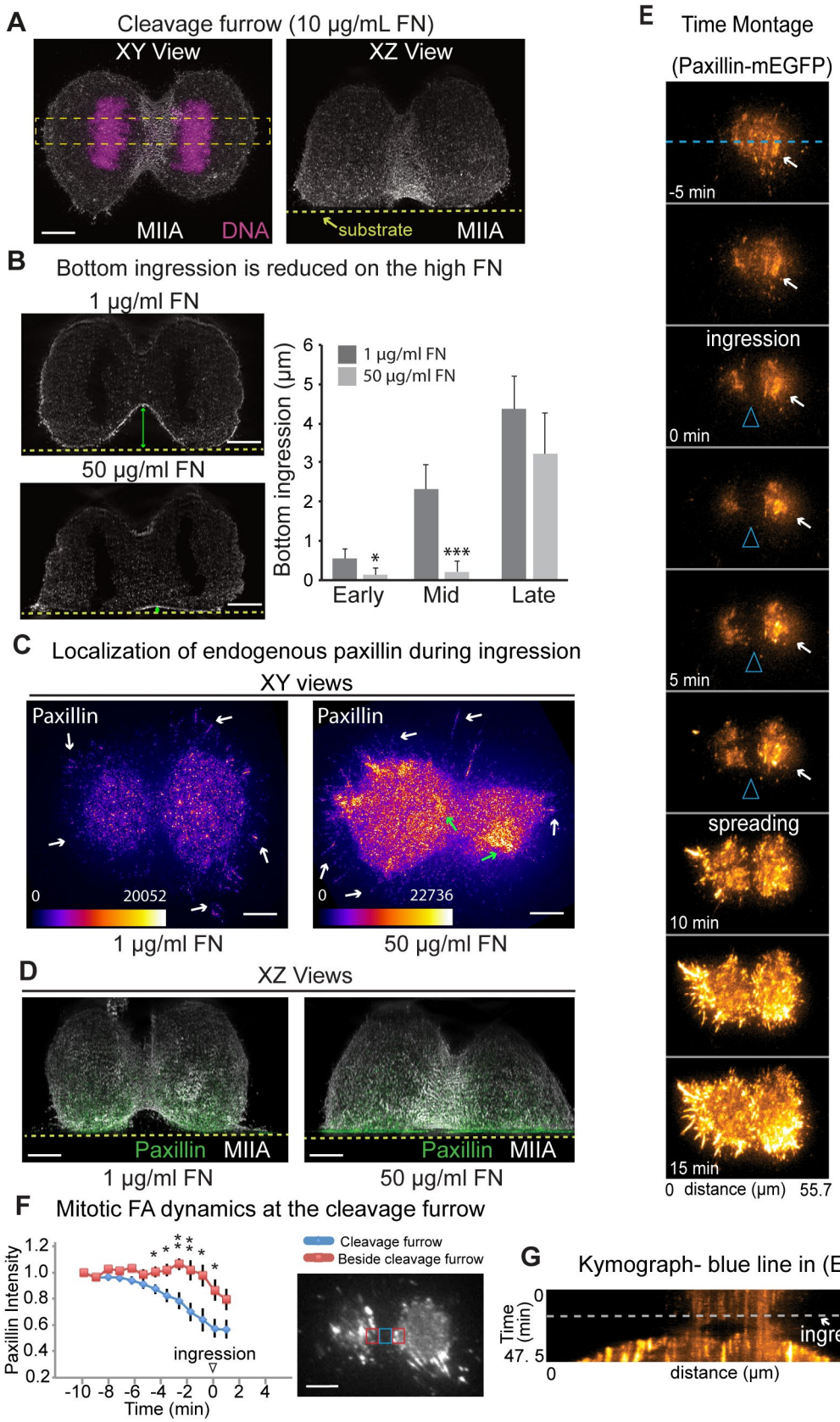
A
Cleavage furrow (10 µg/mL FN)
XY View
XZ View
MIIA
DNA
substrate
MIIA
B
Bottom ingression is reduced on the high FN
1 µg/ml FN
50 µg/ml FN
Bottom ingression (µm)
1 µg/ml FN
50 µg/ml FN
Early
Mid
Late
C
Localization of endogenous paxillin during ingression
XY views
Paxillin
Paxillin
0
20052
0
22736
1 µg/ml FN
50 µg/ml FN
D
XZ Views
Paxillin MIIA
Paxillin MIIA
1 µg/ml FN
50 µg/ml FN
E
Time Montage
(Paxillin-mEGFP)
-5 min
ingression
0 min
5 min
spreading
10 min
15 min
0 distance (µm) 55.7
F
Mitotic FA dynamics at the cleavage furrow
Paxillin Intensity
ingression
Time (min)
Cleavage furrow
Beside cleavage furrow
G
Kymograph- blue line in (E)
Time (min)
ingression
distance (µm)

Figure 2-1- Substrate adhesion controls the symmetry of the cleavage furrow

A) XY and XZ views of the cleavage furrow of a HeLa cell at anaphase cultured on 10 µg/mL FN and stained for endogenous MIIA and DNA. B) XZ views of the cleavage furrow of cells cultured on low (1 µg/mL) and high (50 µg/mL) FN substrates. XZ projections were made from a similar sized ROI as in (A). Ingression from the bottom (shown as double headed green arrow) was measured as the distance between the substrate (dotted yellow line) and the bottom of the cleavage furrow. Cells were grouped based on the height of the cleavage furrow into early (>15 µm), mid (9-15 µm) and late (3-9 µm) stages of ingression. Measurements were made on 34 cells and 42 cells for 1 µg/mL and 50 µg/mL FN, respectively, across 6 independent experiments for each condition. C) Localization of endogenous paxillin underneath the cleavage furrow using SIM. Shown are XY views of HeLa cells at anaphase stained for paxillin, cultured on low and high adhesive substrates. Look up table is fire and color bars show the gray scale values of the images. White arrows show retraction fiber adhesions and green arrows show mitotic FAs. D) Merged XZ views of HeLa cells at anaphase stained for paxillin (green) and MIIA (gray) cultured on low and high adhesive substrates. XY views are shown in Figure S1C. E) TIRF time montage of a HeLa cell expressing Paxillin-mEGFP and H2B-mCherry cultured on high adhesive substrate undergoing anaphase imaged using TIRF microscopy. Ingression starts at 0 min and the arrowheads indicate the position of the cleavage furrow. Arrows denote the side with larger adhesions maintained until the daughter cells start spreading at 10 min. F) Quantification of relative paxillin intensity comparing adhesions underneath the cleavage furrow (red ROI in inset) and immediately adjacent to the cleavage furrow (blue ROI in inset). 0 minutes denotes the ingression of the cleavage furrow. Measurements were made from 7 cells across 5 independent experiments. G) Kymograph created from blue line in (C). Dotted line denotes the onset of ingression. * denotes $p<0.05$ and ** denotes $p<0.01$; Scale bars, 5 µm. Error bars show standard error of the mean.

We next wanted to investigate the molecular mechanisms controlling the function of mitotic FAs. We hypothesized that similar mechanisms control adhesion dynamics during interphase and mitosis. Thus, we targeted molecular players known to regulate adhesion strength during interphase. Inhibition of focal adhesion kinase (FAK) has been reported to stabilize FAs by preventing their disassembly (Webb et al., 2004). Thus, creating stable FAs through FAK inhibition during mitosis should further reduce ingression from the bottom. Therefore, we inhibited FAK with an acute treatment of a specific drug, PF-228 (Slack-Davis et al., 2007). To prevent adhesion disassembly only during mitosis, we treated cells with 1 μM PF-228 for 10 minutes before fixation and immuno-labeling so that any cells analyzed during anaphase would have been targeted during metaphase or later. Drug treatment reduced FAK auto-phosphorylation by 66.7 +/- 9.5% (Figure 2-2) and resulted in larger mitotic adhesions in cells on low FN (Figure 2-2 compared with Figure 2-1, Figure 2-S2). Bottom ingression on high FN was also reduced upon PF-228 treatment compared to control cells. There was also a ~8-fold decrease in bottom ingression during early anaphase and greater than 2-fold reduction during mid anaphase when cells were on low FN (Figure 2-2). Thus, FAK inhibition can enhance asymmetric ingression even when cells are on a low adhesive substrate (Figure 2-2).

Vinculin is part of the molecular clutch that links adhesions to the actin cytoskeleton (Thievessen et al., 2013). To determine if vinculin also serves as a clutch to regulate cleavage furrow ingression, we used siRNA to knockdown endogenous vinculin protein (Figure 2-2). Indeed, we observed knockdown of vinculin caused a nearly 10-fold increase in ingression from the bottom on the high adhesive substrate (Figure 2-2). Taken together, these findings indicate FAK and vinculin regulate cleavage furrow ingression.

Figure 2-2

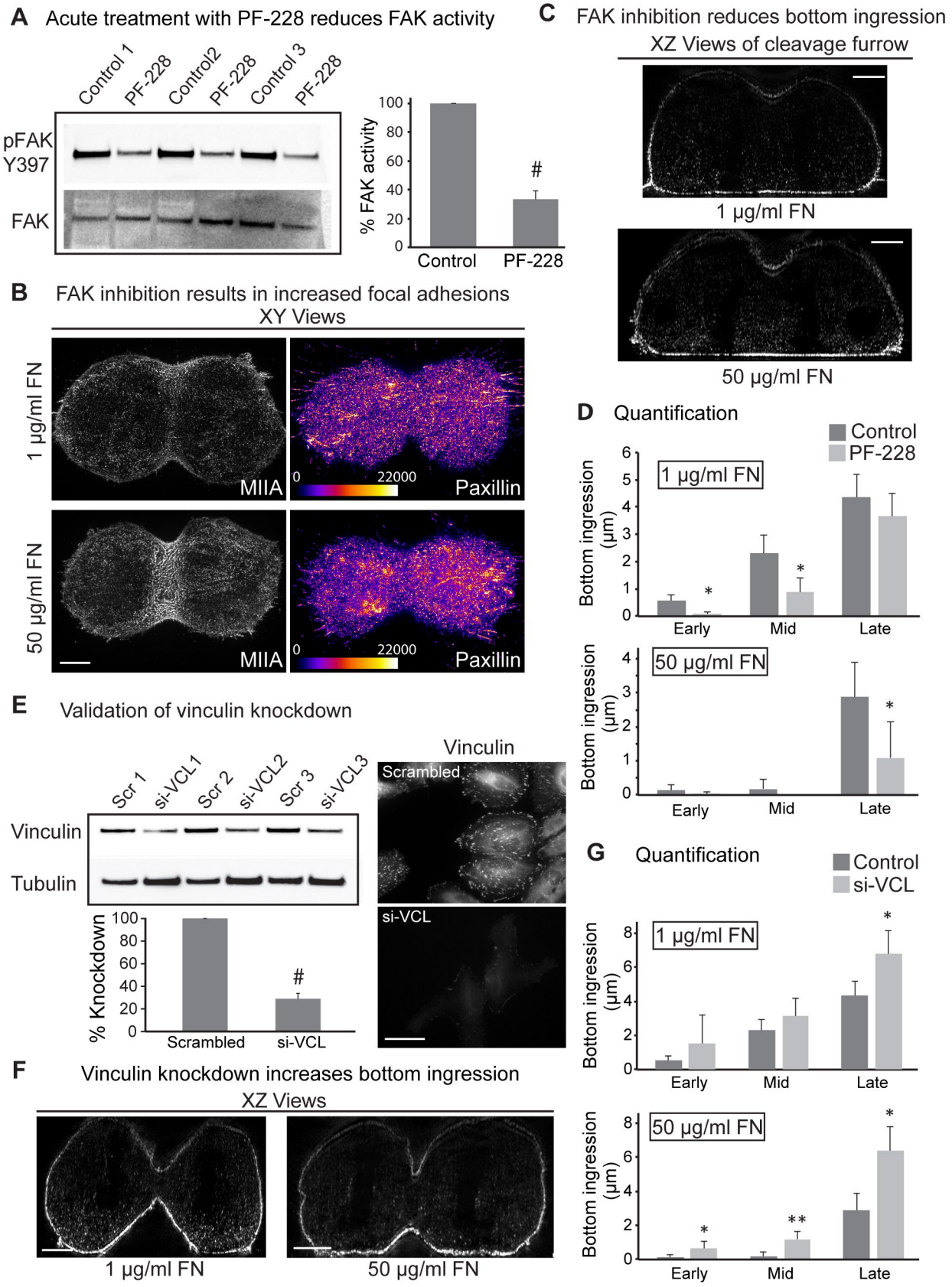
A
Acute treatment with PF-228 reduces FAK activity
Control 1
PF-228
Control2
PF-228
Control 3
PF-228
pFAK Y397
FAK
% FAK activity
100
80
60
40
20
0
#
Control
PF-228
B
FAK inhibition results in increased focal adhesions
XY Views
1 µg/ml FN
50 µg/ml FN
MIIA
Paxillin
0
22000
C
FAK inhibition reduces bottom ingression
XZ Views of cleavage furrow
1 µg/ml FN
50 µg/ml FN
D
Quantification
Control
PF-228
1 µg/ml FN
50 µg/ml FN
Bottom ingression (µm)
Early
Mid
Late
E
Validation of vinculin knockdown
Scr 1
si-VCL1
Scr 2
si-VCL2
Scr 3
si-VCL3
Vinculin
Tubulin
% Knockdown
Scrambled
si-VCL
Vinculin
Scrambled
si-VCL
F
Vinculin knockdown increases bottom ingression
XZ Views
1 µg/ml FN
50 µg/ml FN
G
Quantification
Control
si-VCL
1 µg/ml FN
50 µg/ml FN
Bottom ingression (µm)
Early
Mid
Late

Figure 2-2- Molecular mechanisms governing mitotic FAs

A) Western blot to validate acute inhibition of FAK using the FAK inhibitor (PF-228). Lysates were prepared from cells treated for 10 minutes versus untreated controls from 3 independent experiments. Total FAK was used as loading control. Intensities for each lane were normalized to the respective loading controls. B-C) XY (B) and XZ (C) views of HeLa cells at anaphase stained for MIIA and paxillin, cultured on low (top) and high (bottom) adhesive substrate treated with 1 μM FAK inhibitor PF-228. D) Quantification of bottom ingression comparing FAK inhibitor treated versus untreated control cells cultured on low and high FN substrates. Cells were grouped into early, mid, and late anaphase based on the height of the cytokinetic ring as in Figure 2-1. Measurements were made on 31 cells across 4 independent experiments and 30 cells across 3 independent experiments for 1 and 50 μg/mL FN, respectively. E) Validation of si-RNA knockdown of vinculin using western blotting and immunofluorescence. For western blotting, intensities for each lane were normalized to the respective tubulin loading controls. Each knockdown was then normalized to the respective scrambled (Scr) control. N= 3 independent experiments. For immunofluorescence, control and knockdown HeLa cells were stained for endogenous vinculin. F) XZ views of vinculin knockdown HeLa cells at anaphase cultured on low and high adhesive substrates. G) Quantification of bottom ingression comparing vinculin knockdown versus control cells cultured on low and high adhesive substrates. Cells were grouped into early, mid, and late anaphase as in Fig 2-1. Measurements were made on 17 cells across 3 independent experiments and 24 cells across 4 independent experiments for 1 μg/ml and 50 μg/ml FN, respectively. Scale bars in (B-C) and (F), 5 μm; (E), 100 μm. * denotes $p<0.05$ and ** denotes $p<0.01$. Error bars in (A), (D-E) and (G) show standard error of the mean.

Although single isolated cells are a powerful model for exploring mechanisms that govern the attachment of mitotic FAs to the ECM, cells are often also attached to other cells *in vivo*. This is particularly true for cells within an epithelial sheet. Epithelial cells form FAs on their basal domain and tight junctions and adherens junctions (i.e., cell-cell contacts) on their apical and lateral domains, respectively (Jefferson et al., 2004; Yeatman, 2004). Of note, cleavage furrows of epithelial cells dividing *in vivo* tend to ingress from the basolateral side towards the apical side (Guillot and Lecuit, 2013; Jinguji and Ishikawa, 1992), and this type of asymmetric ingression is required for proper differentiation of neural epithelia (Goulas et al., 2012). We hypothesized a low adhesive state on the bottom (i.e., basolateral side) of epithelial cells could allow the cleavage furrow to detach and pull itself towards cell-cell contacts (i.e., apical). To test this hypothesis, we grew monolayers of MDCK cells on low FN, and found the cleavage furrow did ingress from the bottom (Figure 2-3, top panels in panel B). Cells on high FN showed ~8 fold less ingression from the bottom and more from the top compared to low FN during mid-anaphase (Figure 2-3). This data suggested ECM adhesion determines the shape of the cleavage furrow in mitotic cells that are integrated into epithelial monolayers.

To determine if mitotic adhesions shape the cleavage furrow of epithelial cells in a regulated way, we inhibited FAK and measured furrow ingression. FAK inhibition resulted in a dramatic 16-fold decrease in furrow ingression from the bottom of MDCK cells on the low FN during mid-anaphase, as well as small reduction on high FN during early and late anaphase (Figure 2-3). To further test if FAK inhibition was working through mitotic adhesions to the ECM, we analyzed ingression in cells lacking ECM attachment due to presence of a very soft matrix. For these experiments, we grew MDCK cells in polarized 3D cysts sitting on coverslips (Lee et al., 2007). The basolateral side of the cells was on the outside of the cysts (Figure 2-3, open arrowheads in panel E) and the apical side was on the luminal side (Figure 2-3, closed arrowheads in panel E). In the case of cells at the sides of the cyst that have no attachment to the coverslip in contact with the liquid medium, the cleavage furrow of these cells ingressed completely towards the apical (luminal) side of the cell with or without FAK inhibition (Figure 2-3). Thus, the influence of FAK on furrow-shape requires adhesions to the ECM. To visualize whether epithelial cells *in vivo* also ingress their cleavage furrow from the basolateral domain, we visualized furrow ingression in cells dividing near the base of the crypt of small intestine. We observed that furrow ingression indeed proceeds from the basolateral domain (Figure 2-S3), suggesting that the base of the crypt behaves like a low adhesive environment.

Figure 2-3

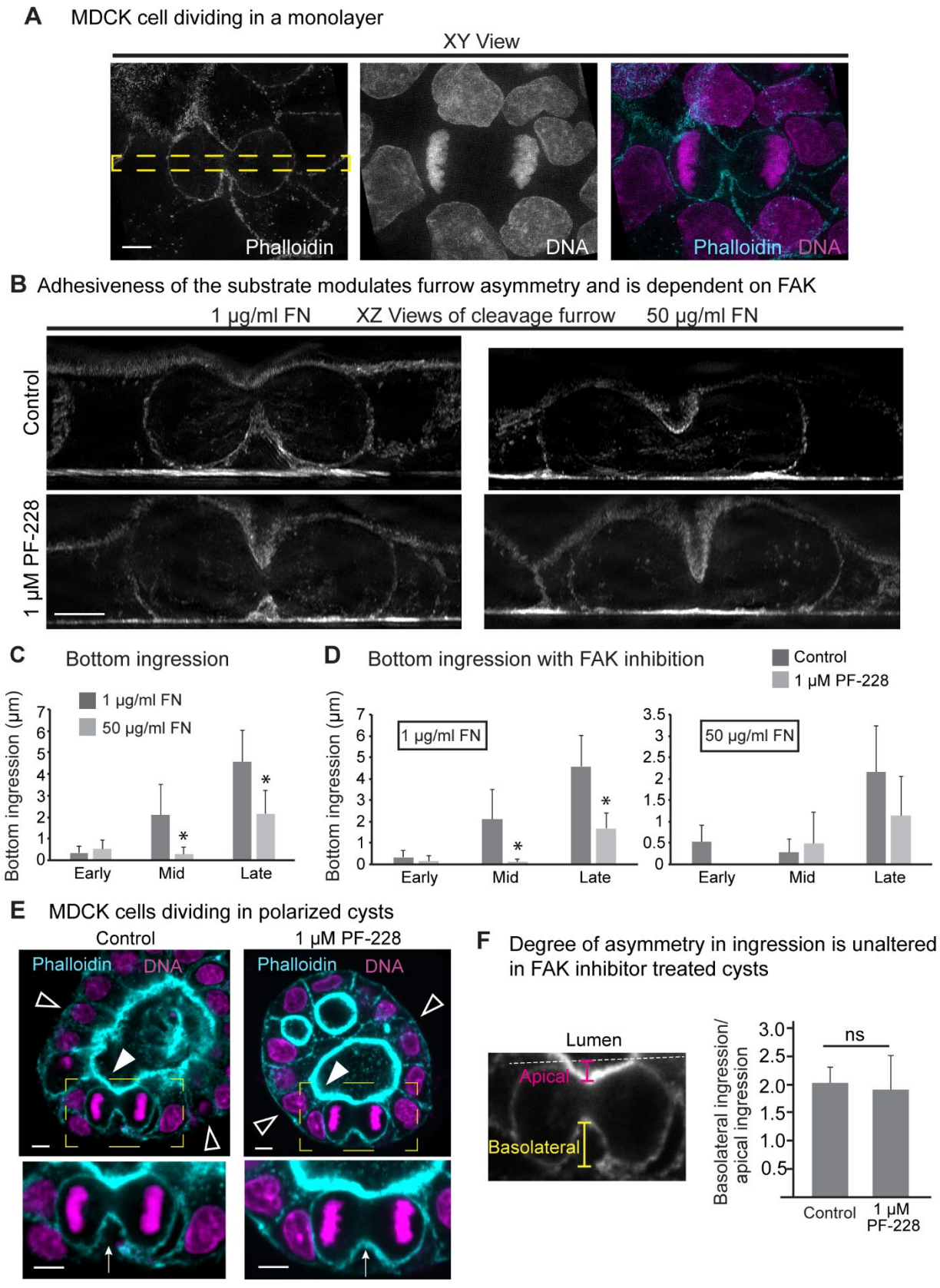
A
MDCK cell dividing in a monolayer
XY View
Phalloidin
DNA
Phalloidin DNA
B
Adhesiveness of the substrate modulates furrow asymmetry and is dependent on FAK
1 µg/ml FN
XZ Views of cleavage furrow
50 µg/ml FN
Control
1 µM PF-228
C
Bottom ingression
1 µg/ml FN
50 µg/ml FN
Bottom ingression (µm)
Early
Mid
Late
D
Bottom ingression with FAK inhibition
Control
1 µM PF-228
1 µg/ml FN
50 µg/ml FN
E
MDCK cells dividing in polarized cysts
Control
1 µM PF-228
Phalloidin DNA
F
Degree of asymmetry in ingression is unaltered in FAK inhibitor treated cysts
Lumen
Apical
Basolateral
Basolateral ingression/ apical ingression
ns
Control
1 µM PF-228

Figure 2-3- Adhesiveness of the substrate controls cleavage furrow shape in epithelial sheets

A) XY view of a cell dividing in a MDCK monolayer cultured on 1 µg/ml FN stained with phalloidin (cyan) and DAPI (magenta) imaged using SIM. B) XZ views of control (top row) and FAK inhibitor treated (bottom row) cells dividing within a monolayer grown on low (left column) and high (right column) adhesive substrates. The XZ projections of the cleavage furrow were created from a thin slice (marked by dotted yellow box in (A)) passing through the long axis of the cell. C) Quantification of basolateral ingression comparing low and high adhesive substrates. D) Quantification of basolateral ingression comparing control and treated cells on low and high adhesive substrates. Cells were grouped into early (>10 µm), mid (6-10 µm) and late (1-5 µm) anaphase based upon the height of the cytokinetic ring. For the graph comparing control cells, measurements were made on 33 cells across 3 independent experiments and 36 cells across 4 independent experiments for 1 µg/ml and 50 µg/ml FN, respectively. For the graph comparing FAK treated cells with control cells, measurements were made on 23 cells for 1 µg/ml FN and 24 cells for 50 µg/ml FN across 3 independent experiments for each condition. E) Cross sections through a MDCK cyst showing cells at anaphase in either control (left) or FAK inhibitor treated (right) cysts stained with phalloidin (cyan) and DAPI (magenta). Shown are maximum projections of six 200 nm Z slices, with magnified views of the region marked by the dotted yellow rectangle below. F) Quantification of degree of asymmetry in furrow ingression comparing control and FAK inhibitor treated cysts. The degree of asymmetry was calculated as ratio of basolateral versus apical ingression as shown in the inset. Measurements were made on 11 control cysts across 5 independent experiments and 4 FAK inhibitor treated cysts across 3 independent experiments. Scale bars: 5 µm; * denotes $p<0.05$.

We next wanted to explore what other cellular processes could be affected by mitotic FAs. Interestingly, during anaphase we noted one daughter was shorter than the other on high FN (Figure 2-1). Corresponding XY views indicated the shorter cell had larger FAs (Figure 2-S1). Indeed, quantification of FAs on either side of the cleavage furrow from our live cell TIRF data confirmed this asymmetric attachment occurs only on the high FN substrate (Figure 2-4). The observed cellular shape during anaphase (Figure 2-1) suggested one pole of the mitotic spindle could be closer to the substrate than the other, characteristic of a tilted spindle in XZ. Therefore, we took two approaches to determine the tilt of an anaphase mitotic spindle by measuring the angle between the substrate and a line joining the centroids of the DNA or the spindle poles marked with centrin (Figure 2-4). Each method yielded statistically identical spindle angles (Figure 2-4). Using these two methods, we noted that on the high adhesive substrate (50 µg/mL FN), anaphase spindles demonstrated a mean angle of 9.7° +/- 3.6°, whereas on low adhesive substrate (1 µg/mL FN), a mean angle of 5.5 +/- 2.4° was calculated (Figure 2-4). To test whether changes in the shape of the cleavage furrow also affect spindle tilt, we measured spindle tilt upon FAK inhibition and vinculin knockdown, which increases and decreases the strength of adhesion, respectively (as noted in Figure 2-2). Upon inhibition of FAK, spindle tilt was significantly increased on the low adhesive substrate. Conversely, with vinculin depletion it was decreased on the high adhesive substrate. In MDCK monolayers, a spindle angle of 0-5° was calculated on either low or high FN. However, upon addition of the FAK inhibitor a mean spindle angle of 5.5° was observed for cells grown on 1 µg/ml FN compared to a mean angle of 3° for control MDCK cells. Thus, in both MDCK and HeLa cells, increasing adhesion by inhibiting FAK causes an increase in spindle tilt.

Of note, we found using a Centrin-GFP cell line that the mother (i.e., older) spindle pole, marked by the spindle pole with a brighter centrin signal (Kuo et al., 2011) (Figure 2-4), was preferentially tilted towards the substrate. We confirmed these results using an alternative approach, where we used an antibody to cenexin, which specifically marks the mother centrosome (Hung et al., 2016; Izumi and Kaneko, 2012; Lange and Gull, 1995), and observed similar results (Figure 2-S4). In addition, we noted that metaphase cells on FN demonstrated a mean spindle angle of 20° towards the substrate (Figure 2-4).

Figure 2-4

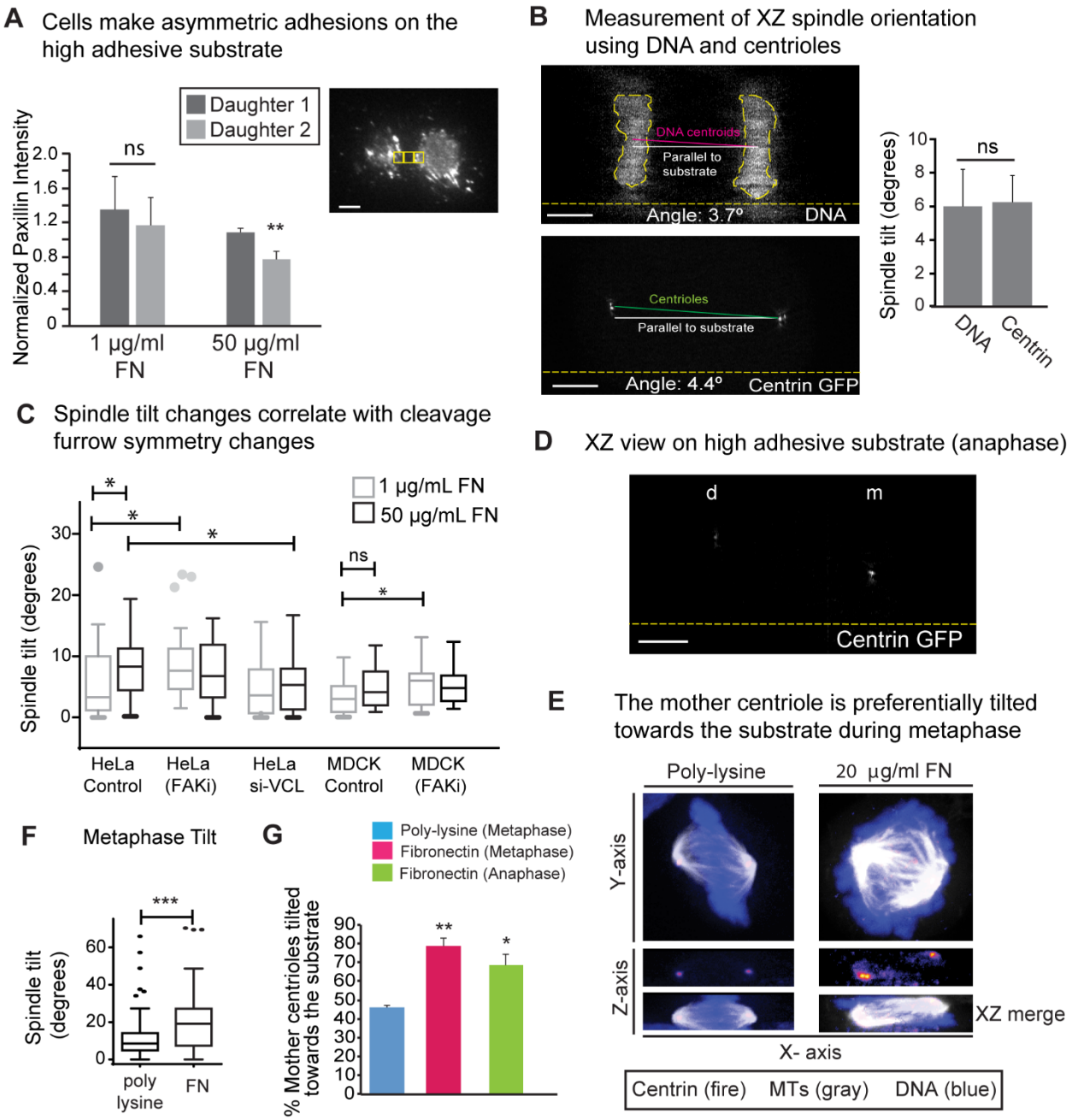

Figure 2-4- Adhesiveness of the substrate modulates the XZ orientation of the spindle

A) Quantification of degree of asymmetry in attachment on low and high adhesive substrates using TIRF. ROIs on either side of the cleavage furrow ROI were compared. Measurements were made from 8 cells across 5 independent experiments as in Figure 2d for 50 µg/mL FN and 4 cells across 4 independent experiments on 1 µg/mL FN. B) Methods used to quantify spindle tilt. XZ tilt of the spindle was calculated by either measuring the angle between the line joining the centroids of the chromosomes (solid magenta line) and the substrate (solid white line) or by measuring the angle between the line joining the centrioles (solid green line) and the substrate (solid white line) using a

HeLa cell line stably expressing GFP centrin. Dotted yellow line shows the substrate. Graph shows comparison of the two methods. Spindle tilt was measured using both methods in 28 cells across 5 independent experiments. C) Tukey plots comparing spindle tilt measured using the DNA centroids method across all experimental conditions tested for HeLa and MDCK cells in the study D) XZ view of a HeLa cell stably expressing centrin GFP at anaphase on a high adhesive substrate showing the mother (m) and daughter (d) centrioles. E) Shown are confocal images of cells in metaphase on FN or poly-L-lysine, with XY and XZ views of DNA (blue), centrin (fire) and tubulin (gray). F) Tukey plots comparing the average spindle tilt on poly-L-lysine versus FN during metaphase. G) Graph comparing the propensity of the mother centriole being tilted towards the substrate during metaphase and anaphase. Scale bars, 5 μm. * denotes $p<0.05$, ** denotes $p<0.01$ and *** denotes $p<0.005$. Error bars in (B) and (D-E) show standard error of the mean.

Discussion

A balance between contraction and adhesion to the substrate has been demonstrated to determine the three-dimensional shape of migrating cells during interphase (Burnette et al., 2014). A similar balance between adhesion and contraction during cytokinesis was first proposed by Fishkind and Wang (Fishkind and Wang, 1993). Our results reveal the molecular underpinnings of this force-balance, namely integrin-based focal adhesion regulated by the vinculin-FAK-paxillin signaling axis. In single cells, our model suggests that strong adhesion to the substrate would create high resistance to the contractile force generated by the contractile ring, in turn resulting in asymmetric ingression from the top of the cell. Under low adhesion conditions, there would be less resistive force and therefore the top and bottom of the cell ingress symmetrically (Figure 2-5). We also show cell-cell contacts in epithelial cells directing the ingression of the cleavage furrow. The resultant shape of the cleavage furrow under low adhesion to the substrate is similar to that usually observed *in vivo*, such as in *Drosophila* embryos (Guillot and Lecuit, 2013), mouse neuroepithelium (Goulas et al., 2012) and intestinal crypts (Jinguji and Ishikawa, 1992) (Figure 2-S3).

Initial biochemical studies investigating the link between cell cycle and adhesion remodeling focused on mapping changes in phosphorylation of focal adhesion signaling layer proteins FAK, p130Cas and paxillin during mitosis (Yamaguchi et al., 1997; Yamakita et al., 1999). How these changes were linked to cell cycle progression however was unclear. It was recently shown that Cdk1 is the master regulator of this process, with low Cdk1 activity during G2 promoting adhesion disassembly (Jones et al., 2018). In further support of these findings, traction forces were found to peak during S-phase, subsequently decreasing during G2, a finding consistent even in epithelial sheets (Uroz et al., 2018; Vianay et al., 2018). These studies have significantly advanced our understanding of adhesion remodeling leading to mitotic entry, while others have uncovered complex adhesion dynamics immediately following mitotic exit.

Figure 2-5

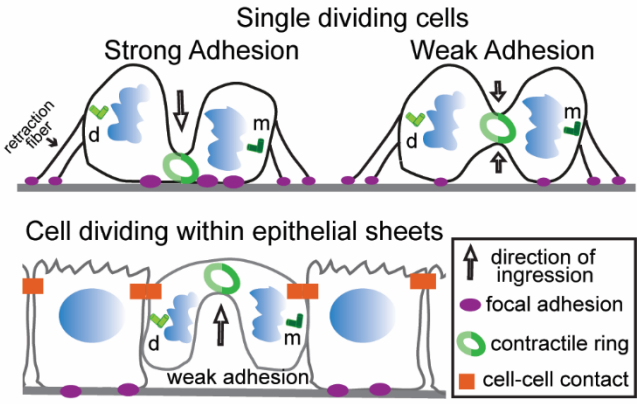

Figure 2-5- Working model

Our model for how mitotic adhesions control the 3D shape of the cleavage furrow of single cells and cells within epithelial monolayers. m and d indicate mother and daughter centriole, respectively.

Early work using substrate wrinkling showed that mitotic cells exert forces on the substrate (Burton and Taylor, 1997). Interestingly, the greatest wrinkling was observed underneath the cleavage furrow during ingression, which then dissipated towards the cell periphery, corresponding to the initiation of cell spreading. This suggests a dynamic redistribution of cell-substrate adhesions during cytokinesis. Recent work has measured matrix deformation throughout mitosis in cell cultured in 3D matrices (Nam and Chaudhuri, 2018). Notably, matrix deformation increased during mitotic progression, peaking during cytokinesis. This suggests that the contractile ring also generates significant forces in 3D environments. Transmission of such forces to the substrate would require cell-matrix contacts to be present immediately following mitotic exit.

Based on our data, we attribute the resistive force largely to the mitotic FAs underneath the cell body. First, they are the largest FAs prominent throughout mitosis (Petridou and Skourides, 2016). Second, we show that mitotic FAs are responsive to adhesiveness of the substrate (Figure 2-2) and are regulated by FAK and vinculin activity (Figure 2-3). Interestingly, we did not observe significant changes in retraction fiber density in response to either substrate adhesiveness or signaling. What then is the role of retraction fibers? Previous work using patterned substrates showed the position of the cleavage furrow and XY orientation of the mitotic spindle is determined by adhesive patterns (Thery et al., 2005). Specifically, the spindle aligns with the axis of strongest external force in XY exerted by retraction fibers or cell-cell contacts (Bosveld et al., 2016; Fink et al., 2011). Furthermore, retraction fibers also maintain the orientation of the spindle parallel to the substrate(Toyoshima and Nishida, 2007). It has recently been reported force generated by retraction fibers activates β-1 integrin on the mid lateral cortex (Petridou and Skourides, 2016). Therefore, the ultimate orientation of the spindle in three dimensions is likely determined by an interplay of retraction fibers maintaining the spindle parallel to the substrate and mitotic FAs pulling the mother centrosome towards the substrate through a yet to be defined mechanism

The XZ orientation of the spindle and specific placement of the oldest mitotic centrosome have been implicated in the stereotyped behavior of germline stem cells and neuroblasts in Drosophila (Januschke et al., 2011; Yamashita et al., 2007) and in several invertebrate cell types (Chen et al., 2014; Hehnly et al., 2015; Izumi and Kaneko, 2012; Januschke et al., 2011; Paridaen et al., 2013; Wang et al., 2009; Yamashita et al., 2007). We observed the mother spindle pole preferentially localizes to the daughter cell with more mitotic FAs. This observation

may explain the original observation by Yamashita et al where the oldest mitotic centrosome remains closer to the niche in dividing germline stem cells (Yamashita et al., 2007), In addition to germline stem cells, mammalian gut stem cells orient their divisions so that the cell that retains contact with the ECM retains stemness (Quyn et al., 2010). Therefore, our findings suggest mitotic FAs may play multiple roles in stem cell homeostasis, including anchoring stem cells to a niche and retention of specific stem cell factors such as recruitment of the mother spindle pole (Wang et al., 2009). Deregulation of normal stem cell differentiation has been implicated to cause tumorigenesis (Reya et al., 2001). Therefore, the balance of adhesive forces determining the position and fate of dividing stem cells could also play a role during tumorigenesis.

Materials and Methods

Cell culture and chemicals

HeLa (ATCC, CCL-2) and HeLa centrin-EGFP(Kuo et al., 2011) cells were cultured in growth media comprised of DMEM (Mediatech, Inc., Manassas, VA, 10-013-CV) containing 4.5 g/L L-glutamine, L-glucose, sodium pyruvate and supplemented with 10% fetal bovine serum (Sigma-Aldrich, St. Louis, MO, F2442). MDCK II cells were generously provided by Dr. Ian Macara. Growth substrates were prepared by coating #1.5 glass coverslips (In Vitro Scientific, D35C4-20-1.5N or D35-20-1.5N) with 1,10 or 50 µg/mL FN (354008, Corning) in PBS (Mediatech, Inc., 46-013-CM) at 37°C for 1 hour. Cells were plated on a growth substrate and then experiments were performed the next day. For protein expression, cells were transiently transfected using Fugene 6 (Promega, Madison, WI, E2691) according to the manufacturer's instructions overnight in a 25-cm^2 cell culture flask (Genessee Scientific Corporation, San Diego, CA, 25-207) before plating on a growth substrate. Culturing of polarized MDCK cysts was done as described previously(Lee et al., 2007). Briefly, MDCK cells were sparsely seeded as single cells on a growth substrate coated with 5 µg/mL laminin and overlaid with 5% reduced growth factor Matrigel (Corning). Polarized cysts were obtained after about a week of incubation, with Matrigel replenished every day.

The FAK inhibitor PF-228 (PZ0117) was purchased from Sigma. Alexa Fluor 488-phalloidin (A12379), Alexa Fluor 488-goat anti-mouse (A11029), Alexa Fluor 488-goat anti-rabbit (A11034), Alexa Fluor 568-goat-anti-rabbit (A11011), Alexa Fluor 568-goat anti-mouse (A11004), Alexa Fluor 647-goat-anti-mouse (A21235), anti-rabbit HRP (65-6120) and anti-mouse HRP (62-6520) antibodies were purchased from Life Technologies (Grand Island, NY). Rabbit-anti-Myosin IIA (909801) was purchased from BioLegends (San Diego, CA). Mouse anti-Paxillin (810051) was purchased from BD Biosciences. Rabbit anti-pFAK Y357 (ab81298) was purchased from Abcam. Mouse anti-FAK (BD Biosciences) was a generous gift from the lab of Dr. Irina Kaverina. Paraformaldehyde (15710) was purchased from Electron Microscopy Sciences (Hatfield, PA). Triton X-100 (BP151100) was purchased from Fischer Scientific (Suwanee, GA).

Plasmids

EGFP-Paxillin-KM-N-10 was a gift from Michael Davidson (Addgene plasmid # 56283).

Drug treatments

Treatment with FAK inhibitor PF-228 was done as described previously(Slack-Davis et al., 2007). Briefly, the drug was diluted to a final concentration of 1 μM in serum free DMEM pre-heated to 37°C and applied for 10 minutes. Following drug treatment, the drug was washed out and cells were fixed for staining. For western blotting, cells were washed with PBS and lysed using Cell Lytic M (Sigma) reagent containing 1X Protease Inhibitor Cocktail (Sigma), 1X Phosphatase Inhibitor Cocktail II (Sigma) and 1 μM PF-228 using scraping.

Knockdown of vinculin using si-RNA

Smart Pool Accell siRNAs against vinculin (E-009288-00-0005) and scrambled control (D-001910-10-05) were purchased from GE Dharmacon. Knockdown experiments were performed in 24 well plates using Lipofectamine 2000 (1690146, Life Technologies) according to the instructions provided by the manufacturer. Knockdown was performed for 72 hours, following which cells were plated on the growth substrate. For western blotting, cells were washed with PBS and lysed using Cell Lytic M reagent (Sigma) containing 1X Protease Inhibitor Cocktail.

Tissue Processing and Staining

Duodenum from the small intestine of 2-month-old C57/BL6 mice was harvested and immediately fixed and sub-dissected in 4% paraformaldehyde in PBS for 30 min. Tissue was then washed in PBS and cryoprotected overnight in 30% sucrose at 4°C before embedding in OCT and freezing over an acetone-dry ice bath. Frozen blocks were stored at -80°C until the time of sectioning. OCT blocks were sectioned using a Leica CM 1950 cryostat, at a thickness of 10 μm and melted on *Superfrost Plus* microscope slides (Fisher Scientific). All slides were kept at -80°C until the time of staining. Slides were thawed and OCT washed out in room temperature PBS three times for 5 min each before staining with AlexaFlour488-conjugated Phalloidin (1:200, Molecular Probes) and DRAQ5 (1:200, ThermoScientific) for 2 hours. After washing in PBS, samples were mounted with ProLong Gold antifade reagent (Molecular Probes) and #1.5 coverslip (Electron Microscopy Sciences).

Metaphase imaging

Cells were seeded on glass coverslips (#1.5, Warner Instruments) and grown to sub-confluence for immunofluorescence confocal microscopy. Cells were then fixed (cold

methanol) and stained as previously described (Bement et al.). Images were taken on a Perkin Elmer spinning disk confocal microscope: Nikon Eclipse Ti microscope, Plan-Apochromat 100x/1.4 Oil DIC objective and a Hamamatsu C9100-50 EMCCD camera. The entire cell was imaged at 0.2-μm step-intervals and displayed as maximum projections (ImageJ). The fluorescence range of intensity was adjusted identically for each image series. Orthogonal images of mitotic spindle were processed with ImageJ software. For measuring spindle angles in 2-dimensional cultures, anti-centrin or centrin-GFP was used to indicate spindle pole positions.

Confocal Microscopy and Image Processing

Confocal imaging of tissue sections was accomplished using a Nikon TiE inverted microscope outfitted with an A1R-plus point-scanning confocal, 100x 1.49NA Apo TIRF objective, and piezo stage (Nikon Instruments, Inc.). After image stack acquisition, datasets were deconvolved offline using Richardson-Lucy 3D deconvolution. Both image acquisition as well as processing, including deconvolution, was accomplished using NIS-Elements software (Nikon Instruments, Inc.)

Structured Illumination Microscopy

SIM imaging and processing was performed on a GE Healthcare DeltaVision OMX equipped with a 60x 1.42 NA Oil objective and sCMOS camera.

Live Cell TIRF microscopy

Live cell TIRF imaging was performed on a Nikon N-STORM microscope using a Nikon 100x Plan Apo 1.49 NA objective and an Andor iXon Ultra EMCCD camera. Cells in metaphase were identified using the H2B mCherry channel, following which images were acquired every 10-30s in TIRF in the green channel. Cells were imaged until they had completed telophase and initiated cell spreading. A camera gain of 110 was used. The hardware was controlled using Nikon Elements AR software.

Western Blotting

Gel samples were prepared by mixing cell lysates with LDS sample buffer (NP0007, Life Technologies) and Sample Reducing Buffer (NP0009, Life Technologies) and boiled at 95°C for 5 minutes. Samples were resolved on Bolt 4-12% gradient Bis-Tris gels (NW04120BOX, Life Technologies). Protein bands were blotted onto a nylon membrane (Millipore). Blots were

blocked using 5% NFDM (33368, Research Products International Corp, Mt. Prospect, IL) in TBST. Antibody incubations were also performed in 5% NFDM in TBST. Blots were developed using Immobilon Chemiluminescence Kit (WBKLS0500, Millipore).

Data Quantification

All image processing was performed on ImageJ. For measuring relative bottom ingression, images were first rotated so that cells were aligned with their long axis parallel to the substrate. 3D projections were then made along the X-axis a thin slice ROI passing through the center of the cell. Relative bottom ingression was measured as the distance from the substrate to the bottom of the cleavage furrow. For measuring aspect ratio of the ring, the cell was rotated 90 degrees so that its long axis was perpendicular to the substrate and an X-projection was created using a thin slice ROI passing through the contractile ring. Ring aspect ratio was measured as the ratio between the horizontal and axial diameter of the contractile ring. Cells were then divided into three stages of anaphase according to the height of the contractile ring. 3-9 μm for late, 9-15 μm for mid and >15 μm for early anaphase for HeLa cells; for MDCK cells, 1-5 μm for late, 5-10 μm for mid and <10 μm for late anaphase. For measurement of degree of asymmetry in cysts, Z-slices were maximum projected and two lines parallel to the long axis of the cell were drawn to mark the lumen and the basal domain. Apical and basolateral ingression was measured as distance between the furrow and the apical or basal plane. Cells across multiple independent experiments were pooled and statistical analyses were performed using Student's T-Test.

For quantification of TIRF data, four ROIs were drawn: one at the cleavage furrow and two on either side of the cleavage furrow, and one in the background. The largest size ROI that could fit all cleavage furrows in the data set was empirically set, and identical sized ROIs were placed on either side of this central ROI. We used identical sized ROIs for all measurements, and they were simply placed by keeping the furrow ROI at the center of the two daughter cells blindly to reduce any bias. All intensities were first background corrected using the average background mean intensity. The ingression of the cleavage furrow was designated as T=0 min and frames from 10 minutes before and after furrow ingression at 1-minute intervals were used for analysis. Each intensity value was normalized to T=-10 min to account for variation in intensity values due to expression levels. Due to asymmetry in attachment of the daughter cells, the cleavage furrow ROI was compared to the brighter adjacent ROI (designated Side 1 in the excel sheet). For quantification of degree of asymmetry in the attachment of cells, we

normalized the intensity values measured from the ROI in the less attached cell to T=-10 min of the brighter ROI (designated Side 2 in the excel sheet). The average normalized intensities were then compared using Mann Whitney U Test, since these data were not assumed to be uniformly distributed.

For quantification of spindle tilt, two methods were employed. In the first method, we measured tilt as the angle between the line joining the centroids of the DNA intensity and the substrate. In the second method, measured tilt as the angle between the substrate and the line joining the centrioles, imaged using a HeLa cell line stably expressing GFP tagged centrin protein. Statistical comparison of these methods showed that they yielded nearly the same value, and we use the DNA method for the remainder of the study.

Graphs were created using Microsoft Excel and GraphPad Prism.

Acknowledgements

We would like to thank the I. Kaverina, I. Macara and R. Ohi labs at Vanderbilt for invaluable discussion and reagents. This work was supported by Vanderbilt International Scholars Program award to N.T and a Career Development Award from NCI SPORE in GI Cancer P50 CA095103 to D.T.B.

Supplementary Figures

Figure 2-S1

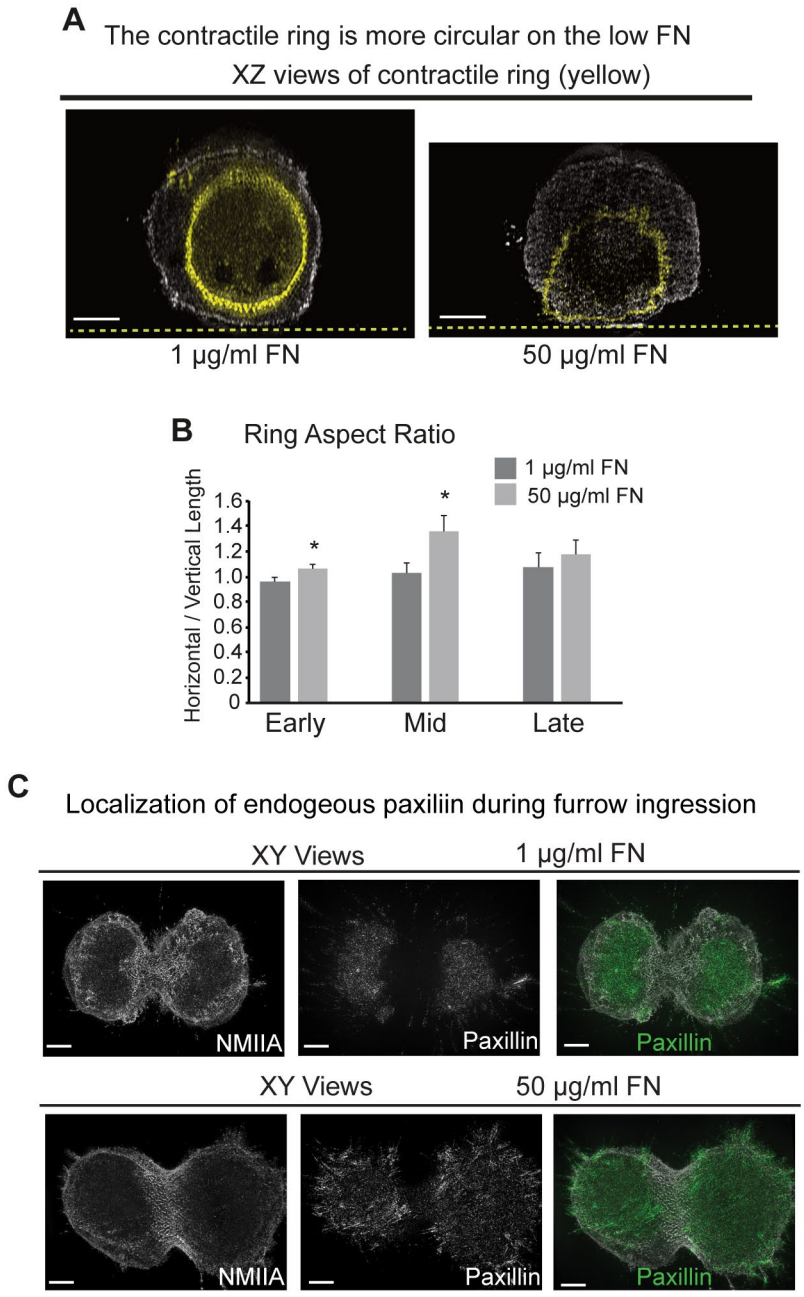

Figure 2-S1- Substrate adhesions control the symmetry of the cleavage furrow

A) XZ views of the contractile ring (pseudo-colored yellow) with respect to the cell body (gray) comparing 1 µg/mL and 50 µg/mL FN. Images were aligned perpendicular to the long axis of the cell and XZ views were created using a similar sized ROI as in Figure 2-1A. B) Quantification of aspect ratio of the ring comparing 1 and 50 µg/mL FN. The aspect ratio was calculated as the ratio of the horizontal to the axial diameter of the ring. Measurements were made on 34 cells and 42 cells for 1 µg/mL and 50

μg/mL FN, respectively, across 6 independent experiments for each condition C) XY views of HeLa cells at anaphase on low and high adhesive substrates stained for endogenous paxillin (green) and MIIA (gray). * denotes $p<0.05$; Scale bars, 5 μm. Error bars show standard error of the mean.

Figure 2-S2

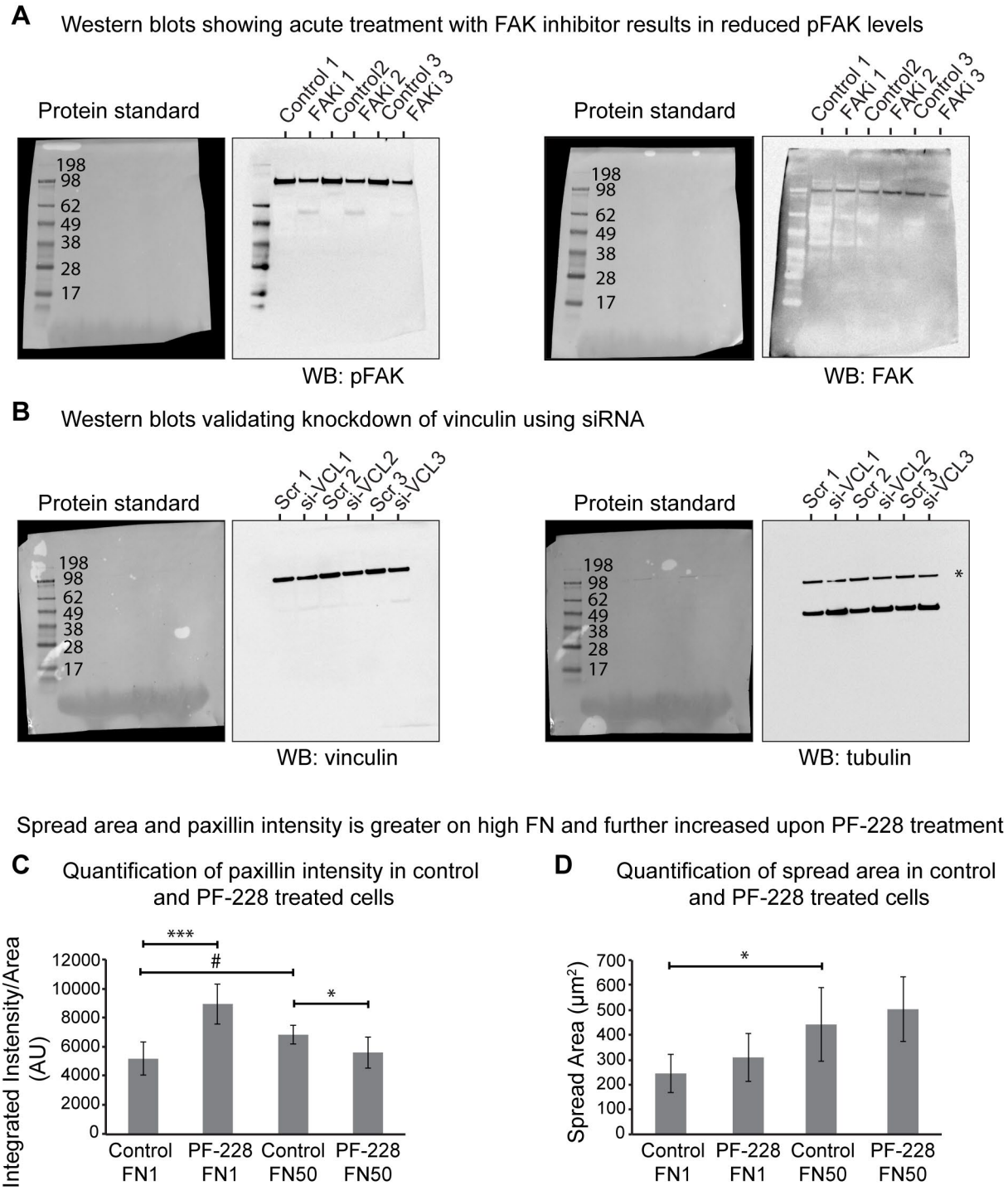

Figure 2-S2- Validation of inhibition of FAK using PF-228 and knockdown of vinculin using siRNA

A) Full western blots representing three independent experiments to validate the inhibition of FAK activity using an acute 10-minute treatment with FAK inhibitor PF-228. B) Full western blots representing three independent experiments to validate the knockdown of vinculin using siRNA.

Asterisk indicates the residual anti-vinculin antibody not removed during the stripping step. C) Quantification of paxillin intensity normalized to the spread area for control and PF-228 treated cells. D) Quantification of spread area during anaphase for control and PF-228 treated cells. Measurements were made on 17 cells across 3 independent experiments, 19 cells across 4 independent experiments, 35 cells across 5 independent experiments and 31 cells across 4 independent experiments for control 1 μg/mL FN, control 50 μg/mL FN, PF-228 treated 1 μg/mL FN and PF-228 treated 50 μg/mL FN respectively. * denotes $p<0.05$; *** denotes $p<0.001$; # denotes $p<0.0001$.

Figure 2-S3

Ingression proceeds from the basolateral domain in cells dividing in small intestinal crypts

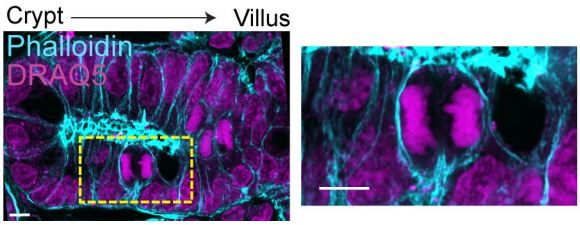

Figure 2-S3- Ingression in mouse intestinal tissue section

Cross section through the duodenum of a mouse small intestine stained with phalloidin (cyan) and DRAQ5 (magenta) with a cell dividing near the base of the crypt, imaged using confocal microscopy. Magnified view corresponding to the dotted yellow rectangle is shown to the right.

Figure 2-S4

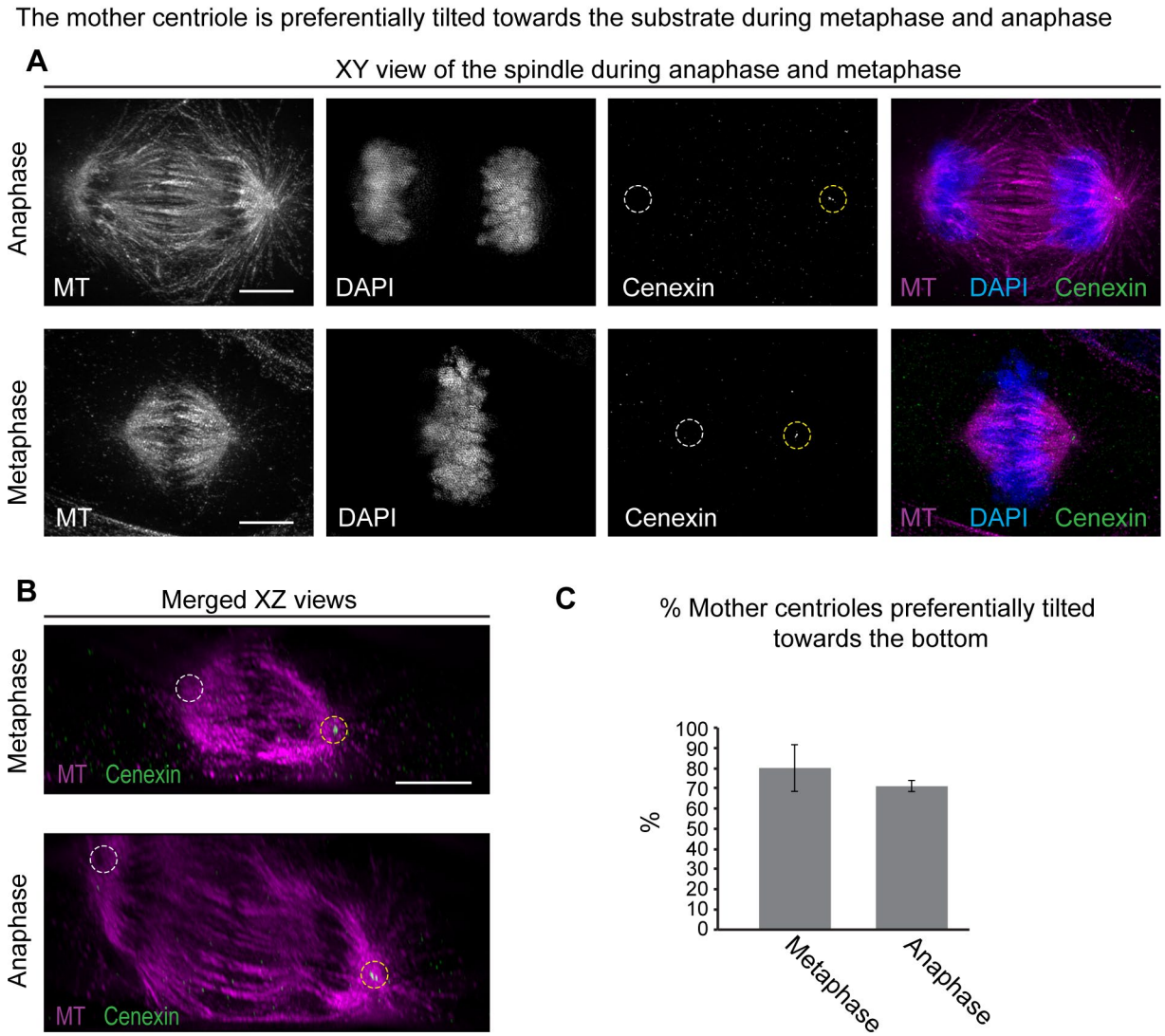

Figure 2-S4- Three-dimensional positioning of the mother centrosome

A) XY views of HeLa cells at anaphase (top row) and metaphase (bottom row) stained for DAPI, microtubules (MT) and cenexin. Cenexin marks the mother centrosome, marked by dotted yellow circle. The daughter centrosome is marked by a dotted white circle. B) XZ views of the cells shown in (A) showing microtubules and cenexin. C) Quantification of the proportion of cells with tilted spindles where the mother centrosome is preferentially tilted towards the substrate. Measurements were made for 15 metaphase spindles and 17 anaphase spindles across 3 independent experiments for each. Error bars represent SEM. Scale bar represents 5 μm.

Chapter 3- The role of myosin-II paralogs during membrane bleb retraction

Taneja, N., Burnette, DT. (2019). *Mol. Biol. Cell 30(9)- 1051-1059*

Introduction

The actin cortex is a thin network of actin filaments underneath the plasma membrane that allows a cell to maintain and change shape in response to internal and external stimuli (Salbreux *et al.*, 2012; Fritzsche *et al.*, 2016; Sezgin *et al.*, 2017). Membrane blebs are created upon a local detachment of the cortex from the membrane, which leads to an influx of cytosol, thus creating a spherical protrusion of the membrane (Salbreux *et al.*, 2012). These specialized protrusions play multiple roles, such as releasing cytoplasmic pressure at the polar cortex during cytokinesis, as well as driving pressure-driven cell migration (Sedzinski *et al.*, 2011; Bergert *et al.*, 2015). As such, the mechanisms driving bleb growth and retraction remain active areas of interest.

The newly formed membrane bleb lacks the majority of cortical components. New cortex assembly occurs on this membrane, with ezrin appearing nearly instantaneously, followed by actin appearing ~2 s after bleb formation, and with non-muscle myosin II (MII) following ~8 s later (Charras *et al.*, 2006). Ezrin was recently shown to recruit MYOGEF to the bleb, which activates RhoA signaling (Jiao *et al.*, 2018). This results in recruitment and activation of MII, which then drives retraction of the bleb. Previous work has suggested that turnover of actin, MII and actin cross-linkers is critical for bleb retraction (Fritzsche *et al.*, 2013). Specifically, the MII regulatory light chain was shown to turn over at rates intermediate between actin and actin cross-linking protein alpha actinin (Fritzsche *et al.*, 2013). It was proposed that this allows myosin II to reorganize actin network architecture, even in the presence of passive cross-links (Fritzsche *et al.*, 2013). Since the regulatory light chain binds multiple MII paralogs, the specific paralog responsible for bleb retraction is unknown. Furthermore, the relationship between turnover of that specific paralog and its correlation with bleb retraction has not been established.

There are three MII paralogs: MIIA, MIIB and MIIC, with mammalian cells commonly expressing MIIA and MIIB (Vicente-Manzanares *et al.*, 2009). Distinctive roles for MII paralogs

have been proposed in multiple contexts, such as stress fiber formation in migrating cells (Beach *et al.*, 2017), cell-cell junction formation in epithelial cells (Smutny *et al.*, 2010), growth cone advance in neurons (Brown and Bridgman, 2003), and pro-platelet formation in mice (Lordier *et al.*, 2008; Bluteau *et al.*, 2012). Here we show evidence for MIIA in specifically driving bleb retraction during cytokinesis. We further show that both motor activity at the N-terminus and regulation of the non-helical tailpiece at the C-terminus control this activity. These experiments have also revealed a correlation between the rate of MII turnover and bleb retraction.

Results

To create a bleb in a controlled manner, we utilized laser ablation as previously described (Tinevez *et al.*, 2009; Sedzinski *et al.*, 2011; Goudarzi *et al.*, 2012). Ablation of the polar cortex in a control cell undergoing cytokinesis resulted in the formation of a bleb followed by retraction over a time period of ~2 min as previously reported (Figure 3-1) (Charras *et al.*, 2008). We depleted either MIIA or MIIB in HeLa cells, which only express these two paralogs (Figure 3-S1) and created blebs. We found that knockdown of MIIA resulted in failure of bleb retraction, while MIIB knockdown did not (Figure 3-1). We observed a similar trend in spontaneously occurring blebs at the polar cortex (Figure 3-1). The lack of an effect on bleb retraction upon MIIB knockdown could result from an inability of MIIB to get recruited to the bleb. To test this, we monitored MIIA and MIIB recruitment to newly formed blebs in live cells co-expressing MIIA mApple and MIIB mEGFP (Figure 3-1). We found both paralogs were recruited to blebs after their formation (Figure 3-1). This was also observed in HAP1 fibroblasts (Figure 3-1). Given that both MII paralogs are recruited to blebs, other mechanisms likely drive the differences we observed in bleb retraction upon knockdown.

Figure 3-1

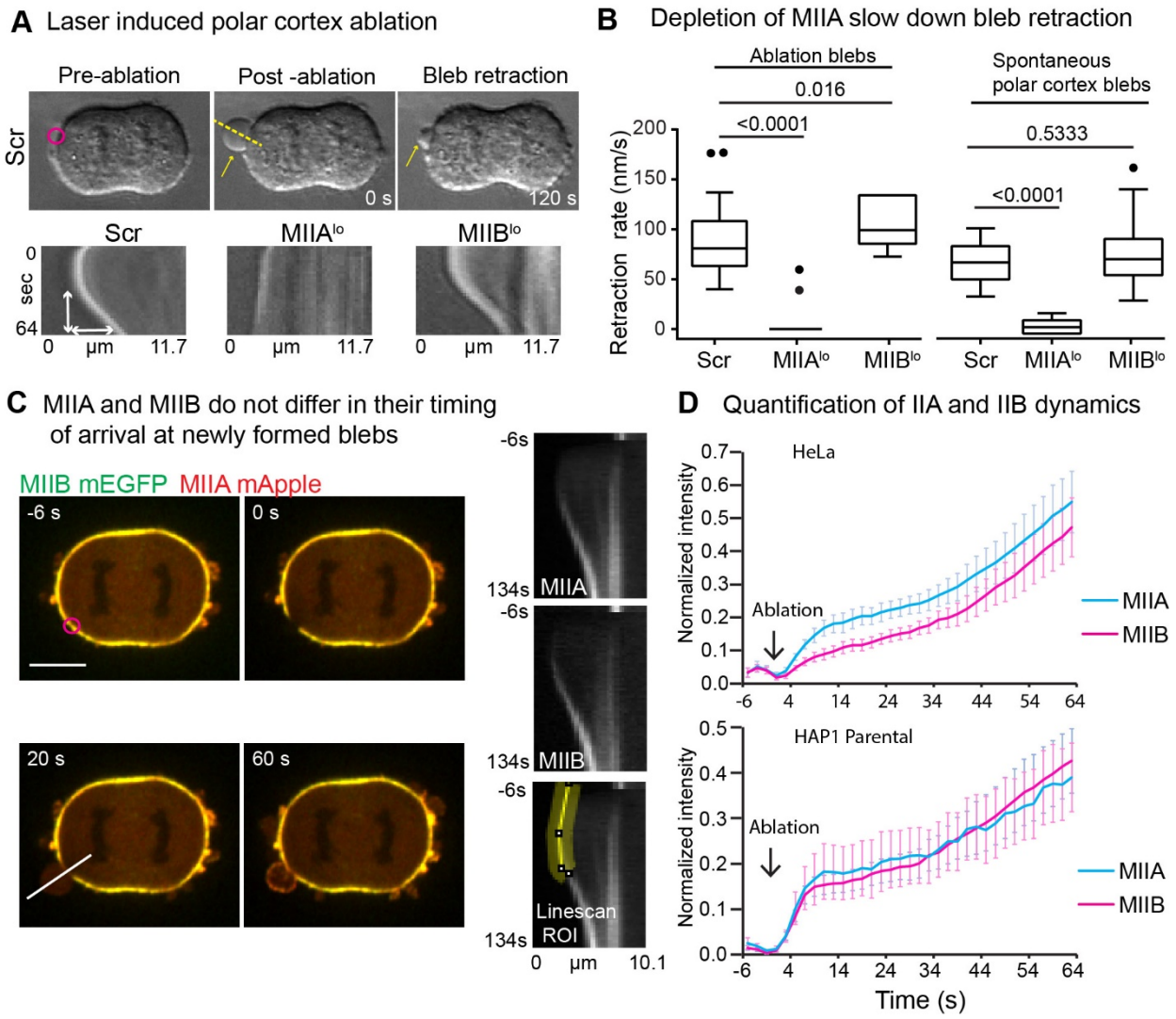

Figure 3-1- MIIA, but not MIIB, is required to drive bleb retraction

A) Laser induced polar cortex ablation in control, MIIA or MIIB depleted HeLa cells. Representative control DIC montage shows ablation ROI (magenta circle) used to create a membrane bleb (yellow arrow). Dotted yellow line represents ROI used to create kymographs. Representative kymographs for each condition are shown below. White arrows show measurement method for calculating retraction rates. B) Tukey plots comparing bleb retraction rates for controlled and spontaneous blebs in control versus MIIA^{lo} or MIIB^{lo} cells. Controlled blebs: n=25 control, 15 MIIA^{lo} and 25 MIIB^{lo} cells from 3 independent experiments. Spontaneous blebs: n=18 control blebs from 9 cells, 15 MIIA^{lo} blebs from 10 cells, 15 MIIB^{lo} blebs from 10 cells over 3 independent experiments. C) Representative time montage of HeLa cell co-expressing MIIA mApple and MIIB mEmerald showing the ablation ROI (magenta circle). Representative kymographs created using the solid white line show MIIA and MIIB recruitment to the bleb. Yellow ROI shows region of the kymograph compared for recruitment (first 60 s). D) Comparison

of IIA and IIB recruitment to blebs in HeLa and HAP1 fibroblasts. n=10 cells for each cell line over 3 independent experiments. Exact p values stated over respective bars. Solid black circles represent outliers. Scale bar: 10 μm.

We next wanted to confirm that MIIA was required to drive bleb retraction. To that end, we used a *myh9* (MIIA) knockout HAP1 cell line we previously generated using CRISPR (Fenix *et al.*, 2016), which only expresses MIIB (Figure 3-S1). We compared bleb retraction rates in this cell line versus the parental HAP1 cells. Knockout of MIIA resulted in failure of bleb retraction in HAP1 *myh9* KO cells (Figure 3-2). Expression of full length MIIA at 72.6 +/- 33% of parental levels restored bleb retraction rates comparable to the parental cell line (Figure 3-2, Table 3-1). Similar levels of MIIB or MIIC expression did not rescue bleb retraction (Figure 3-2, Table 3-1). We next wanted to further test the potential roles of MIIB and MIIC in driving bleb retraction. Therefore, we turned to Cos7 cells, that only express MIIB and MIIC (Even-Ram *et al.*, 2007). While cortex ablation resulted in bleb formation, wild type Cos7 cells failed to retract these blebs (Figure 3-2, UT bar). Overexpression of either MIIB or MIIC did not result in bleb retraction (Figure 3-2). However, Cos7 cells expressing exogenous MIIA did retract their blebs (Figure 3-2). Taken together, our data show that MIIA is required to drive bleb retraction.

MIIA and MIIB primarily differ in their N-terminal motor domain as well as in their C-terminal non-helical tailpiece (Vicente-Manzanares *et al.*, 2009). We first hypothesized that motor activity of MIIA could play a role in bleb retraction. To test this, we expressed MIIA containing a N93K mutation in the motor domain, which results in reduced ATPase activity of MIIA (Hu *et al.*, 2002) (Figure 3-2). Expression of MIIA N93K in HAP1 *myh9* KO cells resulted in significantly slower bleb retraction, suggesting the motor domain of MIIA plays a role in bleb retraction (Figure 3-2). To test whether the motor domain of MIIA is sufficient to drive bleb retraction, we used chimeric motors, where the motor domains of the MIIA and MIIB were swapped (see schematics, Figure 3-2) (Vicente-Manzanares *et al.*, 2008). Expression of MIIB/A, bearing the motor domain of MIIB, and the helical rod and non-helical tailpiece of MIIA, did not rescue bleb retraction (Figure 3-2). On the other hand, expression of MIIA/B, bearing the motor domain of MIIA, and the helical rod and non-helical tailpiece of MIIB significantly rescued bleb retraction (Figure 3-2). Interestingly, the MIIA/B chimera did not rescue bleb retraction rates to the same extent as full length MIIA ($p=0.0009$). This suggests that in addition to the motor domain of MIIA, other factors also contribute to drive bleb retraction.

Figure 3-2

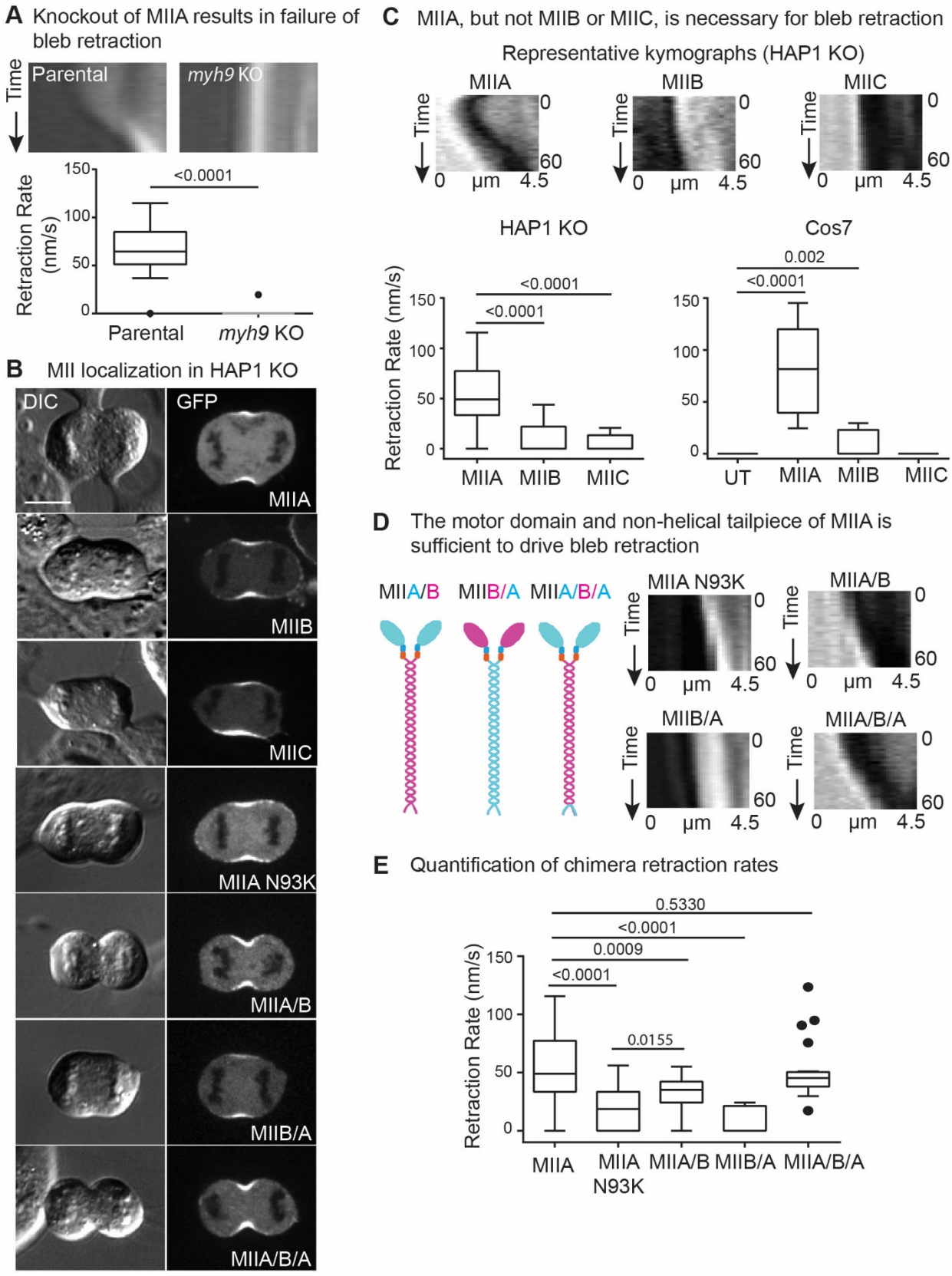
A Knockout of MIIA results in failure of bleb retraction
Time
Parental
myh9 KO
Retraction Rate (nm/s)
150
100
50
0
<0.0001
Parental
myh9 KO
B MII localization in HAP1 KO
DIC
GFP
MIIA
MIIB
MIIC
MIIA N93K
MIIA/B
MIIB/A
MIIA/B/A
C MIIA, but not MIIB or MIIC, is necessary for bleb retraction
Representative kymographs (HAP1 KO)
MIIA
MIIB
MIIC
Time
0
60
0 µm 4.5
HAP1 KO
Cos7
Retraction Rate (nm/s)
<0.0001
<0.0001
0.002
<0.0001
MIIA
MIIB
MIIC
UT
MIIA
MIIB
MIIC
D The motor domain and non-helical tailpiece of MIIA is sufficient to drive bleb retraction
MIIA/B
MIIB/A
MIIA/B/A
MIIA N93K
MIIA/B
MIIB/A
MIIA/B/A
Time
0
60
0 µm 4.5
E Quantification of chimera retraction rates
Retraction Rate (nm/s)
0.5330
<0.0001
0.0009
<0.0001
0.0155
MIIA
MIIA N93K
MIIA/B
MIIB/A
MIIA/B/A

Figure 3-2- The motor domain and non-helical tailpiece of MIIA are sufficient to drive bleb retraction

A) Representative kymographs from HAP1 parental and *myh9* KO cells following cortex ablation. n=21 parental cells and 12 KO cells over 3 independent experiments. B) Representative DIC and fluorescence images showing the localization of MII paralogs and mutants in HAP1 KO cells. C) Representative kymographs from MIIA, MIIB and MIIC expressing HAP1 KO cells following cortex ablation, as in Figure 1. Tukey plots comparing retraction rates in HAP1 KO cells expressing MIIA, MIIB or MIIC, and Cos7 cells expressing MIIA, MIIB, MIIC or untransfected (UT). For HAP1 KO cells, n= 27 MIIA, 10 MIIB and 15 MIIC expressing cells over >3 independent experiments. For Cos7 cells, n= 16 untransfected, 16 MIIA, 11 MIIB and 10 MIIC expressing cells over 3 independent experiments. D) Representative kymographs showing MIIA N93K, MIIA/B, MIIB/A and MIIA/B/A expressing HAP1 KO cells following cortex ablation. E) Retraction rates comparing mutants shown in (D). n= 21 N93K, 18 MIIA/B, 8 MIIB/A and 21 MIIA/B/A expressing cells over >3 independent experiments. MIIA bar is from the same dataset as (C) and is only displayed for comparison. Exact p values stated over respective bars. Solid circles in Tukey plots represent outliers. Scale bar: 10 μm.

Since MIIA and MIIB also differ in their non-helical tailpiece, we hypothesized that the tailpiece of MIIA may also contribute to bleb retraction. Therefore, we created a chimeric motor, bearing the motor domain and non-helical tailpiece of MIIA, and the helical rod domain of MIIB (MIIA/B/A). Expression of this construct at levels similar to MIIA/B (55 +/- 21% for MIIA/B/A versus 48 +/- 10% for MIIA/B) resulted in statistically indistinguishable rates of bleb retraction compared to full length MIIA (Figure 3-2). Taken together, these data show that the motor domain and non-helical tailpiece of MIIA, with the rod domain of either MIIA or MIIB, are sufficient to drive bleb retraction.

Current models of bleb retraction propose that myosin II turnover plays a critical role in bleb retraction (Charras *et al.*, 2008; Fritzsche *et al.*, 2013). We therefore measured the turnover of MIIA and MIIB at the cortex using FRAP, as previously performed for the regulatory light chain (Fritzsche *et al.*, 2013) (Figure 3-3). In HeLa cells, we found MIIA recovered twice as fast as MIIB (Figure 3-3). We confirmed this finding in HAP1 *myh9* KO cells expressing full length MIIA or MIIB (Figure 3-3). Interestingly, MIIC turned over markedly slower than MIIA and MIIB in HAP1 *myh9* KO cells (Figure 3-3). Similar trends were observed in Cos7 cells (Figure 3-3). Taken together, these data suggest the relatively fast turnover of MIIA correlates with its ability to drive bleb retraction.

Figure 3-3

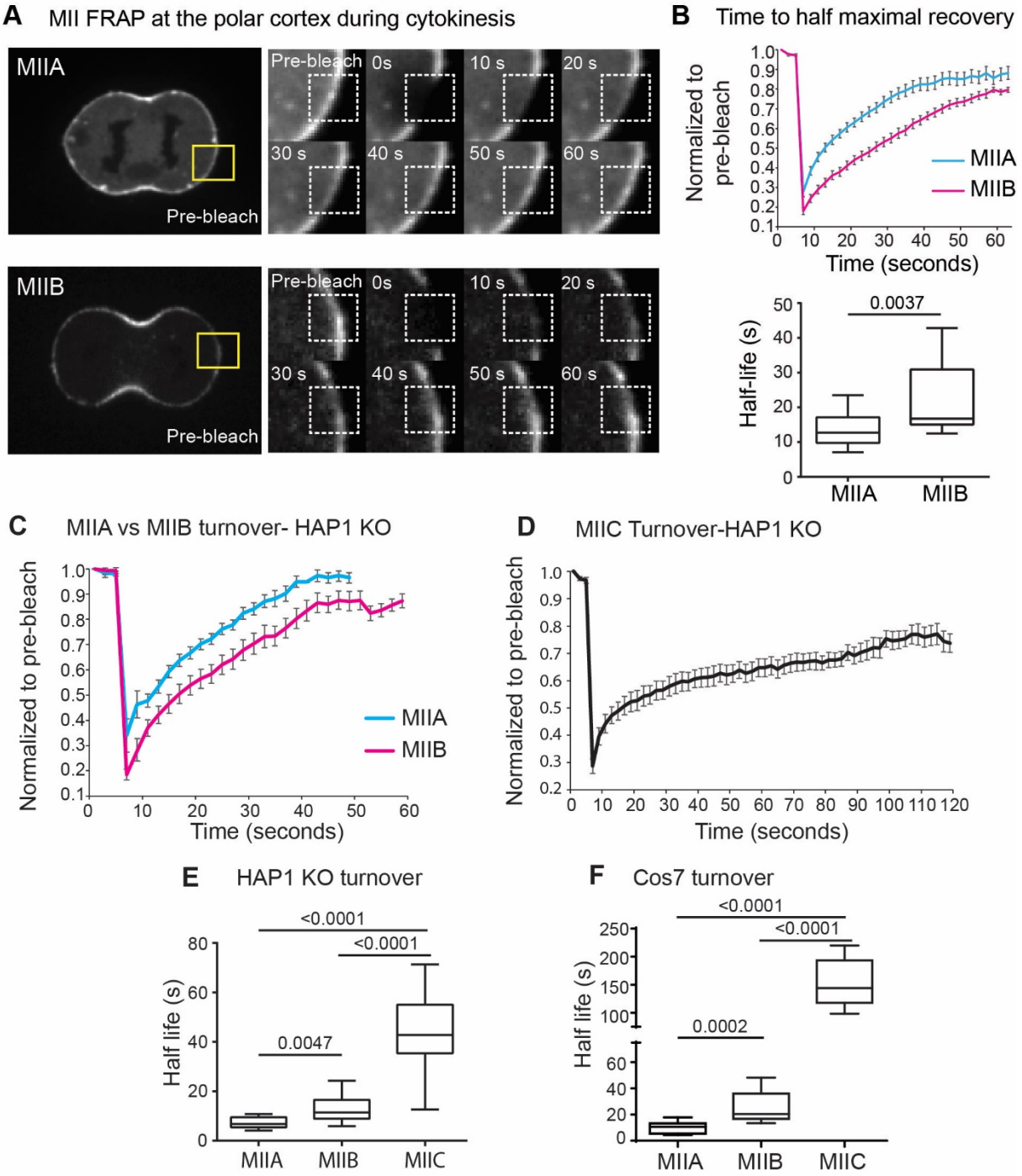

Figure 3-3- MIIA shows fast turnover compared to MIIB and MIIC at the cortex

A) Representative time montages from two separate cells showing FRAP of MIIA and MIIB mEGFP expressed in HeLa cells. Inset shows enlarged view of yellow box. Dotted white box represents bleaching region. B) Averaged FRAP curves for MIIA and MIIB in HeLa cells. n= 15 cells each for MIIA and MIIB over 3 independent experiments. See methods for curve fitting method. C-D) Averaged FRAP curves for MIIA and MIB mEGFP (C), and MIIC mEGFP (D) expressed in HAP1 KO cells. E) Tukey

plots showing time for half-maximal recovery for MIIA, MIIB and MIIC in HAP1 KO cells. n= 11 MIIA, 13 MIIB and 11 MIIC expressing cells over 3 independent experiments. F) Tukey plots showing time for half-maximal recovery for MIIA, MIIB and MIIC in Cos7 cells. n= 11 MIIA, 9 MIIB and 10 MIIC expressing cells over 3 independent experiments. Exact p values stated over respective bars.

To further test if changes in bleb retraction correlated with changes in turnover of MIIA at the cortex, we measured the turnover of the MIIA mutants and chimeras in HAP1 KO cells. MIIA N93K showed a slower recovery than full length MIIA, indicating that lower motor activity correlates with slower turnover (Figure 3-4). Interestingly, the MIIA/B chimera recovered significantly slower than MIIA, but not MIIB (Figure 3-4). This suggests that the non-helical tailpiece of MIIA plays a role in turnover, and its absence in the MIIA/B chimera results in its slower turnover compared to full length MIIA. To test this, we expressed the MIIA/B/A chimera, comprising the motor domain and non-helical tailpiece of MIIA and the helical rod domain of MIIB. The MIIA/B/A chimera rescued turnover rates to levels comparable to full length MIIA, in agreement with our observation that this chimera also rescued bleb retraction rates (Figure 3-4). Taken together, these data suggest that both the motor domain and the non-helical tailpiece of MIIA contribute to its fast turnover relative to MIIB or MIIC. We next wanted to determine the basis for regulation of MIIA turnover by the non-helical tailpiece.

Figure 3-4

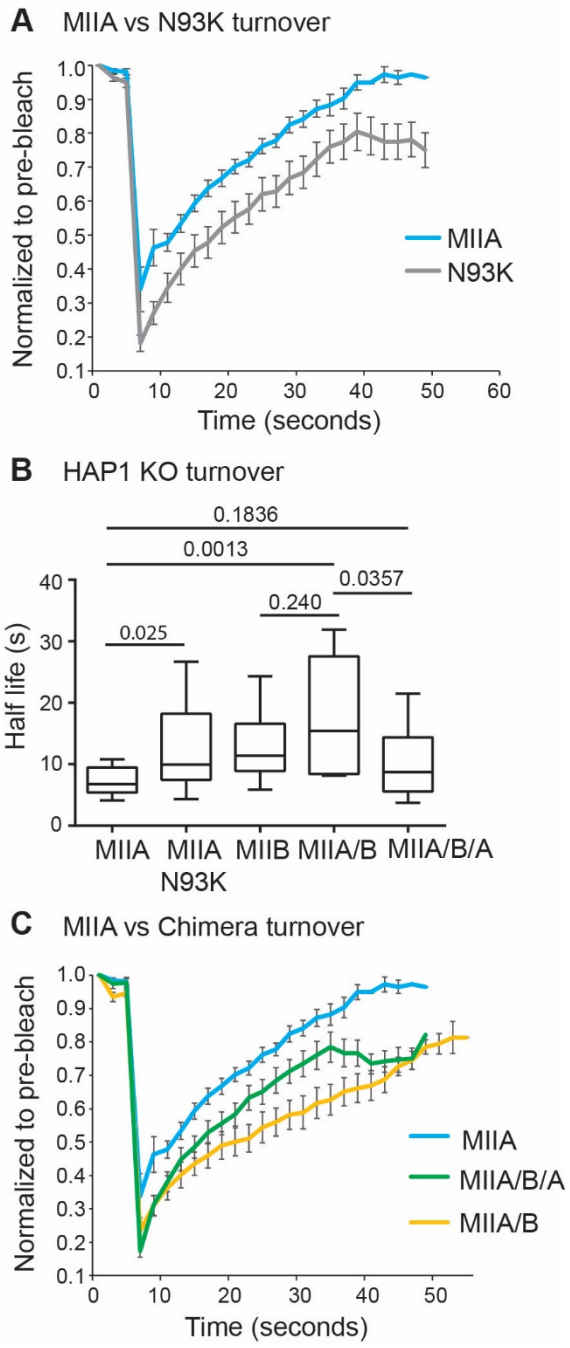

Figure 3-4- The motor domain and non-helical piece of MIIA contribute to turnover at the cortex

A) Averaged FRAP curves for full length MIIA (from Fig. 3-3, panel C) and MIIA N93K mutant. B) Tukey plots comparing time for half-maximal recovery for MIIA, MIIA N93K, MIIA/B, MIIB and MIIA/B/A in HAP1 KO cells. n= 12 N93K, 10 MIIA/B and 13 MIIA/B/A expressing cells over 3 independent experiments. The MIIA and MIIB datasets are the same as Fig. 3-3, panel A, and are only shown for comparison. C) Averaged FRAP curves for HAP1 MIIA KO cells expressing MIIA (from Fig. 3-3, panel

C), MIIA/B, and MIIA/B/A chimera. Exact p values stated over respective bars. Error bars show standard error of the mean.

Previous studies have proposed phosphorylation of the myosin heavy chain at the non-helical tailpiece results in MIIA filament disassembly during interphase (Dulyaninova *et al.*, 2007; Breckenridge *et al.*, 2008; Dulyaninova and Bresnick, 2013). To test whether phosphorylation of the non-helical tailpiece regulates MIIA turnover at the polar cortex during cytokinesis, we expressed an MIIA mutant lacking the non-helical tailpiece (Figure 3-5). Deletion of the non-helical tailpiece significantly slowed MIIA turnover (Figure 3-5). The non-helical tailpiece contains a single phosphorylation site that could regulate turnover (Ser 1943). We therefore created a phospho-null mutant of MIIA at this site (S1943A) and measured turnover using FRAP. We found MIIA S1943A also recovered slower than wild-type MIIA (Figure 3-5). Given the slower turnover of these MIIA tail mutants, we hypothesized that bleb retraction should be slower in these mutants. Indeed, both the MIIA Δtailpiece and MIIA S1943A mutants showed significantly slower bleb retraction (Figure 3-5).

Finally, we wanted to test the distinct role of MIIA in driving bleb retraction during interphase. To that end, we used filamin deficient M2 cells that constitutively bleb during interphase, a classic model system used to study membrane blebbing (Charras *et al.*, 2006; Bovellan *et al.*, 2014) (Figure 3-5). We probed the expression of the three MII paralogs in M2 cells, and found they express all three paralogs (Figure 3-S1). To test their potential roles, we depleted each of the MII paralogs using siRNA knockdown, and measured bleb retraction rates. Knockdown of MIIA, but not MIIB or MIIC significantly impaired bleb retraction, suggesting that MIIA is the paralog that drives bleb retraction even during interphase (Figure 3-5).

Figure 3-5

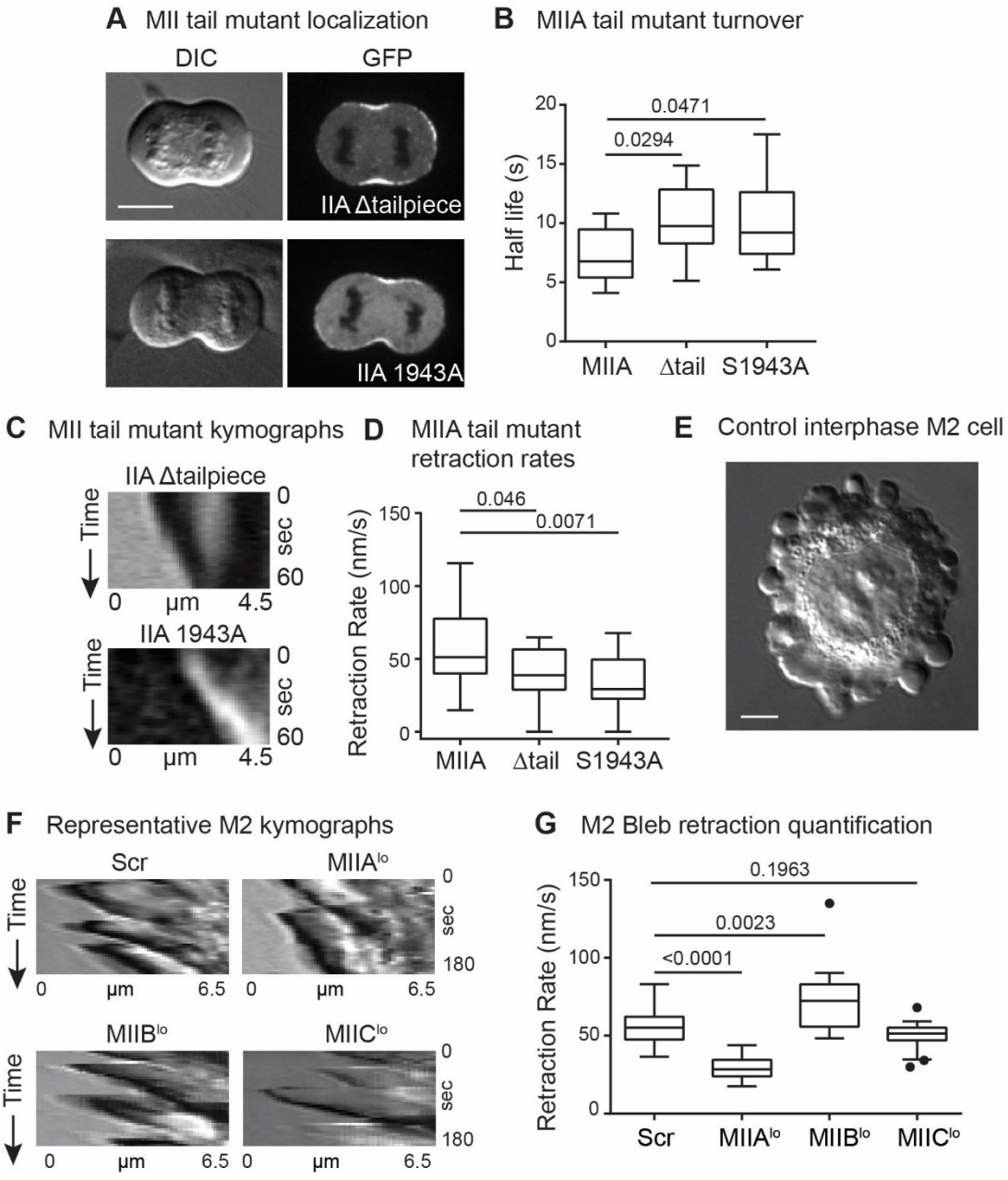

Figure 3-5- Phosphorylation of the non-helical tailpiece regulates turnover at the cortex

A) Representative DIC and fluorescence images showing localization of MII mutants in HAP1 KO cells. B) Tukey plots comparing time for half-maximal recovery for MIIA tail mutants. n= 10 MIIA Δtailpiece and 12 MIIA S1943A expressing cells over 3 independent experiments. The MIIA FRAP dataset is the same as Fig. 3-3, panel C and is only shown for comparison. C) Representative kymographs for MIIA Δtailpiece and MIIA S1943A following cortex ablation in HAP1 KO cells. D) Tukey plots comparing bleb retraction rates in HAP1 KO cells for MIIA tail mutants. n= 17 MIIA Δtailpiece and 15 MIIA S1943A expressing cells over 3 independent experiments. The MIIA dataset is the same in Fig. 3-2, panel C

and is only shown for comparison. E) DIC image of Scr control M2 cell 5 hours post plating. F) Representative kymographs for bleb retraction in Scr versus MIIA^{lo}, MIIB^{lo} and MIIC^{lo} M2 cells during interphase. G) Tukey plots comparing bleb retraction rates for Scr versus MIIA^{lo}, MIIB^{lo} and MIIC^{lo} M2 cells. Scale bar in (A) and (F)- 10 μm and 5 μm, respectively. Exact p values stated over respective bars. Solid circles represent outliers.

Discussion

Here we show that MIIA is the specific paralog that is necessary and sufficient to drive bleb retraction during interphase and cytokinesis. We confirmed this finding using three independent approaches: knocking down MIIA, knocking out MIIA, and expressing IIA in a cell line that does not normally express it. We also showed that the motor domain and the non-helical tailpiece both regulate bleb retraction. The motor domain of MIIA has distinct biophysical properties compared to MIIB and MIIC, namely having higher ATPase activity, as well as spending a smaller proportion of its mechano-chemical cycle bound to actin in the force generating state (i.e. lower duty ratio) (Kovács *et al.*, 2003; Wang *et al.*, 2003). Interestingly, we found these biophysical properties correlated with faster turnover at the cortex compared to MIIB and MIIC.

Reducing MIIA's motor activity using the N93K mutation slowed the turnover of MIIA at the cortex, which correlated with slower bleb retraction. Replacing the motor domain of MIIA with the motor domain of MIIB also slowed down turnover ($p=0.0257$); this construct also did not support bleb retraction. These findings thus establish a link between the turnover rate and motor activity of MIIA. The positive correlation between MIIA turnover and bleb retraction supports previous experimental and theoretical studies suggesting that turnover is critical for bleb retraction (Charras *et al.*, 2008; Fritzsche *et al.*, 2013). A limitation of our current study, as well as previous studies that have measured MII turnover, is that we correlated measurements made at the cortex with bleb retraction rates (Fritzsche *et al.*, 2013). We were unable to combine photo-ablation to create a bleb and photo-bleaching to measure MII turnover within the same bleb.

We further showed that the non-helical tailpiece of MIIA also regulates its turnover. Deletion of this segment resulted in both slower turnover and slower bleb retraction. Of note, this effect was not specific to MIIA since deletion of the non-helical tailpiece of MIIB also resulted in slower turnover of MIIB (Figure 3-S2). Not surprisingly, this did not change MIIB's inability to drive bleb retraction (Figure 3-S2). While the motor domain of MIIA is absolutely required for bleb retraction, the non-helical tailpiece may add an additional layer of regulation. This finding is in agreement with previous studies that have proposed that heavy chain phosphorylation controls MIIA disassembly from filaments (Dulyaninova *et al.*, 2007; Breckenridge *et al.*, 2008; Dulyaninova and Bresnick, 2013). Our finding that Ser1943 regulates bleb retraction also

suggest an important role for Casein Kinase II in regulating MIIA heavy chain phosphorylation, which has been shown to phosphorylate Ser1943 *in vitro* (Kelley and Adelstein, 1990; Dulyaninova *et al.*, 2005). The development of biosensors as well as specific, fast acting inhibitors will likely be necessary to better understand the mechanisms regulating MIIA assembly state during the cell cycle and at the polar cortex.

Membrane blebs play diverse roles in cellular physiology. During cytokinesis, blebs serve as pressure release valves to regulate intracellular pressure and when deregulated, result in dramatic cell shape instabilities and cytokinetic failure (Sedzinski *et al.*, 2011). We have established that MIIA is the major paralog that drives bleb retraction during cytokinesis. Therefore, a high level of MIIA expression may amplify genome instability through deregulation of cell shape during cytokinesis in cancer cells. While we did not find a role for MIIB or MIIC in bleb retraction, it is still possible that they may have other roles at the cortex during cytokinesis. The slower turnover of MIIB and MIIC, combined with their lower ATPase activity may make these paralogs better suited to act as cross-linkers at the cellular cortex, thus maintaining cortex stability. Cells also employ blebbing as a mode of migration, both during development and cancer progression (Blaser et al., 2006; Trinkaus, 1973; Kageyama, 1977; Friedl and Wolf, 2003; Sahai and Marshall, 2003). Interestingly, certain types of cancers up- or down-regulate MII paralogs (Maeda *et al.*, 2008; Derycke *et al.*, 2011). Our finding that MII paralogs have distinct roles in bleb retraction may, thus, have interesting implications for bleb-based cell migration both in developmental and pathological contexts.

Materials and Methods

Cell lines, growth conditions and chemicals

HeLa (ATCC, CCL-2) and Cos7 (ATCC CRL-1651) cells were cultured in growth media comprised of DMEM (Mediatech, Inc., Manassas, VA, #10-013-CV) containing 4.5 g/L L-glutamine, L-glucose, sodium pyruvate and supplemented with 10% fetal bovine serum (Sigma-Aldrich, St. Louis, MO, #F2442). HAP1 *myh9* (MIIA) KO and parental cells were purchased from Haplogen Genomics as previously described (Fenix *et al.*, 2016), and cultured in IMDM medium supplemented with 10% fetal bovine serum. M2 melanoma cells were cultured Minimal Essential Medium supplemented with Earle's salts, 10 mM HEPES and 10% fetal bovine serum. Growth substrates were prepared by coating #1.5 glass coverslips (In Vitro Scientific, #D35-20-1.5N) with 10 µg/mL fibronectin (Corning, NY, #354008) in PBS (Mediatech, Inc., #46-013-CM) at 37 °C for 1 hour.

For protein expression, cells were transiently transfected using Fugene 6 (Promega, Madison, WI, #E2691) as per the manufacturer's instructions overnight in a 24-well tissue culture plate (Corning) before plating on a growth substrate.

Alexa Fluor 488-goat anti-rabbit (#A11034) and Alexa Fluor 568-goat anti-rabbit (#A11036) were purchased from Thermo Fisher Scientific (Waltham, MA). Rabbit anti-myosin IIA (#909801) was purchased from BioLegends (San Diego, CA). Rabbit anti-myosin IIB (#8824S) and myosin IIC (#8189) were purchased from Cell Signaling Technology (Danvers, MA). Mouse anti-tubulin (#T6199) was purchased from Millipore Sigma (Darmstadt, Germany).

Plasmids

MIIA mApple (Addgene, #54929) and MIIB mEmerald (Addgene, #54192) were gifts from Michael Davidson. MIIA mEGFP (Addgene, Cambridge, MA, #11347) was a gift from Robert Adelstein. MIIB mEGFP (Addgene #35691) was a gift from Venkaiah Betapudi. MIIA Δtail (Addgene, #35689) was a gift from Thomas Egelhoff. The mEGFP tagged MIIB/A and MIIA/B chimeras were generously provided by Miguel Vincente Manzanares (Universidad Autonoma de Madrid, Spain). MIIA S1943A and MIIB Δtail were created by mutagenizing MIIA mEGFP and MIIB mEmerald, respectively, using a site directed PCR mutagenesis protocol as described previously (Liu and Naismith, 2008). The A/B/A chimera was created using Gibson Assembly. The fragments corresponding to the rod region of MIIB and corresponding to the

motor and non-helical tailpiece of MIIA were amplified using PCR, following which they were PCR purified and assembled using the NEB HiFi Gibson Assembly Kit according to the instructions provided by the manufacturer.

Live imaging and Fluorescence Recovery after Photobleaching (FRAP)

Live imaging and FRAP experiments were performed on a Nikon Eclipse Ti-E inverted microscope equipped with a Yokogawa CSU-X1 spinning disk head, 1.4 NA 60X oil objective, Andor DU-897 EMCCD and a dedicated 100 mW 405 diode ablation laser, generously provided by the Nikon Centre of Excellence at Vanderbilt University. The instrument was controlled using Nikon Elements AR software. Bleaching was performed for 500 ms using a pixel dwell time of 500 µs and 15% laser power using the same 2.7 µm x 2.7 µm ROI for all FRAP experiments. Samples were maintained at 37°C with 5% CO_2 using Tokai Hit Stage Incubator.

To image endogenous MIIA in fixed HAP1 cells, single optical sections through the middle of the cell were acquired using the 60X objective using the same parameters for GFP as used in the ablation and FRAP experiments. To image M2 cells, we used a Nikon Eclipse Ti widefield system equipped with a 1.45 NA 100X objective with Tokai Hit heated stage.

Cortical ablation

Laser damage induced ablation of the polar cortex was performed on a Nikon Eclipse Ti-E inverted microscope equipped with a Yokogawa CSU-X1 spinning disk head, 1.4 NA 60X oil objective, Andor DU-897 EMCCD and a dedicated 100 mW 405 diode ablation laser, generously provided by the Nikon Centre of Excellence at Vanderbilt University. A 1.4 µm x 1.4 µm ROI was used for all experiments. A DIC and/or fluorescence image was acquired before ablation, followed by ablation using a miniscanner. A pixel dwell time of 500 µs, 50% laser power was used for a duration of 1 second, followed by acquiring DIC or fluorescence images at 2 second intervals.

Knockdown experiments

Smart Pool Accell siRNA against MIIA (myh9 gene, #E-007668, #1- CCGUUGACUCAGUAUAGUU, #2- UCCACAUCUUCUAUUAUCU, #3- GUGUGGUCAUCAAUCCUUA, #4- CUUAUGAGCUCCAAGGAUG), MIIB (myh10 gene, #E-

023017, #1- GGACUAAUCUAUACUUAUU, #2- UGUCAAUGCUUAAAGUAGU, #3- CGAGGAUCCAGAGAGGUAU, #4- CCAAUUUACUCUGAGAAUA) and MIIC (myh14 gene, #E027149, #1- CCAUGAACCGUGAAGUGAC, #2- CCCUCGUUAUUGAUCUAUA, #3- CUCUCACUCUCUACGUAGC, #4- CCCUUGAGUCUAAGUUGGC) were purchased from GE Dharmacon (Lafayette, CO). Knockdown experiments were performed in 24-well plates using Lipofectamine 2000 (Life Technologies, #1690146) as per instructions provided by the manufacturer. Knockdown was performed for 72 hours, after which cells were either plated on the growth substrate for imaging or lysed for western blot experiments.

Western Blotting

Gel samples were prepared by mixing cell lysates with LDS sample buffer (Life Technologies, #NP0007) and Sample Reducing Buffer (Life Technologies, #NP00009) and boiled at 95°C for 5 minutes. Samples were resolved on Bolt 4-12% gradient Bis-Tris gels (Life Technologies, #NW04120BOX). Protein bands were blotted onto a nylon membrane (Millipore). Blots were blocked using 5% dry milk (Research Products International Corp, Mt. Prospect, IL, # M17200-100.0) in TBST. Antibody incubations were also performed in 5% dry milk in TBST. Blots were developed using the Immobilon Chemiluminescence Kit (Millipore, #WBKLS0500).

Calibration of protein expression levels in HAP1 KO cells

For quantification of exogenous plasmid expression in the HAP1 knockout cell line, MIIA GFP was expressed in the KO cell line. Cells were fixed and stained with an antibody against the rod domain of MIIA in the red channel. In parallel, the untransfected parental HAP1 cell line was also fixed and stained for MIIA rod domains in the red channel. GFP expression in the cytoplasm was then calibrated against corresponding intensity of endogenous MIIA in the cytoplasm. The intensity in the cytoplasm was also normalized against the relative enrichment at the polar cortex. Imaging all the GFP tagged mutants with the exact same imaging parameters allowed us to compare expression levels across all mutants tested.

Data Quantification

For quantification of bleb retraction rates, DIC time montages were acquired at 2 second intervals following cortex ablation. Images were first aligned using StackReg plugin in Fiji. A 3-pixel thick line was drawn perpendicular to the cortex boundary as shown in Figure 1A to create a kymograph using MultipleKymograph plugin in Fiji. Retraction rates were calculated

as the ratio of horizontal distance (distance) in nanometers to the vertical distance (time) in seconds (shown as white lines in kymograph in Fig. 1A).

For quantification of timing of arrival in blebs as shown in Figure 1C, fluorescence montages acquired at 2 s intervals were used. 3 time points were acquired prior to ablation. A 3-pixel thick line was drawn perpendicular the cortex boundary and saved in the ROI manager in ImageJ. The same line was then used to create kymographs for both MIIA and MIIB channels. A 15-pixel thick segmented line was then drawn along the retracting cortex boundary starting at the first time point (6 seconds before ablation) until the end of bleb retraction. The intensities were then normalized to the maximum fluorescence for the corresponding channel during bleb retraction. Recruitment dynamics were then compared for the first 60 seconds.

For quantification of FRAP data, confocal time montages acquired at 2 second intervals were first aligned using the StackReg plugin in Fiji, followed by drawing ROIs around the bleached region, an unbleached region, and background. Mean intensity over time was calculated for each of the three ROIs using the Multi Measure function in the ROI manager. Subsequent analysis was performed using the EasyFRAP algorithm in MATLAB as previously described. Briefly, a double normalization was performed to account for background correction and photobleaching, followed by fitting the normalized curves to a second-degree exponential to obtain the half maximal recovery time and mobile fraction (see (Rapsomaniki *et al.*, 2015) for details on fitting equations and normalization). Curves with poor fits (with $R^2 < 0.9$) were not included for analysis. We noted negligible bleaching (<5% for GFP). FRAP curves averaged using entire datasets for display (Figures 3-3 to 3-5) were generated in Excel.

Statistics

Statistical significance was determined using Mann Whitney's U-test using GraphPad Prism. All graphs are represented as Tukey plots showing boxes (with median, Q1, Q3 percentiles), whiskers (minimum and maximum values within 1.5 times interquartile range) and outliers (solid circles). No outliers were removed from the analysis.

Acknowledgements

We thank Matthew Tyska for the gift of M2 melanoma cells, Miguel Vincente-Manzanares for providing the MII chimeras and Karren Hyde, Meredith Weck and MariaSanta Mangione for

valuable feedback and advice. We thank the Nikon Center of Excellence, Vanderbilt University for providing access to the Nikon Spinning Disk microscope and technical support. The raw data generated in the current study is available from the corresponding author upon reasonable request. This work was funded by a MIRA from NIGMS (R35 GM125028) awarded to D.T.B and an American Heart Association Predoctoral Fellowship (18PRE33960551) to N.T. The authors declare no competing financial interest.

Supplementary Figures

Figure 3-S1

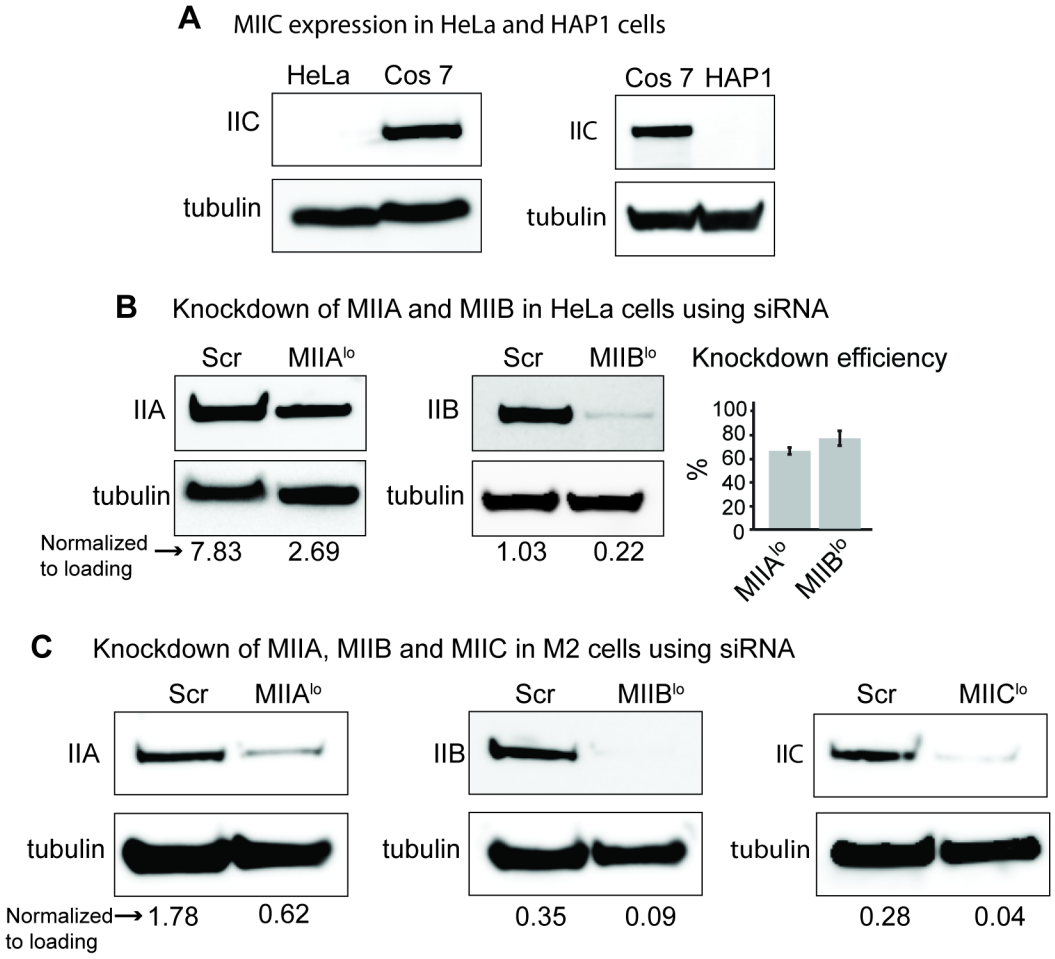

Figure 3-S1- Knockdown and Expression Validation

A) MIIC protein expression in HeLa, Cos7 and HAP1 cells evaluated by western blotting. B) Validation of knockdown of MIIA and MIIB in HeLa cells by western blotting. The normalized ratios compared to loading control (tubulin) are shown below the blots. Graph depicts average of 3 independent experiments. C) Validation of knockdown of MIIA, MIIB and MIIC in M2 cells by western blotting. The normalized ratios compared to loading control (tubulin) are shown below the blots.

Figure 3-S2

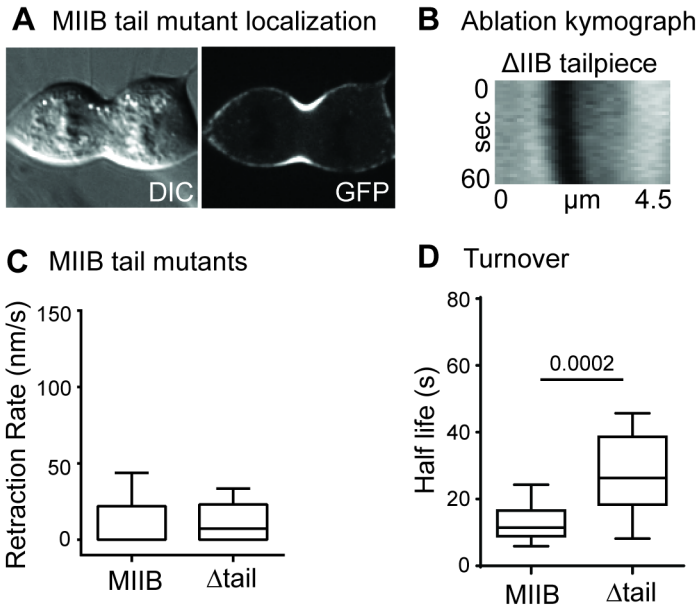

Figure 3-S2- Deletion of non-helical tailpiece of MIIB results in slower turnover

A) Localization of MIIB Δtailpiece in HAP1 KO cells. B) Representative kymograph for MIIB Δtailpiece following ablation in HAP1 KO cells. C) Tukey plots comparing bleb retraction rates for MIIB Δtailpiece. n=10 MIIB Δtailpiece expressing cells over 4 independent experiments. The MIIB dataset is same as used in Fig. 3-2 and is only shown for comparison. D) Tukey plots comparing time for half-maximal recovery for MIIB Δtailpiece. n= 16 MIIB Δtailpiece expressing cells over 3 independent experiments. The MIIB FRAP dataset is the same as Fig. 3-3C and is only shown for comparison. Exact p values stated over respective bars.

Table 3-1- Relative expression of myosin mutants in HAP1 *myh9* KO cells

MII construct	**Expression (%) compared to endogenous MIIA in HAP1 parental cells**
MIIA	72.6 +/- 33.5
MIIB	70.3 +/- 22.1
MIIC	62.6 +/- 29.5
MIIA/B	48.7 +/- 10.1
MIIA N93K	58.8 +/- 22.6
MIIA/B/A	55.7 +/- 21.7
MIIA Δtailpiece	92.5 +/- 35.4
MIIA S1943A	113.8 +/- 44.6

Chapter 4- Myosin-II filament composition tunes cortex tension and regulates cytokinetic fidelity during cell division

Taneja, N., Bersi, MR., Baillargeon, SM., Fenix, AM., Cooper, JA., Ohi, R., Gama, V., Merryman, WD., Burnette, DT. (2020). *Cell Reports* 31(1)

Introduction

The cortex of animal cells is a thin network of actin filaments underneath the plasma membrane. The cortex provides mechanical support to the membrane and organizes protein complexes (Fritzsche et al., 2016; Salbreux et al., 2012; Sezgin et al., 2017). Membrane and actin cross-linkers, in addition to the molecular motor myosin II (MII), organize and remodel this dynamic structure. Through the modulation of its mechanical properties, the cortex allows cells to change shape and generate tension in response to internal and external stimuli. In the case of migratory responses, such as those observed during development and disease progression, the cortex can remodel to produce protrusions such as filopodia, lamellipodia and blebs (Charras and Paluch, 2008; Gardel et al., 2010). During mitosis, the cortex undergoes a series of remodeling events, where it initially allows a cell to round up, and then finally divide into two through the constriction of an equatorial contractile ring (Maddox and Burridge, 2003; Stewart et al., 2011; Surcel et al., 2010).

The cytokinetic phase of cell division presents a major challenge to cortical stability due to the extensive remodeling events required at the cleavage furrow. During cytokinesis, a transient enrichment of MII and actin at the equatorial cortex creates a contractile network that contains highly organized actomyosin ensembles called stacks (Fenix et al., 2016; Fishkind and Wang, 1993; Fujiwara and Pollard, 1976). While both commonly expressed paralogs of MII, MIIA and MIIB, co-assemble in the cleavage furrow (Beach et al., 2014), functional differences in driving ingression have begun to be elucidated. It was recently reported that knockout of MIIA, but not MIIB, leads to slower ingression at the equatorial cortex (Yamamoto et al., 2019). The authors found this correlated with larger MII stacks at the equatorial cortex, calling into question whether formation of stacks is required for force generation at the equatorial cortex, or is inhibitory to furrow ingression (Yamamoto et al., 2019).

While multiple studies have heavily focused on mechanisms driving contractile ring formation and ingression, relatively fewer studies have focused on the polar actomyosin network. At the polar region of dividing cells, the cortex retains the same isotropic organization found in rounded metaphase cells and contains lower MII activity (Bovellan et al., 2014; Levayer and Lecuit, 2012). Accumulation of MII at the cortex creates cortical tension; that, in turn, increases intracellular pressure (Stewart et al., 2011). Excess intracellular pressure is released at the polar cortex by formation and growth of membrane protrusions called blebs (Sedzinski et al., 2011). It was recently reported that knockout of MIIA, but not MIIB, results in reduced polar blebs during cytokinesis and reduced cortex stiffness during metaphase (Yamamoto et al., 2019). The mechanism underlying reduced polar bleb formation upon MIIA knockout remains unclear, since contributions of MIIA and MIIB to cortex tension and intracellular pressure remain unknown.

Perturbation of the polar cortical network can result in shape instability and cytokinetic failure (Guha et al., 2005; Sedzinski et al., 2011). For instance, knockdown of anillin, an actin binding scaffold protein results in a global increase in cortical instability due to enhanced cortical contractility (Sedzinski et al., 2011; Straight et al., 2005). Reducing polar contractility at one pole through local delivery of blebbistatin, an inhibitor of the ATPase activity of MII, results in cytokinetic failure and misplaced cleavage furrows (Guha et al., 2005). This has resulted in the general idea that the cortex of dividing cells is inherently prone to shape instabilities, and cortical contractility therefore must be tightly regulated.

In this study, we investigate the role of MIIA and MIIB in regulating actin cortex mechanics at the equatorial and polar cortex. In contrast with a previous report (Yamamoto et al., 2019), we show that MIIA depletion reduces MII stacks at the cleavage furrow. At the polar cortex, depletion of one paralog leads to compensatory localization of the other, resulting in changes in MIIA/B hetero-filament composition. We further show cortex tension is tuned as a result of these changes in filament composition, with higher MIIA in hetero-filaments correlating with higher cortex tension and intracellular pressure. Perturbation of this tuning results in cell shape instabilities and chromosome missegregation. These findings also uncover a general mechanism that may allow cells to attain a broad range of contractile states to perform various cellular functions requiring cortex contractility.

Results

MIIA templates MII filament ensembles at the equatorial cortex to drive ingression

We first investigated the role of the predominant MII paralogs—MIIA and MIIB—in the two cortical networks during cytokinesis. HeLa cells express MIIA and MIIB, but not MIIC (Taneja and Burnette, 2019). MIIA and MIIB filaments are known to co-assemble in the same filament in the cleavage furrow (Beach et al., 2014). MIIA is required to template MIIB filament stacks at the leading edge of migrating cells during interphase (Fenix et al., 2016). It was recently reported that knockout of MIIA results in larger MIIB stacks in fibroblasts (Yamamoto et al., 2019), suggesting the templating of MII stacks by MIIA does not occur during cytokinesis. To test whether a similar effect occurs in HeLa cells, we depleted MIIA using siRNA ($MIIA^{lo}$ cells, Figure 4-S1). We observed a nearly 50% compensatory increase in total MIIB protein levels in $MIIA^{lo}$ cells (Figure 4-S1).

We used a method we previously developed to measure the length of MII filament stacks using structured illumination microscopy (SIM) (Fenix et al., 2016). Intriguingly, depletion of MIIA significantly reduced the length of MIIB stacks at the cleavage furrow (Figure 4-1, p=0.004). Protein level compensation by MIIA upon MIIB depletion ($MIIB^{lo}$ cells) was more modest (~20%, Figure 4-S1). Consistent with the templating hypothesis, we found no change in MIIA stacks in the cleavage furrow of $MIIB^{lo}$ cells (Figure 4-1). To test whether the differences between our results and a previous report were a result of knockdown in HeLa cells versus knockout in fibroblasts, we also measured stack lengths in MIIA-knockout (KO) HAP1 fibroblasts (Taneja and Burnette, 2019). We found knockout of MIIA also resulted in smaller MIIB stacks (Figure 4-S2).

It was recently proposed that MII stacking is inhibitory to cleavage furrow ingression, with larger MII stacks upon MIIA KO resulting in slower ingression (Yamamoto et al., 2019). Therefore, we hypothesized smaller stacks in $MIIA^{lo}$ cells should result in faster cleavage furrow ingression. Surprisingly, MIIA depletion caused a 1.4-fold reduction in cleavage furrow ingression rates compared to scrambled control siRNA (Scr) or $MIIB^{lo}$ cells (Figure 4-1, p=0.0006 for Scr vs $MIIA^{lo}$). To rule out off-target effects of siRNA knockdown of MIIA, we rescued MIIA depletion using full length siRNA resistant MIIA-mEGFP. Expression of MIIA-mEGFP at 65% of endogenous MIIA levels increased ingression to control rates (Figure 4-1, Table 4-1). Importantly, overexpression of MIIB at 143% of endogenous MIIB levels did not

increase rate of cleavage furrow ingression in MIIA^{lo} cells (Figure 4-1, Table 4-1). This suggested that while the requirement for MIIA in driving faster cleavage furrow ingression was consistent with recent reports (Yamamoto et al., 2019), MII stacking was not inhibitory to furrow ingression.

To test whether MIIA is sufficient to increase furrow ingression rates, we used HAP1 fibroblasts. We first depleted >99% of MIIB using siRNA (Figure 4-1, inset). Knockdown of MIIB in HAP1 parental cells did not result in change in ingression rates, similar to HeLa cells. On the other hand, CRISPR mediated knockout of MIIA resulted in a 1.4-fold reduction in cleavage furrow ingression rates (Figure 4-1, $p<0.0001$ for Parental vs MIIA KO). Expression of MIIA-mEGFP, but not MIIB-mEGFP, increased cleavage furrow ingression rates in HAP1 MIIA KO fibroblasts (Figure 4-1). Interestingly, we also found that the amount of MIIA localized to the equatorial cortex positively correlated with ingression rates in human embryonic stem cell (hESC) colonies, that show a natural gradient of MIIA, but not MIIB levels, within the colony (Figure 4-S2). Taken together, these data show that MIIA, but not MIIB, is necessary and sufficient to drive faster ingression through templating of MII stacks at the cleavage furrow.

Figure 4-1

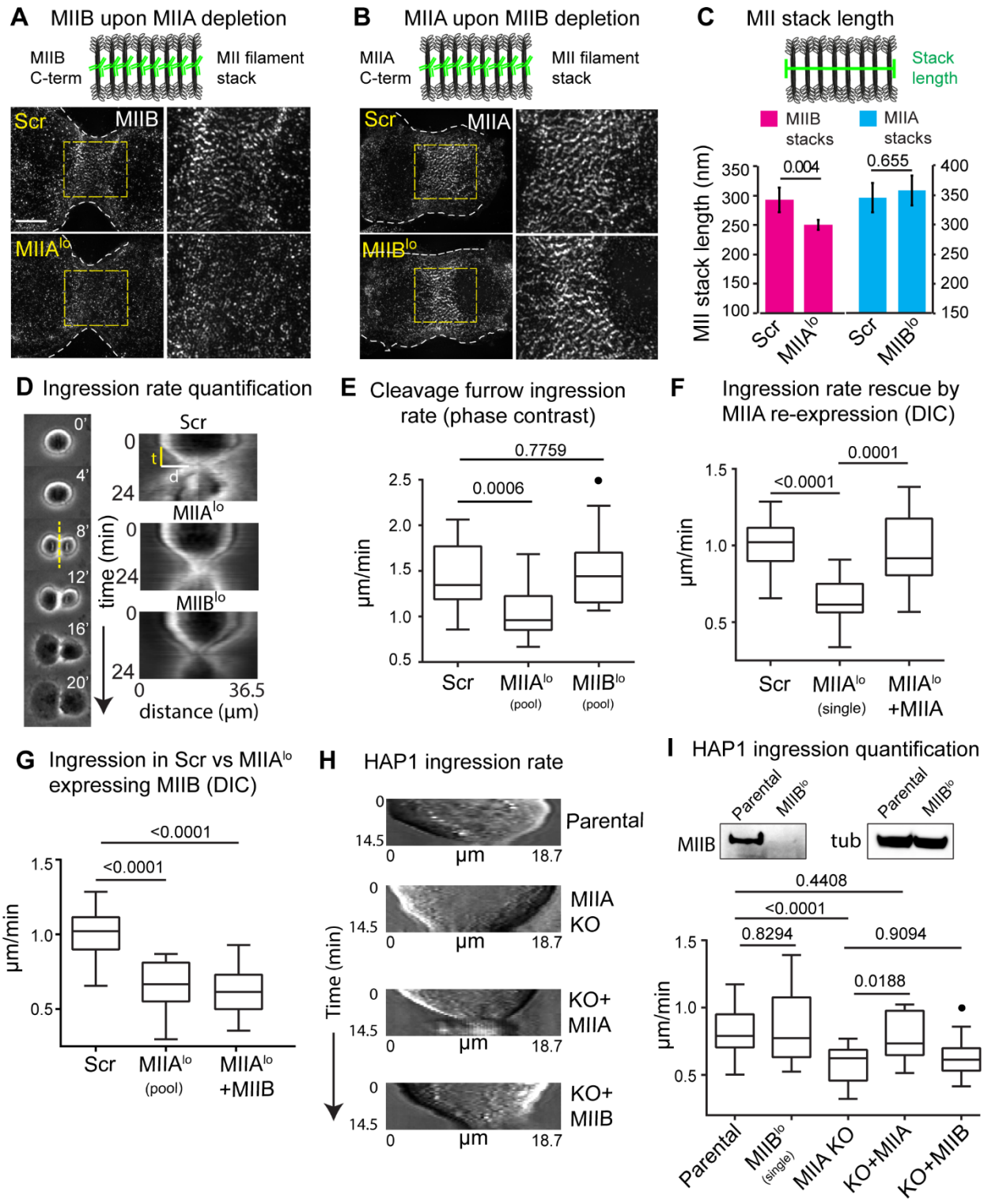

Figure 4-1- MIIA drives furrow ingression through templating of MII stacks

A-B) Endogenous MIIB (A) and MIIA (B) in the cleavage furrow of Scr versus MIIA^{lo} or MIIB^{lo} cells, respectively. Insets: zoom of yellow box. C) Average length of MII stacks. For (A), n=13 Scr cells, N=4 experiments; 17 MIIA^{lo} cells, N=5 experiments. For (B), n=14 Scr and 8 MIIB^{lo} cells, 3 experiments.

Schematic- labeling strategy. D) Furrow ingression rate from phase contrast at 20X magnification. E) Tukey plots of ingression from phase contrast. n=18 Scr, 22 MIIA^{lo} (pooled siRNA) and 20 MIIB^{lo} (pooled siRNA) cells, N=3 experiments. F) Tukey plots of ingression measured independently using DIC at 60X magnification. n=18 Scr, 16 MIIA^{lo} (single siRNA) and 14 MIIA^{lo}+MIIA cells, N=4 experiments. Authors note- phase contrast systematically overestimates distance measurements and gives higher values of ingression. Hence, the Y-axis is scaled differently for panel E. G) Tukey plots of ingression measured independently using DIC. n=15 MIIA^{lo} (pooled siRNA) and 15 MIIA^{lo}+MIIB cells, N=3 experiments. The Scr dataset is the same as (F) and is only displayed for comparison. (H) Representative kymographs of parental, MIIA-KO, MIIA-KO+MIIA-mEGFP and MIIA-KO+MIIB-mEGFP HAP1 cells. (I) Tukey plots of ingression for parental, MIIB^{lo} (single siRNA), MIIA-KO, MIIA-KO+MIIA-mEGFP or MIIA-KO+MIIB-mEGFP HAP1 fibroblasts. n= 11 MIIA KO, 12 MIIA-expressing and 10 MIIB-expressing cells, N=3 experiments. Solid circles represent outliers. Inset- Western blot showing siRNA knockdown of MIIB in parental HAP1 fibroblasts with tubulin as loading control. Scale bar- 5 μm. p values stated over graphs.

Loss of MIIB results in shape instabilities at the polar cortex

Despite no change in furrow ingression in MIIB^{lo} cells, we noted using high-resolution DIC imaging that MIIB^{lo} cells showed dramatic shape instabilities during cytokinesis in the form of large membrane blebs (4.2-fold higher total bleb surface area per min, $p<0.0001$) (Figure 4-2). This result was surprising, since no change in polar blebbing was reported upon knockout of MIIB in fibroblasts (Yamamoto et al., 2019). On the other hand, consistent with the previous report (Yamamoto et al., 2019), MIIA^{lo} cells showed reduced blebbing compared to Scr cells (3-fold lower total bleb surface area per min, $p=0.0096$) (Figure 4-2). The blebbing events in MIIB^{lo} cells were associated with spindle rocking behavior, as has been observed previously upon destabilization of the polar cortex at one pole or depletion of moesin (Carreno et al., 2008; Sedzinski et al., 2011). Expression of siRNA resistant MIIB-mEGFP at 119% of endogenous levels significantly reduced blebbing events in MIIB^{lo} cells (Figure 4-2, Table 4-1). Overexpression of MIIA at 116% of endogenous levels in MIIB^{lo} cells did not reduce blebbing events (Figure 4-2). Conversely, expression of siRNA resistant MIIA-mEGFP in MIIA^{lo} cells rescued blebbing, while overexpression of MIIB-mEGFP in MIIA^{lo} cells did not increase blebbing (Figure 4-2). These data show that the increase and decrease in blebbing were specific to MIIB and MIIA depletion, respectively.

To test if loss of MIIA is associated with reduced blebbing during interphase, we turned to filamin deficient M2 melanoma cells. M2 cells are a classical model for blebbing, since a large proportion of these cells constitutively blebs (Bovellan et al., 2014; Charras et al., 2006; Cunningham, 1995). We found ~50% of Scr M2 cells blebbed. Knockdown of MIIA, but not MIIB, reduced the proportion of blebbing M2 cells (Figure 4-2, Figure 4-S3). Expression of MIIA-mEGFP in MIIA^{lo} M2 cells increased the proportion of blebbing cells (Figure 4-2). These data therefore suggest loss of MIIA is correlated with less frequent blebbing, while loss of MIIB is correlated with more frequent blebbing.

Figure 4-2

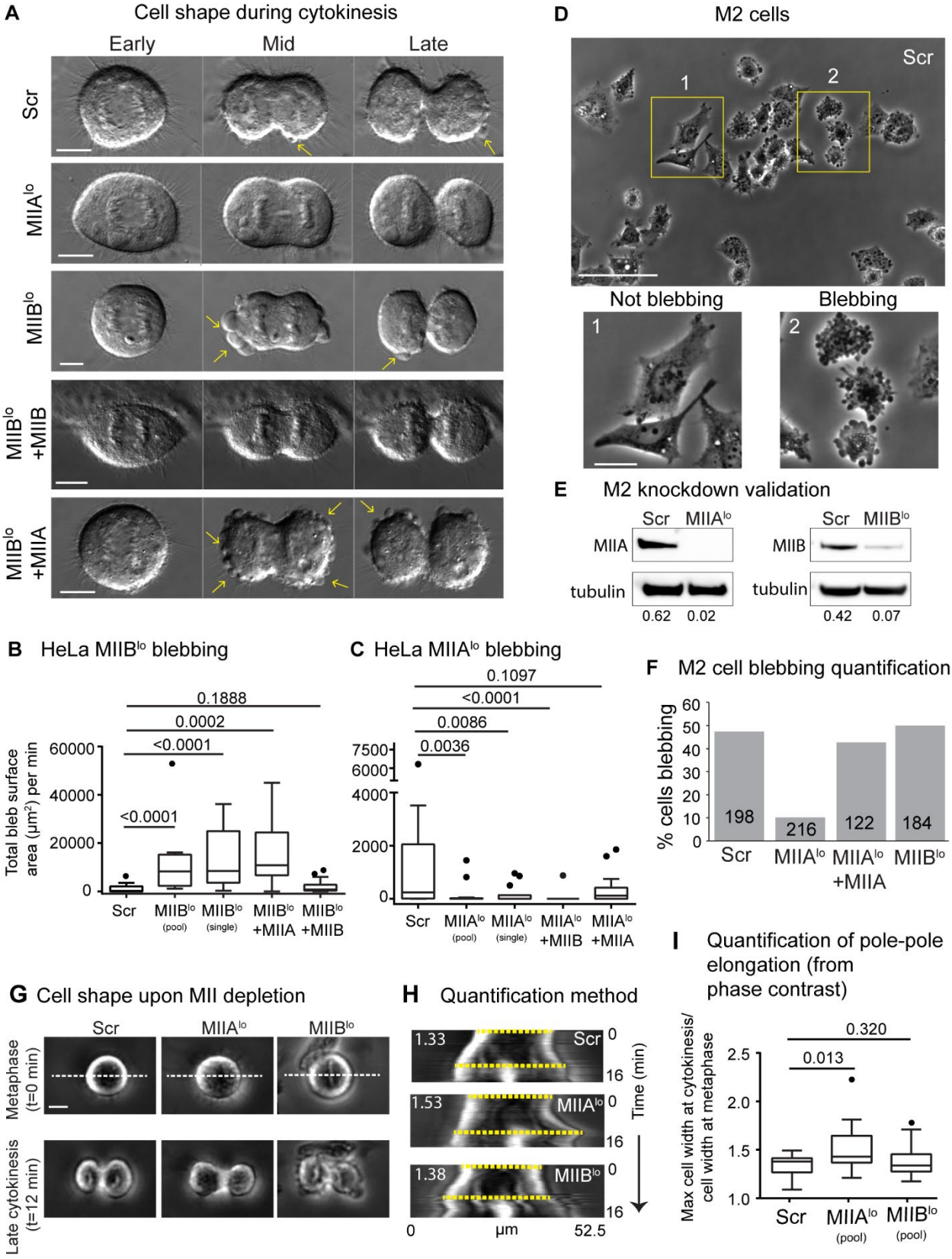
A
Cell shape during cytokinesis
Early
Mid
Late
Scr
MIIA^lo
MIIB^lo
MIIB^lo +MIIB
MIIB^lo +MIIA
D
M2 cells
Scr
1
2
Not blebbing
Blebbing
E
M2 knockdown validation
Scr
MIIA^lo
MIIA
tubulin
0.62
0.02
Scr
MIIB^lo
MIIB
tubulin
0.42
0.07
B
HeLa MIIB^lo blebbing
Total bleb surface area (μm²) per min
0.1888
0.0002
<0.0001
<0.0001
60000
40000
20000
0
Scr
MIIB^lo (pool)
MIIB^lo (single)
MIIB^lo +MIIA
MIIB^lo +MIIB
C
HeLa MIIA^lo blebbing
0.1097
<0.0001
0.0086
0.0036
7500
6000
4000
2000
0
Scr
MIIA^lo (pool)
MIIA^lo (single)
MIIA^lo +MIIB
MIIA^lo +MIIA
F
M2 cell blebbing quantification
% cells blebbing
60
50
40
30
20
10
0
198
216
122
184
Scr
MIIA^lo
MIIA^lo +MIIA
MIIB^lo
G
Cell shape upon MII depletion
Scr
MIIA^lo
MIIB^lo
Metaphase (t=0 min)
Late cytokinesis (t=12 min)
H
Quantification method
1.33
Scr
1.53
MIIA^lo
1.38
MIIB^lo
0
16
Time (min)
0
μm
52.5
I
Quantification of pole-pole elongation (from phase contrast)
Max cell width at cytokinesis/ cell width at metaphase
0.320
0.013
2.5
2.0
1.5
1.0
Scr
MIIA^lo (pool)
MIIB^lo (pool)

Figure 4-2- MII paralog depletion leads to distinct alterations to cell shape

A) Early, mid, and late cytokinesis in Scr, MIIB^{lo}, MIIA^{lo}, MIIB^{lo}+ MIIB-mEGFP and MIIB^{lo}+ MIIA-mEGFP cells. Yellow arrows denote blebs. B-C) Tukey plots of blebbing measured as sum diameter of blebs per minute (B) n= 18 Scr cells, 15 MIIB^{lo} (pooled siRNA) cells, 16 MIIB^{lo} (single siRNA), 15 MIIB^{lo} +MIIB and 10 MIIB^{lo} +MIIA cells, N=4 experiments. C) n=14 MIIA^{lo} (pooled siRNA), 14 MIIA^{lo} (single siRNA), 14 MIIA^{lo} +MIIA and 15 MIIA^{lo} +MIIB cells; N=4 experiments. D) Control M2 cells 5 hours post plating. Insets: examples of not blebbing (1) versus blebbing (2) cells. E) Knockdown of MIIA and MIIB in M2 cells. Intensity of MII bands normalized to tubulin loading control shown below each band. F) Proportion of blebbing cells in Scr, MIIA^{lo}, MIIB^{lo} or MIIA^{lo}+MIIA-mEGFP. Number of cells stated inside bars. G) Scr, MIIA^{lo} and MIIB^{lo} cells at metaphase and late cytokinesis. H) Kymographs were generated using dotted white lines in (G). Dotted yellow lines show the two pole-to-pole lengths used to measure elongation ratio. See methods for quantification details. I) Tukey plots of polar elongation. n=17 Scr, 20 MIIA^{lo} (pooled siRNA) and 18 MIIB^{lo} (pooled siRNA) cells, N=3 experiments. Scale bars in (A, G)- 10 μm, (D)- 100 μm, inset- 25 μm. p values stated over graphs.

The shape instabilities observed in MIIB^{lo} cells led us to further analyze cell shape upon depletion of the two paralogs. Specifically, we noted that MIIA^{lo} cells tended to elongate more than Scr cells during cytokinesis (Figure 4-2). We quantified this cell shape alteration by measuring the increase in pole-to-pole distance during cytokinesis relative to metaphase (Figure 4-2). Indeed, MIIA^{lo} cells showed a 13% longer pole-to-pole distance compared to Scr or MIIB^{lo} cells (Figure 4-2, p=0.013 for Scr versus MIIA^{lo}). Expression of MIIA in MIIA^{lo} cells significantly reduced pole-to-pole elongation (Figure 4-S3). On the other hand, overexpression of MIIB in MIIA^{lo} cells did not rescue this defect (Figure 4-S3). Taken together, our results show that depletion of either paralog leads to distinct alterations to cell shape during cytokinesis.

Depletion of MII paralogs leads to changes in MII localization and hetero-filament composition

MIIA and MIIB co-localize during metaphase and ingression (Yamamoto et al., 2019). We confirmed this by both co-expressing MIIA mApple and MIIB mEmerald in HeLa cells, as well as endogenous labeling (Figure 4-S4). We found that MIIB was cortically enriched as early as metaphase, whereas MIIA was only weakly enriched at the metaphase cortex (Figure 4-S4). After completion of furrow ingression (i.e., late cytokinesis), MIIA enrichment at the cortex was lost, while MIIB remained distinctly enriched at the equatorial cortex (Figure 4-S4). Since there were only subtle differences in MIIA and MIIB localization, other mechanisms must therefore account for the differences in phenotypes observed upon knockdown of MII paralogs; that is, the phenotypes observed are not due to only one paralog localizing to the polar cortex.

We hypothesized that depletion of one paralog could lead to a change in the localization of the other. To test this, we localized endogenous MIIA and MIIB in Scr versus MIIB^{lo} and MIIA^{lo} cells, respectively. At the equatorial cortex, we noted only MIIB compensated for MIIA upon MIIA depletion (Figure 4-S4). On the other hand, depletion of either paralog led to a compensatory increase in localization of the other at the polar cortex (Figure 4-3). We observed this compensatory behavior even at the metaphase cortex (Figure 4-3). Expression of MIIA in MIIA^{lo} cells at 60% of endogenous levels reduced MIIB localization at the cortex (Figure 4-S4, Table 4-1). Similarly, expression of MIIB in MIIB^{lo} cells at 123% of endogenous levels reduced MIIA localization at the cortex (Figure 4-S5). Taken together, our data show

that knockdown of either paralog leads to a change in the relative abundance of the two paralogs at the cortex.

Figure 4-3

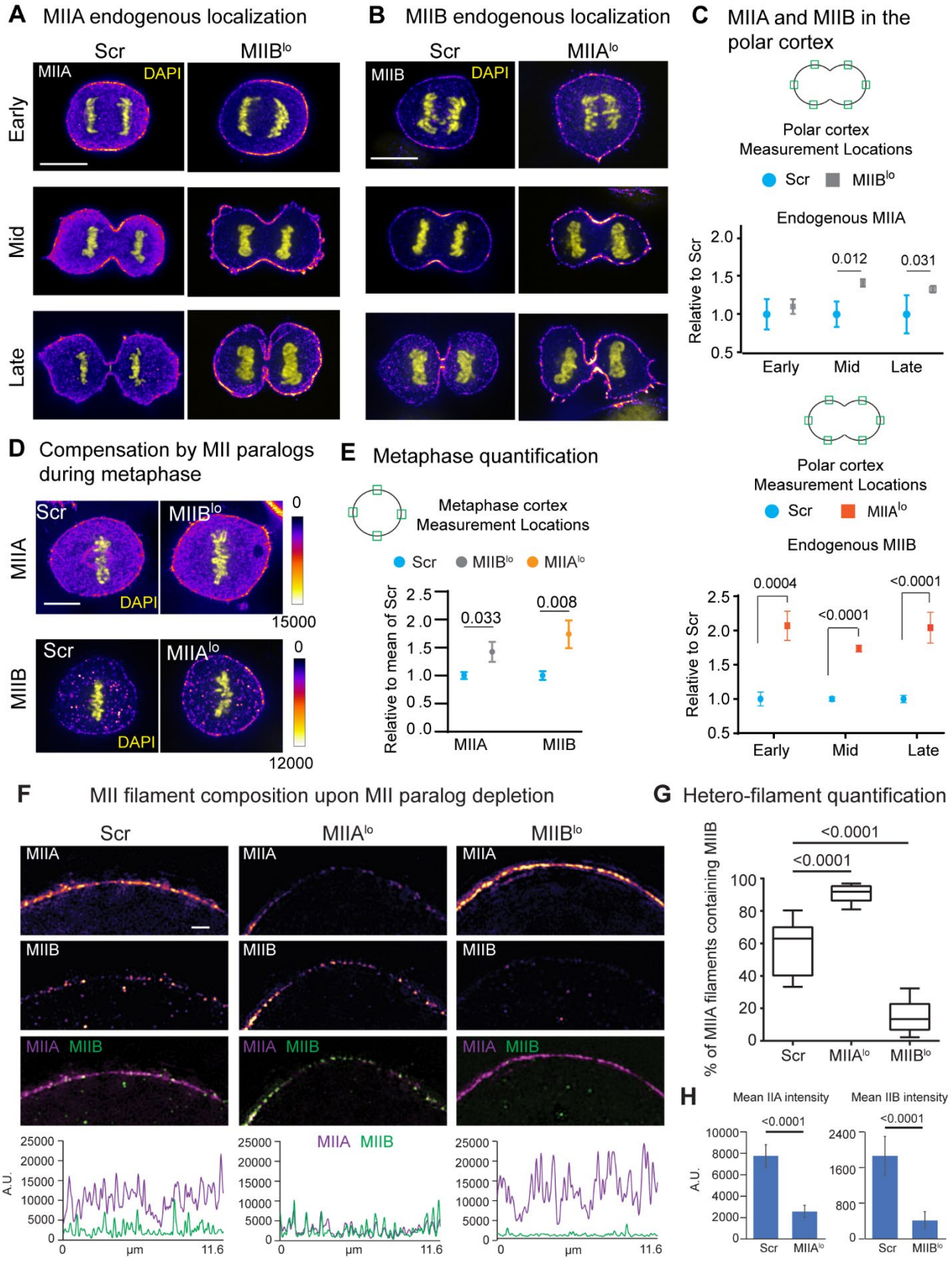
A MIIA endogenous localization
Scr
MIIB^lo
MIIA
DAPI
Early
Mid
Late
B MIIB endogenous localization
Scr
MIIA^lo
MIIB
DAPI
C MIIA and MIIB in the polar cortex
Polar cortex Measurement Locations
Scr
MIIB^lo
Endogenous MIIA
Relative to Scr
2.0
1.5
1.0
0.5
0.012
0.031
Early
Mid
Late
Polar cortex Measurement Locations
Scr
MIIA^lo
Endogenous MIIB
0.0004
<0.0001
<0.0001
Relative to Scr
2.5
2.0
1.5
1.0
0.5
Early
Mid
Late
D Compensation by MII paralogs during metaphase
MIIA
Scr
MIIB^lo
DAPI
0
15000
MIIB
Scr
MIIA^lo
DAPI
0
12000
E Metaphase quantification
Metaphase cortex Measurement Locations
Scr
MIIB^lo
MIIA^lo
Relative to mean of Scr
2.5
2.0
1.5
1.0
0.5
0.0
0.033
0.008
MIIA
MIIB
F MII filament composition upon MII paralog depletion
Scr
MIIA^lo
MIIB^lo
MIIA
MIIB
MIIA MIIB
A.U.
25000
20000
15000
10000
5000
0
0
µm
11.6
G Hetero-filament quantification
<0.0001
<0.0001
% of MIIA filaments containing MIIB
100
80
60
40
20
0
Scr
MIIA^lo
MIIB^lo
H
Mean IIA intensity
Mean IIB intensity
<0.0001
<0.0001
A.U.
10000
8000
6000
4000
2000
0
2400
1600
800
0
Scr
MIIA^lo
Scr
MIIB^lo

Figure 4-3- MII paralog compensation results in altered hetero-filament composition

A-B) Early, mid, and late cytokinesis cells showing endogenous MIIA (A) or MIIB (B) (Fire LUT) in Scr versus MIIB^{lo} or MIIA^{lo} cells, respectively. All compared images were scaled similarly. C) Intensity of MIIA and MIIB at the polar cortex calculated as mean of green ROIs in cartoon insets. For MIIA: n=41 Scr and 48 MIIB^{lo} cells, N=3 experiments. For MIIB: n= 46 Scr and 43 MIIA^{lo} cells, N=3 experiments. D) MIIA and MIIB localization (Fire LUT) during metaphase in MIIB^{lo} and MIIA^{lo} cells, respectively. E) MIIA: n=15 cells each for Scr and MIIB^{lo}, N=3 experiments. MIIB: n= 13 Scr cells and 12 MIIA^{lo} cells, N=3 experiments. F) MIIA and MIIB localization (mpl inferno LUT for single channel) in control versus knockdown cells using SIM. G) Tukey plots showing percentage of MIIA filaments that co-localized with MIIB. Solid circles represent outliers. H) Mean intensity of MIIA and MIIB upon knockdown. n=503, 361 and 354 filaments in Scr, MIIA^{lo} and MIIB^{lo} cells, respectively, from 10 cells per condition; N=3 experiments. Error bars in (C) and (E) represent standard error of weighted mean. Scale bar in (A,B,D)- 10 µm, (F)- 1 µm. p values stated over graphs.

We next wanted to investigate the molecular basis for the compensatory localization of MII paralogs at the polar cortex. While hetero-filaments of MIIA and MIIB have been reported at the cleavage furrow using SIM (Beach et al., 2014) the composition of MII filaments at the polar cortex has remained unexplored. To that end, we performed SIM of endogenous MIIA and MIIB at the polar cortex. We found that 96% of MIIB filaments co-localized with MIIA in control cells, while 58% of MIIA filaments contained MIIB (Figure 4-3). Depletion of MIIA resulted in a significant decrease in MIIA intensity at the cortex, accompanied by a significant increase in the proportion of the residual MIIA filaments containing MIIB (91%, $p<0.0001$) (Figure 4-3). Interestingly, the proportion of MIIB filaments containing MIIA remained unchanged. Conversely, depletion of MIIB resulted in a significant decrease in the proportion of MIIA filaments containing MIIB, with only 15% of MIIA filaments positive for MIIB (Figure 4-3, $p<0.0001$). We again found that ~99% of the residual MIIB was in hetero-filaments with MIIA. Taken together, our results show that knockdown of MIIA results in an increase in the proportion of MIIB-containing hetero-filaments while knockdown of MIIB results in a decrease in the proportion of MIIB-containing hetero-filaments. We next wanted to investigate how these changes in filament composition alter the biophysical properties of the cortex.

Depletion of MIIA results in reduced cortex tension and intracellular pressure

A recent study reported that MIIA, but not MIIB, knockout results in reduced cortex stiffness, which the authors proposed underlies reduction in blebbing (Yamamoto et al., 2019). This is contrary to the well-established concept that cortex tension, not stiffness, is the direct result of actomyosin contractility and thus drives initiation and growth of blebs (Paluch et al., 2005; Tinevez et al., 2009). We therefore investigated how changes in MII filament composition altered cortex tension and stiffness. Micropipette aspiration can be used to measure cortex tension as well as elastic properties of cells to measure stiffness (Brugues et al., 2010; Kee and Robinson, 2013; Tinevez et al., 2009). We chose to perform these measurements during metaphase, since i) we found compensation in localization during metaphase, ii) the metaphase cortex is uniform and devoid of the fluctuations in MII localization that occur at the polar cortex and iii) Polar cortex blebbing would interfere in cortex tension measurements. Consistent with previous reports, we found knockdown of MIIA resulted in reduced cortex stiffness (Figure 4-S5) (Yamamoto et al., 2019). Since $MIIB^{lo}$ cells show a higher degree of blebbing, we expect $MIIB^{lo}$ cells to be stiffer. However, we found stiffness was unaltered in

MIIB^{lo} cells (Figure 4-S5), as also previously reported for MIIB knockout (Yamamoto et al., 2019). These data suggest that changes in stiffness are not sufficient to explain the observed differences in bleb initiation, since stiffness in MIIB^{lo} cells is unaltered despite dramatic increases in blebbing.

We then measured cortex tension using micropipette aspiration and found a significant reduction (~4-fold) in cortex tension in MIIA^{lo} versus Scr cells (Figure 4-4, $p<0.0001$). Expression of MIIA-mEGFP at 72% of endogenous levels increased cortex tension to approximately control levels (Figure 4-4). As an additional control for these measurements, we treated Scr cells with 50 μM blebbistatin, and measured cortex tension. As previously reported, blebbistatin significantly reduced cortex tension (Tinevez et al., 2009) (Figure 4-4).

Conversely, we predicted that MIIB depletion should result in higher cortex tension as MIIB^{lo} cells show more blebbing. MIIB^{lo} cells had ~1.9-fold higher cortex tension compared to Scr cells (Figure 4-4, $p=0.0082$). Expression of MIIB-mEGFP at 197% of endogenous levels in MIIB^{lo} cells resulted in a decrease in cortex tension comparable to control levels (Figure 4-4). Taken together, our results show MIIA depletion results in lower cortex tension, while MIIB depletion results in higher cortex tension, which correlated with the observed frequencies of bleb initiation we observed during cytokinesis (Figure 4-2). Despite increased cortex tension in MIIB^{lo} cells, these cells did not bleb during metaphase. To test if increasing pressure could induce blebbing, we compressed MIIB^{lo} cells in metaphase with a microneedle. We observed MIIB^{lo} cells blebbed 80% of the time upon indentation, while Scr and MIIA^{lo} cells showed negligible blebbing (Figure 4-S5).

Figure 4-4

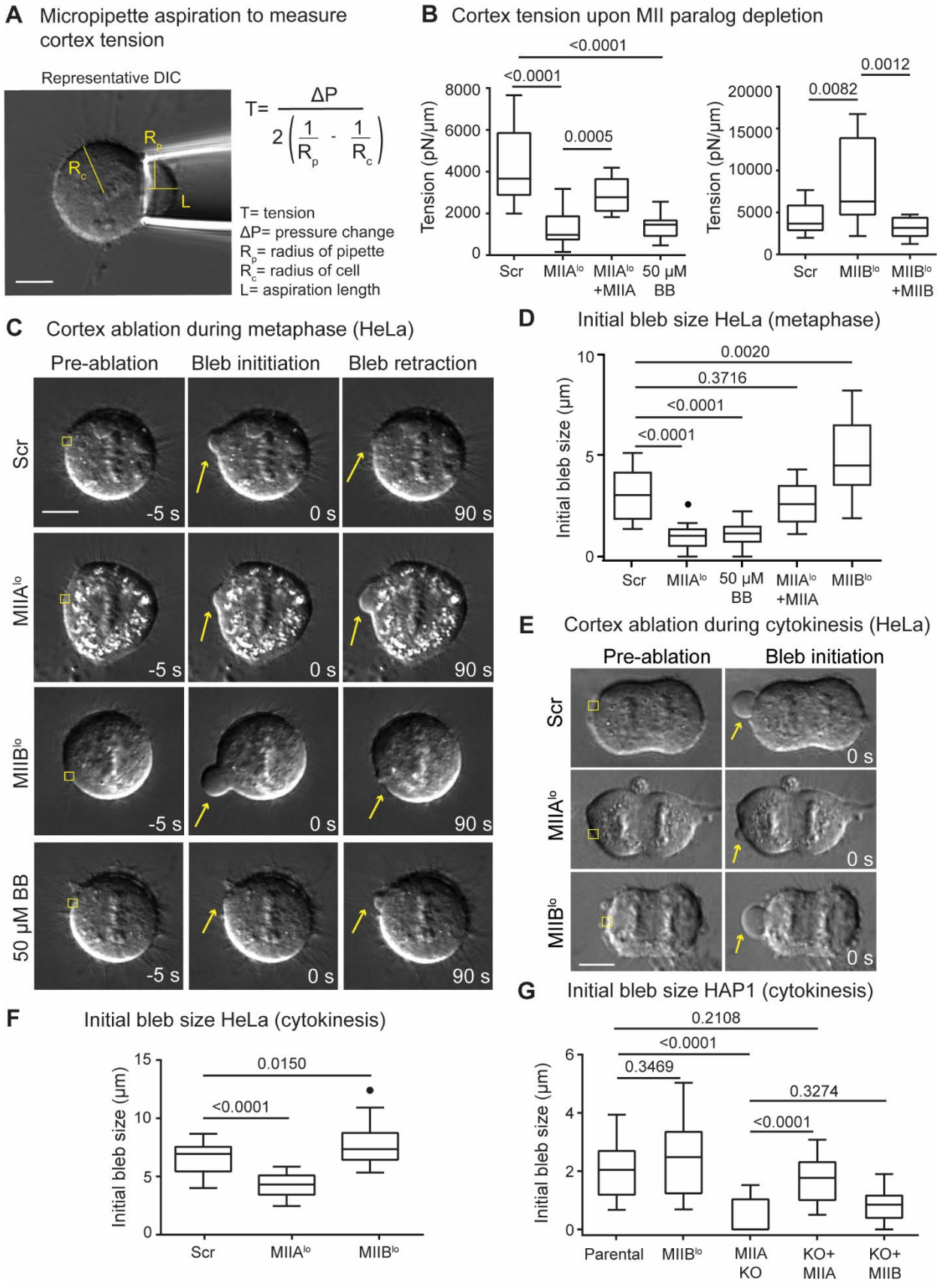
A Micropipette aspiration to measure cortex tension
Representative DIC
$T = \frac{\Delta P}{2\left(\frac{1}{R_p} - \frac{1}{R_c}\right)}$
T= tension
ΔP= pressure change
R_p= radius of pipette
R_c= radius of cell
L= aspiration length
B Cortex tension upon MII paralog depletion
Tension (pN/μm)
Scr
MIIA^lo
MIIA^lo +MIIA
50 μM BB
MIIB^lo
MIIB^lo +MIIB
C Cortex ablation during metaphase (HeLa)
Pre-ablation
Bleb inititiation
Bleb retraction
Scr
MIIA^lo
MIIB^lo
50 μM BB
-5 s
0 s
90 s
D Initial bleb size HeLa (metaphase)
Initial bleb size (μm)
E Cortex ablation during cytokinesis (HeLa)
Pre-ablation
Bleb initiation
F Initial bleb size HeLa (cytokinesis)
G Initial bleb size HAP1 (cytokinesis)
Parental
MIIA KO
KO+ MIIA
KO+ MIIB

Figure 4-4- MIIA is necessary and sufficient to generate cortex tension and intracellular pressure

A) Micropipette aspiration of control cell during metaphase, showing cell radius (R_c), aspirated length (L) and radius of pipette (R_p). Tension was calculated using the mathematical expression shown. B) Tukey plots of cortex tension upon MII paralog depletion. n= 16 Scr, 14 $MIIA^{lo}$, 15 $MIIB^{lo}$, 10 $MIIA^{lo}$ +MIIA-mEGFP, 11 blebbistatin treated and 12 $MIIB^{lo}$ +MIIB-mEGFP cells, N=4 experiments each. C) Scr, $MIIA^{lo}$, $MIIB^{lo}$ and 50 μM blebbistatin treated HeLa cells before ablation, 0 seconds after ablation and 90 seconds after ablation of the metaphase cortex. Yellow squares depict ablation ROI, yellow arrows depict blebs. D) Tukey plots showing initial bleb size during metaphase in HeLa cells. n= 17 Scr, 16 $MIIA^{lo}$, 14 $MIIA^{lo}$ +MIIA, 14 50 μM blebbistatin treated and 18 $MIIB^{lo}$ cells, N=3 experiments. E) Polar cortex ablation in Scr, $MIIA^{lo}$ and $MIIB^{lo}$ HeLa cells during cytokinesis. Yellow squares depict ablation ROI, yellow arrows denote bleb created by ablation. F) Tukey plots of initial bleb size during cytokinesis in HeLa cells. n= 25 Scr, 15 $MIIA^{lo}$ and 25 $MIIB^{lo}$ cells, N=3 experiments. G) Tukey plots of initial bleb size following ablation in HAP1 KO fibroblasts during cytokinesis. n= 12 untransfected MIIA-KO, 26 MIIA, and 11 MIIB expressing cells, N=3 experiments. Scale bars- 10 μm. Solid circles represent outliers. p values stated over graphs.

We next wanted to directly interrogate the relative contributions of MIIA and MIIB to bleb growth. It has been previously reported that MII driven cortex tension promotes bleb growth by creating hydrostatic pressure (Tinevez et al., 2009). Blebs created by disruption of the cortex using localized laser ablation are thought to mimic the initiation of spontaneous blebs (Goudarzi et al., 2012; Tinevez et al., 2009). The size of the bleb created immediately following ablation is positively correlated with the instantaneous intracellular pressure. Ablation of the metaphase cortex of Scr cells resulted in the creation of a bleb, which subsequently retracted over a period of 45-90 seconds, as has been reported previously (Figure 4-4) (Charras et al., 2006; Taneja and Burnette, 2019). Since MIIA^{lo} cells have lower cortex tension, we hypothesized that smaller blebs would be created in these cells. To test this, we created blebs using laser ablation at the metaphase cortex of MIIA^{lo} cells and measured the size of the bleb immediately following ablation (Figure 4-4). Small or no blebs were created immediately following ablation in MIIA^{lo} cells (Figure 4-4, $p<0.0001$ for Scr versus MIIA^{lo}). Interestingly, these blebs failed to retract and instead exhibited a period of slow growth over extended time periods of up to 4 minutes (Figures 4-4 and 4-S6). Expression of MIIA-mEGFP increased bleb size comparable to Scr cells, as well as restored bleb retraction (Figure 4-4). This role of MIIA in driving bleb retraction was consistent with our previous report (Taneja and Burnette, 2019).

Conversely, we hypothesized larger blebs should be created upon depletion of MIIB due to increased cortex tension. We found 1.6-fold larger blebs were created in MIIB^{lo} cells upon laser ablation, and these blebs all successfully retracted (Figures 4-4 and 4-S6; $p=0.0020$ for Scr versus MIIB^{lo}). To test whether the pressure driving bleb growth was specifically generated by MII driven cortex tension, we performed ablation in cells treated with 50 μM blebbistatin. Indeed, blebbistatin treatment mimicked MIIA depletion, with small or no blebs created upon ablation, and exhibited slow bleb growth instead of retraction (Figure 4-4 and 4-S6). Taken together, our results show MIIA driven cortex tension creates larger blebs upon ablation during metaphase.

We next proceeded to test whether MIIA drives growth of larger blebs at the polar cortex during cytokinesis. To that end, we performed laser ablation of the polar cortex during cytokinesis in Scr versus MIIA^{lo} and MIIB^{lo} cells (Figure 4-4). We observed that blebs created at the polar cortex of Scr cells resulted in blebs that were on average larger than those created during metaphase (Figure 4-4, panel F compared to panel D), consistent with the idea that intracellular pressure increases following anaphase onset (Stewart et al., 2011). Depletion of

MIIA resulted in the creation of smaller blebs that failed to retract, while MIIB depletion resulted in larger blebs compared to Scr cells (Figure 4-4).

We then wanted to test whether MIIA is sufficient to drive bleb growth. To that end, we performed laser ablation of the polar cortex of HAP1 fibroblasts. We observed that very small or no blebs were created in MIIA KO cells compared to control parental cells or MIIB^{lo} parental cells (Figure 4-4 and 4-S5). Expression of MIIA, but not MIIB, resulted in restoration of bleb formation upon ablation (Figure 4-4 and 4-S5). To further test if MIIA is sufficient to drive higher bleb growth, we turned to Cos7 cells, that do not express MIIA. Indeed, expression of MIIA, but not MIIB, increased bleb size upon ablation of the polar cortex during cytokinesis (Figure 4-S5). Taken together, our results show that MIIA is both necessary and sufficient to drive the growth of larger blebs.

MII motor domains dictate the relative contribution of MII paralogs

Previous studies have shown that the C-terminus of MII regulates paralog localization (Sandquist and Means, 2008; Vicente-Manzanares et al., 2008). The observed similarities in localization dynamics of MIIA and MIIB at the polar cortex (Figure 4-S4) suggest that the N-terminal motor domains might account for the distinct roles played by the two paralogs during cytokinesis. Most characterizations of MII motor activity *in vitro* has been performed using N-terminal S1 fragments (Kovacs et al., 2003; Rosenfeld et al., 2003; Wang et al., 2003). Therefore, a chimeric MII, bearing the motor domain of MIIB, and the coiled coil domain and tail piece of MIIA (MIIB/A), should be able to rescue blebbing in MIIB^{lo} cells by competing with endogenous MIIA motors at the polar cortex, independent of the tail domain. As expected, this chimeric motor showed a localization pattern similar to MIIA, with weaker cortical enrichment (Figure 4-5), consistent with previous findings that the tail of MIIB determines its subcellular localization (Sandquist and Means, 2008; Vicente-Manzanares et al., 2008). Strikingly, expression of the MIIB/A chimera at levels comparable to full length MIIB (Table S1) resulted in significant suppression of blebbing (Figure 4-5).

Conversely, MIIB is upregulated at the polar cortex in MIIA^{lo} cells (Figure 4-3); therefore, we hypothesized that increasing MIIA motors in the polar cortex should increase blebbing in MIIA^{lo} cells. To test this, we expressed a chimera bearing the motor domain of MIIA and the coiled coil domain and tailpiece of MIIB (MIIA/B) in MIIA^{lo} cells. This construct also faithfully mimicked MIIB localization, showing a clear cortical enrichment, as well as distinct equatorial localization

during late cytokinesis (Figure 4-5). Interestingly, we observed a significant increase in blebbing upon expression of MIIA/B at levels comparable to full length MIIA (Table 4-1) (Figure 4-5). Furthermore, this construct also significantly increased cleavage furrow ingression rates in MIIA^{lo} cells (Figure 4-5). Increased pole-to-pole elongation observed in MIIA^{lo} cells was also rescued by the MIIA/B chimera (Figure 4-5). To test whether suppression of the MIIA and MIIB depletion phenotypes correlated with changes in cortex tension, we performed micropipette aspiration on MIIA^{lo} expressing MIIA/B-mEGFP and MIIB^{lo} cells expressing MIIB/A-mEGFP. In line with our observations for ingression, blebbing and pole-to-pole elongation, we found MIIB/A expression in MIIB^{lo} cells significantly decreased cortex tension, while MIIA/B expression in MIIA^{lo} cells significantly increased cortex tension (Figure 4-5). To test whether these changes in cortex tension resulted in increased bleb growth, we expressed MIIA/B mEGFP and MIIB/A mEGFP in HAP1 MIIA-KO cells and performed cortex ablation during cytokinesis. Expression of MIIA/B, but not MIIB/A significantly increased initial bleb size following ablation (Figure 4-5). Taken together, these data suggest that the motor domain determines the paralog-specific contribution of the two paralogs at the polar and equatorial cortex.

Figure 4-5

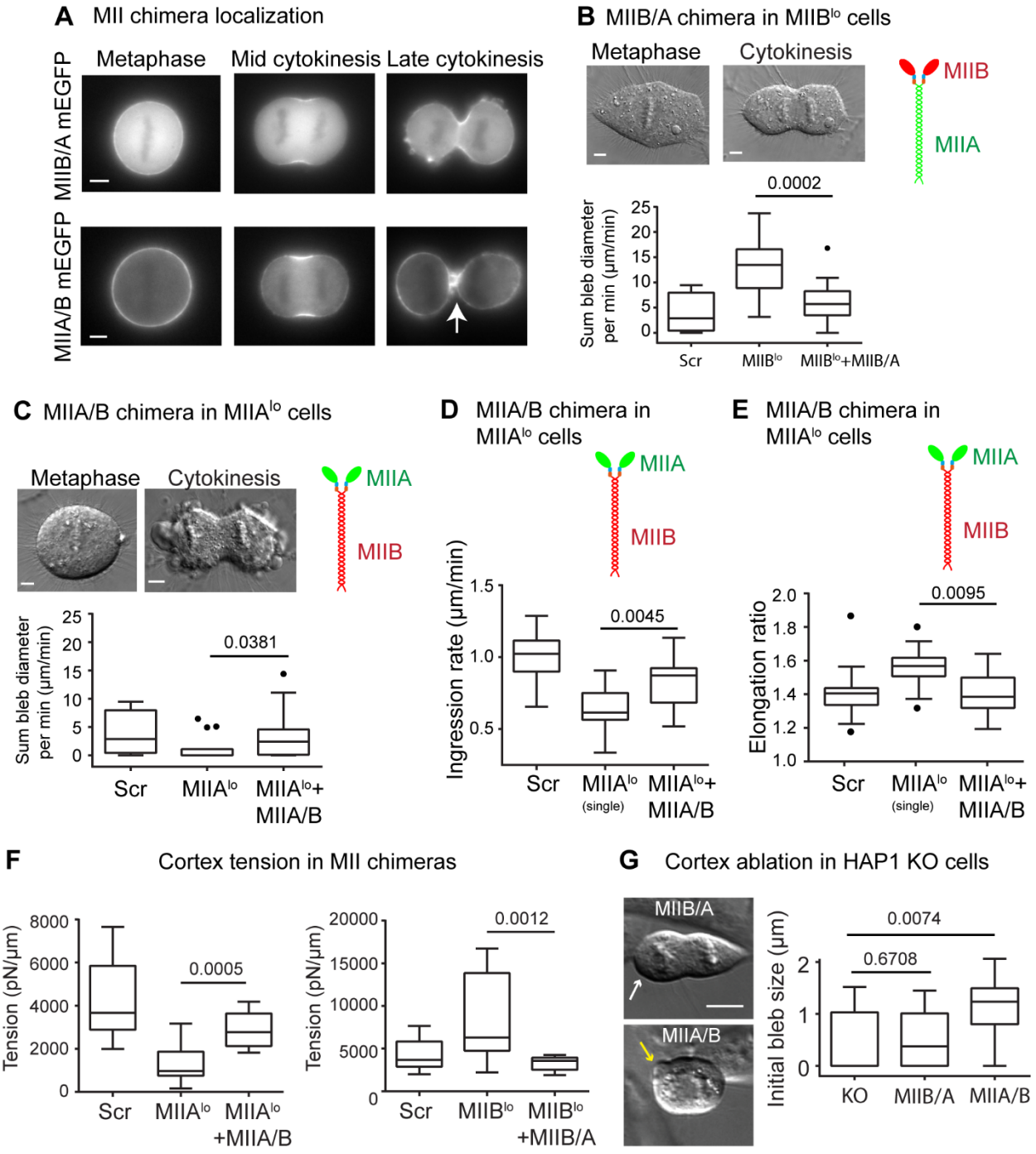

Figure 4-5- Motor domains determine the contribution of MII paralogs to cortical contractility

A) Localization of MIIB/A-mEGFP and MIIA/B-mEGFP chimera in MIIB^{lo} and MIIA^{lo} cells, respectively. Arrow indicates enrichment of MIIA/B at the equatorial cortex during late cytokinesis. B) MIIB^{lo} cell expressing MIIB/A chimera at metaphase and cytokinesis. Tukey plots of blebbing events in MIIB/A expressing cells compared to Scr and MIIB^{lo} (single siRNA). n=16 MIIB^{lo} +MIIB/A cells, N=3

experiments. The Scr and MIIB^{lo} (single) datasets are the same as in Fig. 4-2, panel B and are only shown for comparison. C) MIIA^{lo} cell expressing MIIA/B chimera at metaphase and cytokinesis. n=16 MIIA^{lo} +MIIA/B cells, N=3 experiments. The Scr and MIIA^{lo} (single) datasets are the same as Fig. 4-2 and are only shown for comparison. D) Cleavage furrow ingression rates using DIC comparing MIIA^{lo} cells expressing MIIA/B chimera. n= 16 MIIA^{lo} +MIIA/B cells, N=3 experiments. The Scr and MIIA^{lo} (single) datasets are the same as Fig. 4-1, panel F and are only shown for comparison. E) Pole-to-pole elongation ratios for MIIA^{lo} cells expressing MIIA/B chimera. n=12 MIIA^{lo} +MIIA/B cells, N=3 experiments. The Scr and MIIA^{lo} (single) datasets are the same as Fig. 4-S3 and are only shown for comparison. F) Cortex tension in MIIB/A and MIIA/B chimeras using micropipette aspiration. n= 14 MIIA^{lo} +MIIA/B and 10 MIIB^{lo} +MIIB/A expressing cells over 4 experiments. The Scr, MIIA^{lo} and MIIB^{lo} datasets are the same as in Fig. 4-4, panel B and are only shown for comparison. G) Initial bleb size following ablation in HAP1 KO cells. n=8 MIIB/A, 18 MIIA/B expressing cells, N=3 experiments. Yellow and white arrows denote formation or absence of a bleb, respectively. The control KO dataset is the same as Fig. 4-4, panel G and is only shown for comparison. Scale bars in (A, G) and (B, C)- 10 μm and 5 μm, respectively. Solid circles represent outliers. p values stated over graphs.

MIIB depletion results in cytokinetic failure

We finally wanted to assess the effects of MII paralog depletion upon cytokinetic fidelity. To that end, we measured the proportion of binucleated cells as a proxy for failed cytokinesis. We found that MIIA loss resulted in a mild increase in binucleated cells (Figure 4-6). As an intended control, we measured binucleation in MIIB^{lo} HeLa cells. Surprisingly, we observed a dramatic, nearly 10-fold, increase in binucleated MIIB^{lo} cells relative to Scr cells (Figure 4-6). Expression of siRNA resistant MIIB resulted in a significant decrease in binucleation (Figure 4-6). To test which domain(s) of MIIB was sufficient to rescue the binucleation defect, we expressed the MIIB/A and MIIA/B chimeras in MIIB^{lo} cells. Interestingly, both chimeras partially rescued the binucleation defect (Figure 4-6). This prompted us to investigate the contribution of the two domains to cytokinetic fidelity.

We noted that a subset of binucleated cells were adjacent to an enucleated cell (cytoplast) (Figure 4-6). We wondered whether dramatic spindle oscillation observed during blebbing in MIIB^{lo} cells could lead to this phenotype, where one daughter cell may inherit both sets of chromosomes. Since the MIIB/A chimera suppressed blebbing (Figure 4-5), while the MIIA/B chimera increased blebbing, we hypothesized that expression of these chimeras should alter the proportion of this oscillation-induced binucleation. We first introduced full length MIIB or MIIB/A in MIIB^{lo} cells, both of which suppress blebbing. Expression of both constructs led to a significant decrease in the proportion of cells that were binucleated and adjacent to an enucleated cell (Figure 4-6). Expression of the MIIA/B chimera, which increases blebbing, resulted in a significant increase in the proportion of cells that were binucleated and adjacent to an enucleated cell (Figure 4-6). These data suggested that blebbing positively correlates with increased incidence of oscillation-induced chromosome missegregation.

It was previously theorized that the retraction of large blebs creates large changes in intracellular pressure (Sedzinski et al., 2011). To test whether spindle oscillation was correlated with the retraction of large blebs, we performed closer analysis of oscillation events in MIIB depleted cells. Indeed, spindle displacement was correlated with the retraction of large blebs (Figure 4-7). Furthermore, the extent of displacement positively correlated with the size of the bleb (Figure 4-7). We therefore predicted that cells with higher mean bleb size should show spindle oscillation, rather than cells with higher number of blebs. Indeed, we found that cells showing spindle oscillation had a significantly higher mean bleb size compared to non-

oscillating cells (Figure 4-7). These results show that creation of large blebs increases the probability of spindle oscillation, which could drive chromosome missegregation.

We next wanted to directly visualize oscillation-induced chromosome missegregation in live cells. To that end, we visualized chromosomes using H2B-mCherry and performed live imaging of MIIB^{lo} cells undergoing cytokinesis. Strikingly, we observed that dramatic spindle oscillation in MIIB^{lo} cells did result in one daughter cell inheriting both sets of chromosomes and becoming binucleated, while the other daughter cell was enucleated (Figure 4-7). Furthermore, while the initiation of spindle oscillation correlated with the initiation of polar blebs, subsequent oscillations were accompanied by cortical contractions of entire daughter cells. We found 20.0% of all binucleation events resulted from an oscillation dependent mechanism (Figure 4-7 and 4-S7A). Interestingly, 42.5% of all binucleation events instead resulted from abscission failure in the absence of spindle oscillations, resulting in one binucleated cell (Figure 4-7 and 4-S7). The remaining 37.5% of binucleation events were accompanied by both spindle oscillation and abscission failure, resulting in one binucleated cell (Figure 4-S7).

Figure 4-6

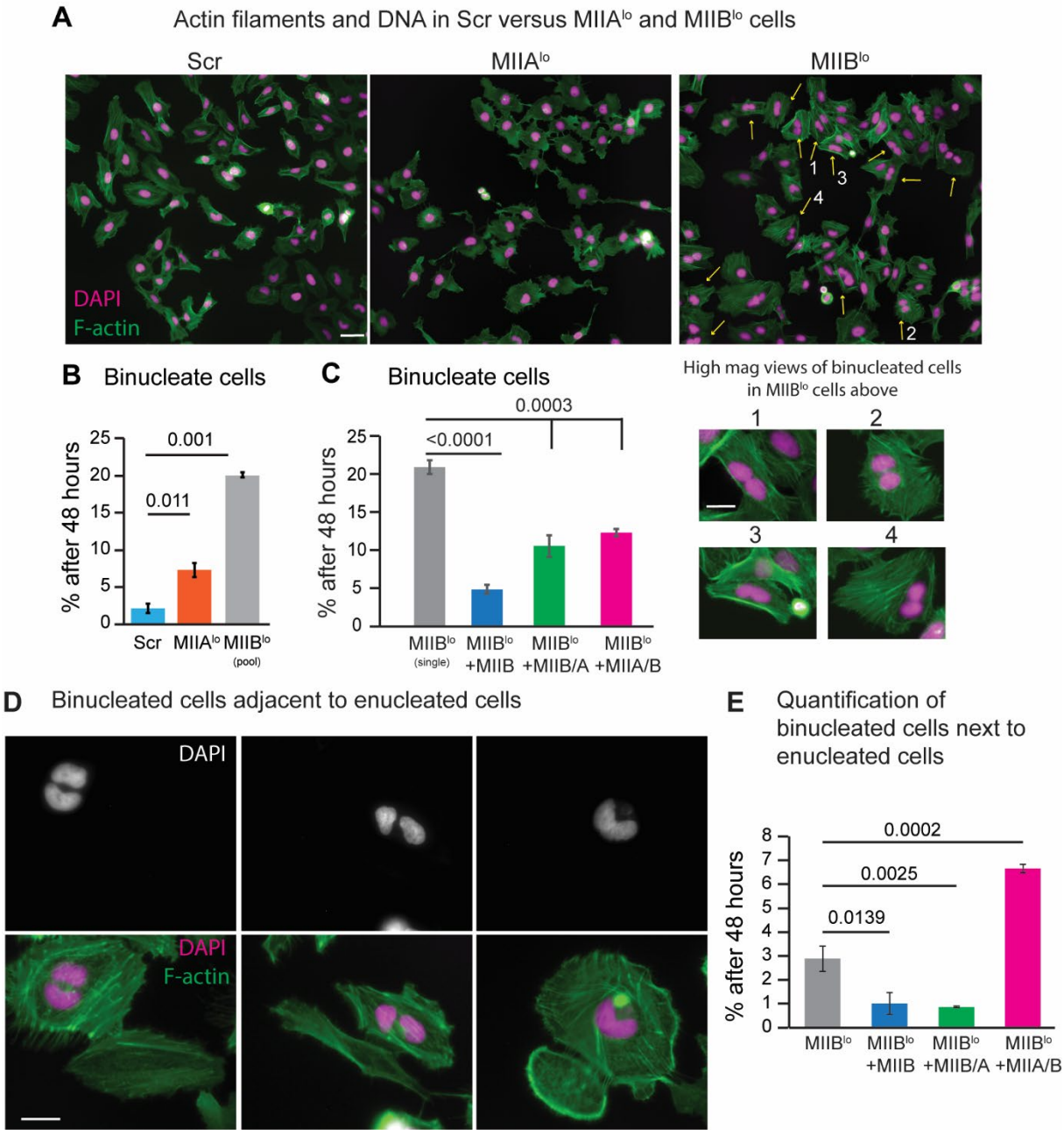

Figure 4-6- MIIB depletion leads to increased binucleation

A) Scr, MIIA^{lo} and MIIB^{lo} cells 48 hours after re-plating showing F-actin (green) and nuclei (magenta). Yellow arrows denote binucleated cells. Inset: higher magnification examples. B) Binucleate cells 48 hours post plating in Scr versus MIIA^{lo} (pooled siRNA) or MIIB^{lo} (pooled siRNA) cells. n>=1000 cells each, N=3 experiments. C) Binucleate cells 48 hours post plating in MIIB^{lo} (single siRNA) versus MIIB^{lo} cells expressing MIIB, MIIB/A or MIIA/B. n= 760 MIIB^{lo} (single), 584 MIIB-expressing, 464 MIIB/A-expressing and 347 MIIA/B-expressing MIIB^{lo} cells, N=3 experiments. D) Representative binucleated MIIB^{lo} cells adjacent to enucleated cells. E) Binucleated cells adjacent to an enucleated cell, as a

fraction of total number of cells. Scale bar in (A)- 50 μm, inset- 25 μm, (D)- 25 μm. Error bars represent standard error of the mean. p values stated over graphs.

To investigate the mechanism for these distinct modes of binucleation, we introduced MII chimeras and measured the relative incidence of oscillation-induced chromosome missegregation and abscission failure. The MIIB/A chimera suppresses blebbing, and therefore should suppress oscillation-induced chromosome missegregation. Indeed, expression of MIIB/A in MIIB^{lo} cells reduced the proportion of oscillation-induced chromosome missegregation, accompanied by an increase in the proportion of cells that underwent abscission failure (Figure 4-7). It was recently proposed that MIIB could play a role in stabilizing the intracellular bridge to facilitate abscission (Wang et al., 2019). In support of this hypothesis, MIIB showed an enrichment at the equatorial cortex at the end of cytokinesis (Figure 4-S4, yellow arrow). Consistent with the tail domain regulating localization, the MIIB/A chimera did not show the late equatorial enrichment at the cortex (Figure 4-5). Taken together, these data suggest that oscillation induced binucleation is suppressed by the ability of the motor domain of MIIB to regulate blebbing.

As opposed to the MIIB/A chimera, the MIIA/B chimera increases blebbing, but still shows enrichment at the equatorial cortex at the end of cytokinesis (Figure 4-5, white arrow). Therefore, this construct should not suppress oscillation-induced chromosome missegregation. Indeed, we observed an increase in the proportion of oscillation induced binucleation (Figure 4-7). Conversely, the proportion of binucleation events accompanied by abscission failure was reduced (Figure 4-7). These data suggest that the tail domain regulates MIIB's ability to facilitate abscission, possibly by driving the late enrichment of MIIB at the equatorial cortex.

Figure 4-7

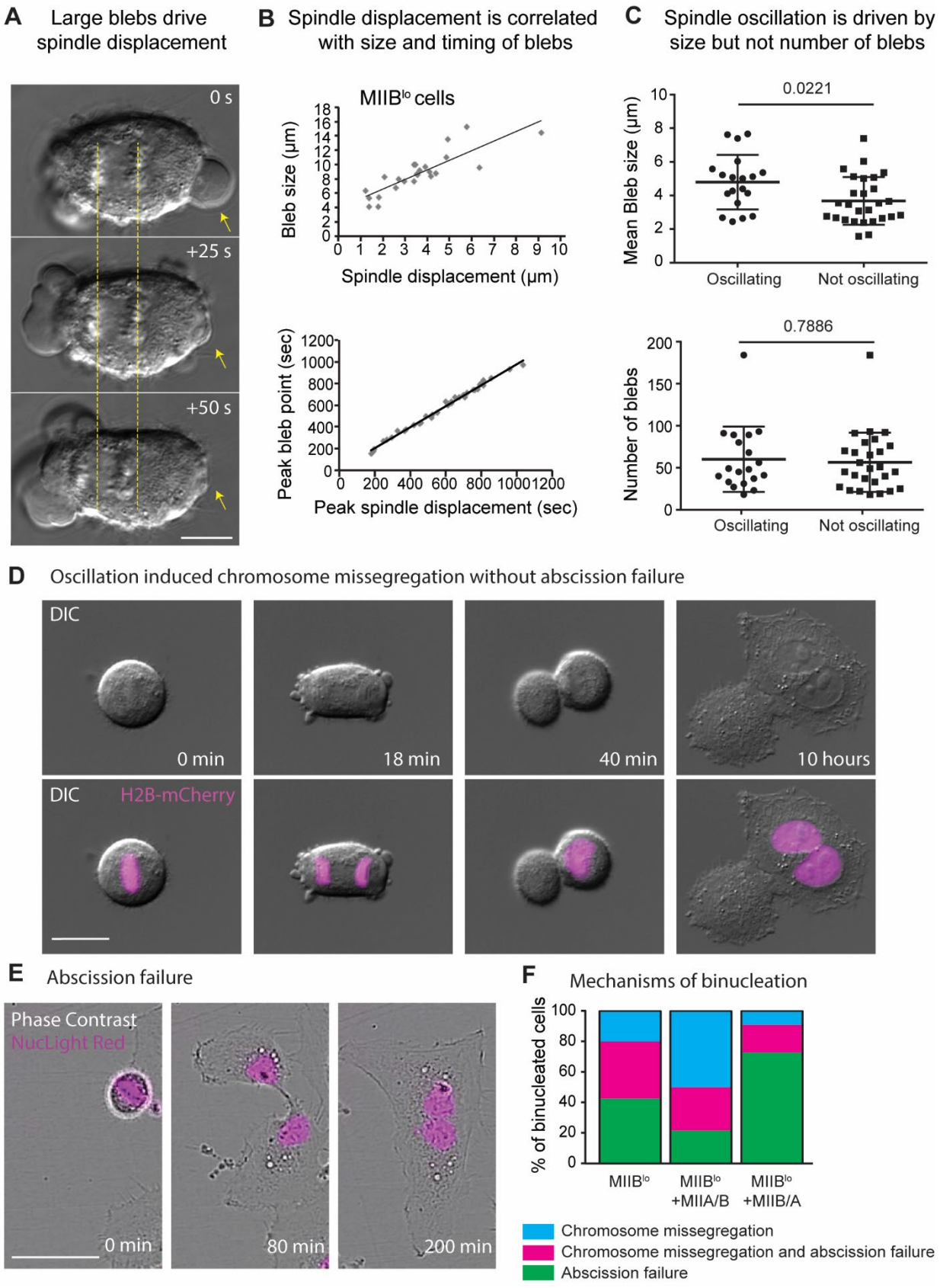
A
Large blebs drive spindle displacement
0 s
+25 s
+50 s
B
Spindle displacement is correlated with size and timing of blebs
MIIBlo cells
Bleb size (µm)
Spindle displacement (µm)
Peak bleb point (sec)
Peak spindle displacement (sec)
C
Spindle oscillation is driven by size but not number of blebs
Mean Bleb size (µm)
0.0221
Oscillating
Not oscillating
Number of blebs
0.7886
Oscillating
Not oscillating
D
Oscillation induced chromosome missegregation without abscission failure
DIC
0 min
18 min
40 min
10 hours
DIC
H2B-mCherry
E
Abscission failure
Phase Contrast
NucLight Red
0 min
80 min
200 min
F
Mechanisms of binucleation
% of binucleated cells
MIIBlo
MIIBlo +MIIA/B
MIIBlo +MIIB/A
Chromosome missegregation
Chromosome missegregation and abscission failure
Abscission failure

Figure 4-7- Loss of MIIB drives binucleation through two distinct mechanisms

A) Time montage showing displacement of the chromosomes (dotted yellow lines) with the retraction of a large bleb (yellow arrow) in a MIIB^{lo} cell. B) Correlation of spindle displacement with the size and timing of blebbing events. Each data point represents a bleb/displacement event plotted over 3 experiments. C) Comparison of oscillating versus non-oscillating cells with respect to bleb size and number of blebbing events. Each data point represents a cell. n= 36 cells, N=6 experiments. D) Representative time montage of spindle oscillation-induced chromosome missegregation upon MIIB depletion. E) Representative time montage showing abscission failure upon MIIB depletion. See Fig. 4-S7 for extended time montage. The ROI used to create the montage was moved to keep the cells centered in the field of view. F) Relative proportions of the modes of binucleation upon MIIB depletion. n=40 MIIB^{lo}, 11 MIIB^{lo}+MIIB/A and 14 MIIB^{lo}+MIIA/B binucleation events. Scale bar in (A)- 10 μm, (D)- 20 μm, (E)- 50 μm. p values stated over graphs.

Discussion

The majority of non-muscle contractile systems observed in animal cells are cortical and modulation of these contractile systems can drive diverse processes during development and disease progression (Levayer and Lecuit, 2012; Salbreux et al., 2012). During cytokinesis, the cortex is organized into two distinct networks: equatorial and polar. We show MIIA and MIIB both localize to the equatorial network in the form of MII filament stacks. Our data reveal that MIIA is required for templating MII filament stacks. In line with this templating activity, MIIA was necessary and sufficient to drive faster cleavage furrow ingression. Interestingly, a recent study also found a requirement for MIIA in driving ingression (Yamamoto et al., 2019). However, they claimed that CRISPR knockout of MIIA results in larger MIIB stacks at the cleavage furrow, and that MII stacking is somehow inhibitory to furrow ingression. A requirement for MIIA in templating MIIB stacks at the leading edge during interphase has been well documented by our group and others (Fenix et al., 2016; Shutova et al., 2014). We therefore find it unlikely that MIIA is not required for templating MII stacks at the cleavage furrow. Our data suggest that organization of MII filaments into stacks is required for faster ingression, consistent with multiple theoretical studies that suggest increased order within cytoskeletal assemblies is associated with higher force generation (Dasbiswas et al., 2019; Friedrich et al., 2011; Zemel et al., 2010).

Our results also shed new light on the mechanics of the polar cortex. During cytokinesis, the polar cortex is characterized by blebbing, which is thought to serve as a mechanism of intracellular pressure release (Sedzinski et al., 2011). Theoretical studies have suggested that blebs are initiated due to surface tension that drives cortex rupture or detachment (Paluch et al., 2005). We found knockdown of MIIA and MIIB had opposing phenotypes on blebbing, with MIIA depletion reducing bleb formation, and MIIB depletion increasing bleb formation. These changes in blebbing correlated with changes in cortex tension. Our results show that MIIA, but not MIIB, generates the majority of surface tension at the cortex. At the molecular level, we speculate this may be driven by increased buckling of actin filaments by MIIA (Murrell and Gardel, 2012).

Figure 4-8

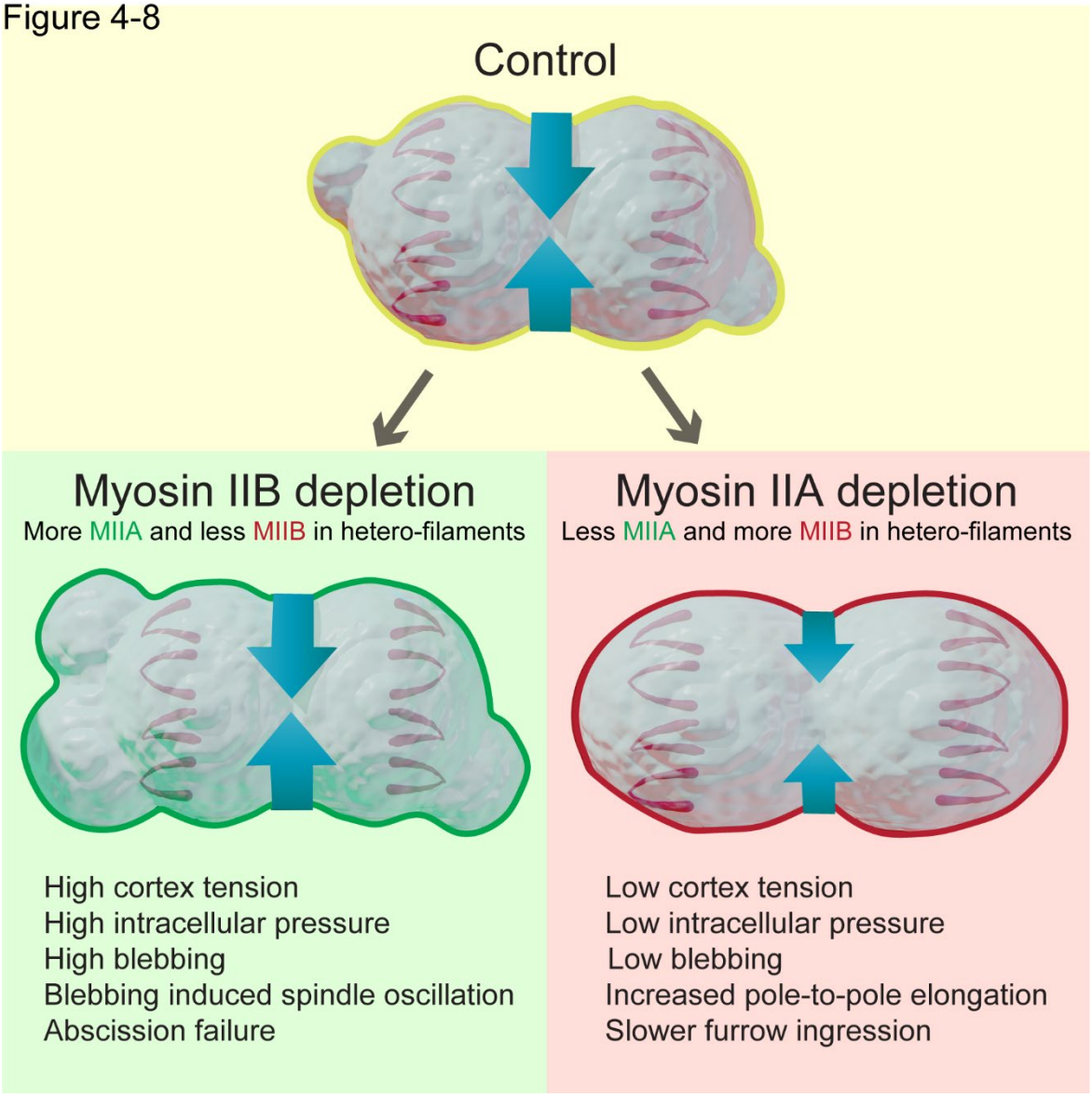

Figure 4-8- Working model on tuning of cortex contractility by MII filament composition

A recent study reported that MIIA, but not MIIB, knockout reduced cortex stiffness (Yamamoto et al., 2019). The study also reported a reduction in the proportion of blebbing cells upon MIIA knockout (0/10 cells), and no changes upon MIIB knockout (8/10 cells in MIIB KO versus 9/10 in control), concluding that changes in stiffness drive the frequencies of blebbing. We also found stiffness remained unchanged upon MIIB depletion (Figure 4-S5). However, blebbing significantly increased upon MIIB knockdown (Figure 4-2). This apparent discrepancy results from the fact that Yamamoto et al reported blebbing as a binary measurement, as opposed to the detailed quantification of the number and size of blebs performed in the current study. Indeed, when simply measuring the frequency of blebbing cells, the increase upon MIIB depletion was not dramatic (14/18 control cells versus 15/15 MIIB^{lo} cells). Furthermore, it is important to note that cortex stiffness is dependent on both the cortex tension (determined by MII contracting actin filaments), and the viscoelastic response of the cortex (determined by actin architecture) (Heer and Martin, 2017; Levayer and Lecuit, 2012; Salbreux et al., 2012). While the role of MII in cortex stiffness is an interesting question, it does not directly pertain to bleb initiation. Indeed, previous work has demonstrated that MII contractility can both stiffen and soften actin gels, depending on ATP levels, suggesting the effects of MII contractility on cell stiffness will be context dependent (Gardel et al., 2008). Taken together, our results show that MIIA generates cortex tension, which drives the initiation of polar blebs during cytokinesis.

Careful measurement of blebbing in MIIB^{lo} cells led us to perform a quantitative analysis of MIIA and MIIB localization at the polar cortex. We found the increase in cortex tension and blebbing upon MIIB depletion was driven by an increase in MIIA localization at the cortex. A similar compensatory localization by MIIB was observed upon MIIA depletion. These data reveal a mechanism to tune cortex tension by altering the relative levels of MIIA and MIIB at the cortex. There are multiple possible mechanisms for achieving this tuning at the molecular level. One possible mechanism is that the two paralogs compete for cortical occupancy; the other mechanism is through modulation of filament composition of MIIA/MIIB hetero-filaments. Super resolution imaging of MIIA and MIIB at the cortex suggests support for the latter mechanism. MIIB showed a high propensity to associate with MIIA filaments, since the majority of MIIB co-localized with residual MIIA at the cortex upon MIIA knockdown. This argues against direct competition between the two paralogs since cortical binding sites were in excess in comparison to the motors. Instead, we found the proportion of MIIA filaments that contained MIIB was altered in the knockdown conditions. Taken together, our results suggest tuning of

cortex tension is achieved through the addition of MIIB to MIIA/MIIB hetero-filaments, rather than by seeding new filaments. Indeed, adding as little as 6 MIIB hexamers to 24 MIIA hexamers was sufficient to tune the properties of the filament to allow processive walking along an actin filament *in vitro* (Melli et al., 2018). This ratio of ~4:1 (MIIA:MIIB) is thus sufficient to change the biophysical properties of the filament *in vitro*.

On face value, this mechanism seems unlikely to work in cells as proteomic analysis has demonstrated that there is vastly more MIIA in HeLa cells than MIIB. The HeLa subtype (CCL-2) used in this study contains 93.5% MIIA and 6.5% MIIB, with no MIIC detected (Bekker-Jensen et al., 2017), yielding a ratio of ~14:1 (MIIA:MIIB). This leads to the question, how could tuning be accomplished with such an apparent abundance of MIIA?

A higher level of MIIB assembles into filaments compared to MIIA *in vitro* at similar concentrations and salt conditions (Murakami et al., 1995; Nakasawa et al., 2005) . It was also reported that ~30% of total MIIB, and only ~8% of total MIIA assembled into filaments in HeLa cells, using the amount of MII which was in the supernatant (i.e., soluble) and cytoskeletal (i.e., insoluble) fractions (Schiffhauer et al., 2019). This group also used the CCL-2 subtype (personal communication). By combining the total amount of MIIA and MIIB from proteomics with the fraction of MIIA and MIIB within filaments, we calculated a 4:1 ratio MIIA:MIIB assembled in filaments (Table 4-2), in agreement with the ratio of MIIA:MIIB to change the properties of a hetero-filament *in vitro*.

We also showed that loss of MIIA, but not MIIB, resulted in lower ingression rates and bleb growth upon ablation in HAP1 fibroblasts. HAP1 cells contain a ratio of 2.4:1 of total MIIA:MIIB measured using proteomics (Jonckheere et al., 2018). We found that 24 +/- 3% of MIIA, and 40% +/- 9% of MIIB was in the cytoskeletal fraction (Figure 4-S8). This yields an effective ratio of 1.5:1 of MIIA: MIIB assembled into filaments in control HAP1 cells (Table 4-2). These data argue against the possibility that the paralog specific roles we observed for MIIA and MIIB are due to biased expression levels of the two paralogs.

Alternatively, the two paralogs could be functionally equivalent, and contractility is simply a function of the total amount of myosin II in the cell. For instance, the lack of rescue in ingression rates observed upon MIIB overexpression in MIIA^{lo} cells could be due to insufficient levels of total myosin II (Figure 4-S8). To test this hypothesis, we compared ingression rates of MIIA^{lo} cells expressing low levels of MIIA versus high levels of MIIB, such that the total amount

of myosin II was equal. Consistent with MIIA uniquely driving faster ingression, MIIA^{lo} cells expressing even low levels of MIIA showed significantly higher ingression rates (Figures 4-S8).

Our data also shows that the motor domain of each MII paralog determines its contribution to cortex tension, with lower duty ratios and higher ATPase activity of MIIA associated with higher cortex tension. We were not surprised that MIIB did not play a larger role in generating cortex tension, since MIIB has a higher duty ratio than MIIA (Kovacs et al., 2003; Rosenfeld et al., 2003; Wang et al., 2003). That is, MIIB binds actin in the force generating state for a larger proportion of its mechano-chemical cycle. Therefore, the canonical view of MIIB has been that it is adapted to maintain tension rather than generate tension, a view supported by previous experimental and theoretical studies (Melli et al., 2018; Milberg et al., 2017; Stam et al., 2015). Modeling studies on cortex tension generation have implicated MIIB as a cross-linker at the cortex since it is a slower motor (Stam et al., 2015). Paralog specific roles for MII have also been observed during regulated exocytosis *in vivo*, where MIIB was hypothesized to serve as a membrane stabilizer, while MIIA was hypothesized to generate tension to expand the fusion pore (Milberg et al., 2017). Here, we provide biophysical measurements in living cells to directly support these long-hypothesized views of MII paralogs in generating tension.

Interestingly, while the motor domain of MIIB was sufficient to tune cortex tension (Figure 4-5), it only partially rescued MIIB's function in maintaining cytokinetic fidelity (Figure 4-6). This line of inquiry revealed two non-mutually exclusive mechanisms of cytokinetic failure upon loss of MIIB. Loss of the motor function of MIIB, required to tune cortex tension, led to increased blebbing at the polar cortex. Retraction of large blebs led to oscillations of the mitotic spindle, resulting in both sets of chromosomes being pushed into one of the daughter cells, while the other daughter became enucleated. These data reveal a mechanism for chromosome missegregation through instabilities in cell shape. We also show that the tail domain of MIIB contributes to abscission, independent of the specific biophysical properties of its motor domain, suggesting that the contribution of the motor or tail domain to MII function will be context dependent.

Our data implicating MIIB in mediating abscission supports previous suggestions that MIIB is important for the completion of abscission (Lordier et al., 2012). A recent study proposed that this function of MIIB in mediating abscission may be achieved through stabilizing the intracellular bridge (Wang et al., 2019). Of note, while the authors implicated MIIB during this process, knockdown of MIIB had no effect on binucleation. The authors proposed this was due

to low knockdown efficiency of MIIB (60%). In our study, we achieved 80% knockdown of MIIB and did observe a significant increase in binucleation. Future studies will be required to reveal the precise mechanical mechanism of intracellular bridge stabilization.

Finally, it is interesting to note that organisms such as worms and flies contain only one MII paralog, leading to the question of how contractility is tuned in these organisms. One potential mechanism may be increased reliance on adhesion dependent cytokinesis. Indeed, organisms such as *Dictyostelium* and adhesive cell lines such as normal rat kidney (NRK) cells can divide without MII activity (Kanada et al., 2005; Neujahr et al., 1997). Another mechanism could involve regulating the amount of each paralog that can assemble into filaments, for instance through PKC activity (Schiffhauer et al., 2019). Finally, oscillations of upstream regulators of MII, which appear to be evolutionarily conserved from flies to mammals (Bement et al., 2015; Machacek et al., 2009; Martin et al., 2009), could regulate the level of MII activation. The mechanism we propose here adds an additional layer of control and tunability, likely acquired later in evolution, when MII paralogs diverged.

Materials and methods

Cell lines and growth conditions

HeLa (ATCC, CCL-2) and Cos7 cells (ATCC, CRL-1651) were cultured in growth media comprised of DMEM (Mediatech, Inc., Manassas, VA, #10-013-CV) containing 4.5 g/L L-glutamine, L-glucose, sodium pyruvate and supplemented with 10% fetal bovine serum (Sigma-Aldrich, St. Louis, MO, #F2442). HAP1 *myh9* (MIIA) KO and parental cells were purchased from Horizon discovery as previously described (Fenix *et al.*, 2016), and cultured in IMDM medium supplemented with 10% fetal bovine serum. M2 melanoma cells were cultured in Minimal Essential Medium supplemented with Earle's salts, 10 mM HEPES and 10% fetal bovine serum. Growth substrates were prepared by coating #1.5 glass coverslips (In Vitro Scientific, #D35C4-20-1.5N or #D35-20-1.5N) with 10 µg/mL FN (Corning, Corning, NY, #354008) in PBS (Mediatech, Inc., #46-013-CM) at 37 °C for 1 hour.

Human embryonic stem cell lines H9 (WA09) were obtained from WiCell Research Institute (Madison, WI). Cells were seeded as undifferentiated colonies on plates coated with Matrigel (Corning, #354277), maintained at 37°C and 5% CO_2, and fed daily with mTeSR (Stem Cell Technologies #05850). Cells were passaged once they reached 80% confluency. For immunofluorescence, cells were plated on Matrigel-coated 35 mm glass bottom culture dishes (MatTek #P35G-0-140C) and experiments were performed the next day.

For protein expression, cells were transiently transfected using Fugene 6 (Promega, Madison, WI, #E2691) as per the manufacturer's instructions overnight in a 25-cm^2 cell culture flask (Genessee Scientific Corporation, San Diego, CA, #25-207) before plating on a growth substrate.

Alexa Fluor-488 phalloidin (#A12379), Alexa Fluor-568 phalloidin (#A12380) and Alexa Fluor 488-goat anti-rabbit (#A11034) were purchased from Life Technologies (Grand Island, NY). Rabbit anti-myosin IIA (#909801) was purchased from BioLegends (San Diego, CA). Rabbit anti-myosin IIB (#8824S and 3404S) was purchased from Cell Signaling Technology (Danvers, MA). The #8824S antibody was used in Figures 4-S1, panels A, C and D; Figure 4-S2, panel A; Figure 4-1, panel A and C; Figure 4-S4, panel B; and Figure 3, panels B-E. The #3404S antibody was used in Figure 4-S1, panel B; Figure 4-S12, panels A-B; Figure 4-S8, panel A; Figure 4-3, panel F; and Figure 4-S5, panel B-C.

Cell Line Authentication

The HeLa cell line used in this study was a gift of Dr. DA Weitz (Harvard University), and the M2 melanoma cells were a gift from Dr. Matthew Tyska. The Burnette lab had these lines authenticated by Promega and ATCC using their 'Cell Line Authentication Service' in 2015 and 2019, respectively. The methods and test results received from Promega and ATCC are as follows:

"Methodology: Seventeen short tandem repeat (STR) loci plus the gender determining locus, Amelogenin, were amplified using the commercially available PowerPlex 18D Kit from Promega. The cell line sample was processed using the ABI Prism 3500xl Genetic Analyzer. Data were analyzed using GeneMapper ID-X v1.2 software (Applied Biosystems). Appropriate positive and negative controls were run and confirmed for each sample submitted.'

"Data Interpretation: Cell lines were authenticated using Short Tandem Repeat (STR) analysis as described in 2012 in ANSI Standard (ASN-0002) Authentication of Human Cell Lines: Standardization of STR Profiling by the ATCC Standards Development Organization (SDO)'

HeLa- CCL-2 results-

"Test Results: The submitted profile is an exact match for the following ATCC human cell line(s) in the ATCC STR database (eight core loci plus Amelogenin): CCL-2 (HeLa)'

M2 results-

"Test Results: Submitted sample, STRA12409 (M2 melanoma), is an exact match to ATCC cell line CRL-2500 (A7). When compared to the reference profile the submitted profile shows and extra #10 allele at the TPOX locus. The cell line, (M2), has been discontinued by ATCC."

Mycoplasma Monitoring: All cell lines were checked for potential mycoplasma infection using DAPI throughout the course of this study.

Plasmids

MIIA mEmerald (Addgene, Cambridge, MA, #54190), MIIA mApple (Addgene, #54929) and MIIB mEmerald (Addgene, #54192) were gifts from Michael Davidson. MIIA mEGFP (Addgene, #11347) was a gift from Robert Adelstein. MIIB mEGFP (Addgene, #35691) was a

gift from Venkaiah Betapudi. The MIIB/A and MIIA/B chimeras were generously provided by Miguel Vincente Manzanares (Universidad Autonoma de Madrid, Spain).

siRNA resistant MIIB and MIIB/A were generated using a modified site directed mutagenesis protocol as described previously (Liu and Naismith, 2008). Three to four codons were modified to ensure siRNA resistance. The MIIB- and MIIB/A-mEGFP constructs were mutated using the following primer sequences- Forward- 5'-GGAAGACCCCGAGAGGTATCTCTTTGTGGACAGGGCTGT-3', Reverse- 5'-CTCTCGGGGTCTTCCAGTCCAGTTCTCTGCGCCAT-3'. Since the individual siRNA against MIIA was targeted to 3'-UTR, the MIIA-mEGFP and MIIA/B-mEGFP plasmids were not mutated.

Phase and DIC imaging

Phase and DIC imaging was performed on a Nikon (Melville, NY) Eclipse Ti-E inverted microscope equipped with a Nikon 1.45 NA 100X Oil DIC, 0.95 NA 40X Air DIC and a 0.4 NA 20X Air Phase objective. Samples were maintained at 37°C with 5% CO_2 using a Tokai Hit Stage Incubator (Shizuoka-ken, Japan).

For quantifying live binucleation events, imaging was performed on an Incucyte S3 (4647, Essen BioScience) microscope, equipped with a 20X objective and maintained in a tissue culture incubator at 37°C and 5% CO_2.

Structured Illumination Microscopy (SIM)

SIM imaging was performed on a GE (Pittsburgh, PA) DeltaVision OMX microscope equipped with a 1.42 NA 60X objective lens and a sCMOS camera, and a Nikon N-SIM microscope equipped with a 1.49 NA 100X objective lens and an EMCCD camera.

Live and Fixed Fluorescence imaging and Cortical Ablation

Live imaging and cortical ablation were performed on a Nikon Eclipse Ti-E inverted microscope equipped with a Yokogawa CSU-X1 spinning disk head, 1.4 NA 60X oil objective, Andor DU-897 EMCCD and a dedicated 100 mW 405 diode ablation laser, generously provided by the Nikon Centre of Excellence at Vanderbilt University. The instrument was controlled using Nikon Elements AR software. For ablation, a 1.4 µm x 1.4 µm ROI was used for all experiments. A DIC and/or fluorescence image was acquired before ablation, followed by ablation using a miniscanner. A pixel dwell time of 500 µs, 50% laser power was used for a

duration of 1 second, followed by acquiring DIC or fluorescence images at 2 second intervals. Samples were maintained at 37°C with 5% CO_2 using Tokai Hit Stage Incubator.

To image MIIA and MIIB in fixed ESC colonies, large image stitching was performed using the 60X objective in Elements software. Z-sections were acquired at 1 μm intervals for the entire stitch and maximum projections were displayed and used for generating line scans. To image endogenous MIIA and MIIB in fixed HeLa cells, single slices through the middle of the cell were acquired using the 60X objective.

Knockdown experiments

Smart Pool Accell siRNA against MIIA (myh9 gene, #E-007668, #1- CCGUUGACUCAGUAUAGUU, #2- UCCACAUCUUCUAUUAUCU, #3- GUGUGGUCAUCAAUCCUUA, #4- CUUAUGAGCUCCAAGGAUG) and MIIB (myh10 gene, #E-023017, #1- GGACUAAUCUAUACUUAUU, #2- UGUCAAUGCUUAAAGUAGU, #3- CGAGGAUCCAGAGAGGUAU, #4- CCAAUUUACUCUGAGAAUA) were purchased from GE Dharmacon (Lafayette, CO). To perform rescue experiments, the following individual siRNAs were used- myh9 – CCGUUGACUCAGUAUAGUU (#A-007668-13-0005) and myh10- CGAGGAUCCAGAGGUAU (#A-023015-15-0005). Knockdown experiments were performed in 24-well plates using Lipofectamine 2000 (Life Technologies, #1690146) as per instructions provided by the manufacturer. Knockdown was performed for 72 hours, after which cells were either plated on the growth substrate for imaging or lysed for western blot experiments.

Western Blotting

Gel samples were prepared by mixing cell lysates with LDS sample buffer (Life Technologies, #NP0007) and Sample Reducing Buffer (Life Technologies, #NP00009) and boiled at 95°C for 5 minutes. Samples were resolved on Bolt 4-12% gradient Bis-Tris gels (Life Technologies, #NW04120BOX). Protein bands were blotted onto a nylon membrane (Millipore). Blots were blocked using 5% NFDM (Research Products International Corp, Mt. Prospect, IL, #33368) in Tris Buffered Saline with Tween-20 (TBST). Antibody incubations were also performed in 5% NFDM in TBST. Blots were developed using the Immobilon Chemiluminescence Kit (Millipore, #WBKLS0500).

Cell indentation assay

A precisely controlled Transfer Man 4R micromanipulator (Eppendorf, Hamburg, Germany) was magnetically attached to the optical table. Indentation pipettes were prepared from borosilicate microcapillary tubes pulled using an automated pipette puller. Metaphase cells were identified using high magnification DIC and their height was approximated. The micropipette was then slowly lowered to gently rest on top of the cell. Upon starting image acquisition, the pipette was lowered continuously for 2 seconds, using the extra-fine movement setting, to compress the cell to half its height. Images were recorded for a minimum of 90 s prior to gently raising the pipette back up. The assay was performed in 35 mm glass bottom dishes with a 20 mm coverslip to allow for the optimal angle and movement of the microcapillary.

Micropipette Aspiration

Microneedles (World Precision Instruments, 0.75 mm inner diameter and 1.0 mm outer diameter) were pulled to a centimeter-long taper using a Narishige PC-100 needle puller. The following parameters were used- 55% maximum current and one light weight (mass = 23.5g). Using a Narishige MF-900 microforge, needles were then cut to a diameter ranging between 10-15 μm. The end of the needle was then fire polished by bringing it close to a heated glass bead to obtain a smooth edge that will successfully attach to the aspirated cell without disrupting the membrane. The microforge was then used to bend the tip of the micropipette needle to a 30-degree angle by positioning the needle vertically at a 0.1 mm distance from the heated glass bead.

To perform micropipette aspiration, the needles were mounted on an Eppendorf Transfer Man 4R micromanipulator that was magnetically attached to the optical table. Cells were visualized using DIC (Plan Apo 0.95 NA, 40X Nikon DIC air objective, with 1.5X optical zoom on a Nikon Eclipse Ti inverted microscope controlled using Elements software). Cells were maintained at 37°C with 5% CO_2 using a Tokai Hit stage incubator. Metaphase cells were identified using the appearance of a tight metaphase plate using DIC. The needle was then positioned close to the cell until the pipette made firm contact with the cell. Negative pressure was then applied using a Fluigent microfluidic pressure control system (Flow EZ) controlled through Fluigent controller software on the microscope computer. Frames were acquired every 2 seconds, with pressure increased by 0.5 mbar every 10 seconds. Cortex tension was then calculated by analyzing the DIC time montages using a custom MATLAB script (Data S1-S2). Tension (T) was calculated as

$$T = \frac{\Delta P}{2(\frac{1}{Rp} - \frac{1}{Rc})}$$

where, ΔP= pressure difference, R_p= radius of pipette, R_c= radius of cell.

Calibration of protein expression using immunofluorescence

Calibration of protein expression was performed using an immunofluorescence based approach as described previously (Figure 4-S9) (Taneja and Burnette, 2019). siRNA resistant MII was introduced into the knockdown cells using transient transfection, plated on glass coverslips, followed by fixation. Untransfected scrambled control cells were prepared in parallel. The two samples were then stained for endogenous MIIA or MIIB in the red channel. The samples were then imaged using the same parameters for the red and green channels in growth medium at 37°C as performed for the actual experiment. GFP intensity measured in the cytoplasm was then calibrated against the endogenous (red) signal relative to the scrambled control. The intensity in the cytoplasm was also normalized against relative enrichment in the cytoplasm as well as background. This analysis was performed for every different objective lens used in the study. Since we used the same imaging parameters for GFP throughout the experiments this allowed us to compare levels to endogenous.

Quantification of soluble and insoluble fractions in HAP1 fibroblasts

HAP1 parental fibroblasts were seeded into 24-well culture plates (CytoOne CC7682-7524) and grown to 75% confluence. Cells were then trypsinized, followed by recovery in growth medium on an orbital shaker for 10 minutes. Cells were pelleted at 200xg, washed once in PBS, and then lysed using Cell Lytic M reagent (Sigma C2978) containing 1X protease inhibitor cocktail (Sigma P8340) for 45 minutes on ice. Cell lysates were centrifuged for 10 min at 15000 rpm at 4°C. The supernatant (soluble fraction) was diluted in LDS Sample buffer (Life Technologies #NP0007) and Reducing buffer (Life Technologies #NP00009). The pellet (insoluble fraction) was the resuspended in LDS Sample Buffer and Reducing buffer. The two fractions were boiled at 95°C for 5 minutes and subsequently analyzed by western blotting. Note that the actual fractions obtained by this method may vary from previous reports (Schiffhauer et al., 2019) since we did not use ATP in our lysis buffer, which would promote release of MII from the insoluble fraction into the soluble fraction. Therefore, our values for the insoluble fraction tend to be higher.

Data Quantification

For quantification of MII stack length (Figure 4-1), a 15 μm by 8 μm region of interest containing the cleavage furrow was cropped from maximum projected SIM micrographs. Owing to the smaller size of HAP1 fibroblasts, a 5 μm by 8 μm region of interest containing the cleavage furrow was used. Only bright, in-focus, objects were included in the analysis. Measurements were made manually with individual lines saved as ROIs in Fiji and then exported for calculation of average stack length. Separate investigators acquired and analyzed the data for stack length quantification. The investigator analyzing the data was blinded.

For measuring the rate of cleavage furrow ingression, phase contrast or DIC time montages were recorded at 30 second intervals. Individual montages were cropped and aligned using the StackReg plugin in Fiji. Kymographs were created using the Multiple Kymograph plugin with a 3-pixel thick line drawn across the equator. Ingression rates were calculated as the change in distance (in μm) divided by the amount of time (in min) between the start and end of ingression (Figure 4-1). The start of ingression was defined as the first instance of deformation of the cell boundary, and the end of ingression was defined as when the cell boundary stopped deforming. Asymmetric furrowing was occasionally observed in HAP1 fibroblasts. In these instances, the predominant side of the cleavage furrow was measured. In the case of symmetrical ingression, the left side of the kymograph was arbitrarily used (Figure 4-1).

To quantify blebbing (Figure 4-2), DIC time-lapse recordings at 30 second intervals were used. We manually counted blebs using the line tool in Fiji, between the time point immediately following the end of Anaphase A (sister chromatids no longer move away from each other; this was also verified by making a kymograph across the long axis of the cytokinetic cell) and the end of cleavage furrow ingression. The longest axis of every bleb (most frequently the diameter since blebs were roughly circular in shape) that was in focus and could be accurately measured was counted for quantification. The diameter of every bleb measured for the duration of the movie was summed. This was then normalized to the number of minutes for which the analysis was performed.

To quantify ingression rates within hESC colonies (Figure 4-S3), images were recorded at 30 second intervals. Distance within the colony was measured in “cell radii” from the edge. The colonies were assumed to be composed of concentric circular cell layers increasing in number from the edge. For any given dividing cell, its position was determined by counting the smallest

number of cell radii to reach the edge. Ingression rates were measured using the MultipleKymograph plugin in Fiji. Kymographs where the cell boundary could not be ascertained were discarded.

To quantify cell shape changes upon MII knockdown (Figure 4-2), we measured the increase in pole-to-pole elongation during cytokinesis relative to metaphase. A line was drawn across the long axis of the cell from phase contrast time montages. We observed that the distance between the cell boundary during metaphase is smallest immediately before the onset of anaphase, which is in agreement with the general idea that maximal de-adhesion must occur for cell-cycle progression (Jones et al., 2018; Marchesi et al., 2014). Following anaphase onset, pole-to-pole expansion was observed, until ingression is completed, which was then followed by poles moving closer together again prior to cell spreading. We measured the pole-to-pole distance immediately upon anaphase onset (as shown in schematic, Figure 4- 2), and the maximal pole-to-pole distance before they come closer together (as shown in schematic, Figure 4-2). This was also visually confirmed in the live cell montages. These widths were used to calculate the pole-to-pole elongation ratio.

To generate the endogenous polar cortex and equatorial cortex localization profiles upon MII paralog knockdown (Figure 4-3), cells were grouped into early (>20 μm), mid (6-20 μm) and late cytokinesis (<6 μm) based on degree of furrow closure, as done previously (Taneja et al., 2016). Polar cortex intensity was calculated as the mean fluorescence averaged from 6 ROIs (1.8 μm^2 area) placed in the same positions (see inset schematics, Figure 4-3). Due to the non-uniform distribution of cortical signals, this approach allowed us to get an unbiased measurement of mean cortical intensity at the polar cortex. Equatorial cortex intensity was calculated as mean fluorescence of 2 ROIs (1.8 μm^2 area) placed on each side of the furrow. Mean equatorial or polar cortex intensities were then averaged within the cytokinesis groups. Any perturbations were normalized to the mean of the control data sets.

To quantify changes in filament composition upon MII paralog depletion (Figure 4-3), two-channel images SIM were first aligned in all dimensions in Fiji. Following alignment, a 5 μm by 15 μm crop from a single optical section from the 2-channel overlay was used for quantification of hetero-filaments at the cortex. Each distinct punctum was quantified as a filament. In instances of puncta located close together, a line scan was drawn across region, and each distinct peak in intensity was quantified as a filament. Puncta localized in the cytoplasm were

not counted. The same staining and imaging parameters were used for all the experiments to allow comparison of MII intensity within the filaments.

For quantification of binucleate cells (Figure 4-6), a large stitch of cells stained with phalloidin and DAPI was acquired using a 20X objective (shown in Figure 4-S1 or smaller field of view shown in in Figure 4-6). Binucleate cells were manually counted using the multi-point tool in Fiji. Cells very close together in clusters and whose boundaries could not be accurately discerned were not included in the analysis.

To correlate spindle displacement with blebbing (Figure 4-7), DIC time-lapse imaging was performed at 5 second intervals. A 3-pixel thick line was drawn parallel to the long axis of the cytokinetic cell and kymographs were created using the Multiple Kymograph plugin in Fiji. The pixel values for the timepoint at which bleb growth was maximal was noted, in parallel with the pixel value for the timepoint at which the chromosomes were displaced to the maximal extent. The plot in Figure 4-7 was created by plotting all such events across multiple cells.

To quantify the different modes of binucleation (Figure 4-7), live imaging of MIIB^{lo} cells was performed as follows. Cells were seeded on 24-well cell culture dishes. Knockdown was performed 24 hours following seeding. 48 hours after initiation of knockdown, live nuclear labeling was performed using the NucLight Red reagent (used at a dilution of 1/2000 in DMEM) for 6 hours prior to imaging. Time lapse montages were acquired at 20X magnification at 10-minute intervals. A binucleation event was classified as “chromosome missegregation without abscission” if, i) a clear frame was observed where the DNA signal was detected in only one daughter cell, ii) the boundary between the daughter cells could be clearly discerned. A binucleation event was classified as “abscission failure” if, i) no frame was observed where the DNA signal was detected in only one daughter cell, ii) the daughter cells fail to separate with or without the appearance of a midbody. Events showing both of the above features were classified as “chromosome missegregation with abscission failure.

Statistics

Statistical significance for averaged data from multiple experiments, which is always depicted using bar graphs, was determined using unpaired, 2-tailed, homoscedastic Student’s T-test performed on Excel. For data pooled from multiple experiments, always depicted as Tukey plots, Mann Whitney U-test was performed on GraphPad Prism. Error bars in all bar graphs represent standard error of the mean, while Tukey plots were represented with boxes (with

median, Q1, Q3 percentiles), whiskers (minimum and maximum values within 1.5 times interquartile range) and outliers (solid circles). No outliers were removed from the analysis.

For graphs displaying percentages, no error bar was displayed and the data over more than 3 experiments was pooled. Due to the pooled approach for the endogenous MII localizations in HeLa cells, error bars depict standard error of weighted means, where the weights were determined based on how many cells from a particular experimental replicate were allocated to a particular group (e.g. Early, Mid, Late). The weighted standard deviation was calculated to remove any bias from individual experiments, using the formula

$$sd_w = \sqrt{\frac{\sum_{i=1}^{N} w_i (x_i - \bar{x}_w)^2}{\frac{(N' - 1)\sum_{i=1}^{N} w_i}{N'}}}$$

where w_i is the weight for the i^{th} observation, N' is the number of non-zero weights, and x_w is the weighted mean of the observations.

Supplementary Figures

Figure 4-S1

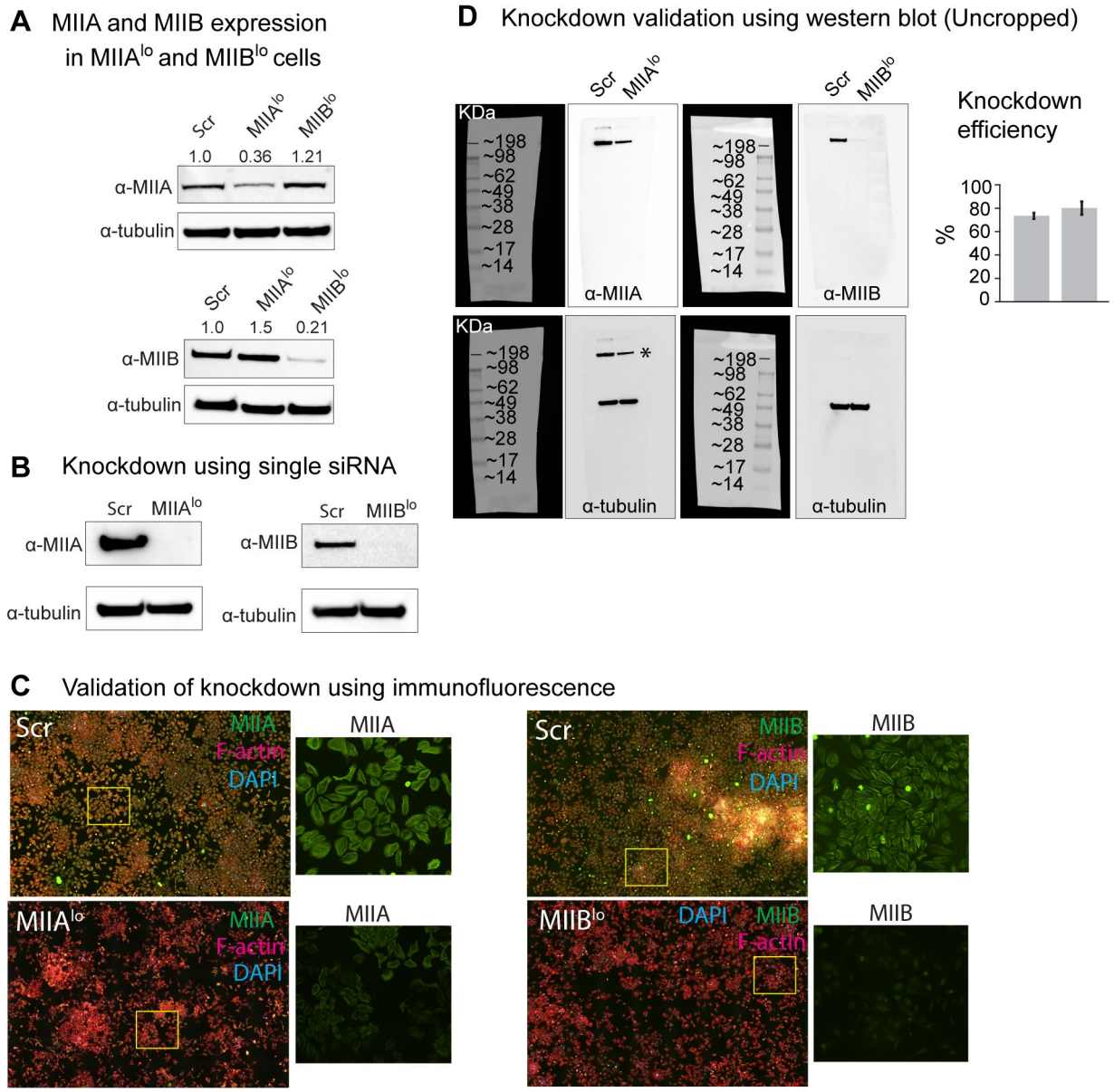

Figure 4-S1- Characterization of MII paralogs in HeLa cells

A) MIIA and MIIB expression upon depletion of the other paralog. Tubulin was used as loading control. The numbers represent expression normalized to loading control with scrambled control set to 1. B) Knockdown of MIIA and MIIB using individual siRNA. The numbers represent MII band intensity normalized to loading control. C) Large stitches of Scr, MIIA^{lo} and MIIB^{lo} cells stained for F-actin, DAPI and the depleted paralog. Insets: Enlarged view of yellow box. D) Uncropped representative western blot from another experiment validating MIIA and MIIB knockdown. Tubulin was used as loading control

for normalization and calculation of knockdown efficiency. N=5 independent knockdowns. *, leftover MIIA bands from blot stripping. Error bars represent standard error of the mean.

Figure 4-S2

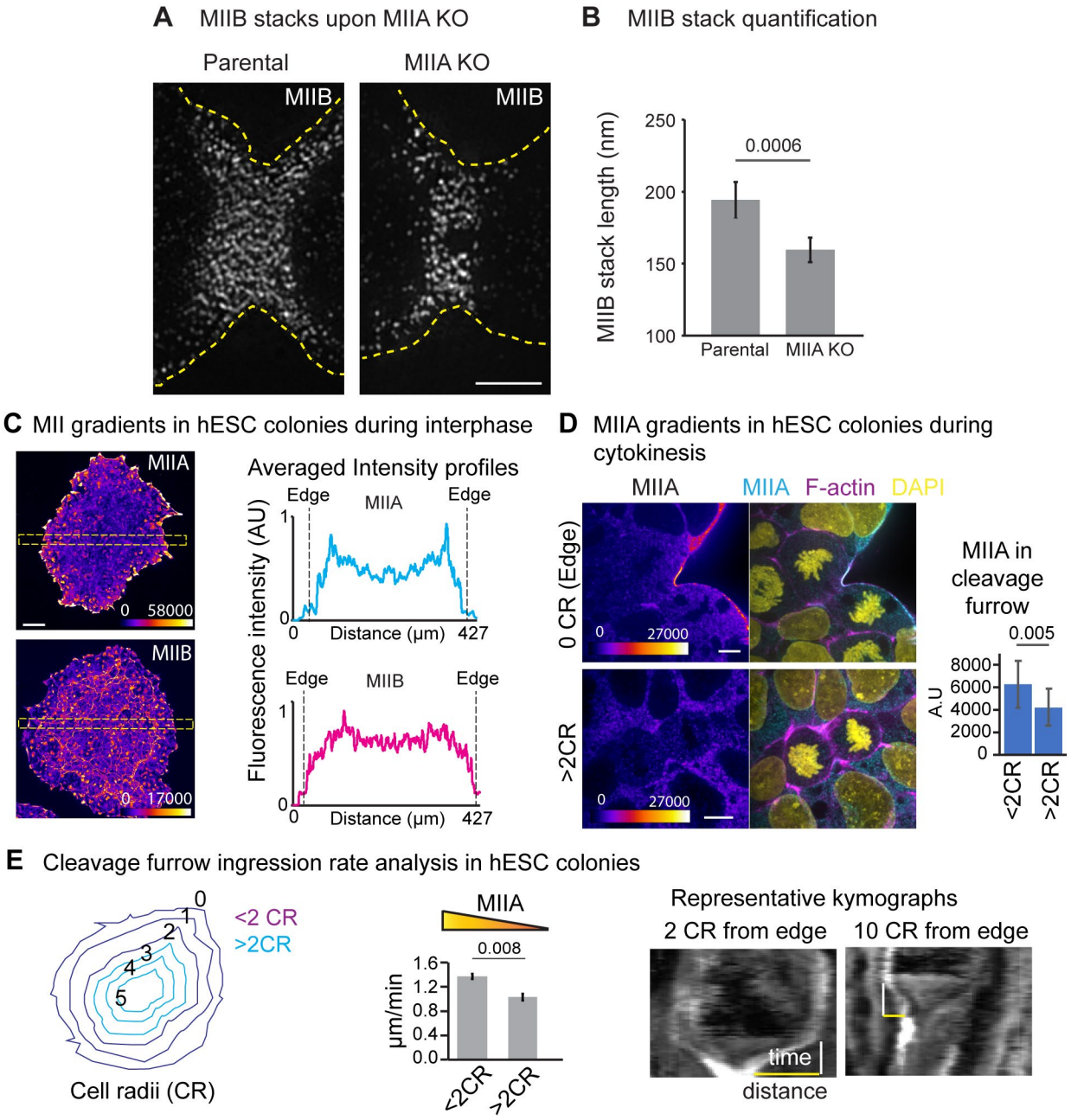

Figure 4-S2- Role of MIIA in stacking in HAP1 and ingression in H9 cells

A) Representative SIM micrographs showing a 720 nm Z-projection of the cleavage furrow of dividing HAP1 parental versus MIIA KO cells, showing MIIB localization. B) Quantification of MIIB stacks. For parental, n=821 measurements from 10 cells; For KO, n=932 measurements from 10 cells; N=3 independent experiments. C) We sought a system where natural gradients of MIIA exist, for which we turned to hESC colonies, that show a gradient of MIIA with high MIIA at the edge and less in the center. MIIB was showed no gradient in localization. We used this system to test whether MIIA levels correlate with faster ingression. hESC colonies stained for endogenous MIIA or MIIB (Fire LUT). Line scans from

yellow box averaged over 12 30° rotations. D) Representative dividing cells and expression of MIIA in the cleavage furrow of dividing cells close to (<2CR) or away from (>2CR) the edge of a hESC colony. Intensity matched micrographs show endogenous MIIA staining represented using Fire LUT. Quantification from 14 <2CR and 17 >2CR cells from 10 separate colonies. E) Representative kymographs from phase contrast time montages of hESCs dividing 2 CR or 10 CR from the edge of the colony and cleavage furrow ingression rates of cells dividing in hESC colonies. n=61 cells from 5 colonies over 3 independent experiments. Cell position was represented as cell radii (CR) away from the edge assuming a spherical colony with each concentric layer of cells spanning 1 cell radius (see inset schematic). Scale bar in (A), (C) and (D)- 2.5 μm, 50 μm and 10 μm, respectively. Error bars in (B,E) represent standard error of the mean; Error bars in (D) represent standard deviation. p values depicted over respective bar graphs.

Figure 4-S3

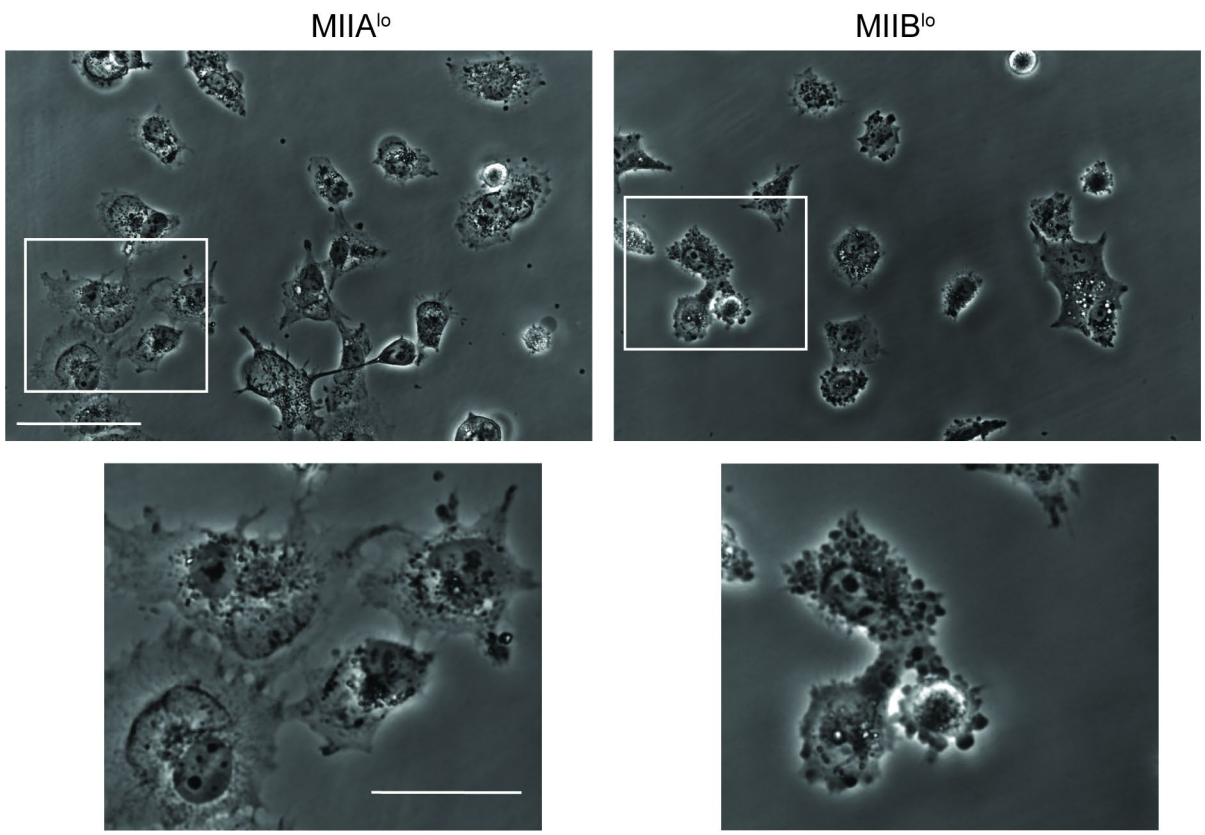

Figure 4-S3- Depletion of MII in M2 cells and pole-to-pole elongation rescue in HeLa cells

A) Representative fields of view of MIIA^{lo} and MIIB^{lo} M2 cells at 5 hours post plating. Insets- Enlarged views of white box. B) MIIA depletion results in increased pole-to-pole elongation during cytokinesis. Tukey plots of polar elongation measured independently using DIC. n= 15 Scr,12 MIIA^{lo} (pooled siRNA), 13 MIIA^{lo} (single siRNA), 13 MIIA^{lo} +MIIA and 11 MIIA^{lo} +MIIB cells over 3 independent experiments. Solid circles represent outliers. Scale bar- 100 μm.

Figure 4-S4

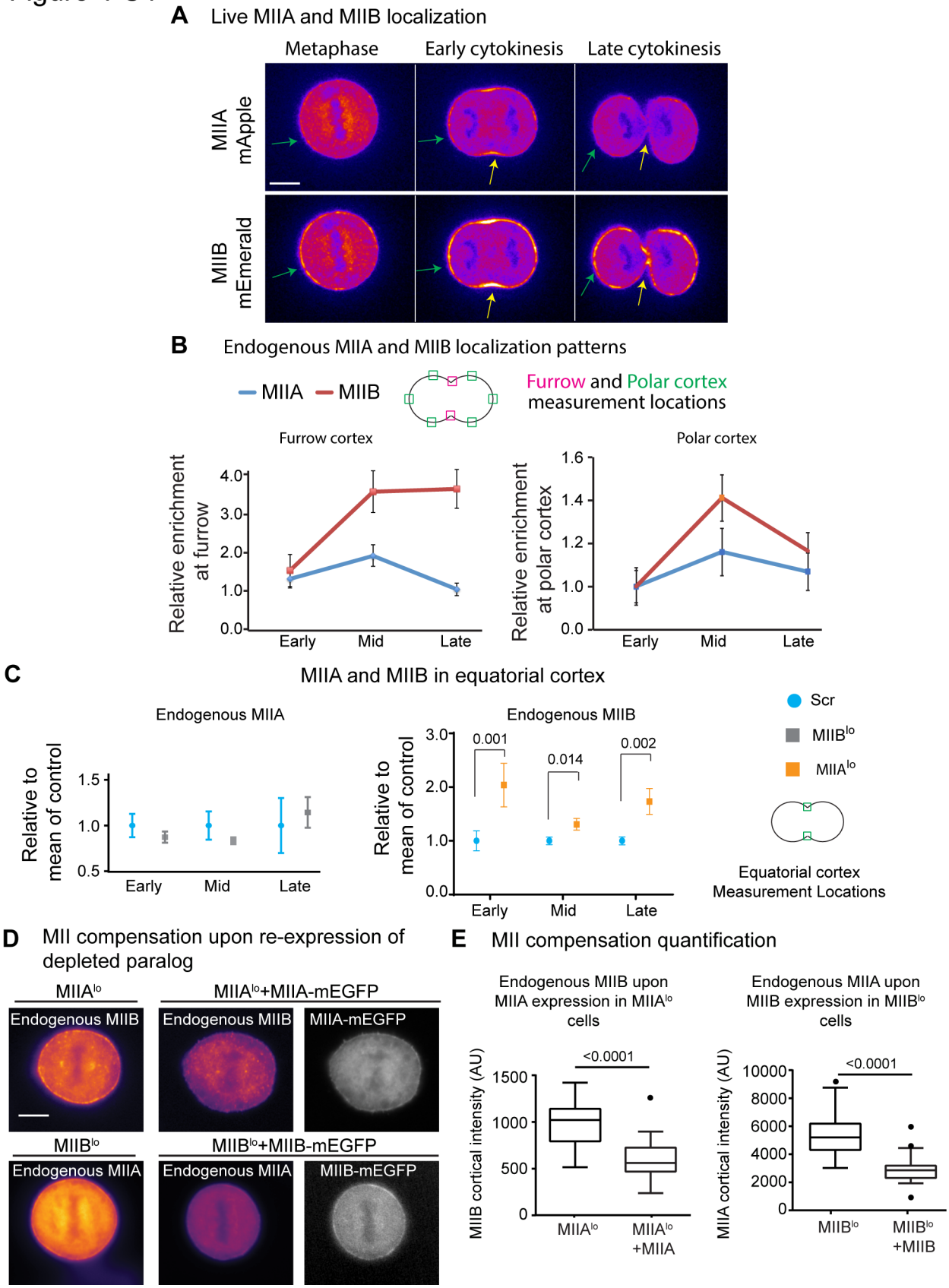
A
Live MIIA and MIIB localization
Metaphase
Early cytokinesis
Late cytokinesis
MIIA mApple
MIIB mEmerald
B
Endogenous MIIA and MIIB localization patterns
MIIA
MIIB
Furrow and Polar cortex measurement locations
Furrow cortex
Polar cortex
Relative enrichment at furrow
Relative enrichment at polar cortex
Early
Mid
Late
C
MIIA and MIIB in equatorial cortex
Endogenous MIIA
Endogenous MIIB
Relative to mean of control
0.001
0.014
0.002
Scr
MIIB^lo
MIIA^lo
Equatorial cortex Measurement Locations
D
MII compensation upon re-expression of depleted paralog
MIIA^lo
MIIA^lo+MIIA-mEGFP
Endogenous MIIB
MIIA-mEGFP
MIIB^lo
MIIB^lo+MIIB-mEGFP
Endogenous MIIA
MIIB-mEGFP
E
MII compensation quantification
Endogenous MIIB upon MIIA expression in MIIA^lo cells
Endogenous MIIA upon MIIB expression in MIIB^lo cells
MIIB cortical intensity (AU)
MIIA cortical intensity (AU)
<0.0001
MIIA^lo
MIIA^lo +MIIA
MIIB^lo
MIIB^lo +MIIB

Figure 4-S4- MIIA and MIIB localization and compensation during metaphase and cytokinesis

A) Live cell montage of HeLa cell co-expressing MIIA-mApple and MIIB-mEmerald. Green and yellow arrows highlight polar and equatorial cortex, respectively. B) Enrichment of endogenous MIIA and MIIB at the furrow and the polar cortex in control cells at mid, early, and late cytokinesis. For MIIA: 42 cells measured over 3 independent experiments. For MIIB: 48 cells measured over 3 independent experiments. Representative images of control MIIA and MIIB endogenous localization can be found in Fig. 4-3, panels A and B. C) Quantification of MIIA and MIIB at the equatorial cortex. Intensity was calculated as mean of green ROIs in cartoon insets. See Methods for detailed quantification scheme. For MIIA: n=41 Scr cells and 48 $MIIB^{lo}$ cells over 3 independent experiments. For MIIB: n= 43 $MIIA^{lo}$ and 46 Scr cells over 3 independent experiments. D) Images showing MIIB localization in $MIIA^{lo}$ versus $MIIA^{lo}$ +MIIA-mEGFP cells and MIIB localization in $MIIA^{lo}$ versus $MIIA^{lo}$ +MIIA-mEGFP cells. E) Tukey plots for MIIB or MIIA cortical intensity. For endogenous MIIB, n= 28 $MIIA^{lo}$ and 18 $MIIA^{lo}$ +MIIA cells over 3 independent experiments. For endogenous MIIA, n= 34 $MIIB^{lo}$ and 25 $MIIB^{lo}$ +MIIB cells over 3 independent experiments. Scale bar- 10 μm. Solid circles represent outliers. Error bars represent standard error of the mean. p values stated over respective bars.

Figure 4-S5

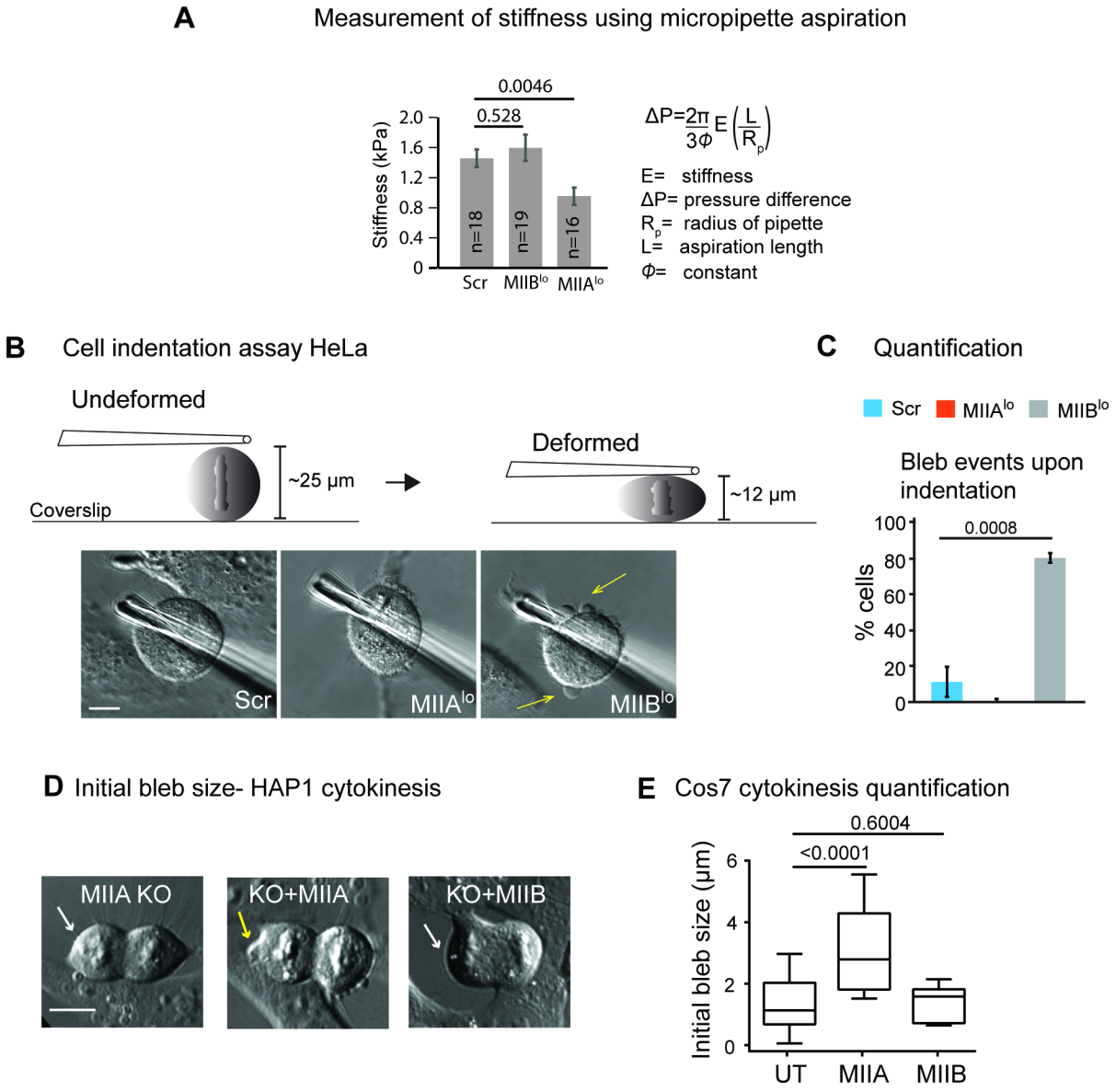

Figure 4-S5- Measurement of cortex stiffness, cell indentation assay and polar ablation

A) Stiffness using micropipette aspiration during metaphase. Number of cells stated inside respective bars. N= 3 independent experiments. B) Cell indentation assay design. DIC montage of Scr, MIIA^{lo} and MIIB^{lo} cells upon indentation. C) Quantification of blebbing events. n=16 Scr, 11 MIIA^{lo} and 21 MIIB^{lo} cells over 3 independent experiments. D) Representative images of polar cortex ablation in HAP1 MIIA KO fibroblasts during cytokinesis. White arrows indicate no bleb was created while yellow arrows indicate creation of bleb following polar cortex ablation. E) Tukey plots of initial bleb size following ablation during cytokinesis in Cos7 cells. n= 15 untransfected (UT), 15 MIIA and 11 MIIB expressing cells over 3 independent experiments. Scale bar- 10 μm. Solid circles represent outliers. Error bars represent standard error of the mean. p values stated over respective bars.

Figure 4-S6

Extended montages for bleb expansion and retraction upon metaphase ablation

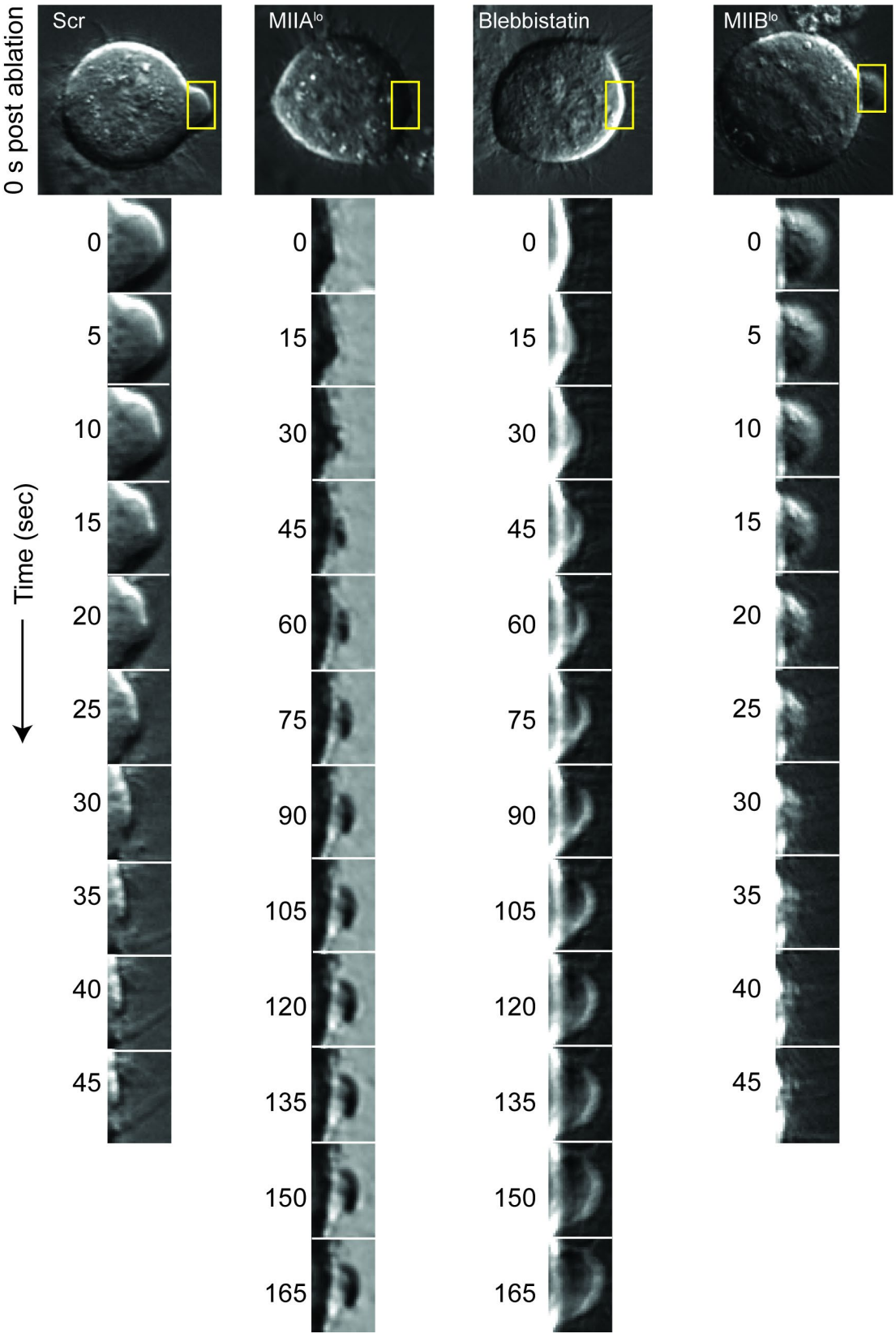

Figure 4-S6- Extended montage of ablation

Montage corresponds to yellow box. Control, MIIA^{lo}, MIIB^{lo} and blebbistatin-treated cells at metaphase are shown.

Figure 4-S7

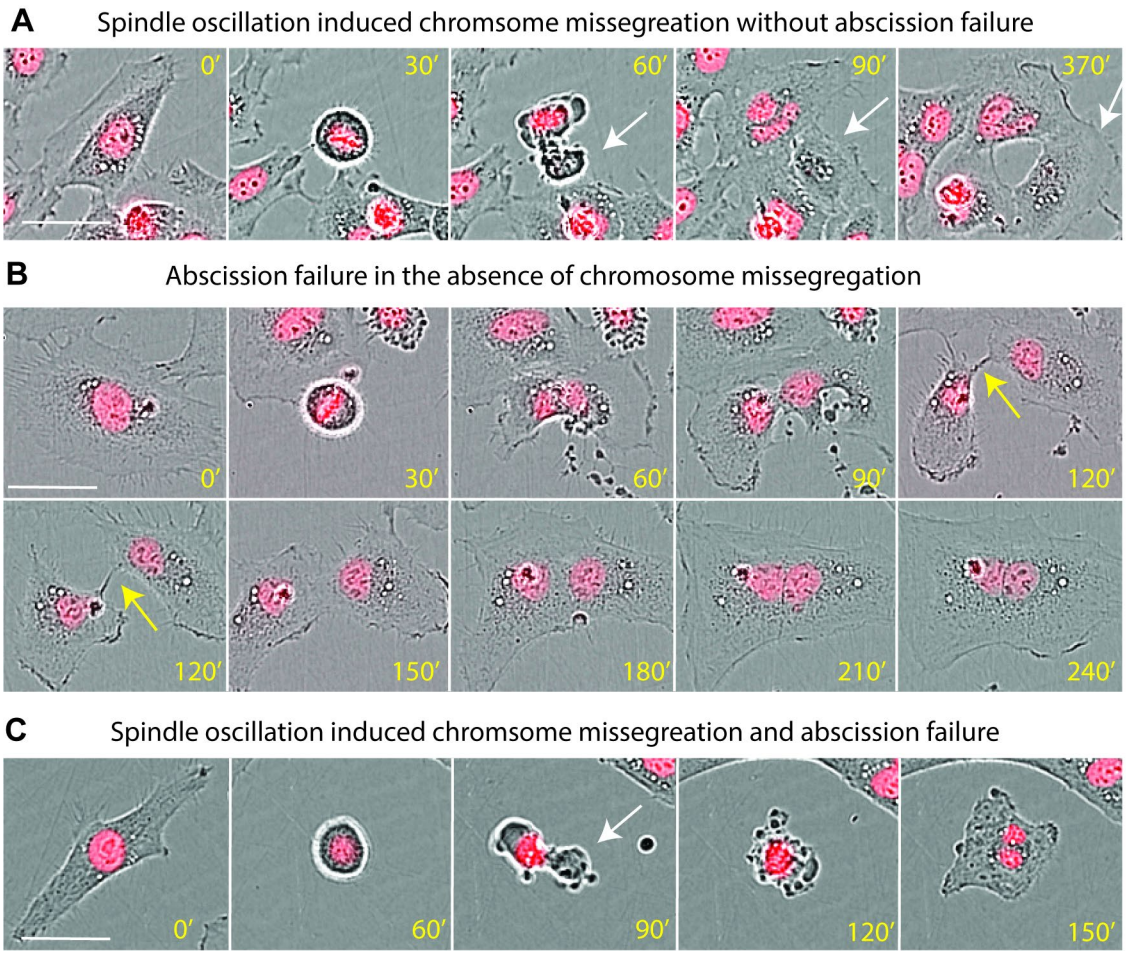

Figure 4-S7- Different modes of binucleation upon MIIB depletion

A) Representative time montage showing spindle oscillation induced chromosome missegregation followed by successful abscission. White arrow marks the daughter cell lacking any DNA signal. B) Representative time montage showing abscission failure in the absence of blebbing induced chromosome missegregation. Note the persistence of the intracellular bridge (yellow arrow) preceding fusion of the two daughter cells. C) Representative time montage showing both spindle oscillation white arrow denotes daughter cell without any DNA signal), as well as failure to complete abscission. The ROI used to create the montage was moved to keep the cells centered in the field of view. Live labeling of nuclei was performed using the NucLight Red reagent (see STAR Methods). Scale bar- 40 μm.

Figure 4-S8

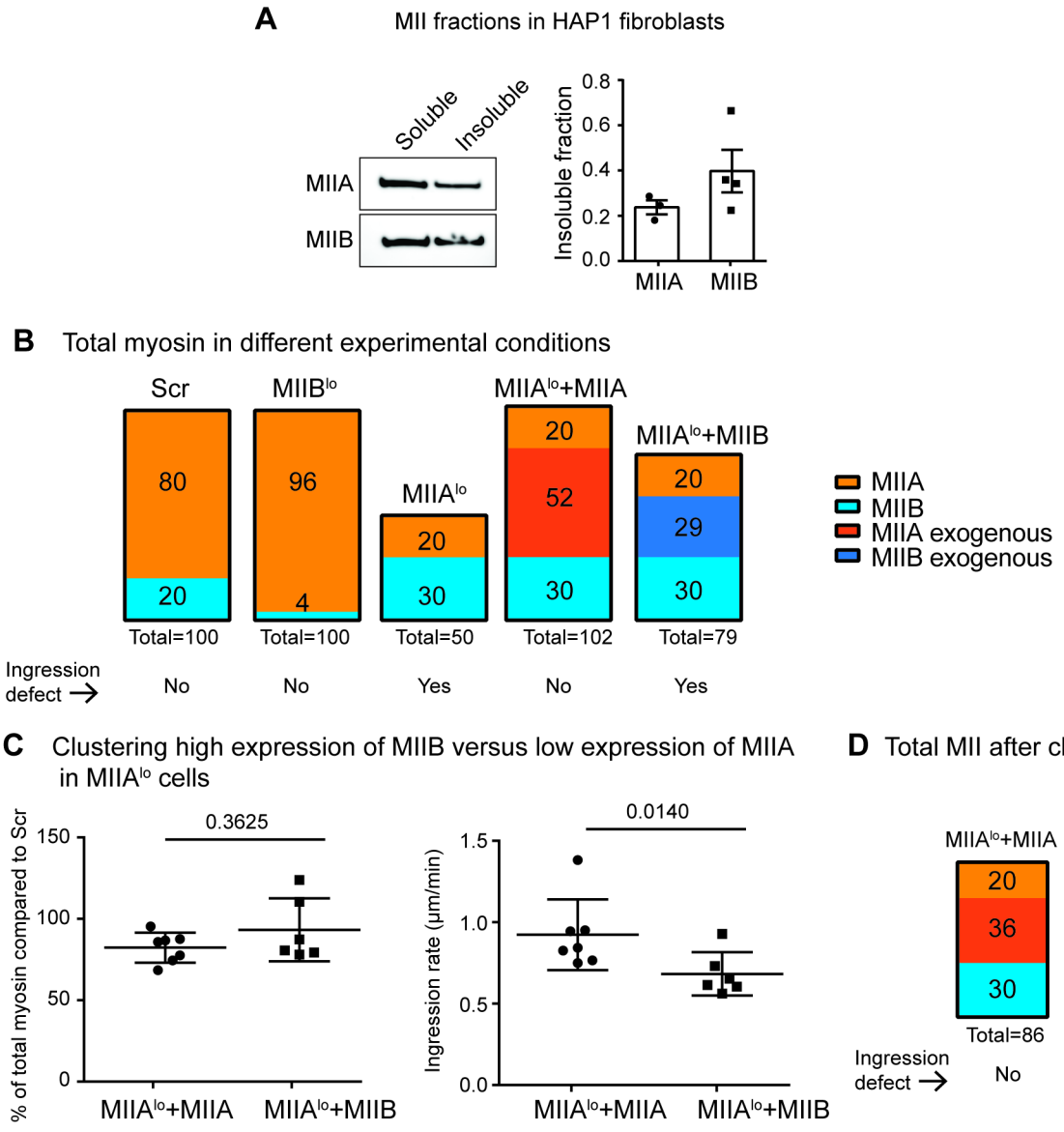

Figure 4-S8- HAP1 cell fractionation and clustering of ingression with expression in HeLa cells

A) Quantification of soluble and insoluble fractions of MIIA and MIIB using Western blotting. Error bars show standard error of the means. N= 3 independent experiments for MIIA and 4 independent experiments for MIIB. See STAR Methods for fractionation method. Cell line used is HAP1 parental fibroblasts. B) Total myosin in different experimental conditions. A 4:1 ratio of MIIA:MIIB was used as the starting proportion of the two myosins (Table 4-2). For knockdown efficiencies, 75% was used for MIIA and 80% for MIIB (Figure 4-S1). The increase in MII paralog expression was 1.5-fold for MIIB in MIIA knockdown, 1.2-fold for MIIA in MIIB knockdown, yielding the corresponding increase in proportions. The amount of exogenous expression was calculated by multiplying the average expression by the endogenous proportion of the MII paralog in Scr cells (values from Table S1, 143%

for MIIB and 65% for MIIA). C) Ingression rates were plotted for MIIA^{lo} cells with lowest expression of exogenous MIIA and highest expression of exogenous MIIB, such that the total myosin was equal. MIIA expression correlated with significantly higher ingression rates. D) Graphical representation of total myosin II when clustering lowest MIIA expression versus highest MIIB expression in MIIA^{lo} cells.

Figure 4-S9

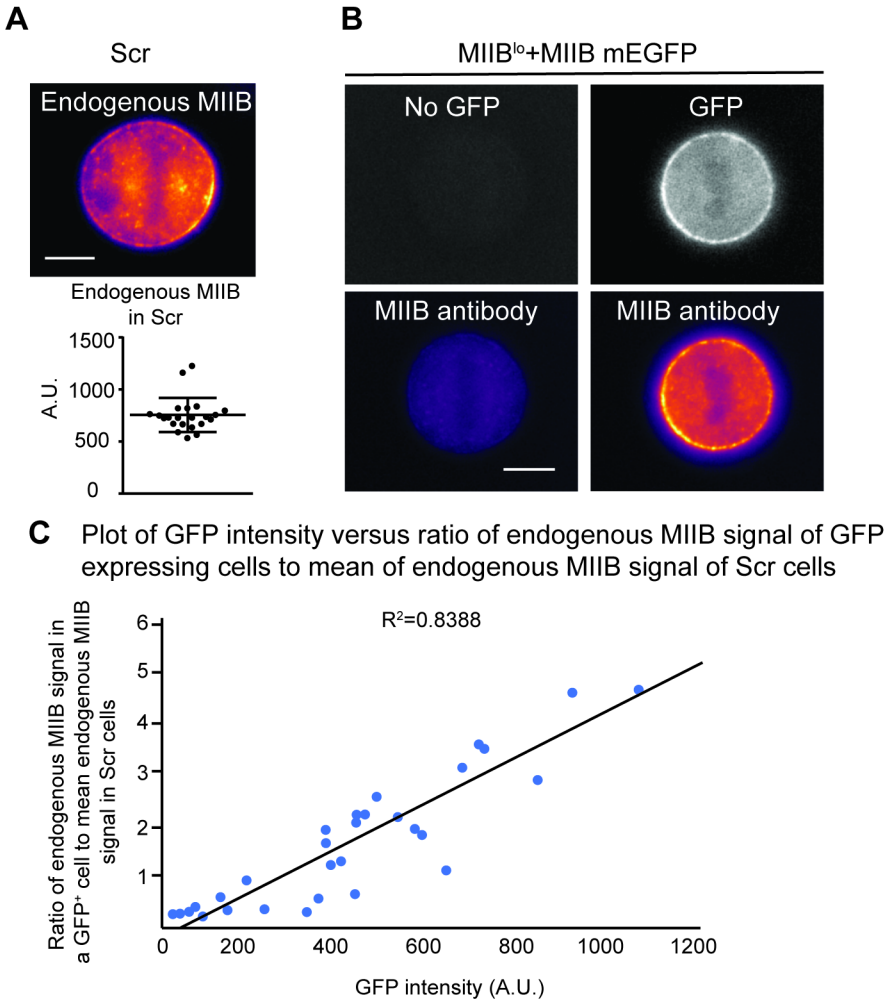

Figure 4-S9- Calibration of protein expression using immunofluorescence

A) Representative example of endogenous MIIB localization in Scr cells. Graph shows the distribution of cortical signals measured using 21 cells. Error bars show standard deviation. See STAR Methods for detailed quantification method. B) Two examples of endogenous MIIB localization in MIIB^{lo} cells re-expressing full length MIIB-mEGFP. In the first example (left), a cell with no GFP expression is shown. In the second example, a cell expressing GFP is shown. Endogenous MIIB is colored using mpl-inferno LUT. C) Using several cells expressing varying levels of GFP, the GFP signal was plotted against the ratio of the endogenous MIIB signal of GFP expressing cells to the mean of the endogenous MIIB intensity in Scr cells (plotted in (A)). By using the same imaging parameters for every experiment, this allowed us to extrapolate the expression in our rescue experiments with respect to wild type levels using the linear fit of the plot above. Scale bar- 10 μm.

Table 4-1- Relative expression of MII in different experiments

Construct/Condition	Expression relative to endogenous
Time-lapse DIC	
IIA-mEGFP in MIIA^{lo}	65 +/- 35%
IIA/B-mEGFP in MIIA^{lo}	65 +/- 22%
IIB-mEGFP in MIIB^{lo}	127 +/- 32%
IIB/A-mEGFP in MIIB^{lo}	119 +/- 45%
IIB-mEGFP in MIIA^{lo}	143 +/- 90%
IIA-mEGFP in MIIB^{lo}	116 +/- 52%
Compensatory Localization	
IIA-mEGFP in MIIA^{lo}	63 +/- 24%
IIB-mEGFP in MIIB^{lo}	123 +/- 70%
Micropipette Aspiration	
IIA-mEGFP in MIIA^{lo}	72 +/- 41%
IIA/B-mEGFP in MIIA^{lo}	89 +/- 42%
IIB-mEGFP in MIIB^{lo}	197 +/- 56%
IIB/A-mEGFP in MIIB^{lo}	185 +/- 65%

Note- Standard deviations are reported

Table 4-2- MIIA and MIB ratios in HeLa and HAP1 cells based on proteomics

Reference	Cell type	Method	Proportion	IIA/B ratio	IIA/IIB in filaments
Bekker-Jensen et al, 2018	HeLa CCL-2	Proteomics	93.5/6.5	14:1	4:1
Jonckheere et al, 2018	HAP1	Proteomics	70/30	2.4:1	1.5:1

IIA/B in filaments = IIA (total)/ IIB (total) * IIA (fil)/ IIB (fil)
HeLa assembled fractions from Schiffhauer et al, 2019- IIA (fil)- 0.08, IIB (fil)= 0.3
HAP1 assembled fractions from current study (Fig. 4-S11)- IIA (fil)- 0.24, IIB (fil)= 0.4

Chapter 5- The role of cell substrate adhesion in driving the maturation of sarcomeres in cardiac myocytes

Taneja, N.*, Neininger, AC.*, Burnette, DT. (2020). *Mol. Biol. Cell. 31(12)*
(** contributed equally)*

Introduction

The heart generates contractile force through the shortening of sarcomeres, which consist of myosin “thick” filaments forming sliding interactions with actin “thin” filaments. Actin filaments of adjacent sarcomeres are cross-linked by α-actinin-2 at Z-discs, which are important sites for intracellular signaling and mechanical stability of cardiomyocytes (Knoll et al., 2011; Kovacic-Milivojevic et al., 2001). The basic functional unit of contraction within a cardiomyocyte is the myofibril, comprised of a series of sarcomeres. In healthy cardiomyocytes, contractile forces generated by myofibrils are balanced by adhesive forces, specifically at cell-extracellular matrix (ECM) contacts (referred to as costameres), which transfer these forces to the ECM, and at cell-cell contacts (referred to as intercalated discs) (Liu et al., 2016; Samarel, 2005). Loss of this force balance can lead to detrimental phenotypes and disease states (Dabiri et al., 2012; Samarel, 2005). Previous work has shown that cell-ECM contacts comprise the majority of sites of force generation during early cardiomyocyte spreading, during the time window of myofibril assembly (McCain et al., 2012). These sites of force generation are subsequently transferred to cell-cell contacts as cells start to form intercalated discs.

Early studies of cultured primary chick cardiomyocytes localized adhesion proteins, such as vinculin, to the ends of myofibrils, and proposed that “adhesion plaques” serve as sites of myofibril assembly (Lu et al., 1992). This idea was supported by multiple genetic studies performed in the skeletal muscle of worms and fruit flies (Bloor and Brown, 1998; Hresko et al., 1994; Volk et al., 1990). Knockout of proteins involved in cell-ECM adhesion, such as integrin or perlecan, resulted in fewer myofibrils compared to the knockout of myofibril components themselves. Thus, the genetic evidence suggests that cell-ECM adhesion is upstream of myofibril assembly (Sparrow and Schock, 2009). It has additionally been shown that inhibiting contraction of cultured rat primary cardiomyocytes results in a loss of adhesions (Sharp et al.,

1997; Simpson et al., 1993). Conversely, modulating the size of adhesions by varying substrate stiffness can modulate the contractile properties of cardiomyocytes (Hersch et al., 2013; Jacot et al., 2008). This indicates that there is feedback between cardiomyocyte adhesion and contractile function. Despite this evidence, the mechanistic relationship between cell-ECM adhesion and myofibril assembly has remained unclear. This has been in part due to multiple conflicting models of myofibril assembly itself (Sanger et al., 2005).

Of the multiple competing models of myofibril assembly that have been proposed, the Template (a.k.a., Pre-myofibril) model has the most experimental support. First proposed by Howard Holtzer in 1984, the Template model postulated that “Non-Muscle Stress Fiber-Like Structures (NMSFLS)” are the precursors of myofibrils (Dlugosz et al., 1984). We have recently shortened Holtzer’s initialism to MSFs (Muscle Stress Fibers) for brevity (Fenix et al., 2018). While there was substantial evidence from fixed cultured myocytes and tissue to support the Template/Pre-myofibril model, there was little dynamic data directly demonstrating the transition of MSFs to myofibrils (Dlugosz et al., 1984; Rhee et al., 1994). We have recently utilized human iPSC-derived cardiomyocytes (hiCMs) to capture this transition (Fenix et al., 2018). hiCMs are transcriptionally similar to embryonic and neonatal cardiomyocytes, a time at which sarcomere assembly is occurring *in vivo*. We reported that freshly plated hiCMs did not have sarcomeres and subsequently assembled them over 4-16 hours after plating (Fenix et al., 2018). Live-cell imaging of either actin or α-actinin-2 revealed that MSFs move away from the edge and obtain sarcomeres over time.

Studies in primary skeletal myocytes from β1 integrin-deficient mice proposed that cell-ECM adhesion could regulate the transition of MSFs to myofibrils, rather than the formation of MSFs themselves (Schwander et al., 2003). In fixed cells, the authors observed that inactivation of β1 integrin led to a lack of myofibrils, but not MSFs (Schwander et al., 2003). A more recent study, however, claimed a new model of sarcomere assembly, where cell-ECM adhesion sites serve as the site for centripetal nucleation of sarcomeres (Chopra et al., 2018). In this model, a sarcomere-containing myofibril directly grows out of an adhesion, without the need for a template (i.e. MSFs). The authors imaged α-actinin-2, which marks both focal adhesions and the Z-lines of myofibrils. Indeed, a cursory glance at the movies presented gives the impression that the Z-lines are streaming out of adhesions. However, closer frame-by-frame inspection of the data revealed that these events were pre-formed myofibrils coming from the dorsal surface of the cell to the ventral (in focus) surface. We have now experimentally

demonstrated this phenomenon (Fenix et al., 2018). It is important to note that we were only able to capture these events after 24 hours post-plating, which is the time window in which Chopra et al. imaged their hiCMs.

Here, we sought to investigate the role of cell-ECM adhesion in myofibril assembly within the context of the Template/Pre-myofibril model. By combining high resolution three-dimensional imaging and multiple perturbations to focal adhesion assembly, we show that (1)- Dorsal stress fiber-like actin-based structures couple myofibrils to focal adhesions, (2)- Focal adhesions do not serve as the direct site for nucleation of myofibrils or MSFs, and (3)- Stronger coupling to the ECM correlates with the ability of MSFs to mature into myofibrils.

Results

The spatiotemporal relationship between cell-ECM adhesion and myofibril maturation

We first wanted to explore how adhesions, which are present on the ventral surface of the cell, are connected to myofibrils on the dorsal surface of the cell. We noticed that the relative organization of the focal adhesions and contractile structures (i.e., MSFs and myofibrils) bore a striking resemblance to that of mesenchymal crawling non-muscle cells (Figure 5-1). Indeed, we have previously noted that MSFs were similar in their organization to stress fibers found on the dorsal surface of mesenchymal cells called actin arcs (Fenix et al., 2018). In mesenchymal cells, actin arcs are connected to focal adhesions through specialized actin filament-based structures called dorsal stress fibers (DSFs) (Hotulainen and Lappalainen, 2006). To test if DSF-like structures exist in hiCMs, we examined the actin filament channel throughout the axial (Z) dimension (Figure 5-1, Figure 5-S1). We found that diffraction limited imaging was not able to resolve the relative axial positions of different actin filament structures, especially those close to the edges of hiCMs (Figure 5-S2). For this reason, we imaged actin filaments with structured illumination microscopy (SIM), which provides a ~2X increase in axial resolution. SIM revealed that strands of actin filaments extended from the ventral surface of the cell up to the dorsal surface (Figure 5-1). These strands ended in the MSFs and myofibrils on the dorsal surface (Figure 5-1, Figure 5-S1).

We next wanted to experimentally test if DSFs were mechanically coupled to MSFs and myofibrils. We hypothesized that the contractile MSFs and myofibrils could be pulling on DSFs. Therefore, we predicted that cutting DSFs would result in MSFs/myofibrils moving away from the edge of the cell. To test this possibility, we cut a DSF that appeared connected to either an MSF (Figure 5-1) or a myofibril (Figure 5-1) using a high intensity focused laser. We found that cutting of the DSF resulted in translocation of the MSF or myofibril away from the edge (Figure 5-1). To further test mechanical coupling, we also cut a myofibril that was attached to two DSFs; one on either end. Upon cutting, the two halves of the myofibril retracted away from each other along with the DSF each half was attached to. Taken together, the localization and laser dissection experiments suggest that DSFs mechanically connect MSFs and myofibrils to adhesions.

Figure 5-1

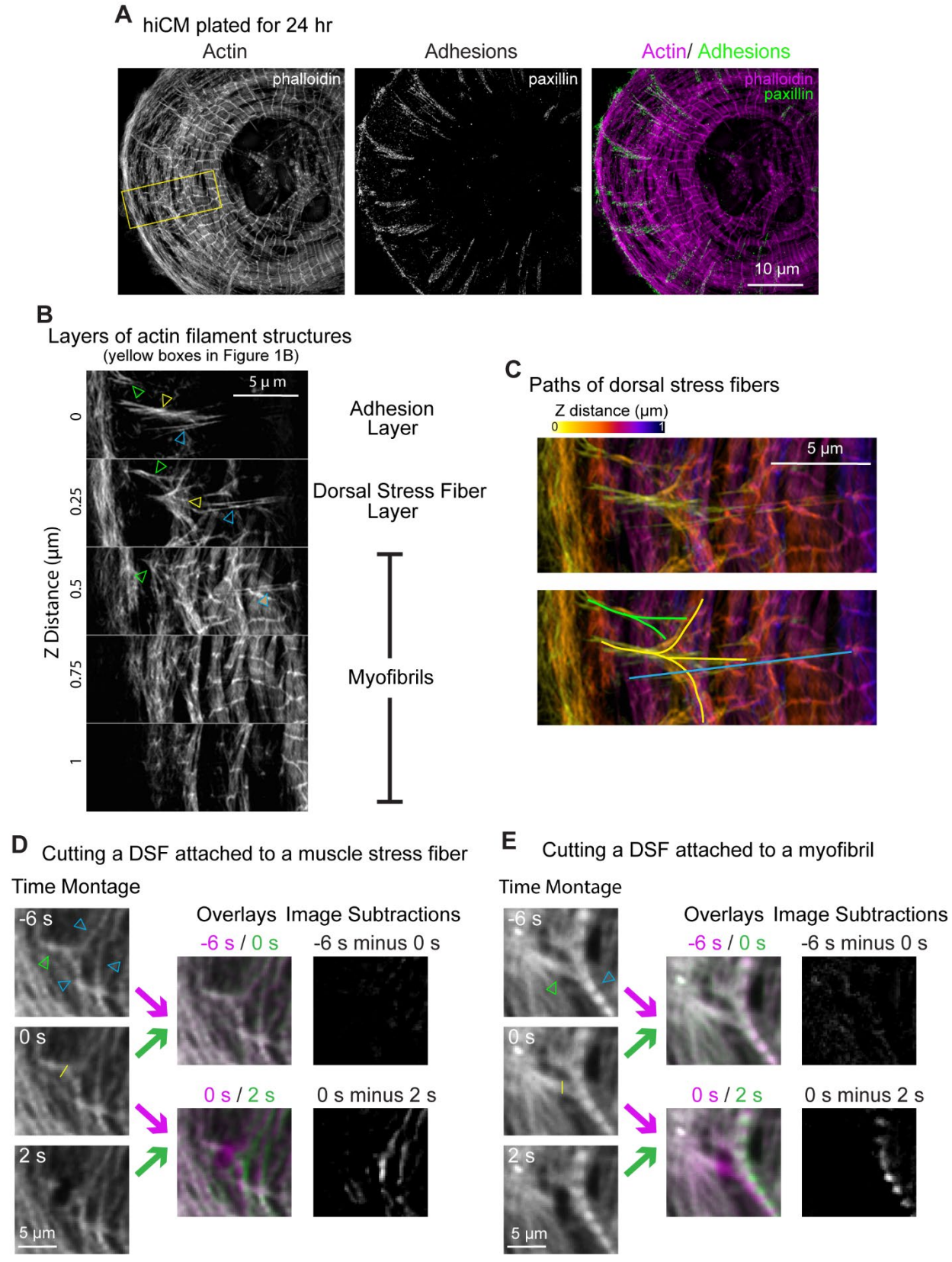

Figure 5-1- 3D organization of myofibrils and dorsal stress fibers

A) SIM of actin filaments (magenta) and paxillin (green) in hiCM plated for 24 hours. B) SIM showing the layers of actin filaments in the axial (Z) dimension from the box in (A). Arrowheads denote different dorsal stress fibers. C) 3D color projection of the data in (B). Lines denote the different dorsal stress fibers denoted in (B). D-E) Focused laser mediated cutting of DSF attached to an MSF (D) or a myofibril (E) in hiCM expressing Lifeact-mApple at 16 hours post plating. Green arrowheads denote dorsal stress fibers and blue arrowheads denote MSF or myofibril. Yellow line denotes cut site. Temporal color-coded overlays and image subtractions show the change in positioning of the MSF or myofibril following cutting of the dorsal stress fiber. See Figure 5-S1 for uncropped views of cells.

Given the physical connection between focal adhesions and myofibrils, we next investigated if there was a temporal relationship between the relative assembly of the two structures. We imaged actin filaments and paxillin in live hiCMs during the transition of MSFs into the first myofibrils. We use the term “myofibril maturation” to describe this transition. This should not be confused with “cardiomyocyte maturation”, which involves transcriptional and metabolic changes over developmental time scales (Jiang et al., 2018). As previously demonstrated, MSFs translocate away from the edge and obtain sarcomeres over time (Fenix et al., 2018). The purple arrowheads in Figure 5-2 denote this phenomenon. The paxillin channel revealed that focal adhesions also elongate during this same period (Figure 5-2, green arrowhead). Consistent with how dorsal stress fibers form in mesenchymal cells (Hotulainen and Lappalainen, 2006), we observed the appearance of dorsal stress fiber-like connections between the elongating adhesions and maturing myofibrils (Figure 5-2, yellow arrowheads). We next wanted to quantify the potential relationship between adhesion growth and myofibril maturation over time.

As focal adhesions mature, their area increases (Geiger et al., 2009). Similarly, when myofibrils mature, the length of their Z-lines increase (Dabiri et al., 1997). Therefore, we used total area of focal adhesions as a proxy for adhesion maturity and Z-line length as a proxy for myofibril maturity. To identify focal adhesions, we localized the adhesion protein, paxillin (Figure 5-2). To identify Z-lines, we localized α-actinin-2 (Figure 5-2). We then used a computer-assisted analysis method we developed to measure Z-line length and adhesion area in hundreds of cells during hiCM spreading (Figure 5-S3). We analyzed cells that were allowed to spread for 6 hours, 24 hours, and 1 week post-plating (Figure 5-2). We chose these time points based on our previous observations on the timing of myofibril maturation. At 6 hours post-plating, most hiCMs were characterized by immature myofibrils with punctate Z-lines (i.e., Z-bodies). By 24 hours, hiCMs contained myofibrils with elongated Z-lines. As suggested by our live data, we observed a strong positive correlation between the extent of adhesion and myofibril maturity at 6 hours, 24 hours, and up to 1 week post-plating (Figure 5-2). We next wanted to further establish the relationship between cell-ECM adhesion and myofibril maturation by altering components of the adhesion machinery and measuring the effects on myofibril maturation.

Figure 5-2

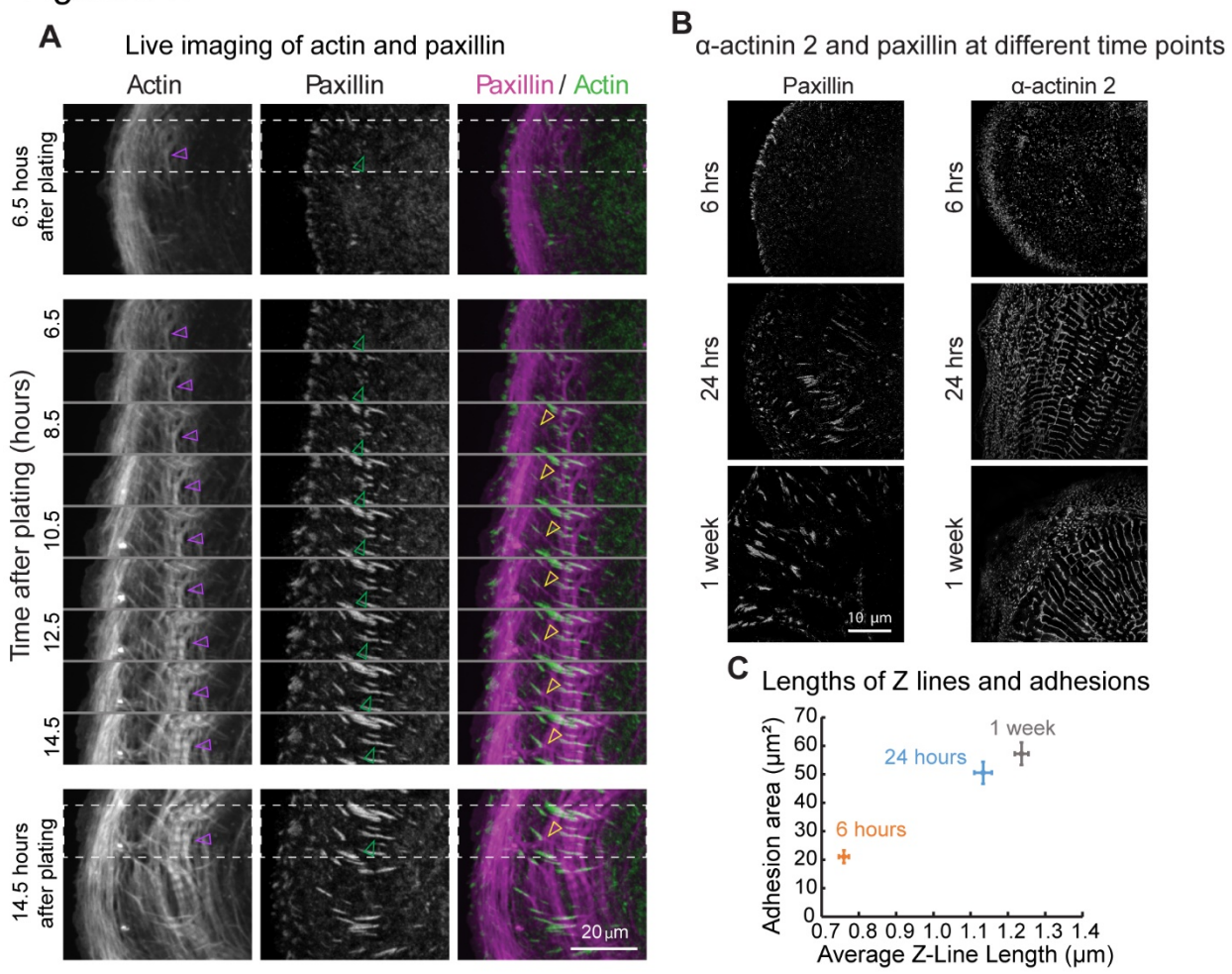

Figure 5-2- Dynamics of adhesions and myofibril maturation

A) Time montage of actin labeled with Lifeact-mEmerald and paxillin-mCherry during myofibril assembly. The first frame (top) and last frame (bottom) are separated by a time montage of the regions shown in the boxes (dotted lines). The purple arrowhead denotes an MSF becoming a myofibril. The green arrowhead denotes a growing adhesion. The yellow arrowhead denotes an extending dorsal stress fiber. B) Representative SIM images of endogenous paxillin and α-actinin-2 in hiCMs plated from 6 hours, 24 hours, or 1 week. C) Quantification of Z-line lengths and adhesion area in hiCMs plated for 6 hours, 24 hours, and 1 week. Z-line measurements: 6H: n= 58 cells, N= 4 independent experiments; 24H: n= 75 cells, N= 4 independent experiments; 1 Week: n=81 cells, 3 independent experiments. Adhesion measurements: 6H; n= 38 cells, N= 5 independent experiments; 24H: n= 48 cells, N= 5 independent experiments; 1 Week: n= 28 cells, N= 3 independent experiments.

Decreasing cell-ECM adhesion results in attenuation of myofibril maturation

We chose to start with vinculin, a component of focal adhesions that links the adhesion to the actin cytoskeleton (Carisey and Ballestrem, 2011). It was predicted two decades ago by Howard Holtzer and colleagues that vinculin would play a role during myofibril assembly (Lu et al., 1992). Furthermore, knockout of vinculin in hiCMs has been shown to alter the organization of Z-lines (Chopra et al., 2018). We depleted vinculin using a pooled siRNA approach and found a significant reduction in paxillin-positive area (Figure 5-3). To test if reduction in vinculin altered myofibril maturation, we measured the length of Z-lines after 24 hours of spreading, since this is the time point at which most control cells contained myofibrils (Fenix et al., 2018). Knockdown of vinculin resulted in a significant reduction in Z-line length (Figure 5-3). This reduction in Z-line length was in agreement with previously published data (Chopra et al., 2018). We next wanted an additional measure of myofibril maturation. The incorporation of the large Z-disc protein titin is considered a marker for maturation of myofibrils (Sanger et al., 2005). We localized the N-terminal region of titin, which should localize on either side of Z-lines (Figure 5-3) (Wang and Greaser, 1985). In control cells plated for 24 hours, we found distinct organization of titin at a mean distance of 4.1 +/- 2.3 μm from the edge (Figure 5-3). Knockdown of vinculin resulted in severe disruption of overall titin organization, with the first titin structures localizing 9.5 +/- 3.8 μm from the edge (Figure 5-3). The effects of vinculin knockdown on adhesion area, Z-line length and titin organization were recapitulated using a single siRNA mediated knockdown approach (Figure 5-S4).

Figure 5-3

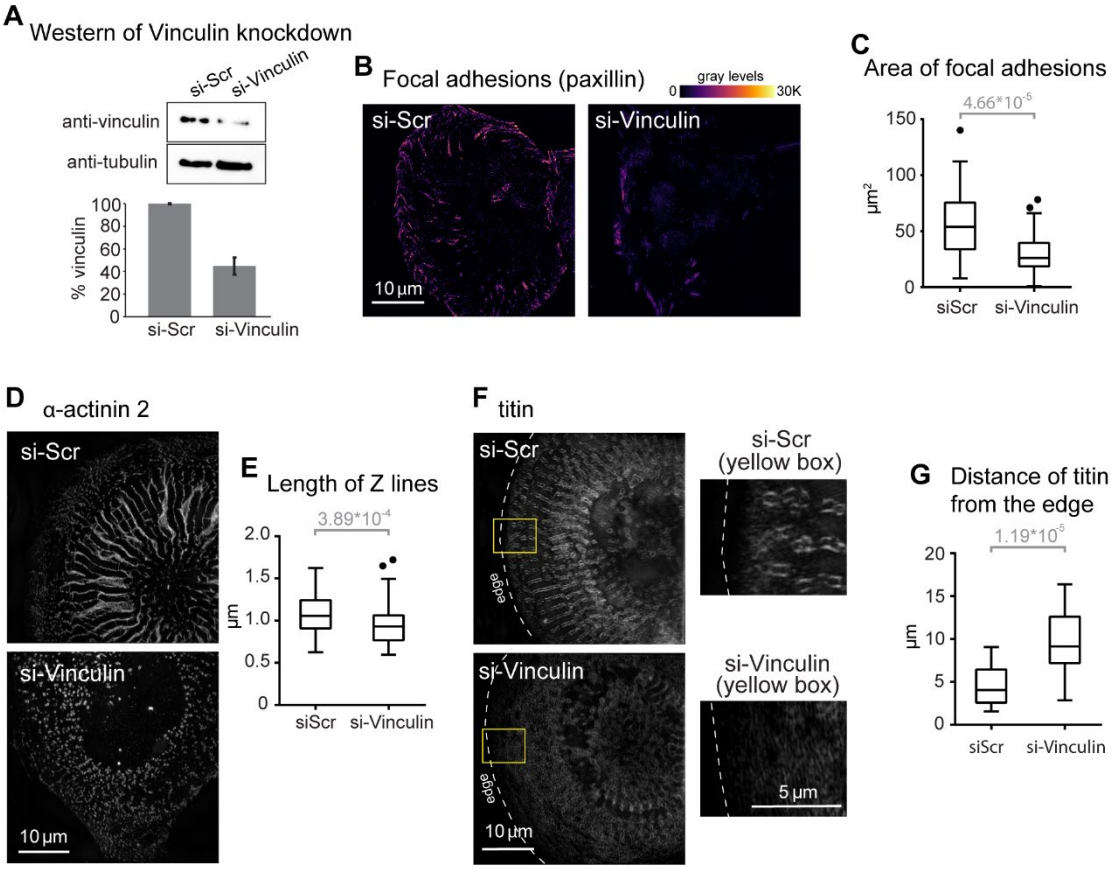

Figure 5-3- Knockdown of vinculin results in attenuation of myofibril maturation

A) Representative western blot for vinculin knockdown using siRNA. Tubulin was used as a loading control. Knockdown efficiency was calculated from 4 independent experiments. B) Paxillin localization (single optical section) in hiCMs treated with either scrambled or vinculin siRNA. C) Quantification of adhesion area. si-Scr: n= 54 cells, N= 6 independent experiments; si-Vinculin: n= 30 cells, N= 4 independent experiments. D) α-actinin-2 localization (maximum Z-projection) in hiCMs treated with either scrambled or vinculin siRNA. E) Quantification of average length of Z-lines. si-Scr: n= 131 cells, N= 6 independent experiments; si-Vinculin: n= 69 cells, N= 5 independent experiments. F) Localization of titin in hiCMs treated with either scrambled or vinculin siRNA. G) Quantification of distance of titin localization from the cell edge. si-Scr: n= 19 cells, N= 3 independent experiments; si-Vinculin: n= 21 cells, N= 3 independent experiments. Exact p-values stated in graphs.

In non-muscle cells, vinculin is thought to act as a clutch that mechanically couples focal adhesions to actin stress fibers (e.g., actin arcs) to impede their rearward translocation (Thievessen et al., 2013). As a result, we asked if vinculin could also be slowing the translocation of MSFs. We previously reported that MSFs translocate away from the edge and then slow down as they transition into myofibrils, which undergo little translocation (Fenix et al., 2018). Therefore, we quantified the rate of rearward movement of MSFs in control versus vinculin depleted cells. We used kymography to measure the rates of MSF translocation (Figure 5-4). In control cells, we found MSFs underwent rearward translocation at comparable rates as our previous report (Figure 5-4). Vinculin knockdown resulted in a significant increase in MSF translocation rates (Figure 5-4). This is consistent with a potential role for cell-ECM adhesion in slowing the translocation of MSFs. We next wanted to test if reduction of adhesion size through altering other adhesion components could also attenuate myofibril maturation.

Figure 5-4

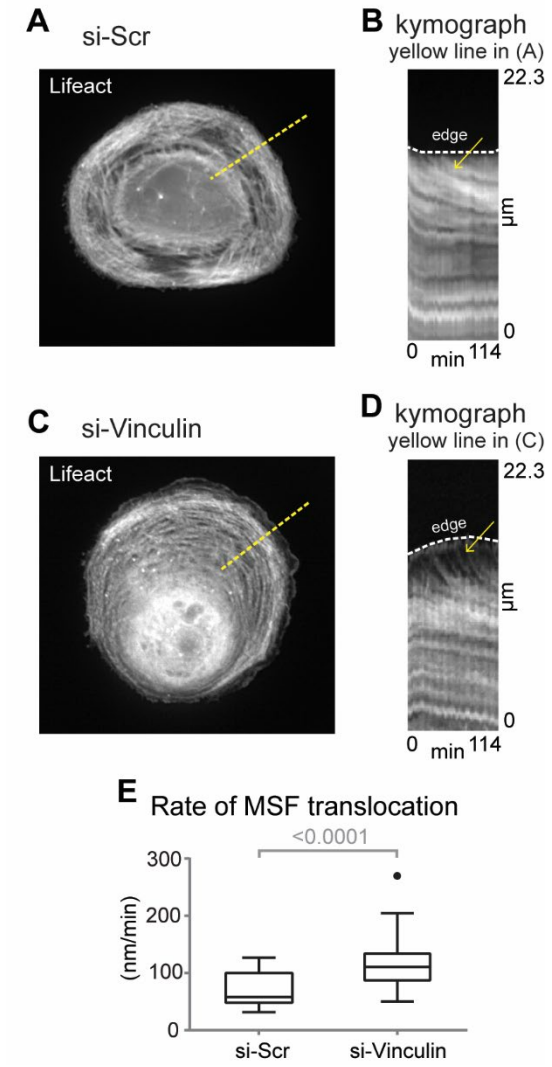

Figure 5-4- Knockdown of vinculin results in faster translocation of muscle stress fibers

A) Control (scrambled siRNA-treated) cell expressing Lifeact-mApple 16 hours post-plating. B) Kymograph generated using yellow line in (A). Yellow arrow denotes MSFs translocating away from the edge (dotted white line). E) Vinculin depleted cell expressing Lifeact-mApple 16 hours post-plating. D) Kymograph generated using yellow line in (C). Yellow arrow denotes MSFs translocating away from the edge (dotted white line). E) Quantification of MSF translocation rates in control versus vinculin-depleted cells. si-Scr: n= 30 MSFs from 19 cells; si-Vinculin: n= 22 MSFs from 14 cells; N= 3 independent experiments. Exact p-values stated in graphs.

Talin is a focal adhesion protein that directly binds β integrins through its N-terminal “head” domain and to vinculin through its C-terminal “tail” domain (Dumbauld et al., 2013). As a result, talin binding to vinculin leads to focal adhesion strengthening by linking vinculin to integrins (Case et al., 2015). It has been previously reported that overexpression of the head domain of talin acts in a dominant negative manner, resulting in attenuation of focal adhesion signaling (Tan et al., 2015). We hypothesized that expression of talin head domain should result in reduction in focal adhesion area, similar to vinculin knockdown. Therefore, we measured paxillin-positive area in hiCMs expressing talin head-mEGFP (Figure 5-5). We found a marked decrease in focal adhesion area in hiCMs expressing talin head-mEGFP versus control cells (Figure 5-5 and 5-S5). We also found that this decrease in adhesion area correlated with a decrease in Z-line length, as well as an increase in the distance from the edge at which titin localizes (Figure 5-5). The rate of MSF translocation also increased in hiCMs expressing talin head-mEGFP (Figure 5-5).

Figure 5-5

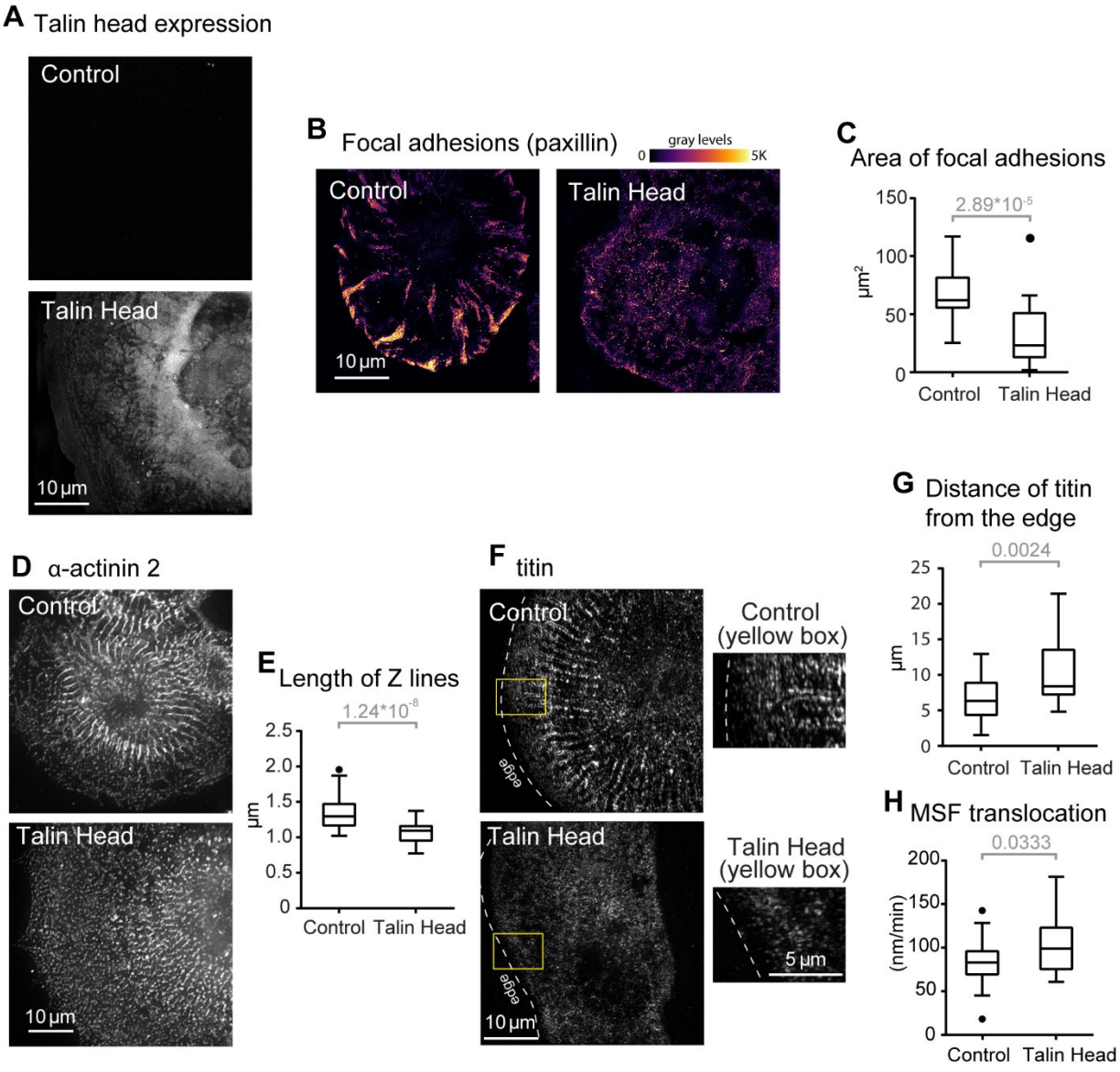

Figure 5-5- Expression of talin head domain results in attenuation of myofibril maturation

A) Representative hiCM expressing talin head-mEGFP versus non-expressing hiCM. B) Paxillin localization (single optical section) in hiCM overexpressing talin head-mEGFP versus a non-expressing hiCM. C) Quantification of adhesion area. Non-expressing: n= 21 cells; talin head-mEGFP: n= 22 cells, N= 3 independent experiments each. D) α-actinin-2 localization (maximum Z-projection) in hiCM overexpressing talin head-mEGFP versus a non-expressing hiCM. E) Quantification of average Z-lines length . Non-expressing: n= 43 cells; talin head-mEGFP: n= 36 cells; N= 3 independent experiments each. F) Localization of titin in hiCM overexpressing talin head-mEGFP versus a non-expressing hiCM. G) Quantification of distance of titin localization from the cell edge. Non-expressing: n= 19 cells; Talin head: n= 21 cells, N= 3 independent experiments each. H) Quantification of MSF translocation rates in

control hiCMs versus hiCMs overexpressing talin head=mEGFP. Control: n= 25 MSFs from 16 cells; talin head-mEGFP: n= 26 MSFs from 17 cells; N= 3 independent experiments. Exact p-values stated in graphs.

We next investigated the role of focal adhesion kinase (FAK), which is a key scaffolding and signaling protein at focal adhesions necessary for regulating focal adhesion growth (Parsons et al., 2000). A previous study has suggested that knocking down FAK in skeletal muscle precursors (i.e., myoblasts) reduced focal adhesions as well as attenuated myofibril formation (Quach and Rando, 2006). We asked whether this role for FAK is conserved in cardiomyocytes. To that end, we depleted hiCMs of FAK using a pooled siRNA approach (Figure 5-6) and first measured focal adhesion area. Consistent with previous reports (Quach and Rando, 2006), we found a significant reduction in focal adhesion area upon knockdown of FAK (Figure 5-6). In correlation with this reduction in adhesion, we found a decrease in Z-line length as well as an increase in the distance from the edge at which titin localized (Figure 5-6). We verified these phenotypes using single siRNA mediated knockdown of FAK (Figure 5-S4). Furthermore, depletion of FAK resulted in increased rates of MSF translocation (Figure 5-6). Taken together, we used four different methods to reduce focal adhesions in hiCMs. Our data suggest that reducing focal adhesion area correlates with attenuation of myofibril maturation and an increase in rate of MSF translocation. We next wanted to increase adhesion area to test if it would result in increased or accelerated myofibril maturation.

Figure 6

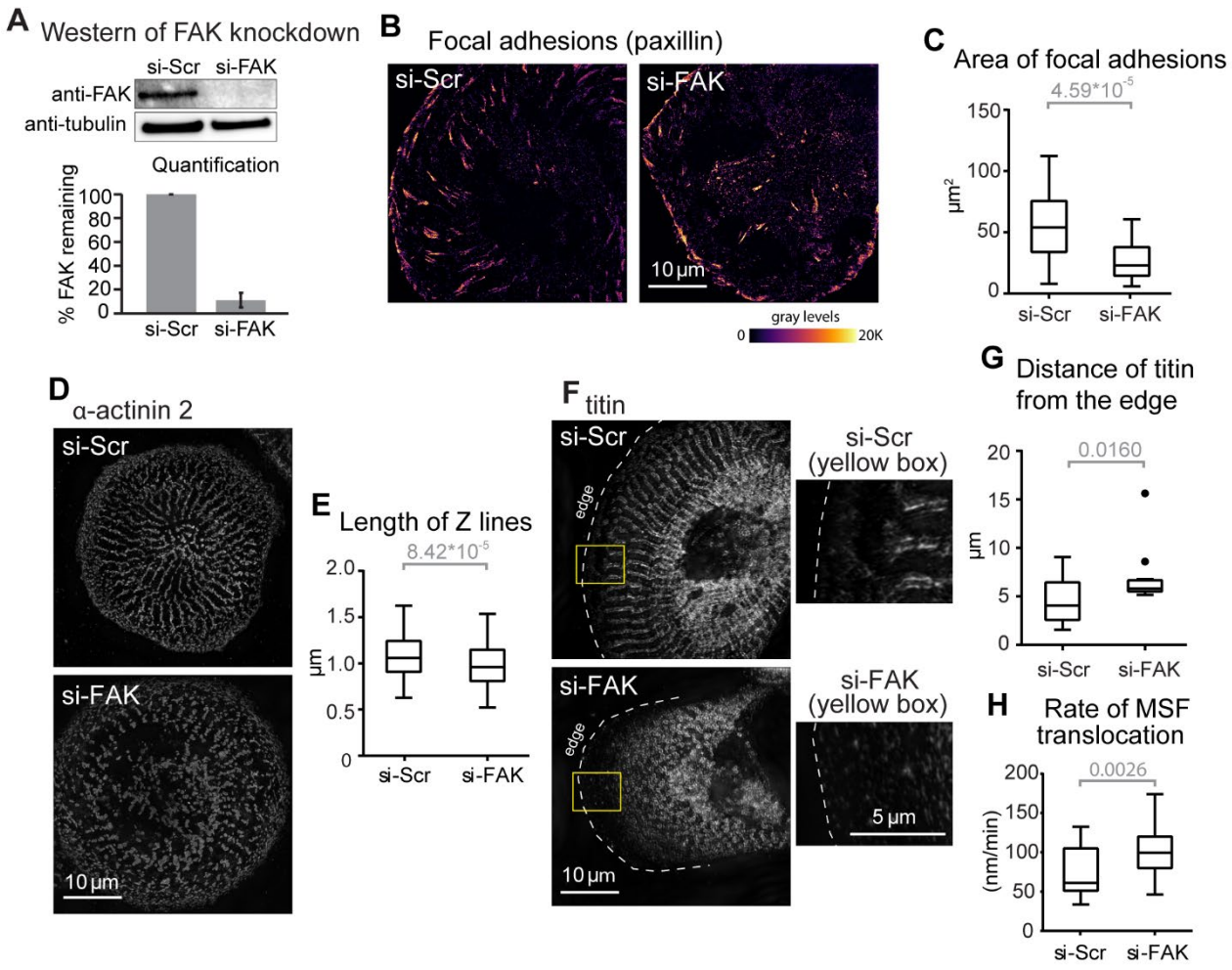

Figure 5-6- Knockdown of FAK results in attenuation of myofibril maturation

A) Representative western blot for FAK knockdown using siRNA. Tubulin was used as a loading control. Knockdown efficiency was calculated from 3 independent experiments. B) Paxillin localization (single optical section) in hiCMs treated with either scrambled or FAK siRNA. C) Quantification of adhesion area in FAK depleted cells. si-FAK: n= 36 cells, N= 4 independent experiments. The si-Scr dataset is the same as in Fig. 5-3, panel C. D) α-actinin-2 localization (maximum Z-projection) in hiCMs treated with either scrambled or FAK siRNA. E) Quantification of average length of Z-lines in FAK-depleted cells. si-FAK: n= 106 cells, N= 4 independent experiments. The si-Scr dataset is the same as in Fig. 5-3, panel E. F) Localization of titin in hiCMs treated with either scrambled or FAK siRNA. G) Quantification of distance of titin localization from the cell edge. si-FAK: n= 12 cells, N= 3 independent experiments. The si-Scr dataset is the same as in Fig. 5-3, panel F. H) Quantification of MSF translocation rates in FAK-depleted cells versus scrambled siRNA-treated hiCMs. si-FAK: n= 25 MSFs

from 16 cells; N= 3 independent experiments. The si-Scr dataset is the same as in Fig. 5-4, panel E. Exact p-values stated in graphs.

Increasing ECM adhesion results in precocious myofibril maturation

It has been shown in non-muscle cells that pharmacologically disrupting the kinase activity of FAK leads to inhibition of adhesion turnover without affecting adhesion assembly, resulting in increase in adhesion area (Slack-Davis et al., 2007; Taneja et al., 2016). Therefore, we used a specific small-molecule inhibitor, PF-228, to disrupt the kinase activity of FAK in hiCMs. The autophosphorylation of FAK at Y397 is classically used as a readout for FAK kinase activity (O'Brien et al., 2014; Schaller et al., 1994; Slack-Davis et al., 2007). We found that treatment of hiCMs with PF-228 led to a nearly complete loss of localization of pFAK from adhesions (Figure 5-7). Treatment of hiCMs with PF-228 led to a small increase in focal adhesion area at 24 hours post-plating, but this was not significant (Figure 5-S6). Furthermore, there was a significant, but small change in Z-line length (Figure 5-S6). We wondered whether any potential effects of FAK inhibition could be observed at earlier time points in plating when the first myofibrils are assembling. We previously showed that the first myofibrils arise 4-16 hours after plating (Fenix et al., 2018). Therefore, we chose to investigate the relationship between focal adhesions and myofibrils at 6 hours post plating. Indeed, we found that at 6 hours post-plating, hiCMs treated with PF-228 had a significantly higher adhesion area (Figure 5-7). Strikingly, we found that hiCMs treated with PF-228 also had significantly longer Z-lines, as well as closer titin localization to the edge (Figure 5-7). Furthermore, we found that PF-228-treated hiCMs had slower rates of MSF translocation compared to control hiCMs (Figure 5-7). We next wanted to test if the correlation between an increase in adhesion area and precocious myofibril assembly was specific to FAK inhibition. Therefore, we wanted to increase focal adhesion size without any genetic or pharmacological perturbations.

Figure 5-7

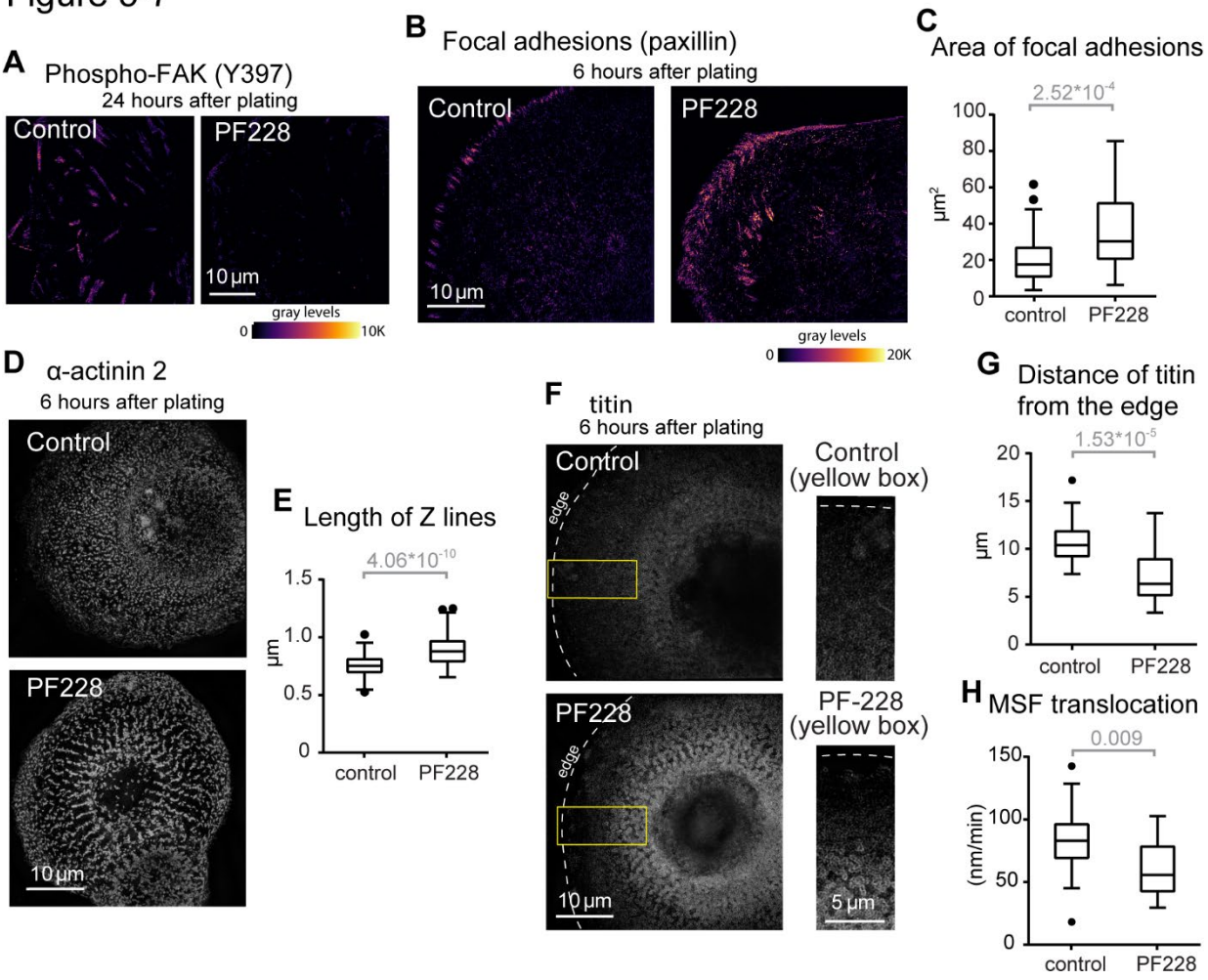

Figure 5-7- Inhibition of FAK kinase activity results in precocious myofibril maturation

A) Localization of pFAK Y397 in control or 3 µM PF-228-treated hiCMs 24 hours post-plating. B) Paxillin localization (single optical section) in control versus PF-228-treated hiCMs 6 hours post-plating. C) Quantification of adhesion area in PF-228-treated cells. Control: n= 38 cells, N= 5 independent experiments. PF-228: n= 44 cells, N= 4 independent experiments. D) α-actinin-2 localization (maximum Z-projection) in control versus PF-228-treated hiCMs 6 hours post-plating. E) Quantification of average length of Z-lines in PF-228-treated hiCMs. Control: n= 58 cells, N= 4 independent experiments; PF-228: n= 107 cells, N=4 independent experiments. F) Localization of titin in control versus PF-228 treated hiCMs after 6 hours of spreading. G) Quantification of distance of titin localization from the cell edge. Control: n= 23 cells; PF-228: n= 23 cells; N= 3 independent experiments each. H) Quantification of MSF translocation rates in PF-228 treated cells versus control. PF-228: n= 24 MSFs from 17 cells; N= 3 independent experiments. The control data set is the same is in Fig. 5-5, panel H. Exact p-values stated in graphs.

It has been shown in non-muscle cells that increasing the concentration of the extracellular matrix protein, fibronectin, leads to larger focal adhesions (Gupton and Waterman-Storer, 2006; Taneja et al., 2016). As our standard procedure, we plate hiCMs on glass coverslips coated with 10 μg/mL fibronectin. As such, all the previous experiments presented here were performed with this coating concentration. To test if increasing fibronectin would increase focal adhesion area in hiCMs, we plated them on glass coverslips coated with 50 μg/mL fibronectin, as we have done previously using non-muscle cells (Taneja et al., 2016). At 6 hours post-plating we found that hiCMs plated on 50 μg/mL fibronectin had a higher paxillin-positive adhesion area compared to control hiCMs plated on 10 μg/mL fibronectin (Figure 5-8). This increase in adhesion area correlated with an increase in Z-line length as well as closer titin localization to the edge (Figure 5-8). The rate of MSF translocation was also significantly slower compared to control hiCMs plated on 10 μg/mL fibronectin (Figure 5-8). Of note, focal adhesion area and Z-line length were not significantly different for hiCMs plated on 10 or 50 μg/mL fibronectin at 24 hours post-plating, similar to what we observed with FAK inhibition (Figure 5-S6). Taken together, our data suggest that increasing focal adhesion area correlated with precocious myofibril maturation.

Figure 5-8

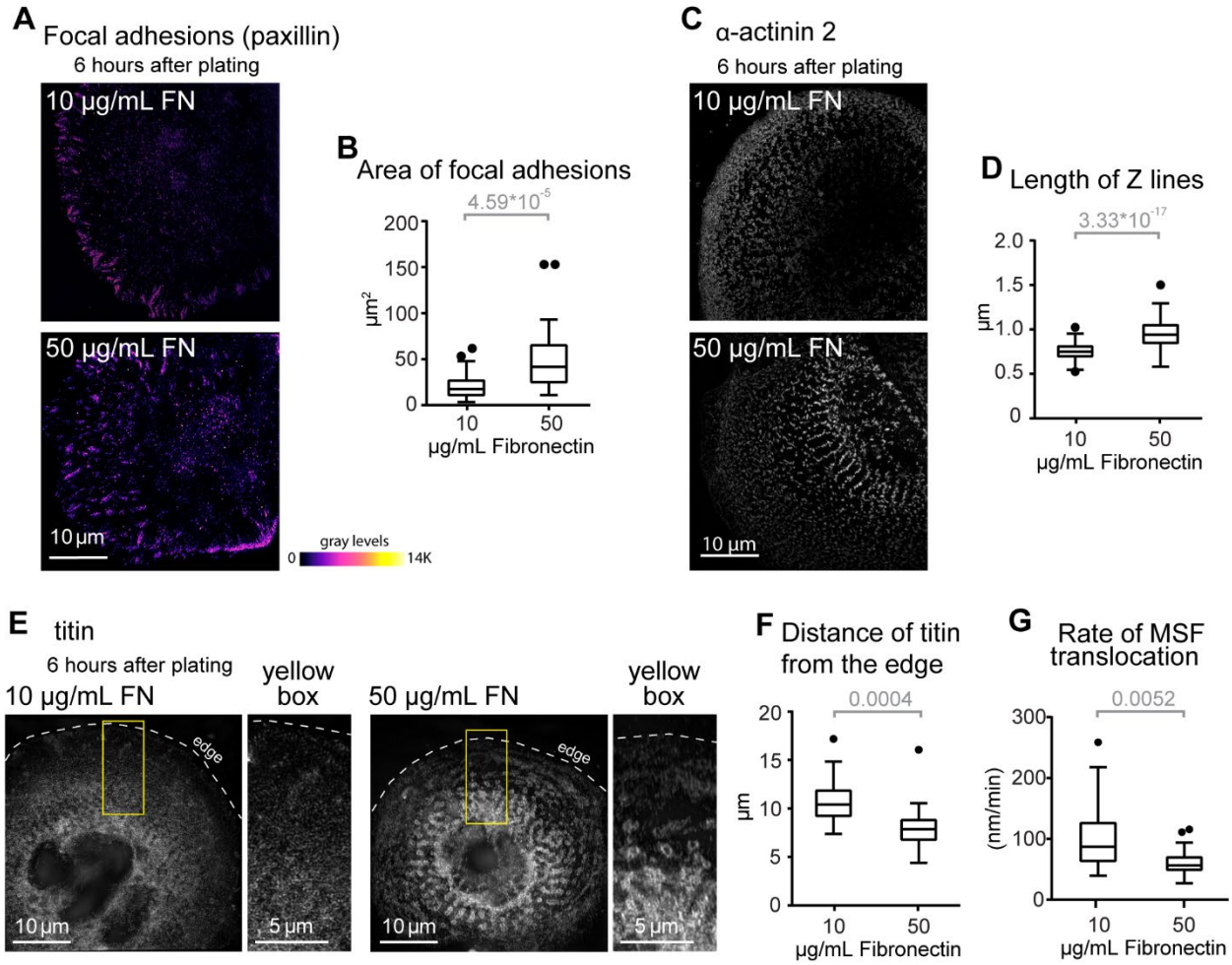

Figure 5-8- Increasing fibronectin concentration results in precocious myofibril maturation

A) Paxillin localization (single optical section) in hiCMs plated on either 10 µg/mL or 50 µg/mL fibronectin. B) Quantification of adhesion area in hiCMs plated on either 10 µg/mL or 50 µg/mL fibronectin. 50 µg/mL: n= 47 cells, N= 5 independent experiments. The 10 µg/mL dataset is the same as Fig. 5-7, panel C. C) α-actinin-2 localization (maximum Z-projection) in hiCMs plated on either 10 µg/mL or 50 µg/mL fibronectin. D) Quantification of average length of Z-lines in hiCMs plated on either 10 µg/mL or 50 µg/mL fibronectin. 50 µg/mL: n= 201 cells, N= 6 independent experiments. The 10 µg/mL dataset is the same as Fig. 5-7, panel E. E) Localization of titin in hiCMs plated on either 10 µg/mL or 50 µg/mL fibronectin. F) Quantification of distance of titin localization from the cell edge. 50 µg/mL: n= 23 cells, N= 3 independent experiments. The 10 µg/mL dataset is the same as Fig. 5-7, panel F. G) Quantification of MSF translocation rates in hiCMs plated on either 10 µg/mL or 50 µg/mL fibronectin. 50 µg/mL: n= 20 MSFs from 12 cells; N= 3 independent experiments. The 10 µg/mL dataset is the same as in Fig. 5-5, panel H. Exact p-values stated in graphs.

DIAPH1 is required for the maturation of myofibrils

We next wanted to further investigate the mechanism controlling substrate coupling during myofibril maturation. As dorsal stress fibers form the connection between adhesions and myofibrils, we hypothesized that reducing this connection could lead to less mature myofibrils. In non-muscle cells, the actin filament nucleator DIAPH1 is known to be critical for focal adhesion growth and its depletion results in fewer and smaller focal adhesions (Fessenden et al., 2018; Riveline et al., 2001). We previously showed that DIAPH1 is expressed in hiCMs using RNAseq (Fenix et al., 2018). In that study, we also showed that another formin, FHOD3, is critical for the assembly of myofibrils (Fenix et al., 2018). However, FHOD3 only localized to MSFs and myofibrils but not to dorsal stress fibers (Fenix et al., 2018). To examine whether DIAPH1 localized to dorsal stress fibers, we expressed DIAPH1-mEGFP. In contrast to FHOD3, we found that DIAPH1 localized to the actin filaments of dorsal stress fibers (Figure 5-9). Furthermore, depletion of DIAPH1 using siRNA resulted in a reduction of dorsal stress fibers but not MSFs (Figure 5-9).

We next examined if DIAPH1 knockdown reduced focal adhesions and myofibril maturation. Indeed, we found that hiCMs did have a significant reduction in focal adhesion area after DIAPH1 depletion using pooled siRNA (Figure 5-9). Further establishing the correlation between focal adhesion area and myofibril maturation, we found a significant decrease in Z-line length (Figure 5-9). There was also an increase in the distance from the edge at which titin localized in DIAPH1-depleted cells (Figure 5-9). The phenotypes observed for focal adhesion area, Z-line length and titin organization were recapitulated using a single siRNA mediated knockdown of DIAPH1. Further supporting the hypothesis that DIAPH1 is required for substrate coupling in hiCMs, we found a significant increase in the rate of MSF translocation (Figure 5-9).

Figure 5-9

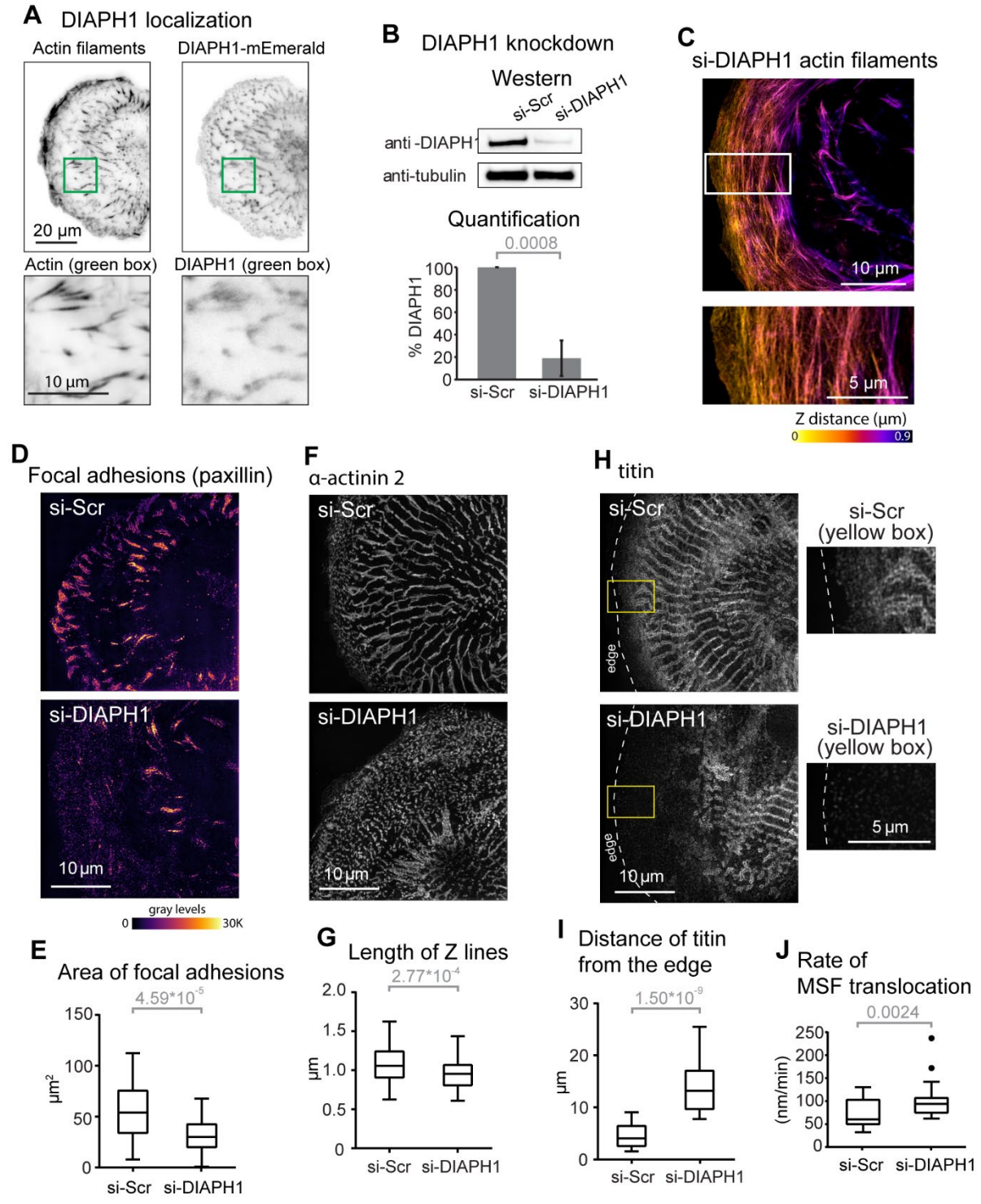

Figure 5-9- Knockdown of DIAPH1 results in attenuation of myofibril maturation

A) Total internal reflection microscopy (TIRF) image showing the ventral section of an hiCM spread for 24 hours. Actin filaments (phalloidin) and DIAPH1-mEmerald are shown in inverted gray. Note the co-localization of DIAPH1 with actin filaments associated with focal adhesions.

B) Representative western blot for DIAPH1 knockdown using siRNA. Tubulin was used as a loading control. Knockdown efficiency was calculated from 3 independent experiments. C) 3D SIM of actin filaments in a si-DIAPH1 KD hiCM at 24 hours post plating. Note the lack of prominent dorsal stress fibers. D) Paxillin localization (single optical section) in hiCMs treated with either scrambled or DIAPH1 siRNA. E) Quantification of adhesion area in DIAPH1- depleted cells. si-DIAPH1: n= 33 cells, N= 4 independent experiments. The si-Scr dataset is the same as Fig. 5-3, panel C. F) α-actinin-2 localization (maximum Z-projection) in hiCMs treated with either scrambled or DIAPH1 siRNA. G) Quantification of average length of Z-lines in DIAPH1-depleted cells. si-DIAPH1: n= 58 cells, N= 3 independent experiments. The si-Scr dataset is the same as Fig. 5-3, panel E. H) Localization of titin in hiCMs treated with either scrambled or DIAPH1 siRNA. I) Quantification of distance of titin localization from the cell edge. si-DIAPH1: n= 23 cells, N= 3 independent experiments. The si-Scr dataset is the same as Fig. 5-3, panel F. J) Quantification of MSF translocation rates in DIAPH1 depleted cells versus scrambled siRNA-treated hiCMs. si-DIAPH1: n= 25 MSFs from 16 cells; N= 3 independent experiments. The si-Scr dataset is the same as in Fig. 5-4, panel E. Exact p-values stated in graphs.

Discussion

Here we present a new model of how cell-ECM adhesions regulate the maturation of sarcomere-containing myofibrils (Figure 5-10). We started by examining the architecture of focal adhesions relative to the contractile machinery in hiCMs during *de novo* assembly of myofibrils. Sarcomeres formed on the top (dorsal) surface of the cell (Fenix et al., 2018), while adhesions matured on the bottom (ventral) surface of the cell. In striking resemblance to the architecture of actin stress fibers in non-muscle cells, we found thin, actin-based connections spanning the axial distance between focal adhesions and myofibrils. We showed using laser-mediated cutting that dorsal stress fibers mechanically link both MSFs and myofibrils to focal adhesions. Live imaging of adhesions and actin filaments during myofibrillogenesis revealed that these structures arise and elongate out of focal adhesions as MSFs translocate away from the edge and mature into myofibrils. This results in the long axis of focal adhesions being parallel to the long axis of Z-lines.

In our attempt to modulate adhesion area, our results have implicated a canonical adhesion pathway that is well-characterized in non-muscle cells. We started with the hypothesis that this canonical signaling axis would be conserved in cardiomyocytes. Previous super-resolution studies have elaborated the nanoscale architecture of focal adhesions, revealing layers of focal adhesion components (Kanchanawong et al., 2010). Here we modulate each of these layers and reveal multiple positive correlations between the extent of adhesion and myofibril maturation. We modulated the integrin layer by increasing the concentration of fibronectin, the signaling layer by modulating talin and FAK, the force transduction layer by modulating vinculin and the actin regulatory layer by modulating DIAPH1. Interestingly, these data revealed that the perturbations that led to reduced adhesion area and decreased MSF maturation correlated with an increase in the rate of MSF translocation, while the perturbations that led to increased adhesion resulted in a decrease in the rate of MSF translocation.

Figure 5-10

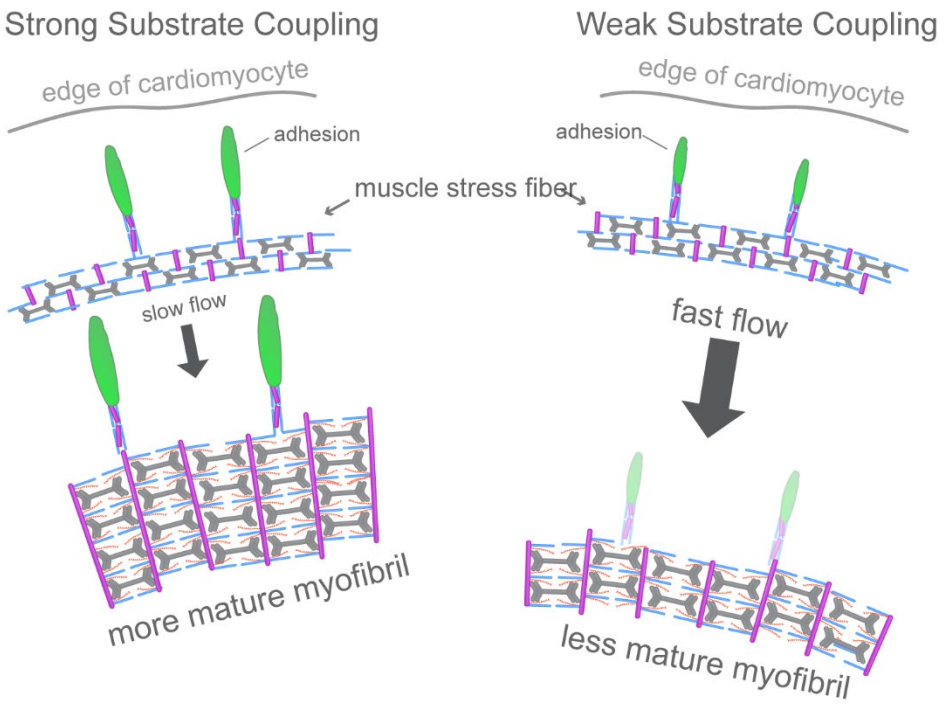

Figure 5-10- Conceptual model for role of substrate adhesion in myofibril maturation

Increasing cell-ECM adhesion results in greater mechanical coupling of muscle stress fibers to the ECM through dorsal stress fibers. This is accompanied by slowing down of muscle stress fibers as they translocate away from the edge. Greater substrate coupling leads to the transition of the muscle stress fiber to a myofibril, possibly by increased mechanical forces. Decreasing cell-ECM adhesion leads to reduced mechanical coupling, accompanied by faster translocation of muscle stress fibers and an inability to mature into force-generating myofibrils.

The inverse relationship between the rate of MSF translocation and the extent of adhesion parallels observations made in migrating cells. In migrating cells, adhesions slow the movement of actin arcs (Alexandrova et al., 2008; Burnette et al., 2011), which are the orthologs of MSFs (Fenix et al., 2018). Actin arcs are physically linked to focal adhesions through dorsal stress fibers (Burnette et al., 2014; Hotulainen and Lappalainen, 2006). DIAPH1 has been shown to be required for dorsal stress fiber assembly in non-muscle cells (Hotulainen and Lappalainen, 2006). Therefore, it was not surprising that knockdown of DIAPH1 led to an increase in the rate of MSF translocation. Dorsal stress fibers are linked to adhesions through vinculin, which has been proposed to act as a “clutch” in non-muscle cells (Thievessen et al., 2013). Indeed, MSF translocation was also accelerated upon vinculin depletion. Talin mechanically links vinculin to integrins. In non-muscle cells, overexpression of the head domain of talin disrupts the ability of endogenous talin to bind integrins, thus effectively losing this mechanical coupling (Tan et al., 2015). In line with the vinculin depletion phenotype, overexpression of the head domain of talin also accelerated MSF translocation.

These multiple correlations between cell-ECM adhesion and MSF translocation, as well as direct mechanical coupling through DSFs, strongly suggest a role for mechanical forces in the maturation of myofibrils. Focal adhesions are ideally suited for allowing an increase in tension since they can both sense and adapt to the magnitude and direction of mechanical forces (Janostiak et al., 2014; Swaminathan et al., 2017). Components such as integrins, talin and vinculin are mechano-sensitive (del Rio et al., 2009; Katsumi et al., 2005; Pasapera et al., 2010); that is, they change their structural conformation upon application of mechanical forces. Furthermore, it was reported that only a small proportion of talin molecules at cell-ECM attachment sites in the *Drosophila* flight muscle experience significant forces, suggesting a large pool of talin is primed for adapting to changes in load (Lemke et al., 2019). Therefore, our data support a model where adhesions could serve as load bearing sites and allow an increase in mechanical tension in MSFs, which would allow their maturation into myofibrils (Figure 10). Indeed, in the flight muscles of *Drosophila*, the establishment of cell-ECM sites with tendons precedes the maturation of stress fibers to myofibrils (Lemke and Schnorrer, 2017).

A bidirectional interplay between myofibrils and cell-ECM adhesion has also been implicated using computational modeling, where it was proposed that myofibrils and stress fibers form along the maximal principal stress direction (Yuan et al., 2017). Interestingly, cell-ECM

adhesion was dominant over the contribution of cell shape to determine the direction of stress; “immature” iPSC derived cardiomyocytes with uniformly arranged smaller adhesions formed radially arranged myofibrils on square micropatterns, while more mature neonatal cardiomyocytes with larger adhesions formed linear substrate attached myofibrils (Yuan et al., 2017). Our data agrees with these theoretical predictions, since trypsinized hiCMs form radially arranged focal adhesions at early time points (6 hours, Figure 5-2, panel B), and thus form radially arranged myofibrils. At later time points (beyond 24 hours), as adhesions grow larger, a symmetry breaking process occurs where these myofibrils linearize and become substrate attached.

A recent study claimed to have delved into the fundamental mechanics of sarcomere assembly, where they propose that myofibrils stream out of “protocostameres” (i.e., focal adhesions) through a “centripetal” assembly mechanism (Chopra et al., 2018). It is important to note again that the authors made these claims about “*de novo”* sarcomere assembly during a time window when sarcomeres are already assembled. The apparent appearance of myofibrils perpendicular to focal adhesions was interesting, and different than the parallel arrangement we find during sarcomere assembly. This is an effect of imaging the ventral plane of the cell and capturing the pre-formed myofibrils falling down from the dorsal surface; a phenomenon observed routinely in non-muscle cells (Hotulainen and Lappalainen, 2006; Tojkander et al., 2015). In non-muscle cells, actin arcs on the dorsal surface fuse with at least two dorsal stress fibers as they move to the ventral surface and convert to a ventral stress fiber with an adhesion at both ends (Hotulainen and Lappalainen, 2006; Tojkander et al., 2015). The data from (Chopra et al., 2018) appears to support such a mechanism of creating ventrally attached myofibrils, and may be a manifestation of the symmetry breaking that occurs at later stages of hiCM spreading. We speculate DSFs are key structures that may relay the direction of principal stress from adhesions to MSFs or myofibrils.

Furthermore, (Chopra et al., 2018) reported that knockout of β-myosin II led to a decrease in sarcomere content. This led the authors to propose that a force balance between β-myosin II, but not other myosin II paralogs, and focal adhesions directs the centripetal assembly of sarcomeres. Interestingly, subsequent studies have called into question the relative roles of the myosin II paralogs during sarcomere formation (Fenix et al., 2018; Yang et al., 2018). Another lab has also generated β-myosin II knockout hiCMs, and sarcomere formation in these cells still occurs (Yang et al., 2018). This calls into question the requirement for β-myosin II in

sarcomere formation. Furthermore, we have recently shown that knockdown of “non-muscle” myosin IIs does lead to attenuation of sarcomere formation (Fenix et al., 2018). These requirements are also mirrored in Drosophila flight muscles, where non-muscle myosin II-mediated tension, but not muscle myosin II, was required for the increased ordering in actin filaments (Loison et al., 2018).

It is important to note that our data suggests that centripetal assembly does, in part, contribute to myofibril formation. Centripetal assembly is likely to be the mechanism of nucleating the connections between myofibrils and focal adhesions (i.e., dorsal stress fibers). The concept of centripetal assembly was first proposed in 1984 in non-muscle cells, where stress fibers arise at the edge and elongate in a “centripetal” manner towards the middle of the cell (Wang, 1984). Subsequent studies established this mode of assembly to be driving dorsal stress fiber formation, but not the assembly of actin arcs (Hotulainen and Lappalainen, 2006). This concept of centripetal assembly was applied to myofibril formation as early as 1990, where vinculin “plaques” at the edge were proposed to give rise to the precursors of myofibrils (Lu et al., 1992). Our data argues while myofibrils do not directly arise from adhesions through centripetal assembly, dorsal stress fibers that link myofibrils to adhesions are likely to arise due to centripetal assembly. In support of this idea, disruption of β1 integrin in skeletal muscle *in vitro* led to the absence of mature myofibrils, but not MSF-like structures (Schwander et al., 2003).

Cell-cell adhesion is another source of balancing forces generated by myofibrils (Liu et al., 2016). However, cell-cell adhesion is still unknown to play a significant role in *de novo* myofibril assembly. It has been demonstrated previously that cell-ECM adhesion sites are responsible for the majority of traction force generation during early cardiomyocyte spreading; as the cell continues to spread and makes cell-cell contacts, load-bearing sites are transferred to cell-cell contact sites (McCain et al., 2012). As such, it is interesting to note that focal adhesion proteins such as FAK and vinculin also localize to intercalated discs once they form (Koteliansky and Gneushev, 1983; Yi et al., 2003). Indeed, a recent study found that vinculin localizes to cell-cell-adhesion sites under increased load in zebrafish hearts *in vivo,* driving the thickening of myofibrils (Fukuda et al., 2019). Determining the mechanisms driving the localization of such proteins to sites of increased load should be the focus of future studies.

Finally, we show a similar actin architecture in spreading hiCMs, namely a force generating contractile stress fiber (i.e., muscle stress fibers and myofibrils) connected to a load bearing

structure (i.e., focal adhesion) via a non-contractile stress fiber (i.e. dorsal stress fiber), that is commonly observed in mesenchymal cells. It is interesting to note while this architecture is conserved, there are minor differences in the regulatory mechanisms between the formation of muscle stress fibers and actin arcs (Fenix et al., 2018). We speculate that this may allow a mesodermal progenitor cell to modify the same mechanical system to perform two distinct functions, cell migration in the case of mesenchymal lineages, and sarcomere assembly in the case of cardiac lineages.

Materials and methods

Cell culture

Human iPSC-derived cardiomyocytes (CMM-100-012-000.5, Cellular Dynamics, Madison, WI) were cultured as per manufacturer's instructions in proprietary manufacturer provided cardiomyocyte maintenance medium in polystyrene 96-well cell culture plates.

Cells were maintained at 37°C and 5% CO_2. For re-plating hiCMs onto glass substrates, cells were washed 2 times with 100 µL 1x PBS with no Ca^{2+}/Mg^{2+} (PBS*, 70011044, Gibco, Grand Island, NY). PBS* was completely removed from hiCMs and 40 µL 0.1% Trypsin-EDTA with no phenol red (15400054, Gibco, Grand Island, NY) was added to hiCMs and incubated at 37°C for 2 minutes. Following incubation, the cells were washed 3 times with trypsin, the plate rotated 180 degrees, and washed another 3 times. Trypsinization was then quenched by adding 160 µL of culture media and total cell mixture was pipetted into a 1.5 mL Eppendorf tube. Cells were centrifuged at 200xg for 5 minutes, and the supernatant was aspirated. The cell pellet was re-suspended in 200 µL of culture media and plated on 35 mm dishes with a 10 mm glass bottom (D35-10-1.5-N; CellVis, Sunnydale, CA) pre-coated with 10 µg/mL fibronectin (354008, Corning) for 1 hr at 37°C.

Chemicals

FAK inhibitor PF-228 (PZ0117) was purchased from Sigma. Alexa Fluor 488-phalloidin (A12379), Alexa Fluor 568-phalloidin (A12380), Alexa Fluor 488-goat anti-mouse (A11029), Alexa Fluor 488-goat anti-rabbit (A11034), Alexa Fluor 568-goat-anti-rabbit (A11011), and Alexa Fluor 568-goat anti-mouse (A11004) antibodies were purchased from Life Technologies (Grand Island, NY).

Mouse anti-Paxillin (1:200, 610051) and mouse anti-FAK (1:500, 610088) antibodies were purchased from BD Biosciences. Rabbit anti-FAK pY357 (1:200, ab81298) was purchased from Abcam. Mouse anti-α-actinin 2 (1:200, A7811) was purchased from Sigma Aldrich. Titin (9D10) antibody was purchased from the Developmental Studies Hybridoma Bank (University of Iowa). Primary antibody conjugation was performed using Mix-n-Stain kits (92233) purchased from Biotium (Fremont, CA) according to the instructions provided by the manufacturer. Paraformaldehyde (15710) was purchased from Electron Microscopy Sciences

(Hatfield, PA). Triton X-100 (BP151100) was purchased from Fischer Scientific (Suwanee, GA).

Fixation and immunostaining

Cells were fixed with 4% paraformaldehyde (PFA) in PBS at room temperature for 20 min and then permeabilized for 5 min with 1% Triton X-100/4% PFA in PBS as previously described (Burnette et al., 2014). For actin visualization, phalloidin 488 or 568 in 1× PBS (15 µl of stock phalloidin per 200 µl of PBS) was used for 2 hours at room temperature. For immunofluorescence experiments, cells were blocked in 10% bovine serum albumin (BSA) in PBS for 20 min, followed by antibody incubations.

For visualizing titin, a live cell extraction was performed to remove cytoplasmic background as described previously (Burnette et al, 2011). Briefly, a cytoskeleton-stabilizing live-cell extraction buffer was made fresh containing 2 ml of stock solution (500 mM 1,4-piperazinediethanesulfonic acid, 25 mM ethylene glycol tetra acetic acid, 25 mM $MgCl_2$), 4 ml of 10% polyoxyethylene glycol (PEG; 35,000 molecular weight), 4 ml H2O, and 100 µl of Triton X-100, 10 µM paclitaxel, and 10 µM phalloidin. Cells were treated with this extraction buffer for 1 min, followed by a 1-min wash with wash buffer (extraction buffer without PEG or Triton X-100). Cells were then fixed with 4% PFA for 20 min, followed by antibody labeling. VectaShield with DAPI (H-1200, Vector Laboratories Inc., Burlingame, CA) was used for mounting.

Protein Expression

For protein expression in hiCMs, 200 ng plasmid and 0.4 µl ViaFect (E4981, Promega, Madison WI) were added to a total of 10 µl of Opti-MEM (ThermoFisher, Waltham, MA) and added to a single well of hiCMs in a 96 well plate. The transfection was incubated overnight (~16 hrs) prior to plating for imaging.

Plasmids

All plasmids used in this study are available from Addgene (Cambridge, MA). mCherry-Alpha-Actinin-2-N-18 was a gift from Michael Davidson (Addgene plasmid # 54974). mApple-Lifeact-7 was a gift from Michael Davidson (Addgene plasmid # 54747). mEmerald-Lifeact-7 was a gift from Michael Davidson (Addgene plasmid # 54148). mCherry-Paxillin-22 was a gift from Michael Davidson (Addgene plasmid # 55114) (Paszek et al., 2012). EGFP-Talin-H-18 was a

gift from Michael Davidson (Addgene plasmid # 56448). EGFP-Talin-CW-18 was a gift from Michael Davidson (Addgene plasmid # 56446).

Knockdown experiments

Knockdowns for FAK (PTK2), DIAPH1 and VCL were performed using Accell SmartPool siRNA (PTK2: E-003164-00-0005; DIAPH1: E-010347-00-0005; VCL: E-009288-00-0005; scrambled control: D-001910-10-05) purchased from GE Dharmacon. Experiments were performed in 96-well culture plates, using the TransIT-TKO transfection reagent using instructions provided by the manufacturer (MIR2154, Mirus Bio). Single siRNA-mediated knockdown experiments were performed using PTK2: A-003164-21-0005; DIAPH1: A-010347-14-0005; VCL: A-009288-13-0005; and scrambled control: D-001910-10-05 purchased from GE Dharmacon. Three consecutive rounds of knockdown were performed to deplete protein levels. Following knockdown, cells were re-plated onto glass substrates for 24 hours and fixed for immunofluorescence or lysed for western blotting.

Western Blotting

Gel samples were prepared by mixing cell lysates with LDS sample buffer (Life Technologies, NP0007) and Sample Reducing Buffer (Life Technologies, NP0009) and boiled at 95°C for 5 minutes. Samples were resolved on Bolt 4-12% gradient Bis-Tris gels (Life Technologies, NW04120BOX). Protein bands were blotted onto a nylon membrane (Millipore). Blots were blocked using 5% nonfat dry milk (Research Products International Corp, Mt. Prospect, IL, M17200) in TBST. Antibody incubations were also performed in 5% NFDM in TBST. Blots were developed using the Immobilon Chemiluminescence Kit (Millipore, WBKLS0500).

Structured Illumination Microscopy

SIM imaging and processing was performed using a GE Healthcare DeltaVision OMX equipped with a 60×1.42 NA Oil objective and sCMOS camera or using a Nikon N-SIM equipped with a 100X 1.49 NA Oil objective and EMCCD camera.

Fluorescence, live-cell microscopy, and focused laser mediated cutting

High-resolution wide-field fluorescence images (for Z-line measurement) and live imaging of actin filaments (to measure MSF translocation rates) were acquired on a Nikon Eclipse Ti equipped with a Nikon 100× Plan Apo 1.45 numerical aperture (NA) oil objective and a Nikon DS-Qi2 CMOS camera. Live imaging for Figure 5-2 and focused laser mediated cutting for

Figure 5-1 was performed on a Nikon Spinning Disk confocal microscope equipped with a 60X 1.4 NA objective and an Andor iXON Ultra EMCCD camera, provided by the Nikon Center of Excellence, Vanderbilt University. Cutting of dorsal stress fibers was performed using a 100 mW UV laser (Coherent technologies) at 75% power, using a dwell time of 500 µs for a total period of 1 second. TIRF imaging was performed using a Nikon TiE inverted light microscope equipped with a 100x/1.49 NA TIRF objective, and an Andor Neo sCMOS camera. was Cells were maintained at 37°C with 5% CO2 using a Tokai Hit stage incubator.

Quantification and statistical analysis

To measure Z-line length in hiCMs, Z-sections were acquired at 200 nm intervals using widefield imaging at 100X with 1.5 Zoom. Images were deconvolved with the Automatic deconvolution using Nikon Elements software. All α-actinin 2 structures were 3D thresholded manually in Nikon Elements using the clean algorithm 3 times. The lengths of the major axis of each body were exported from Elements for the calculation of Z-line length. Using a length minimum exclusion criterion of 0.2 µm, Z-line lengths were calculated using MATLAB (supplementary software).

To measure sum adhesion area of hiCMs, one single Z-slice of a reconstructed SIM image where the focal adhesions were in focus was selected. Focal adhesions were thresholded and the sum area was measured in Fiji, using a size minimum exclusion criterion of 0.1 μm^2.

For measurement of the distance of titin to the edge (Figure 5-3), we measured the length of a line from the edge to the first titin ring in Fiji. The researcher analyzing the data was blinded to treatment groups.

For measurement of MSF translocation rates, hiCMs were transfected with Lifeact-mApple and allow to spread for 16 hours post plating. Two Z-sections were acquired, one at the ventral plane and one 0.5 µm above the ventral plane, at 2-minute intervals for a total time of 2 hours. Maximum Z-projections were performed on the time montages, followed by alignment of the image stacks using the StackReg plugin in Fiji. A 3-pixel thick line was drawn parallel to the direction of MSF translocation to create a kymograph, following which the rates were measured for MSFs. 1-3 trajectories were counted for each cell.

Statistical significance was determined using unpaired two-tailed Student's t-tests performed in MATLAB or Excel. Each experiment was performed a minimum of 3 times and each cell was counted as a data point and was pooled over the biological replicates. All data was displayed

as Tukey plots, which were represented with boxes (with Q1, median, Q3 percentiles), whiskers (minimum and maximum values within 1.5 times interquartile range) and outliers (solid circles). No outliers were removed from the analysis. For western blot graphs, error bars represent standard error of the means.

Key Resources

REAGENT or RESOURCE	SOURCE	IDENTIFIER
Antibodies		
Mouse monoclonal anti-alpha actinin 2 (Clone EA-53)	Sigma	A7811
Mouse monoclonal anti-paxillin	BD Biosciences	610051
Rabbit polyclonal anti- DIAPH1	Bethyl Laboratories	A300-078A
Mouse monoclonal anti-FAK	BD Biosciences	610088
Rabbit monoclonal anti-pFAK Y397	Abcam	Ab81298
Mouse monoclonal anti-Titin (9 D10)	DHSB	9D10
Goat anti-mouse 488	LifeTechnologies	A11001
Goat anti-rabbit 488	LifeTechnologies	A11034
Goat anti-mouse 568	LifeTechnologies	A11004
Goat anti-rabbit 568	LifeTechnologies	A11036
Bacterial and Virus Strains		
Biological Samples		
Bovine Serum Albumin	RPI	A30075-100.0
Chemicals, Peptides, and Recombinant Proteins		
Phalloidin Alexa Fluor 488	Life Technologies	A12379
Phalloidin Alexa Fluor 568	Life Technologies	A12380
FAK inhibitor PF-573228	Sigma	PZ0117
PBS, 10X, Ca^{2+}/Mg^{2+} free	Gibco	70011-044

Paraformaldehyde, 16%	Electron Microscopy Sciences	15710
PBS, 10X, with Ca^{2+}/Mg^{2+}	Corning	46-013-CM
0.5% Trypsin	Gibco	15400-054
0.1% Gelatin	Sigma	ES-006-B
Dimethyl Sulfoxide	Sigma	276855
Vectashield with DAPI	Vector	H-1200
Triton X-100	Fisher Scientific	BP151100
Critical Commercial Assays		
Mix-N-Stain Antibody Labeling kit	Biotium	92233
Deposited Data		
Experimental Models: Cell Lines		
iCell cardiomyocytes^2 kit	Cell Dynamics International	CMC-100-012-000.5
Experimental Models: Organisms/Strains		
Oligonucleotides		
SMART Pool siRNA against human FAK 5’-AAACGUCGAAAAUUGAUUG-3’,5’-AAACGUCGAAAAUUGAUUG-3’, 5’-CAGCAUUUCGUCAUAAGGC-3’, 5’-AGACAACCCAACUUCAAAG-3’	Horizon Discovery	E-003164-00-0005
SMART Pool siRNA against human DIAPH1 5’- CUGUCUUUGAAUCCAACAC-3’, 5’-CACUAAUAAUAAAUAACCA-3’, 5’-UGAUAUUGAAGCCAAAAGC-3’, 5’-AAGUCAUCCAUCUCCAUGC-3’	Horizon Discovery	E-010347-00-0005

SMART Pool siRNA against human VCL 5'-UUCGAAUUUUGAUUGAAGC-3', 5'-CAACCUUAAUAAAUGCUGG-3', 5'-AGUCUAUGGAGGCCAAUGC-3', 5'-ACAAAUCCUAGCUUAUAAA-3'	Horizon Discovery	E-009288-00-0005
Recombinant DNA		
mApple-Lifeact	Addgene	54747
mEmerald-Lifeact	Addgene	54148
mCherry-Paxillin	Addgene	55114
mCherry-Alpha-actinin-2	Addgene	54974
Talin Head-mEGFP	Addgene	56448
Talin-mEGFP	Addgene	56446
Software and Algorithms		
MATLAB code to analyze Z-line length and adhesion area	This study	
Fiji (Fiji Is Just ImageJ)	NIH	
Nikon Elements	Nikon	
Other		

Acknowledgements

We thank the Nikon Center of Excellence, Vanderbilt University, for providing access to the Nikon spinning-disk microscope and technical support. We thank Matthew Tyska for providing access to his TIRF microscope. The raw data generated in the current study are available from the corresponding author upon reasonable request. This work was funded by a Maximizing Investigators' Research Award (MIRA) from the National Institute of General Medical Sciences (R35 GM125028) awarded to D.T.B., an American Heart Association Predoctoral Fellowship (18PRE33960551) to N.T. and Vanderbilt University School of Medicine Program in Developmental Biology training grant T32-HD007502 to A.C.N.

Supplementary Figures

Figure 5-S1

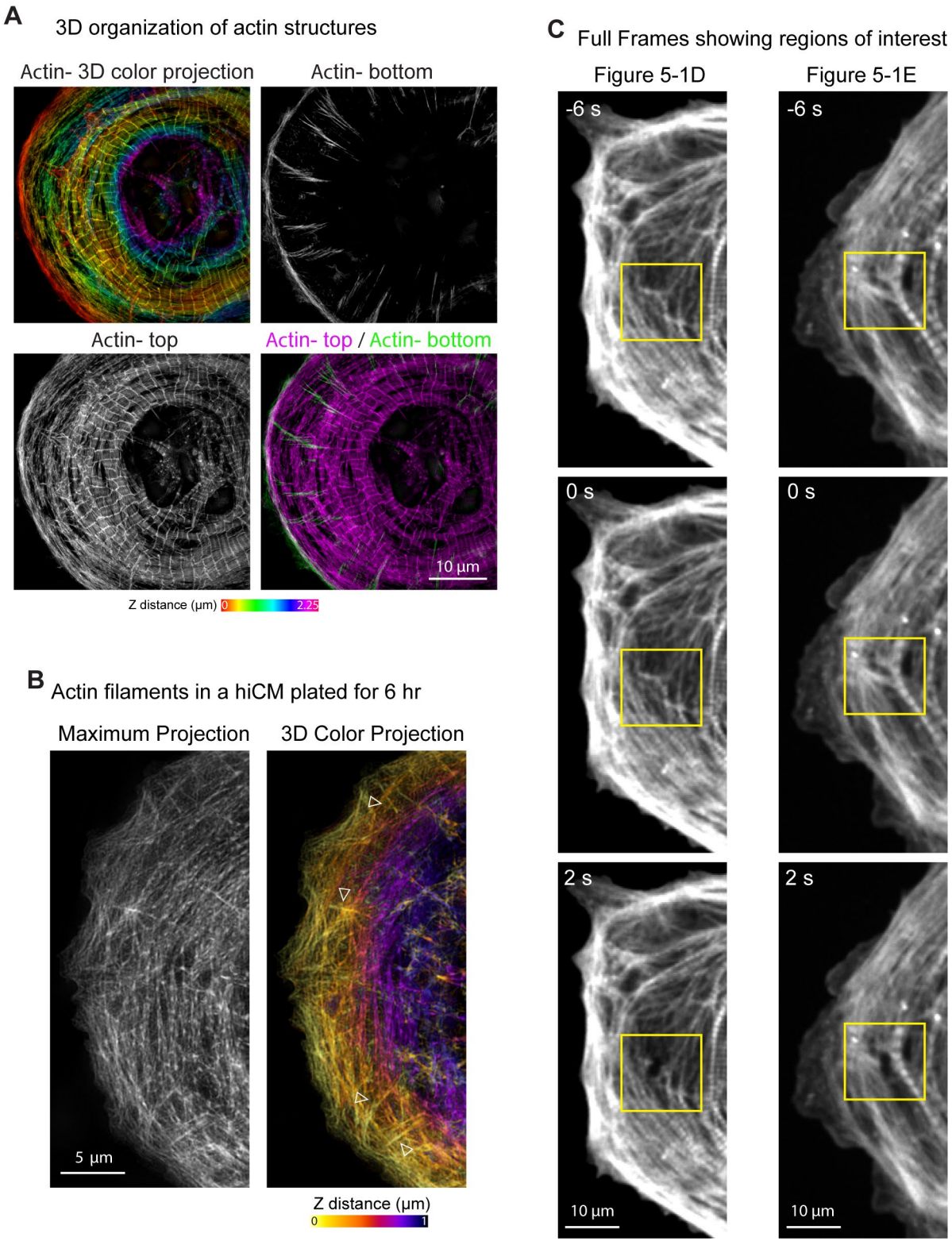

Figure 5-S1- 3D organization of actin structures using SIM

A) Different views of the SIM micrograph in Figure 5-1. Top left: Color-coded Z-projection of actin filaments as performed for Fig. 1C in Fenix et al, 2018. Total Z-depth used was 2.25 μm. Top right: “bottom” optical section showing the actin filaments associated with adhesions. Bottom left: Maximum project of Z sections excluding the bottom section. This “top” view is comprised of mostly dorsal actin filament structures. Bottom right: Overlay of “top” section (magenta) with “bottom” section (green) showing actin filament populations in myofibrils and adhesions, respectively. B) SIM of actin filaments in hiCM plated for 6 hours. Layers of actin filaments in the axial dimension are displayed using a color-coded Z-projection. Arrowheads show different dorsal stress fibers. B) Uncropped view showing region of interest used in Figure 5-1D and 5-1E.

Figure 5-S2

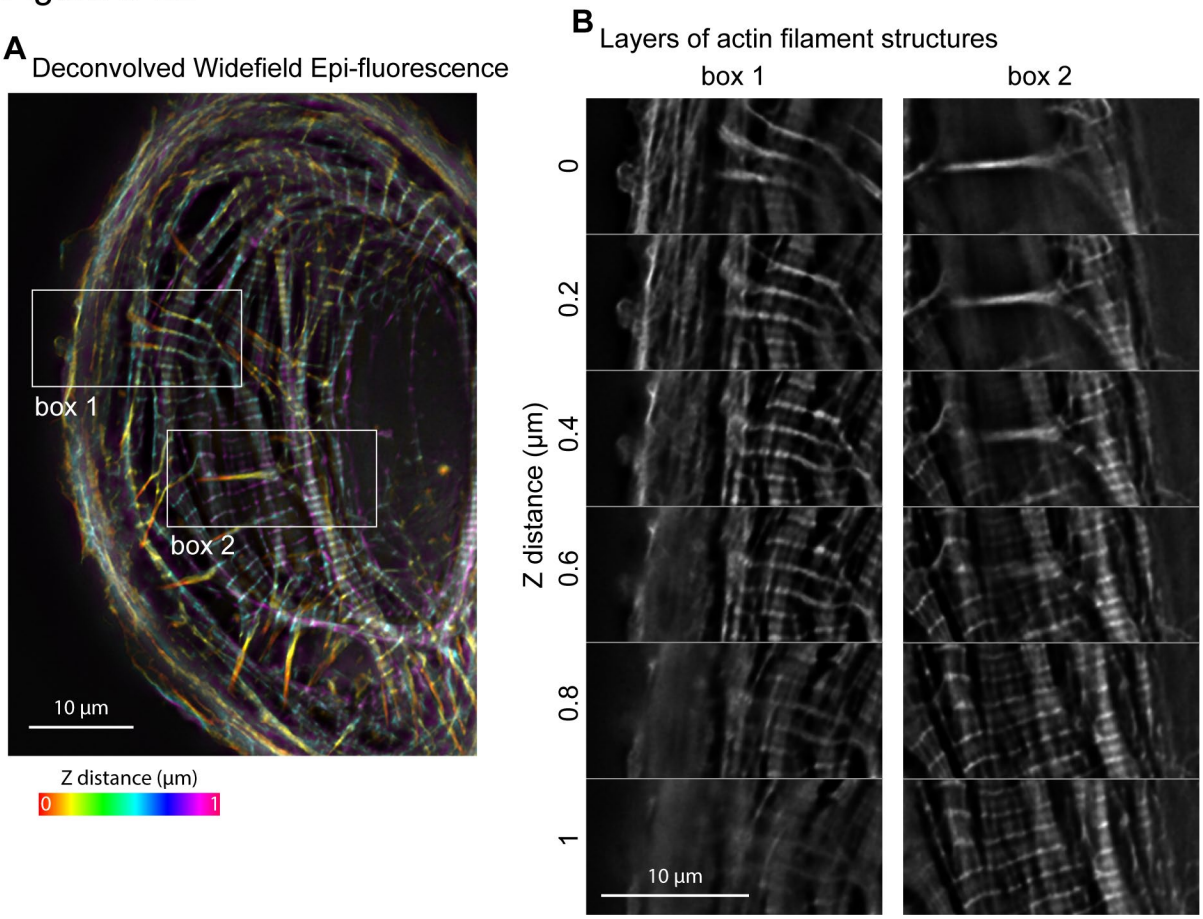

Figure 5-S2- Deconvolution widefield microscopy of actin filaments in hiCMs

A) Color-coded Z-projection of actin filaments in hiCM spread for 24 hours, acquired using a widefield microscope at 150X magnification and using 0.2 µm Z-steps. The image was deconvolved using Nikon Elements software. B) Montages of ROIs depicted by box1 and box2 in (A). Each montage shows individual Z-sections depicting similar layering of actin filaments as shown by SIM in Figure 5-1.

Figure 5-S3

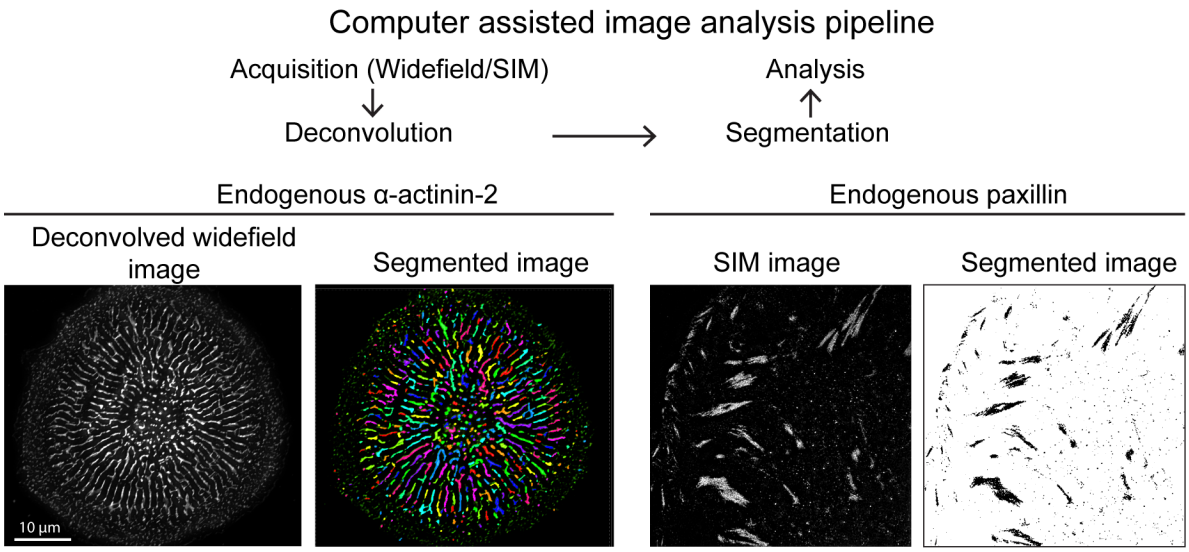

Figure 5-S3- Computer assisted image analysis pipeline

For measurement of α-actinin-2 Z-line lengths, widefield fluorescence image stacks (gray) were deconvolved and segmented using Nikon Elements Software (colorized binary file). The long axis lengths of Z-bodies/lines were exported to MATLAB and data was filtered and processed to generate a mean Z-line measurement for each cell. For paxillin quantification, SIM micrographs were used for thresholding in FIJI. Filtering and further analysis was performed in MATLAB.

Figure 5-S4

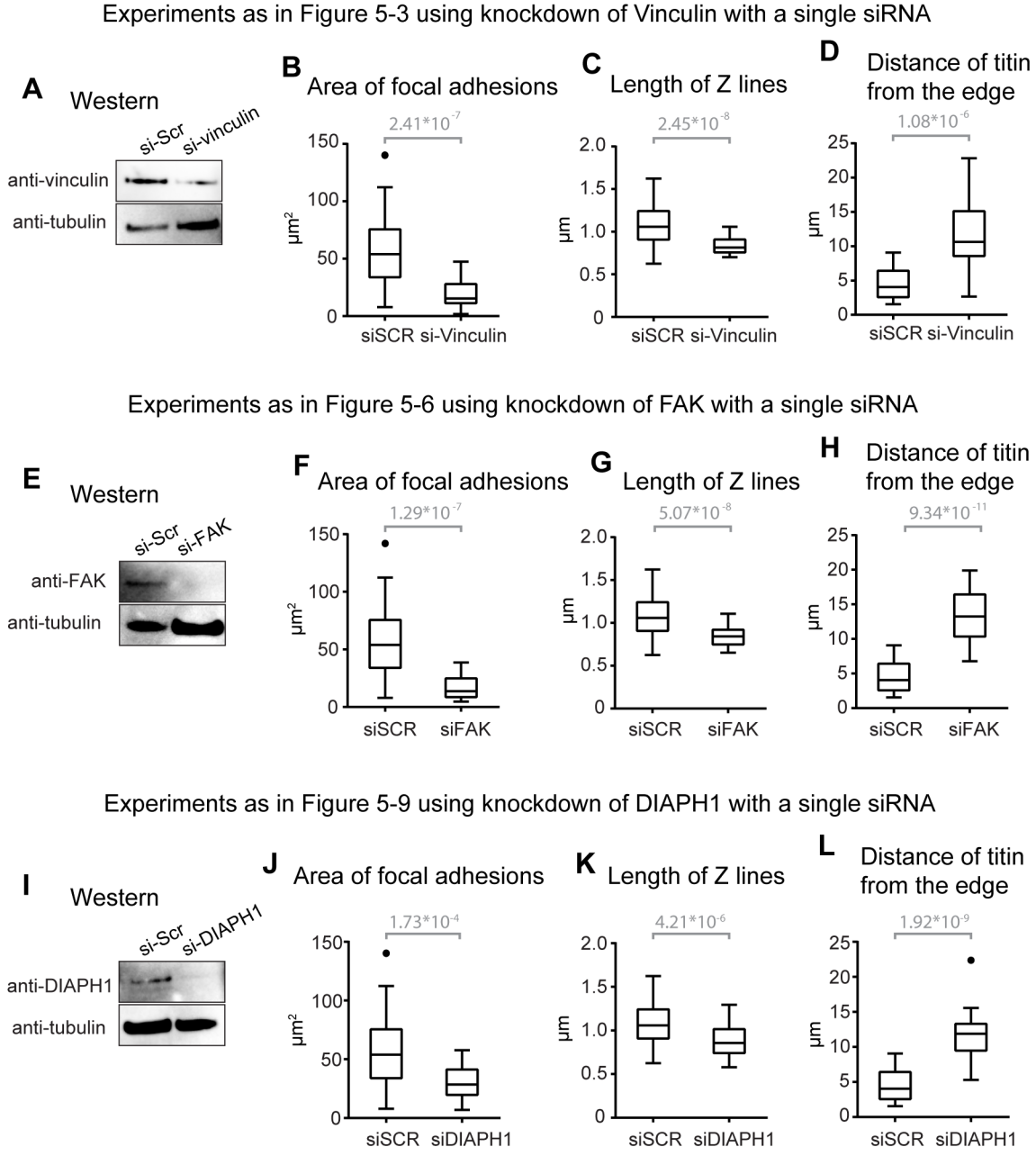

Figure 5-S4- Effects of knockdown using single siRNAs

A) Western blot for Vinculin knockdown using a single siRNA. Tubulin was used as a loading control. B) Quantification of adhesion area in Vinculin-depleted cells. si-Vinculin: n= 20 cells, N= 3 independent experiments. The si-Scr dataset is the same as Fig. 5-3, panel D. C) Quantification of average length of Z-lines in Vinculin-depleted cells. si-Vinculin: n= 30 cells, N= 3 independent experiments. The si-Scr dataset is the same as Fig. 5-3, panel E. D) Quantification of distance of titin localization from the cell edge. si-Vinculin: n= 21 cells, N= 3 independent experiments. The si-Scr dataset is the same as Fig. 5-3, panel F. E) Western blot for FAK knockdown using a single siRNA. Tubulin was used as a loading

control. F) Quantification of adhesion area in FAK-depleted cells. si-FAK: n= 20 cells, N= 3 independent experiments. The si-Scr dataset is the same as Fig. 5-3, panel D. G) Quantification of average length of Z-lines in FAK-depleted cells. si-FAK: n=31 cells, N= 3 independent experiments. The si-Scr dataset is the same as Fig. 5-3, panel E. H) Quantification of distance of titin localization from the cell edge. si-FAK: n= 21 cells, N= 3 independent experiments. The si-Scr dataset is the same as Fig. 5-3, panel F. I) Western blot for DIAPH1 knockdown using a single siRNA. Tubulin was used as a loading control. J) Quantification of adhesion area in DIAPH1-depleted cells. si-DIAPH1: n= 20 cells, N= 3 independent experiments. The si-Scr dataset is the same as Fig. 5-3, panel D. K) Quantification of average length of Z-lines in DIAPH1-depleted cells. si-DIAPH1: n= 30 cells, N= 3 independent experiments. The si-Scr dataset is the same as Fig. 5-3, panel E. L) Quantification of distance of titin localization from the cell edge. si-DIAPH1: n= 21 cells, N= 3 independent experiments. The si-Scr dataset is the same as Fig. 5-3, panel F.

Figure 5-S5

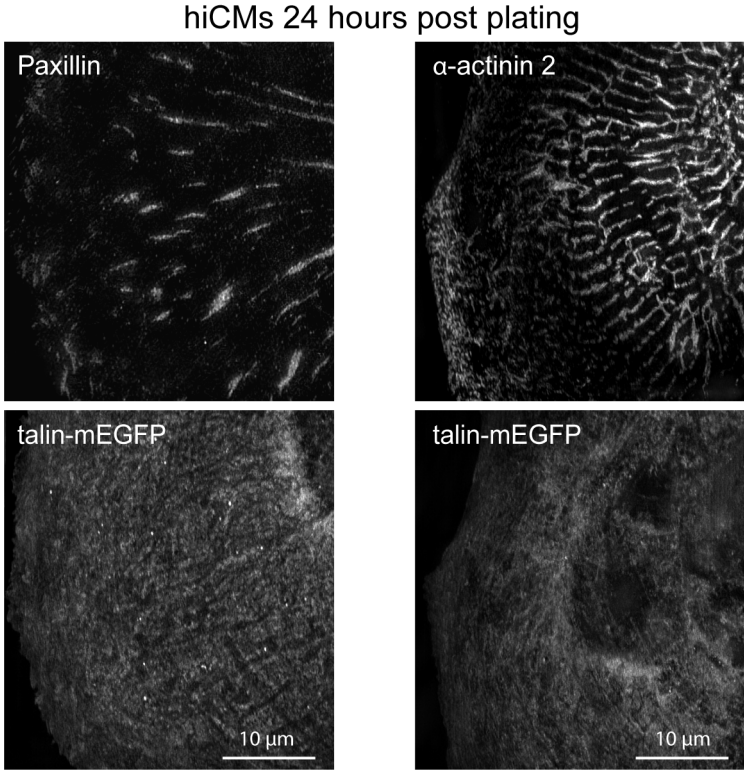

Figure 5-S5- Full length talin expression in hiCMs

Paxllin (top left panel) and α-actinin 2 (top right panel) in hiCMs that are expressing talin-mEGFP (bottom panels).

Figure 5-S6

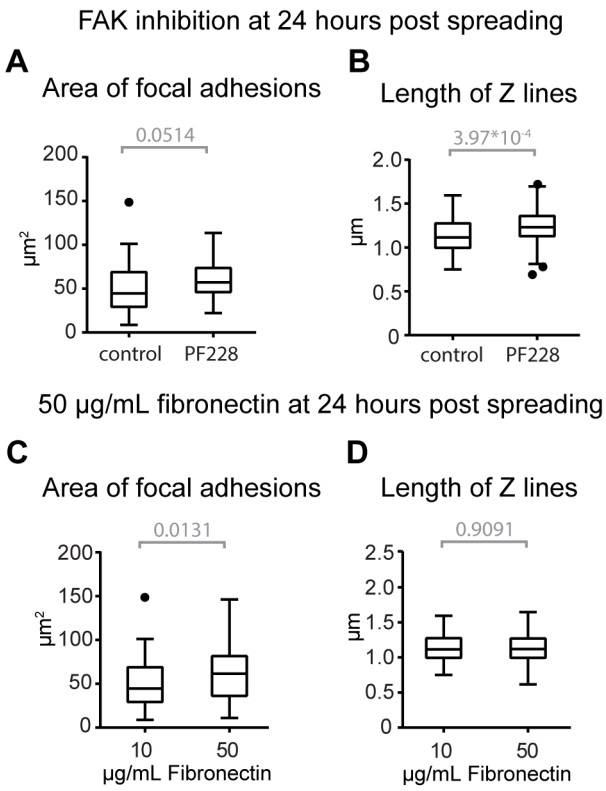

Figure 5-11- Effects of FAK inhibition and increased FN concentration on Z-lines and adhesions

Tukey plots of Z-line lengths and adhesion area upon FAK inhibition (A-B) and increasing fibronectin concentration (C-D) in hiCMs spread for 24 hours. Z-lines: Control: n= 75 cells, N= 3 independent experiments; PF-228: n= 128 cells, N= 4 independent experiments; 50 µg/mL fibronectin: n= 204 cells, N= 6 independent experiments. Adhesions: Control: n= 48 cells, N= 5 independent experiments; PF-228: n= 39 cells, N= 4 independent experiments; 50 µg/mL fibronectin: n= 59 cells, N= 6 independent experiments. Exact p-values stated over graphs.

Chapter 6- The role of FAK signaling in myofibril mechanics

Taneja, N., Bersi, M.R., Rasmussen, M.L., Gama, V., Merryman, W.D., Burnette, D.T.

2020. *Cytoskeleton* (in press)

Introduction

The functional unit of contraction within striated muscle is the myofibril, which is comprised of sarcomeres arranged in series. Sarcomeres are complex protein assemblies, the core of which comprises “thick” muscle myosin-II filaments interacting with “thin” actin filaments. The barbed ends of actin filaments from adjacent sarcomeres are cross-linked by α-actinin-2 to form the sarcomere borders known as Z-discs (Knoll et al., 2011). Interactions between the multiple components within sarcomeres ultimately determine their mechanical properties. For example, the giant protein titin spans half the length of the sarcomere, with its N-terminal domain binding the Z-disc and its C-terminal domain extending to the M-line (Maruyama, 1997). The complete list of factors controlling the mechanical properties of myofibrils continues to be elucidated.

Titin has long been established as a major contributor to the myofibrillar mechanical properties required for proper heart function. The PEVK domain of titin behaves like a molecular spring, generating passive tension within the myocardium against stretch, as experienced in the heart during peak diastole (Granzier and Irving, 1995; Granzier and Labeit, 2004). Furthermore, interactions between actin and the titin PEVK domain lead to viscous damping of myofibrils by impeding actin filament sliding (Kulke et al., 2001; Linke and Fernandez, 2002). At longer length scales, viscous damping in the myocardium is thought to be provided by collagen fibrils in the extracellular matrix (ECM) (Granzier and Irving, 1995). Previous studies have demonstrated that faster shortening of myofibrils has a higher energetic cost (Gibbs and Chapman, 1985; He et al., 2000). Thus, viscous damping reduces this energetic cost of contraction and contributes to an overall increased efficiency of energy consumption in the heart (Caporizzo et al., 2018).

Cardiomyocytes interact with the ECM at specialized sites called costameres, which anchor the Z-lines closest to the cell membrane to the extracellular matrix (Samarel, 2005). We have previously established a role for cell-ECM adhesion in myofibril assembly, using human iPSC-derived cardiomyocytes (hiCMs) as a model system (Taneja et al., 2020b). Cell-ECM sites

transmit mechanical forces from immature myofibrils (muscle stress fibers) to the substrate, promoting their maturation.

Focal adhesion kinase (FAK) is a key regulatory protein present at cell-ECM sites which regulates adhesion formation and turnover (Parsons et al., 2000). A role for FAK in contributing to heart mechanics has also been well established *in vivo*. Cardiac specific knockout of FAK results in an ability to respond to increased load in the heart (DiMichele et al., 2006; Peng et al., 2006). On a mechanistic level, FAK performs both scaffolding and signaling functions (Sulzmaier et al., 2014). FAK phosphorylates a variety of targets, including itself at Tyr397, which is required for adhesion disassembly (Sulzmaier et al., 2014). Inhibition of this auto-phosphorylation using the inhibitor PF-228 results in stabilization of focal adhesions (Slack-Davis et al., 2007; Taneja et al., 2016). Treatment of hiCMs with PF-228 results in stabilization of focal adhesions, longer Z-line lengths and increased incorporation of titin (Taneja et al., 2020b). However, the effect of stabilization of adhesions by FAK on the mechanical properties of myofibrils remains unknown.

In non-muscle cells, FAK regulates actin cytoskeleton stability and cell stiffness (Fabry et al., 2011; Mierke et al., 2017). Stress fibers that are attached on either end to the ECM have higher tension compared to those that are not directly coupled to the ECM (Lee et al., 2018). Given the role of FAK in regulating cellular mechanics, and its role in load adaptation in the heart, here we specifically investigate its role in modulating the mechanical properties of myofibrils at the cellular level. Using laser-assisted dissection of myofibrils, we show that inhibition of FAK results in increased myofibril viscosity. We further show that these changes in mechanics are not mediated by changes in electrophysiology.

Results and Discussion

Laser ablation is a widely used biophysical tool to assay the mechanical properties of cytoskeletal systems, such as stress fibers, epithelial cell-cell junctions and myofibrils (Fernandez-Gonzalez et al., 2009; Lee et al., 2018; Taneja et al., 2020b). We have previously used this technique to interrogate cortex mechanics during cell division, as well as testing mechanical coupling between cell-ECM adhesions and myofibrils (Taneja et al., 2020a; Taneja et al., 2020b). Myofibrils are considered complex mechanical systems. Conceptually, they can be thought of as a series of springs and dashpots (sarcomeres), which lend both elasticity and viscosity to the mechanical response, respectively. We used an existing mechanical framework to estimate these properties using the dynamics of myofibril retraction following laser-assisted dissection (Lee et al., 2018).

We have previously described the dynamics of myofibril assembly using hiCMs as a model system (Fenix et al., 2018). hiCMs are transcriptionally similar to neonatal or embryonic cardiac myocytes (DeLaughter et al., 2016; Kuppusamy et al., 2015). As such, they lose their myofibrils upon trypsinization, and re-form them within 24 hours after plating (Fenix et al., 2018). We plated hiCMs on glass coverslips coated with fibronectin and allowed them to spread overnight. We then performed laser-assisted dissection of pre-formed myofibrils (Figure 6-1). Similar to the response of stress fibers, the newly created ends of the myofibrils retracted away from each other, reaching a steady-state separation over ~60 seconds. Kymographs were used to track the retraction profile of each end (Figure 6-1). Note, the hiCMs continued to beat during the duration of myofibril retraction (see horizontal lines in kymograph, Figure 6-1, panel B). Using a custom MATLAB script based on edge detection, we segmented the retracting ends of the myofibril and fitted the trajectories to a standard Kevin-Vogt viscoelastic solid framework widely used for stress fibers and cell-cell junctions in non-muscle cells (Fernandez-Gonzalez et al., 2009; Kumar et al., 2006; Lee et al., 2018).

Figure 6-1

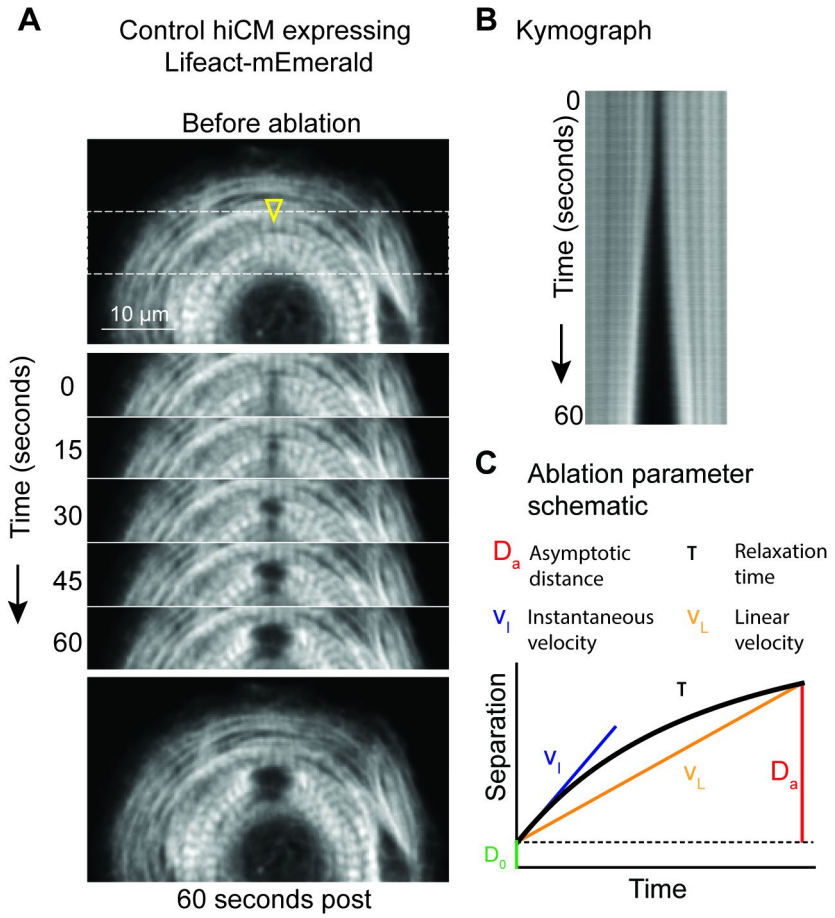

Figure 6-1- Laser-assisted dissection to assess mechanical properties of myofibrils

A) Representative control hiCM at 16 hours post re-plating. Yellow arrowhead shows ablation site. Dotted white rectangle was used to create montage of myofibril retraction over 60 seconds. B) Kymograph showing retraction profile of myofibril shown in (A). C) Schematic showing different parameters obtained from analysis of the kymographs using custom code in MATLAB.

We obtained estimates for both linear velocity (v_L) and instantaneous velocity (v_I), which are related to the release of myofibril tension (Figure 6-1). Faster retraction velocity is indicative of higher myofibril tension. The asymptotic distance (D_a) is the maximal distance between the two retracting ends as they reach a steady-state separation. As a proof-of-concept, we turned to investigating the effect of the inhibition of actomyosin contractility by blebbistatin on the mechanical properties of myofibrils. Actomyosin contractility is known to be the primary driver of active tension generation in both muscle and non-muscle systems (Gordon et al., 2000; Murrell et al., 2015).

We expressed Lifeact-mApple (actin filament marker) in hiCMs and allowed them to spread overnight prior to treatment with the myosin II ATPase inhibitor blebbistatin (Straight et al., 2003). We noted that myofibril contraction was immediately attenuated upon addition of blebbistatin, as previously demonstrated (Fedorov et al., 2007). Furthermore, we found that 66.7% of cells contained at least one myofibril that adopted a bent or buckled shape upon blebbistatin treatment (Figure 6-2). Laser-mediated dissection resulted in an initial separation followed by progressive retraction of the dissected myofibril ends. We found a significant increase in the initial separation (D_0) immediately following dissection (2.37 ± 0.23 μm for control versus 3.08 ± 0.22 μm for blebbistatin, $p=0.036$). Consistent with the idea that myosin II ATPase activity is required for active tension generation, both linear velocity and instantaneous velocity were significantly decreased upon dissection of blebbistatin-treated myofibrils (Figure 6-2). To assess the viscoelastic properties of myofibrils, we also calculated the viscous relaxation time (τ). Longer relaxation times are indicative of higher viscous damping, while a shorter relaxation time is indicative of lower viscous damping within the myofibril. We found a significant decrease in both the asymptotic distance as well as relaxation time upon blebbistatin treatment (Figure 6-2). Taken together, this data indicates that our laser mediated dissection approach recapitulates current models of myofibril contractility.

Figure 6-2

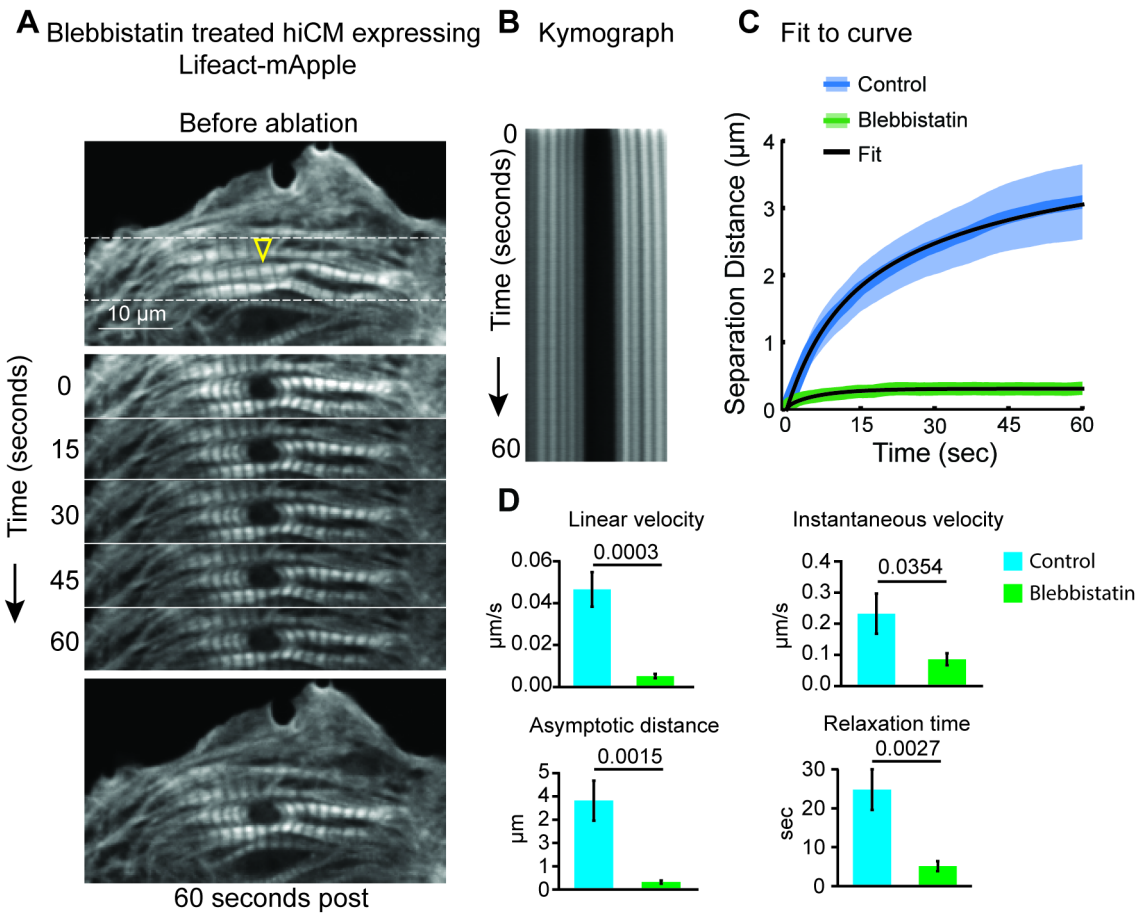

Figure 6-2- Myofibril dissection upon blebbistatin treatment

A) Representative hiCM at 16 hours post re-plating treated with 100 µM blebbistatin. Yellow arrowhead shows ablation site. Dotted white rectangle was used to create montage of myofibril retraction over 60 seconds. B) Kymograph showing retraction profile of myofibril shown in (A). C) Retraction profile of control versus blebbistatin treated cells. Shaded regions show confidence intervals while solid line shows the average. D) Linear velocity, instantaneous velocity, asymptotic distance, and relaxation time in control versus blebbistatin-treated cells. n= 13 control hiCMs, 12 blebbistatin-treated hiCMs, N=3 experiments. Error bars represent standard error of the means. Exact p values stated in graphs.

We then turned to investigating the role of FAK inhibition of the mechanical properties of myofibrils. We expressed Lifeact-mEmerald in hiCMs and allowed them to spread overnight prior to treatment with two different doses of two different inhibitors of FAK kinase activity, PF-228 and Defactinib (Kang et al., 2013; Slack-Davis et al., 2007). Expression of Lifeact tagged with mApple or mEmerald did not have any effects on any of the measured parameters in control hiCMs. Either PF-228 or Defactinib treatment did not attenuate hiCM beating. Furthermore, we found no significant difference in the initial separation distance (D_0) immediately following dissection. Both PF-228 and Defactinib treatment resulted in a small, but significant decrease in both the linear velocity and instantaneous velocity of retraction, suggesting a decrease in tension (Figure 6-3). No changes in the asymptotic distance were observed (Figure 6-3). Furthermore, we found a significant increase in the relaxation time with Defactinib following dissection, suggesting an increase in the viscous damping experienced by the myofibril. PF-228 only had an effect on relaxation time with the higher concentration (Figure 6-3).

A previous study in non-muscle cells has shown that PF-228 can activate BK Ca channels (So et al., 2011). We therefore wanted to confirm the changes in cardiomyocyte mechanics were caused by changes in material properties of the myofibril, rather than potential effects of FAK inhibition on electromechanical properties of the hiCMs. That is, we wanted to test whether FAK inhibition caused changes in myocyte excitability, which could then affect sarcomere contraction through excitation-contraction coupling and as a result, retraction dynamics. To that end, we performed electrical recordings of hiCMs using Microelectrode Array (MEA) technology (Figure 6-4). This non-invasive label free approach allows the measurement of field potentials in thousands of cells (Asai et al., 2010). We found that inhibition of FAK kinase activity using either PF-228 or Defactinib had no effect on the beat period, spike amplitude and field potential duration (Figure 6-4). Taken together, our results suggest that FAK inhibition alters the viscoelastic properties of myofibrils through altered mechanical signaling rather than changes in the electrophysiological properties of the cells.

Figure 6-3

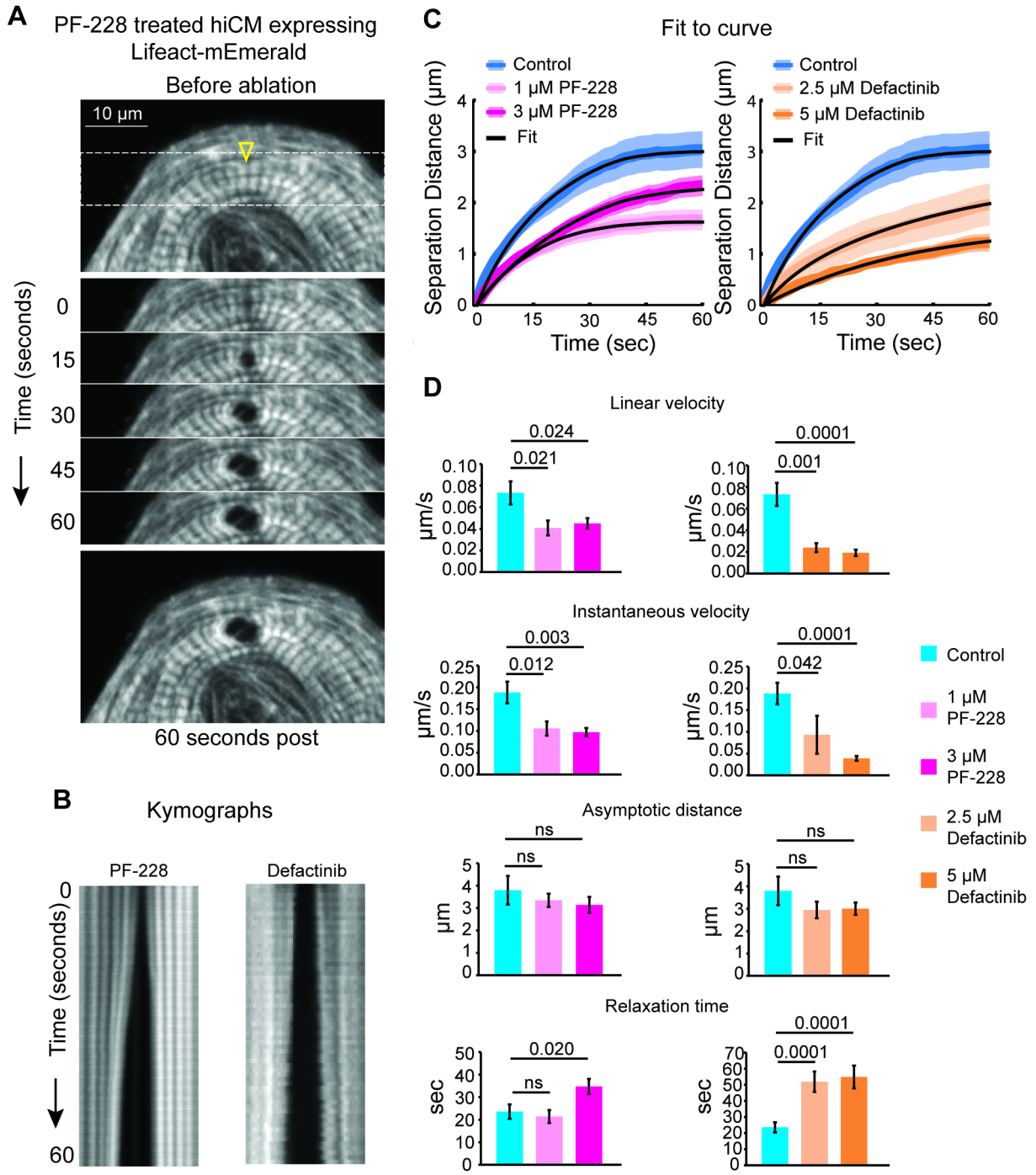

Figure 6-3- Myofibril dissection upon FAK inhibition

A) Representative hiCM at 16 hours post re-plating treated with 3 µM PF-228. Yellow arrowhead shows ablation site. Dotted white rectangle was used to create montage of myofibril retraction over 60 seconds. B) Kymograph showing retraction profile of myofibril in PF-228 (shown in (A)) and Defactinib treated hiCMs. C) Retraction profile of control versus PF-228 and Defactinib treated cells. Shaded regions show confidence intervals, solid line shows the average. D) Linear velocity, instantaneous

velocity, asymptotic distance, and relaxation time in control versus PF-228 and Defactinib treated cells. n= 18 control hiCMs, n=15 1 μM PF=228 treated, n=24 3 μM PF-228-treated, n=11 2.5 μM Defactinib and n=14 5 μM Defactinib treated hiCMs, N=3 experiments. Error bars represent standard error of the means. Exact p values stated in graphs.

Figure 6-4

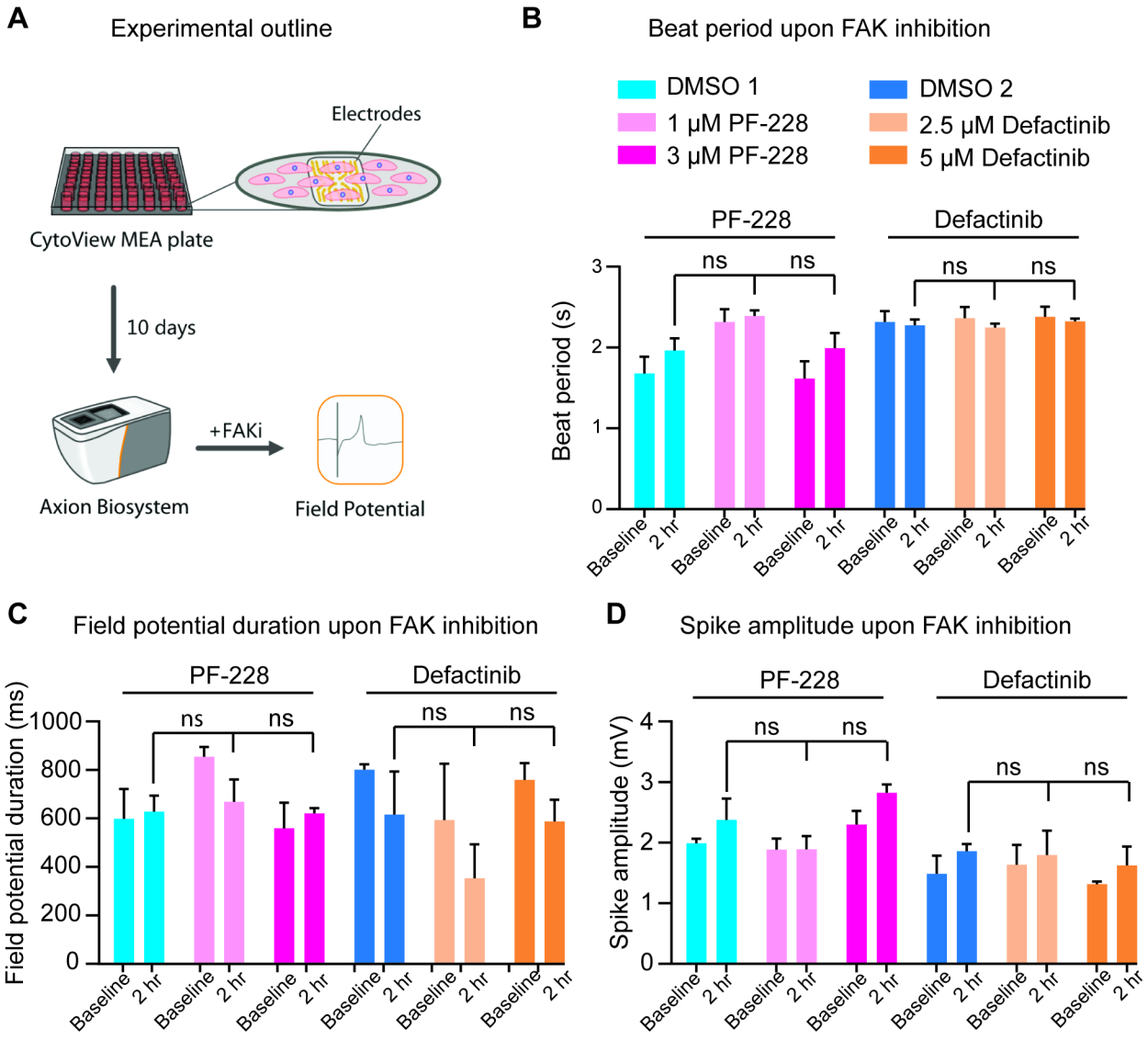

Figure 6-4- Electrophysiology upon FAK inhibition

A) Schematic showing experimental workflow. See Methods for further details. B) Beat period, spike amplitude and field potential duration upon treatment of hiCMs with PF-228 or Defactinib measured using Axion MEA system. N=3 independent experiments with 3 technical replicates (wells) per experiment for PF-228 and 2 technical replicates for Defactinib. Each technical replicate comprises recordings from 16 electrodes from 20,000 cells. Error bars show standard error of the means.

In this study, we use laser-mediated myofibril dissection as a tool to assess the viscoelastic properties of myofibrils. The interpretation of such data requires mechanical descriptions of myofibril contraction. As such, we have employed a standard Kelvin-Voigt element commonly used to describe stress fibers or cell-cell junctions in non-muscle cells (Fernandez-Gonzalez et al., 2009; Kumar et al., 2006). Using this framework, we found a good agreement between model fit and measured retraction dynamics of control and treated hiCMs. We further validated our approach by performing myofibril dissection experiments on blebbistatin-treated hiCMs. We found a decrease in tension as indicated by decreased linear and instantaneous velocity measurements. We also noted a decrease in the viscosity (as indicated by decreased relaxation time). Blebbistatin treatment attenuates myofibril contraction and as such, the myofibril showed minimal separation following the initial ablation. Since relaxation time is an estimate of the time to reach the asymptotic distance, this indicates blebbistatin-treatment significantly reduces the viscous damping of the myofibril response. This would indicate actomyosin contractility endows myofibrils with their viscoelastic mechanical response, however additional techniques would be necessary to fully assess viscosity in the absence of actomyosin contractility.

Interestingly, we also found that blebbistatin treated hiCMs displayed bent conformations of myofibrils that relaxed immediately following laser-assisted dissection. This relaxation correlated with an increase in the initial separation distance immediately following myofibril dissection. It is well-appreciated that myofibrils have passive elasticity that is independent of actomyosin contractility and largely dependent on titin (Linke and Fernandez, 2002). The instantaneous relaxation of the myofibril upon dissection and lack of any subsequent retraction is suggestive of this kind of elastic response.

In this study, we have found a role for FAK signaling in determining the viscoelastic properties of the myofibril. The precise mechanism by which FAK inhibition increases myofibril viscosity remains unclear. Previous studies have implicated actin-titin interactions, collagen fibrils and microtubule tyrosination as potential regulators of myofibril viscosity (Caporizzo et al., 2018; Granzier and Irving, 1995; Kulke et al., 2001). We have previously found that FAK inhibition results in stabilization of cell-ECM adhesions, which leads to increased incorporation of titin (Taneja et al., 2020b). Therefore, one possible mechanism could be due to increased actin-titin interactions mediated by increased cell-ECM adhesion. Alternatively, FAK inhibition may be altering microtubule stability by altering tyrosination, as has been reported previously in

fibroblasts (Palazzo et al., 2004). These hypotheses are not mutually exclusive and future studies will be required to elucidate the exact mechanism(s) by which FAK regulates myofibril mechanics.

Materials and Methods

Cell Culture

Human induced pluripotent stem cell derived cardiomyocytes (hiCMs) were purchased fully differentiated from Cell Dynamics International (Cat. CMM-100-012-000.5). hiCMs were thawed in proprietary Plating Medium according to the manufacturer's instruction in 96-well tissue culture plates at 50,000 cells per well. Cells were subsequently maintained using manufacturer-provided proprietary Maintenance Medium in a cell culture incubator at 37°C and 5% CO_2. Media was exchanged every 2 days as recommended by the manufacturer. Exogenous expression was performed using Viafect (Promega, Cat. E4981). 200 ng of plasmid DNA was used to transfect one well of a 96-well culture plate according to the manufacturer's instructions.

For ablation experiments, one well of hiCMs (50,000 cells) was re-plated onto 35 mm dishes with 10 mm glass bottom well (CellVis, Cat. D35-10-1.5-N) as described in detail previously (Fenix et al., 2018). The growth substrate was coated with 10 µg/mL fibronectin (Corning, Cat. 354008) for one hour prior to use. Briefly, cells were washed twice with 100 µl washes of PBS, followed by incubation in 40 µl of 0.1% Trypsin for 2 minutes at 37°C. The well was rinsed with the trypsin and cell detachment was confirmed using a brightfield microscope. Following trypsinization, 160 µl of Maintenance Media was added to the well and cells were collected for centrifugation. Cells were spun at 200 x g for 3 minutes. The supernatant was removed, and the pellet was resuspended in 200 µl of Maintenance Media and plated on the fibronectin-coated coverslip. Cells were allowed to spread for 16 hours prior to ablation. At this time point, myofibrils are on the dorsal surface of the cell (Fenix et al., 2018).

For experiments using the Axion bioanalyzer, hiCMs were thawed onto a 48-well CytoView MEA plate (Axion Biosystems, Cat. M768-tMEA-48B) coated with 50 µg/mL fibronectin at 20,000 cells per well. Cells were cultured for 10 days prior to experimental treatments.

Chemicals

FAK inhibitor PF-228 (PZ0117) and blebbistatin (B0560) were purchased from Sigma. Defactinib (S7654) was purchased from Selleckchem. Treatment was performed for 2 hours prior to laser-assisted dissection.

Plasmids

Plasmids used in the study are available from Addgene. mApple-Lifeact-7 (Addgene plasmid # 54747) and mEmerald-Lifeact-7 (Addgene plasmid # 54148) were gifts from Michael Davidson.

Laser-assisted dissection

Focused laser mediated myofibril dissection was performed as described previously. Myofibril dissection was performed on a Nikon Spinning Disk confocal microscope equipped with a 60X 1.4 NA objective and an Andor iXON Ultra EMCCD camera, provided by the Nikon Center of Excellence, Vanderbilt University. Dissection was performed using a 100 mW UV laser (Coherent technologies) at 50% power, using a dwell time of 500 µs for a total period of 1 second using a Stimulation Line ROI of 2 µm length. Cells were maintained at 37°C and 5% CO_2 using a Tokai Hit stage incubator. Three pre-ablation images were acquired at 2 second intervals. Following ablation, images were acquired using continuous acquisition at a net acquisition rate of 138 ms per frame. For the Defactinib experiments, the frame rate was 1 second.

Laser-assisted dissection data analysis

To quantify myofibril mechanical properties, individual myofibrils were subjected to laser-assisted dissection to induce separation. Following visible separation, kymographs were drawn along the separation axis to visualize the time-varying end-to-end distance. Using a custom edge detection algorithm based on the Canny filter, edge profiles were defined based on gradients in the kymograph image and the separation distance $L(t)$ was computed as one-half of the distance between the upper and lower edge profiles at each image frame. Separation profiles were then fit to a standard Kelvin-Voigt viscoelastic solid model of the form,

$$L(t) = D_0 + D_a\left(1 - exp\left(-\frac{t}{\tau}\right)\right)$$

to identify two viscoelastic parameters: the asymptotic distance $\mathrm{D_a}$ and the relaxation time constant τ. Note that the asymptotic distance parameter has been shown to be correlated with elastic energy dissipation, whereas the relaxation time constant is representative of the ratio of viscosity to elasticity in the material. Hence, increasing τ indicates a more viscous response and vice-versa. Additionally, any initial damage induced by the laser was accounted for by defining an offset distance D_0.

Impedance assays

The Axion Biosystems analyzer was used to measure contractility and impedance in hiCMs as described previously (Rasmussen et al., 2020). Recordings were taken for 5 minutes at baseline and after two hours of drug treatment. Cell were maintained at 37°C and 5% CO_2 during recording. Cells were assayed using the standard cardiac analog mode setting with 12.5 kHz sampling frequency to measure spontaneous cardiac beating. The Axion instrument was controlled using Maestro Pro firmware version 1.5.3.4. Cardiac beat detector settings are as follows: Beat Detection Threshold 300 μV; Min. Beat Period 250 ms; Max. Beat Period 5 s; Synchronized Beat Maximum Propagation Delay 30 ms; Minimum Active Channels Ratio 50.00%; Running Average Beat Count 10.

Statistical analysis

Statistical analysis was performed in GraphPad and Excel. The comparison of retraction parameters was performed using students T-test while comparison of electrophysiological properties was performed using two-way ANOVA. All error bars represent standard error of the means.

Acknowledgements

We thank Nikon Center of Excellence at Cell Imaging Shared Resource at Vanderbilt University for access to the Nikon Spinning Disk microscope and technical support, and Dr. Kevin Ess for access to the Axion Biosystems MEA analyzer. This work was funded by a MIRA from NIGMS (R35 GM125028) to D.T.B., an American Heart Association Predoctoral Fellowship (18PRE33960551) to N.T., an American Heart Association Predoctoral Fellowship (19PRE34380515) to M.L.R., a MIRA (R35-GM128915) to V.G. and a MIRA (R35-HL135790) to W.D.M. The authors declare no competing interest.

Chapter 7- Summaries and Future Directions

Chapter 2- Summary

Cells must be able to constantly monitor their extracellular environment to make critical decisions such as cell cycle progression and cell fate determination. Cell-ECM and cell-cell adhesions are the two primary structures that are highly adapted for mechanotransduction. Numerous studies in epithelia have established the importance of cell-cell adhesion during cell division. For instance, these studies have shown how epithelial cells preserve epithelial barrier function during the remodeling of cell-cell junctions during mitosis (Guillot and Lecuit, 2013). The role of cell-ECM adhesion during cytokinesis in epithelia has largely been ignored since these adhesions are thought to completely disassemble during cytokinesis. In support of this, the cleavage furrow ingresses from the basolateral side in most epithelial cells. Our results have shown that epithelial cells in monolayers still respond to changes in ECM composition and integrin signaling. We show that increase in cell-ECM adhesion either using FAK inhibition or increasing fibronectin concentration results in increased ingression from the apical side. These results have implications in cancer, where tumors are often found to be stiffer. This increased stiffness is likely to strengthen cell-ECM adhesion during mitosis, potentially causing stress at apical junctions. This could disrupt epithelial integrity and promote metastasis, both of which are hallmarks of cancer.

Cell-ECM adhesion during cytokinesis in single cells has also been largely understudied despite early observations that adherent cells ingress primarily from the dorsal side. Most studies instead focused on retraction fibers. Our results have shown that cells actively regulate their focal adhesions through the paxillin-vinculin-FAK axis during cytokinesis. We further showed that the extent of cell-ECM adhesion also regulates the XZ orientation of the mitotic spindle and the placement of the older centrosome. These results have important implications in cell fate regulation. Stem cells require a specialized extracellular environment termed as “stem cell niche” to maintain stemness. This niche usually comprises specialized cells as well as ECM and is therefore a combination of chemical and physical cues. Our study establishes a link between sensing of physical cues and placement of the older centrosome, which is a key cell fate determinant.

Chapter 2- future directions

Our results have generated several interesting hypotheses and questions. An interesting future avenue of investigation would be to determine the molecular mechanisms underlying the regulation of spindle orientation by cell-ECM adhesions. There are several non-mutually exclusive mechanisms that could contribute to this regulation.

i) Contribution of cortical contractility: In cells cultured on highly adhesive substrates, we observed that the daughter cell with more mitotic focal adhesions was flatter and contained a mitotic centrosome that was closer to the substrate. It is possible that cortical contractility on top of the cell is simply pushing down on the spindle. This could be tested using a combination of patterned substrates with asymmetric adhesive islands and treating single daughter cells with blebbistatin.

ii) Astral pulling: Alternatively, asymmetric distribution of adhesions at the bottom of the cell could create a physical cue that activates astral pulling pathways. There is also an inherent asymmetry between the two mitotic centrosomes that occurs do the nature of centrosome duplication during S-phase of the cell cycle (Fu et al., 2015). The mother (older) mitotic centrosome has been shown to have distinct microtubule organizing and signaling activities compared to the daughter mitotic centrosome (younger) (Hung et al., 2016; Piel et al., 2000). Given this asymmetry, it is interesting to speculate how different signals from two centrosomes might affect spindle-positioning pathways. For example, Plk1 signaling from centrosomes has been shown to negatively regulate the recruitment of cortical dynein (Kiyomitsu and Cheeseman, 2012). In addition, the mother centriole protein, Cenexin, a known Plk1 scaffold, also is an integral component in modulating appropriate spindle orientation (Soung et al., 2009).

iii) Actin clouds: The mechanical link between the actin cytoskeleton and the spindle may be mediated by a population of actin that communicates with or even is regulated by the centrosome. Indeed, the subcortical actin cloud, which is nucleated from centrosomes, has been implicated as a potential link between the actin cortex and the spindle (Kwon et al., 2015). Specifically, the actin cloud may act as a conduit to transfer mechanical forces from the cortex to the spindle. Biophysical studies

could shed light on the dynamics and mechanical properties of actin clouds, and how they influence the positioning of the spindle.

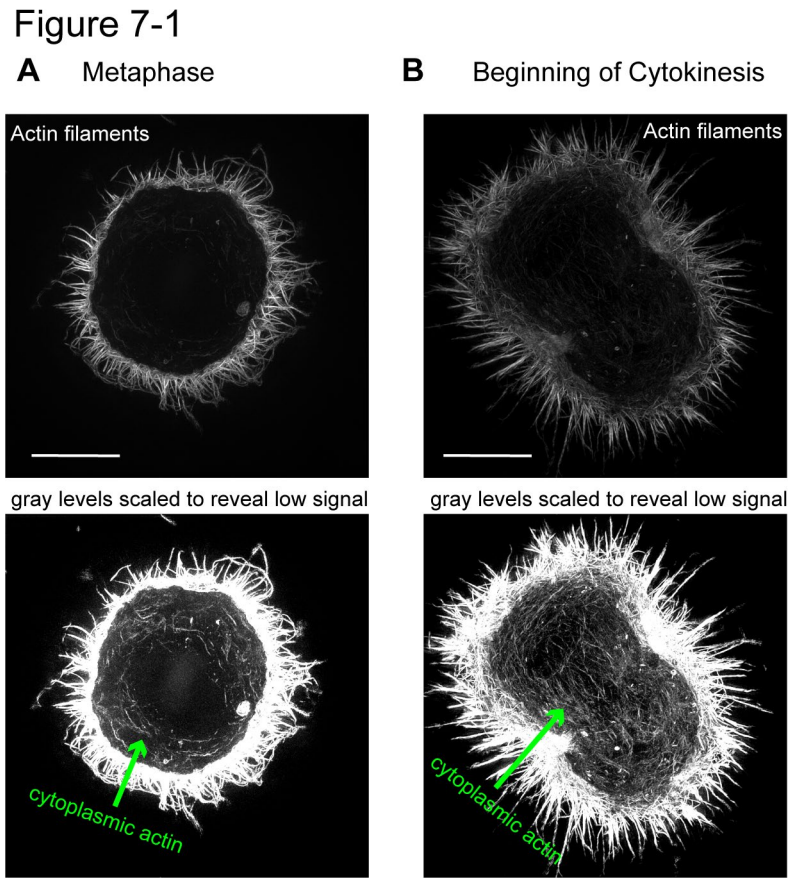

Figure 7-1- Subcortical actin during metaphase and cytokinesis

SIM images of HeLa cells at metaphase (A) and cytokinesis (B) stained with Phalloidin to visualize actin filaments. The top panel is scaled so that the cortical actin is visible, while the bottom panel is scaled so that the sub-cortical population of actin filaments is visible. Scale bar: 10 μm.

Chapter 3- Summary

Our results showing that MIIA is the sole myosin-II paralog that drives the retraction of membrane blebs has important implications for processes such as cell migration and cell division, both of which can be influenced by the dynamics of bleb retraction. Furthermore, we found that the ability to drive membrane bleb retraction depends on both the motor activity of MIIA as well as its rapid turnover. It was previously suggested that turnover of the motor is required for the bleb cortex to remodel as it undergoes cycles of retraction (Fritzsche *et al.*, 2013). Interestingly, the non-helical tailpiece of MIIA heavy chain also contributed to turnover rate of the motor. This suggests that motor disassembly through phosphorylation of the non-helical tailpiece acts as an additional layer of regulation. The upstream kinases that regulate this process in a physiologically relevant manner remain to be elucidated.

One potential kinase that has been implicated in the assembly state of MIIB is PKC. It was recently proposed that regulation of motor disassembly by heavy chain phosphorylation sets a set point level of MIIB that is incorporated into myosin filaments (Schiffhauer et al., 2019). The levels of PKC in different cell lines appeared to be correlated with the proportion of MIIB in filaments versus in the cytoplasmic pool. It would be interesting to further investigate this mode of regulation with respect to driving blebbing-regulated processes. Development of biosensors of PKC activity would be required to test whether heavy chain phosphorylation is an actively regulated process or remains fixed in different cell lines. Similarly, biosensors of other putative kinases such as TRPM7 or Casein Kinase II could reveal new insight into this additional layer of regulation of myosin activity.

Chapter 3- Future Directions

Blebs are one of the least studied cellular protrusions and understanding their physiological functions is an area of active interest in the field. Given our findings relating to paralog specific roles in driving bleb retraction, it would be interesting to investigate the impact of differential paralog expression in different cancer cell lines in the context of bleb-based migration. Previous studies have shown that bleb-based migration is optimal under conditions of low

adhesion in a three-dimensional environment (Bergert et al., 2015). Therefore, cancer cell lines selected based on myosin paralog expression could be screened for their bleb-based migratory capacity in three-dimensional matrices such as collagen or Matrigel. We would predict that cell lines high in MIIA expression would be able to migrate better in three-dimensional matrices. Furthermore, it would be interesting to explore the signaling pathways altered in cancer cells for their role in regulating myosin assembly through heavy chain phosphorylation. Indeed, multiple putative kinases have been implicated in cancer. These kinases and their role in heavy chain phosphorylation could therefore be targeted in cancer therapies.

Chapter 4- Summary

In this study, we have established a new mechanism by which the contractile state of the actin cortex can be regulated, namely through the composition of myosin-II hetero-filaments. It was previously demonstrated in vitro that addition of just 6 MIIB hexamers to 24 MIIA hexamers allowed the bipolar filament to undergo processive movement on actin filaments (Melli et al., 2018). Our results thus reveal a fundamental behavior of myosin-II at the actin cortex. MIIA, based on its high ATPase activity and fast turnover is adapted at generating high surface tension within the actin cortex. Interestingly, this increase in cortex tension has different outcomes depending on network architecture. At the cleavage furrow, where actin filaments are more ordered and bundled, addition of MIIA to hetero-filaments drives increased myosin stacking and faster cleavage furrow ingression. At the polar cortex, which is more isotropic, increased cortex tension results in a higher probability of bleb initiation. MIIB on the other hand has lower ATPase activity and slower turnover, suggesting a hetero-filament containing higher number of MIIB filaments is more likely to act as a cross linker in the actin cortex and maintain network stability under increased load. A balance between the two activities, determined by the relative amount of MIIA and MIIB in filaments is required to maintain mechanical equilibrium in the cell during cytokinesis. We found that deregulation of this balance, such as by removal of MIIB, had disastrous consequences for the cell, with increased polar blebbing and spindle oscillation induced chromosome missegregation.

Chapter 4- Future Directions

These results open multiple lines of investigation that could be pursued further. These are summarized below.

i) Feedback between contractility and myosin-II filament composition: Cell lines display a wide variation in myosin-II paralog expression. For instance, some cell lines such as Cos7 do not express MIIA, while some HeLa subtypes (HeLa-Clontech) do not express MIIB. However, all these cell lines are capable of proliferation without

defects. This suggests that multiple mechanisms exist to regulate contractility. Therefore, cell lines that only express MIIA likely down-regulate contractility through other mechanisms. Possible mechanisms include either a basally reduced level of MIIA incorporated into filaments through heavy chain phosphorylation, increased phosphorylation of Tyr 118 on the regulatory light chain, down-regulation of MIIA expression overall, reduced ROCK activity, or altered actin architecture. Identifying the pathways that cells use to sense contractility will yield new insights into cortical mechanics.

ii) Effect of myosin-II activity on actin turnover and architecture: While our data strongly supports that MIIA activity increases cortex instability by increasing cortex tension, how it achieves this at the nanoscale is less clear. There is preliminary evidence that knockdown of MIIB in HeLa cells leads to increased actin turnover. In contrast, in HAP1 MIIA-KO cells, expression of MIIA slowed actin turnover. Therefore, a thorough and comprehensive study measuring actin turnover in cell lines containing different levels of MIIA and MIIB could yield insight into how MIIA- or MIIB-containing hetero-filaments affect actin stability. A commonly used technique to assay actin architecture is scanning electron microscopy (SEM). While SEM does not reach the resolution needed to identify single actin filaments, it can be used to quantify the pore size of the cortex, which can be used to estimate the viscoelastic properties of the cortex (Bovellan et al., 2014). Therefore, it would be interesting to test for instance how the actin network architecture is altered in cells with high levels MIIB in hetero-filaments. This could then be related back to the mechanical properties such as cortex tension and stiffness measured using micropipette aspiration.

iii) Using enucleated cells as models for cellular organization: We found that MIIB depleted cells show dramatic blebbing, which can induce spindle oscillation mediated chromosome missegregation. This creates a binucleated cell and an enucleated. Our preliminary data suggests that these contain organized actin structures such as stress fibers. It would be interesting to further explore whether these cells inherit spindle poles or any microtubules, and how they organize their organelles in the absence of a nucleus and a microtubule organizing center.

Figure 7-2

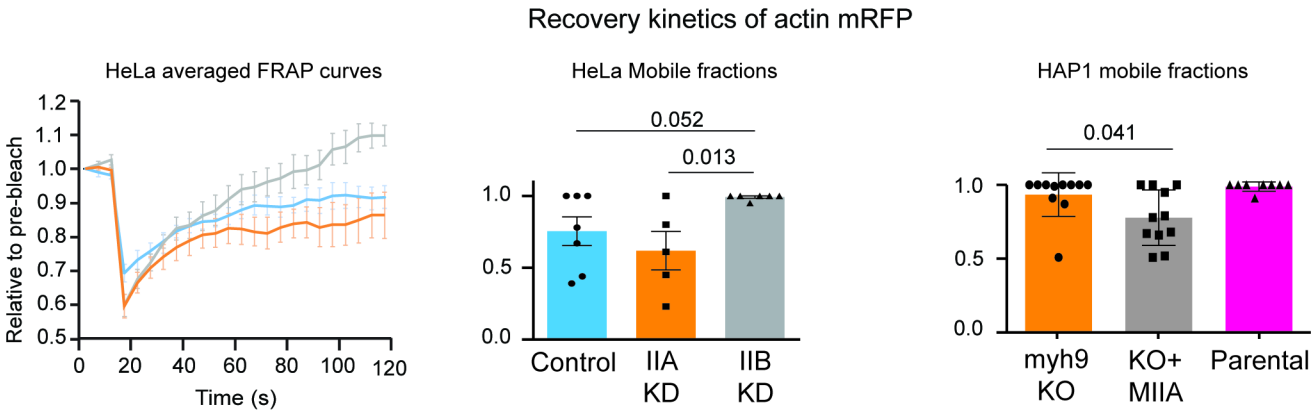

Figure 7-2- Role of MII contractility in cortical turnover

Averaged curves are shown for the recovery kinetics of actin-mRFP following FRAP experiments during metaphase. The grey curve shows MIIB knockdown, the blue curve shows control cells, and the orange curve shows MIIA knockdown cells. On the right, the mobile fractions in HeLa cells and HAP1 cells are shown. For HeLa cells: n= 7 control cells, 5 MIIA knockdown cells and 6 MIIB knockdown cells over 3 experiments. For HAP1 cells: n= 11 myh9 KO cells, 11 KO cells expressing MIIA-mEGFP and 8 parental HAP1 cells over 2 experiments. Error bars show standard deviation for HAP1 cells and standard error of the mean for HeLa cells.

Chapter 5- Summary

In this study, we have elucidated the role of cell-ECM adhesion in myofibril assembly using human iPSC-derived cardiac myocytes as a model system. A role for cell-ECM during myofibril assembly has been proposed for decades but the precise mechanism by which this occurs remains poorly understood. In contrast to the recently proposed model where cell-ECM adhesions act as the nucleation site for myofibrils, we have revealed using live imaging that this observation was merely an artifact of imaging the ventral plane. Instead, cell-ECM adhesions were required for the transition of muscle stress fibers to myofibrils. We found that cell-ECM adhesions act as mechanosensitive structures that allow the buildup of the force generating capacity of the muscle stress fiber by increasing substrate coupling during the maturation process. As a proxy for substrate coupling, we showed that extent of adhesion negatively correlated with the rate of rearward translocation of muscle stress fibers. We establish the required for cell-ECM adhesion in driving myofibril maturation using multiple perturbations, such as modulation of fibronectin concentration, knockdown of FAK, overexpression of the head domain of talin, knockdown of vinculin and inhibition of FAK kinase activity. In all cases, there was a strong correlation between the extent of adhesion and the average length of Z-lines.

Importantly, we also found that the formin DIAPH1 was required to mediate the coupling between adhesions and muscle stress fibers through the nucleation of specialized connecting fibers called dorsal stress fibers. Interestingly, the overall actin architecture was highly reminiscent of non-muscle cells, where dorsal stress fibers mediate the connection between focal adhesions and actin arcs. A previous study from the lab also showed that the organization of muscle stress fibers is similar to actin arcs, albeit with some mechanistic differences. Muscle stress fibers do not require the Arp 2/3 complex to form, and instead require the formin FHOD3. This study therefore adds to the mounting evidence that cells have repurposed the existing contractile machinery to perform specialized functions such as cell migration and muscle contraction. Future studies could explore the upstream regulatory pathways that control formin function, as well as the evolution of contractile networks, specifically what factors allow the divergence of stress fibers in muscle versus non-muscle cells.

Chapter 5- Future Directions

i) Regulation of DIAPH1 and mechanics of dorsal stress fibers: While the current results establish the requirement of adhesions in myofibril assembly, multiple molecular mechanisms remain to be elucidated. The formin DIAPH1 was required to nucleate dorsal stress fibers that couple muscle stress fibers and cell-ECM adhesions. Some interesting future lines of investigation could explore the upstream regulatory pathways that activate DIAPH1 at adhesion sites. Furthermore, the mechanism by which an actively elongating dorsal stress fiber physically associates with the muscle stress fiber as it moves away from the edge of the cell remains unknown. Live super-resolution imaging of actin filaments and adhesions using iSIM could yield insights into this process.

ii) The nanoscale architecture of the transition zone: Using an N-terminal antibody of titin, we found that titin forms “rings” around α-actinin puncta present in MSFs. On the other hand, myofibrils are characterized by straight stripes of titin. The region where this transition occurs also coincides with the present of co-filaments of MIIB and β-CMII. Therefore, understanding the nanoscale architecture of this region would likely yield insight into the structural changes that occur when an MSF transitions into a myofibril. Importantly, which structural change is mechanically regulated by coupling to the substrate? These studies will require live super-resolution imaging complemented by ultrastructural techniques such as STED microscopy or Platinum Replica Electron Microscopy.

iii) Role of cell-substrate adhesion on myofibril remodeling: Myofibril assembly is only the initial step required for force generation at the tissue level. Myofibrils across multiple cells should be able to generate force along a polarized direction. How this occurs at the level of a single myofibril is not understood. Previous modeling and biophysical studies have suggested that stress fibers assemble and mature along the axis of greatest physical stress. Our results suggest that adhesions could serve as the structures that sense this axis of principal stress, and through dorsal stress fibers relay this information to newly assembled myofibrils. This idea is also consistent that increased force generation requires increased buildup of order in a contractile system. Based on phalloidin intensity, a muscle stress fiber contains less

actin, and is also inherently less ordered than a myofibril. To acquire its higher force generating capacity, the forces generated by the nascent myofibril must be balanced by resistive forces. Cell-ECM adhesions could serve as an adaptive load bearing structure during this process. To gain insight into this process, long term imaging of cardiomyocytes under different adhesive conditions or using patterned substrates would be required.

iv) Role of cell-cell adhesion on myofibril assembly and remodeling: Cardiomyocytes in both developing and adult organisms also form cell-cell contacts in addition to cell-ECM contacts. The role of cell-cell adhesion has been explored and investigated previously, but how and when cardiac myocytes form the first cell-cell adhesions remains unknown. Given the complex nature of cell-cell adhesions in mature myocytes, where the intercalated disc comprises gap junctions mediated by connexins, adherens junctions mediated by N-cadherin, and desmosomes mediated by intermediate filaments. There are several unanswered questions regarding cell-cell adhesion formation in cardiomyocytes. What is the order of assembly of these three different types of junctions in culture and *in vivo*? How does cell shape and myofibril organization get altered upon formation of the first cell-cell contacts in culture and *in vivo*? What is the individual contribution of the three classes of cell-cell junctions to mechanotransduction? Experiments combining cardiac myocytes derived from iPSCs expressing fluorescently tagged reporters at the endogenous locus of cell-cell adhesion proteins such as N-cadherin, β-catenin, Cx43 and desmoplakin, and in vivo imaging of developing zebrafish hearts will be necessary to address these questions.

Chapter 6- Summary

In this study, we have provided an additional source of regulation of the viscoelastic properties of the contracting cardiomyocyte, namely through FAK signaling. Previous studies have implicated collagen, actin-titin interactions, and microtubule tyrosination in the regulation of myofibril viscosity (Caporizzo et al., 2018; Granzier and Irving, 1995; Kulke et al., 2001). We show that acute inhibition of FAK signaling reduces the elastic component of myofibrils and increases viscous dampening during myofibril contraction . FAK is a major integrator of physical cues and interacts with multiple cellular pathways (Geiger et al., 2009). Indeed, it has been a target for cancer therapies for decades. FAK is also implicated in the hypertrophic response required for load adaptation in the heart. Our results thus have important implications for the potential cardiotoxic effects of these FAK inhibitors. Alteration of the mechanical properties of contracting myocytes is likely to have adverse effects on heart function. Future studies should address the mechanisms by which FAK regulates myofibril viscosity.

Chapter 6- Future Directions

i) Mechanisms underlying the increased viscosity of myofibrils upon FAK inhibition: There are multiple hypotheses that can be proposed that can explain this behavior of myofibrils upon FAK inhibition. Previous studies have shown that FAK inhibition can alter microtubule tyrosination, which has already been implicated in regulating myofibril viscosity. Alternatively, FAK inhibition may be altering actin-titin interactions. In support of this idea, FAK inhibition leads to faster incorporation of titin into muscle stress fibers at early points in cell spreading. A quantitative analysis of titin in myofibrils upon acute FAK inhibition would be required to test this hypothesis.

ii) Role of component turnover in myofibril mechanics: It is possible that acute FAK inhibition may not alter titin incorporation in fully formed myofibrils. Instead, the effect of FAK inhibition may be mediated by alteration of component turnover, such as that of sarcomeric actin, titin and α-actinin that could alter actin-titin interactions. In support of this hypothesis, our preliminary data has shown that FAK inhibition

slowed down the turnover of α-actinin at Z-lines of fully formed myofibrils (Figure 7-3). Fluorescence Loss after Photo-activation experiments would be required with cardiac actin and titin to investigate the role of component turnover during this process.

iii) Role of myosin-II ATPase activity in myofibril mechanics: In this study, we found that inhibition of myosin-II ATPase activity using blebbistatin resulted in buckling of myofibrils suggesting that they store elastic energy despite inhibition of myosin activity. Upon ablation of a single myofibril, the entire network underwent straightening. Further investigating this interesting phenotype could yield insight into the role myosin-II contractility has in maintenance of myofibrils.

Figure 7-3

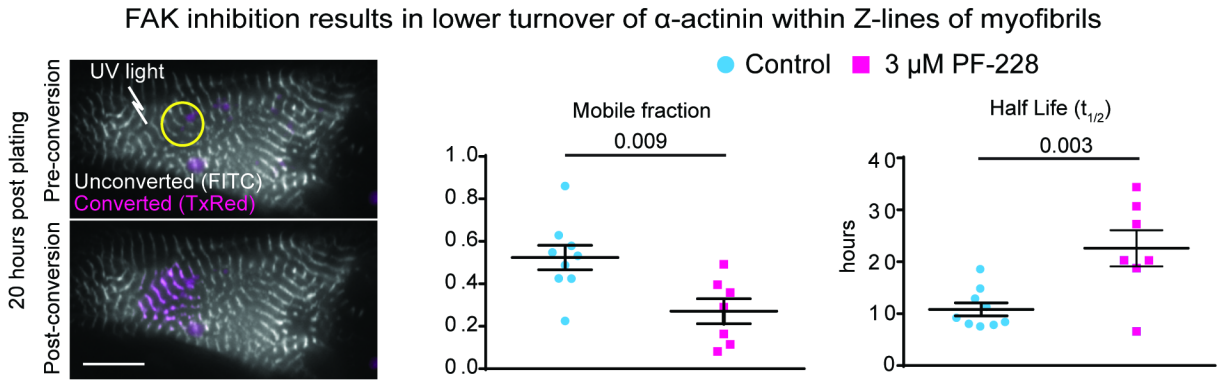

Figure 7-3- FAK inhibition slows α-actinin-2 turnover at Z-lines

Shown are images of hiCM expressing α-actinin-2 tdEos before (top) and after (bottom) photoconversion. Yellow circle shows stimulation ROI. Unconverted tdEos is shown in gray and converted tdEos is shown in magenta. The mobile fraction and half life from decay curves is shown on the right for control myocytes versus myocytes treated with 3 μM PF-228. n= 9 control cells and 7 PF-228 treated cells. The code for curve fitting was written by Abigail Neininger. Scale bar: 10 μm.

Overall Conclusions and Perspectives

In this collection of studies on cell division and cardiomyocyte contraction, some common threads, and basic organizational principles of actomyosin networks have emerged. The ability to generate contractile force at a membrane tethered actomyosin network to drive cell shape changes is a fundamental feature of all animal cells. This implies that actomyosin networks are ancient structures that have undergone multiple rounds of divergent evolution as organisms have evolved more diverse cell types and tissues. The studies described above have extensively focused on the role and regulation of myosin-II at the mammalian actin cortex.

Myosin-II has been studied for over a century. Elegant biochemical studies have revealed the mechanochemical cycle of myosin-II and multiple levels of regulation it can undergo. However, each of these mechanisms has been studied either in isolated contexts *in vitro* or at the level of cellular scale functions such as cell division and migration. Our studies have revealed a highly complex regulatory machinery that controls the contractile activity of myosin-II at the actin cortex. For instance, myosin-II activity can be tuned to both cross-link a network to sustain tension, or actively generate it and cause network instability through the composition of myosin-II hetero-filaments (Chapter 4). Phosphorylation of the heavy chain of myosin-II can alter its turnover at the cortex and hence its ability to remodel an actively retracting membrane bleb (Chapter 3). Myosin-II turnover is also regulated by its motor domain itself, with higher ATPase activity of MIIA driving its faster turnover (Chapter 3). We have also shown that two upstream kinases, MLCK and ROCK differentially regulate myosin-II turnover at the mitotic cortex. ROCK inhibition prevents the cortical recruitment of myosin-II, while MLCK inhibition prevents its turnover (Figure 7-4). Differential phosphorylation states of the Regulatory Light Chain can thus play a role in regulating the contractility of the motor. More recently, a study also showed a role for the phosphorylation of Tyr155 of the RLC being inhibitory to the myosin-II assembly (Aguilar-Cuenca et al., 2020). This regulation was controlled by presence of growth factors (Aguilar-Cuenca et al., 2020). Role for other types of modification of myosin-II will continue to emerge. Therefore, a systems level understanding of myosin-II regulation at the transcriptional and post-transcriptional levels in different cellular contexts should be the goal of future studies.

Our studies have also shed light on how this actin cortex is repurposed to perform very different functions, but still retain some mechanical principles in these systems. During cell division, a balance between contractile forces generated by the contractile ring, and adhesive forces generated by focal adhesions drive the generation of the three-dimensional shape of the cleavage furrow as well as the orientation of the mitotic spindle (Chapter 2). In a migrating cell, the balance between contraction of actin arcs is balanced by adhesive forces of focal adhesions to generate cell flattening (Burnette et al., 2014). In a spreading cardiac myocyte, contractile forces generated by muscle stress fibers and balanced by focal adhesions to facilitate the maturation of these structures into myofibrils (Chapter 5). Interestingly, despite having different components, flow rates and regulatory mechanisms, both muscle stress fibers and arcs have a similar mechanical configuration- a force generating stress fiber, anchored to a load bearing focal adhesion via a non-contractile axially spanning stress fiber. We speculate that this mechanical configuration may be a more widely applied apparatus in force generating system. This hypothesis would suggest that similar connections should exist between the contractile ring and focal adhesions. We attempted to localize dorsal stress fiber like connection from the contractile ring to the substrate in dividing cells but found that even SIM was unable to resolve these structures. Higher resolution techniques may be necessary to resolve the nanoscale architecture of the interface between the contractile ring and adhesions.

Figure 7-4

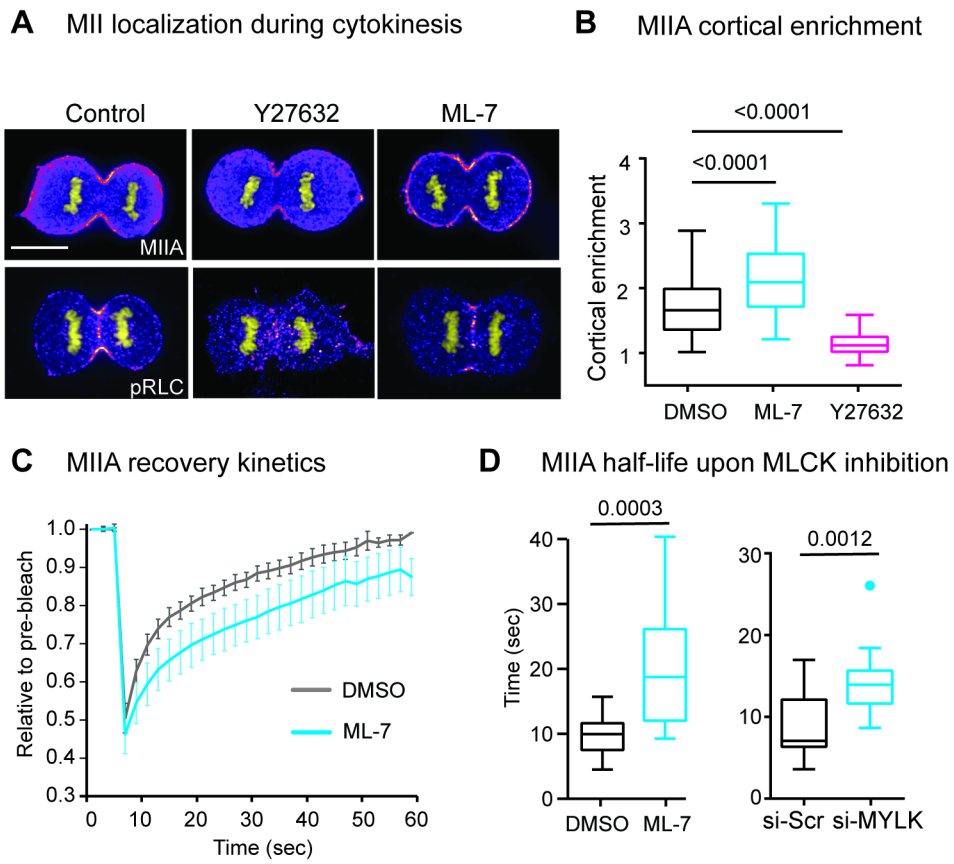

Figure 7-4- MLCK regulates turnover while ROCK regulates recruitment

A) Localization of MIIA heavy chain and phosphorylated regulatory light chain (S19) during cytokinesis in control, ML-7 treated and Y27632 treated cells. Images are displayed using Fire LUT. B) Quantification of cortical enrichment of MIIA heavy chain in control, ML-7 treated and Y27632 treated cells. n= 42 DMSO treated, 52 ML-7 treated and 38 Y27632 treated cells over 3 experiments. C) Recovery kinetics of MIIA at the metaphase cortex following FRAP. D) Tukey plots showing half-life of MIIA recovery upon FRAP. n= 15 DMSO treated,13 ML-7 treated,15 si-Scr and 15 si-MYLK cells over 3 experiments. Scale bar: 10 μm.

REFERENCES

Aguilar-Cuenca, R., C. Llorente-Gonzalez, J.R. Chapman, V.C. Talayero, M. Garrido-Casado, C. Delgado-Arevalo, M. Millan-Salanova, J. Shabanowitz, D.F. Hunt, J.R. Sellers, S.M. Heissler, and M. Vicente-Manzanares. 2020. Tyrosine Phosphorylation of the Myosin Regulatory Light Chain Controls Non-muscle Myosin II Assembly and Function in Migrating Cells. *Curr Biol*. 30:2446-2458 e2446.

Alexandrova, A.Y., K. Arnold, S. Schaub, J.M. Vasiliev, J.J. Meister, A.D. Bershadsky, and A.B. Verkhovsky. 2008. Comparative dynamics of retrograde actin flow and focal adhesions: formation of nascent adhesions triggers transition from fast to slow flow. *PLoS One*. 3:e3234.

Andersen, J.S., C.J. Wilkinson, T. Mayor, P. Mortensen, E.A. Nigg, and M. Mann. 2003. Proteomic characterization of the human centrosome by protein correlation profiling. *Nature*. 426:570-574.

Asai, Y., M. Tada, T. G. Otsuji, and N. Nakatsuji. 2010. Combination of Functional Cardiomyocytes Derived from Human Stem Cells and a Highly-Efficient Microelectrode Array System: An Ideal Hybrid Model Assay for Drug Development. *Current Stem Cell Research & Therapy*. 5:227-232.

Barr, F.A., and U. Gruneberg. 2007. Cytokinesis: placing and making the final cut. *Cell*. 131:847-860.

Bays, J.L., and K.A. DeMali. 2017. Vinculin in cell-cell and cell-matrix adhesions. *Cell Mol Life Sci*. 74:2999-3009.

Beach, J.R., L. Shao, K. Remmert, D. Li, E. Betzig, and J.A. Hammer, 3rd. 2014. Nonmuscle myosin II isoforms coassemble in living cells. *Curr Biol*. 24:1160-1166.

Bekker-Jensen, D.B., C.D. Kelstrup, T.S. Batth, S.C. Larsen, C. Haldrup, J.B. Bramsen, K.D. Sorensen, S. Hoyer, T.F. Orntoft, C.L. Andersen, M.L. Nielsen, and J.V. Olsen. 2017. An Optimized Shotgun Strategy for the Rapid Generation of Comprehensive Human Proteomes. *Cell Syst*. 4:587-599 e584.

Bement, W.M., M. Leda, A.M. Moe, A.M. Kita, M.E. Larson, A.E. Golding, C. Pfeuti, K.C. Su, A.L. Miller, A.B. Goryachev, and G. von Dassow. 2015. Activator-inhibitor coupling between Rho signalling and actin assembly makes the cell cortex an excitable medium. *Nat Cell Biol*. 17:1471-1483.

Bergert, M., A. Erzberger, R.A. Desai, I.M. Aspalter, A.C. Oates, G. Charras, G. Salbreux, and E.K. Paluch. 2015. Force transmission during adhesion-independent migration. *Nat Cell Biol*. 17:524-529.

Bertocchi, C., Y. Wang, A. Ravasio, Y. Hara, Y. Wu, T. Sailov, M.A. Baird, M.W. Davidson, R. Zaidel-Bar, Y. Toyama, B. Ladoux, R.M. Mege, and P. Kanchanawong. 2017. Nanoscale architecture of cadherin-based cell adhesions. *Nat Cell Biol*. 19:28-37.

Billington, N., A. Wang, J. Mao, R.S. Adelstein, and J.R. Sellers. 2013. Characterization of three full-length human nonmuscle myosin II paralogs. *J Biol Chem*. 288:33398-33410.

Bloor, J.W., and N.H. Brown. 1998. Genetic analysis of the Drosophila alphaPS2 integrin subunit reveals discrete adhesive, morphogenetic and sarcomeric functions. *Genetics*. 148:1127-1142.

Bosveld, F., O. Markova, B. Guirao, C. Martin, Z. Wang, A. Pierre, M. Balakireva, I. Gaugue, A. Ainslie, N. Christophorou, D.K. Lubensky, N. Minc, and Y. Bellaiche. 2016. Epithelial tricellular junctions act as interphase cell shape sensors to orient mitosis. *Nature*. 530:495-498.

Bovellan, M., Y. Romeo, M. Biro, A. Boden, P. Chugh, A. Yonis, M. Vaghela, M. Fritzsche, D. Moulding, R. Thorogate, A. Jegou, A.J. Thrasher, G. Romet-Lemonne, P.P. Roux, E.K. Paluch, and G. Charras. 2014. Cellular control of cortical actin nucleation. *Curr Biol*. 24:1628-1635.

Braunwald, E. 2017. Cardiomyopathies: An Overview. *Circ Res*. 121:711-721.

Brugues, J., B. Maugis, J. Casademunt, P. Nassoy, F. Amblard, and P. Sens. 2010. Dynamical organization of the cytoskeletal cortex probed by micropipette aspiration. *Proc Natl Acad Sci U S A*. 107:15415-15420.

Burnette, D.T., S. Manley, P. Sengupta, R. Sougrat, M.W. Davidson, B. Kachar, and J. Lippincott-Schwartz. 2011. A role for actin arcs in the leading-edge advance of migrating cells. *Nat Cell Biol*. 13:371-381.

Burnette, D.T., L. Shao, C. Ott, A.M. Pasapera, R.S. Fischer, M.A. Baird, C. Der Loughian, H. Delanoe-Ayari, M.J. Paszek, M.W. Davidson, E. Betzig, and J. Lippincott-Schwartz. 2014. A contractile

and counterbalancing adhesion system controls the 3D shape of crawling cells. *The Journal of Cell Biology*. 205:83-96.
Burton, K., and D.L. Taylor. 1997. Traction forces of cytokinesis measured with optically modified elastic substrata. *Nature*. 385:450-454.
Caporizzo, M.A., C.Y. Chen, A.K. Salomon, K.B. Margulies, and B.L. Prosser. 2018. Microtubules Provide a Viscoelastic Resistance to Myocyte Motion. *Biophysical Journal*. 115:1796-1807.
Carisey, A., and C. Ballestrem. 2011. Vinculin, an adapter protein in control of cell adhesion signalling. *European journal of cell biology*. 90:157-163.
Carreno, S., I. Kouranti, E.S. Glusman, M.T. Fuller, A. Echard, and F. Payre. 2008. Moesin and its activating kinase Slik are required for cortical stability and microtubule organization in mitotic cells. *J Cell Biol*. 180:739-746.
Case, L.B., M.A. Baird, G. Shtengel, S.L. Campbell, H.F. Hess, M.W. Davidson, and C.M. Waterman. 2015. Molecular mechanism of vinculin activation and nanoscale spatial organization in focal adhesions. *Nat Cell Biol*. 17:880-892.
Charras, G., and E. Paluch. 2008. Blebs lead the way: how to migrate without lamellipodia. *Nat Rev Mol Cell Biol*. 9:730-736.
Charras, G.T., C.K. Hu, M. Coughlin, and T.J. Mitchison. 2006. Reassembly of contractile actin cortex in cell blebs. *J Cell Biol*. 175:477-490.
Chen, C.T., H. Hehnly, Q. Yu, D. Farkas, G. Zheng, S.D. Redick, H.F. Hung, R. Samtani, A. Jurczyk, S. Akbarian, C. Wise, A. Jackson, M. Bober, Y. Guo, C. Lo, and S. Doxsey. 2014. A unique set of centrosome proteins requires pericentrin for spindle-pole localization and spindle orientation. *Curr Biol*. 24:2327-2334.
Chopra, A., M.L. Kutys, K. Zhang, W.J. Polacheck, C.C. Sheng, R.J. Luu, J. Eyckmans, J.T. Hinson, J.G. Seidman, C.E. Seidman, and C.S. Chen. 2018. Force Generation via beta-Cardiac Myosin, Titin, and alpha-Actinin Drives Cardiac Sarcomere Assembly from Cell-Matrix Adhesions. *Dev Cell*. 44:87-96 e85.
Chugh, P., A.G. Clark, M.B. Smith, D.A.D. Cassani, K. Dierkes, A. Ragab, P.P. Roux, G. Charras, G. Salbreux, and E.K. Paluch. 2017. Actin cortex architecture regulates cell surface tension. *Nat Cell Biol*. 19:689-697.
Cianfrocco, M.A., M.E. DeSantis, A.E. Leschziner, and S.L. Reck-Peterson. 2015. Mechanism and regulation of cytoplasmic dynein. *Annu Rev Cell Dev Biol*. 31:83-108.
Ciobanasu, C., B. Faivre, and C. Le Clainche. 2014. Actomyosin-dependent formation of the mechanosensitive talin-vinculin complex reinforces actin anchoring. *Nat Commun*. 5:3095.
Cramer, L., and T.J. Mitchison. 1993. Moving and stationary actin filaments are involved in spreading of postmitotic PtK2 cells. *J Cell Biol*. 122:833-843.
Cunningham, C.C. 1995. Actin polymerization and intracellular solvent flow in cell surface blebbing. *J Cell Biol*. 129:1589-1599.
Dabiri, B.E., H. Lee, and K.K. Parker. 2012. A potential role for integrin signaling in mechanoelectrical feedback. *Prog Biophys Mol Biol*. 110:196-203.
Dabiri, G.A., K.K. Turnacioglu, J.M. Sanger, and J.W. Sanger. 1997. Myofibrillogenesis visualized in living embryonic cardiomyocytes. *Proceedings of the National Academy of Sciences of the United States of America*. 94:9493-9498.
Das, T., B. Payer, M. Cayouette, and W.A. Harris. 2003. In vivo time-lapse imaging of cell divisions during neurogenesis in the developing zebrafish retina. *Neuron*. 37:597-609.
Dasbiswas, K., S. Hu, A.D. Bershadsky, and S.A. Safran. 2019. Registry Kinetics of Myosin Motor Stacks Driven by Mechanical Force-Induced Actin Turnover. *Biophys J*. 117:856-866.
del Rio, A., R. Perez-Jimenez, R. Liu, P. Roca-Cusachs, J.M. Fernandez, and M.P. Sheetz. 2009. Stretching single talin rod molecules activates vinculin binding. *Science*. 323:638-641.
DeLaughter, D.M., A.G. Bick, H. Wakimoto, D. McKean, J.M. Gorham, I.S. Kathiriya, J.T. Hinson, J. Homsy, J. Gray, W. Pu, B.G. Bruneau, J.G. Seidman, and C.E. Seidman. 2016. Single-Cell Resolution of Temporal Gene Expression during Heart Development. *Developmental Cell*. 39:480-490.

DiMichele, L.A., J.T. Doherty, M. Rojas, H.E. Beggs, L.F. Reichardt, C.P. Mack, and J.M. Taylor. 2006. Myocyte-restricted focal adhesion kinase deletion attenuates pressure overload-induced hypertrophy. *Circ Res*. 99:636-645.

Dlugosz, A.A., P.B. Antin, V.T. Nachmias, and H. Holtzer. 1984. The relationship between stress fiber-like structures and nascent myofibrils in cultured cardiac myocytes. *The Journal of cell biology*. 99:2268-2278.

Donaudy, F., R. Snoeckx, M. Pfister, H.P. Zenner, N. Blin, M. Di Stazio, A. Ferrara, C. Lanzara, R. Ficarella, F. Declau, C.M. Pusch, P. Nurnberg, S. Melchionda, L. Zelante, E. Ballana, X. Estivill, G. Van Camp, P. Gasparini, and A. Savoia. 2004. Nonmuscle myosin heavy-chain gene MYH14 is expressed in cochlea and mutated in patients affected by autosomal dominant hearing impairment (DFNA4). *Am J Hum Genet*. 74:770-776.

Dumbauld, D.W., T.T. Lee, A. Singh, J. Scrimgeour, C.A. Gersbach, E.A. Zamir, J. Fu, C.S. Chen, J.E. Curtis, S.W. Craig, and A.J. Garcia. 2013. How vinculin regulates force transmission. *Proceedings of the National Academy of Sciences of the United States of America*. 110:9788-9793.

Engler, A.J., S. Sen, H.L. Sweeney, and D.E. Discher. 2006. Matrix elasticity directs stem cell lineage specification. *Cell*. 126:677-689.

Enserink, J.M., and R.D. Kolodner. 2010. An overview of Cdk1-controlled targets and processes. *Cell Div*. 5:11.

Fabry, B., A.H. Klemm, S. Kienle, T.E. Schäffer, and W.H. Goldmann. 2011. Focal adhesion kinase stabilizes the cytoskeleton. *Biophysical Journal*. 101:2131-2138.

Farina, F., J. Gaillard, C. Guerin, Y. Coute, J. Sillibourne, L. Blanchoin, and M. Thery. 2016. The centrosome is an actin-organizing centre. *Nat Cell Biol*. 18:65-75.

Fedorov, V.V., I.T. Lozinsky, E.A. Sosunov, E.P. Anyukhovsky, M.R. Rosen, C.W. Balke, and I.R. Efimov. 2007. Application of blebbistatin as an excitation-contraction uncoupler for electrophysiologic study of rat and rabbit hearts. *Heart Rhythm*. 4:619-626.

Fenix, A.M., A.C. Neininger, N. Taneja, K. Hyde, M.R. Visetsouk, R.J. Garde, B. Liu, B.R. Nixon, A.E. Manalo, J.R. Becker, S.W. Crawley, D.M. Bader, M.J. Tyska, Q. Liu, J.H. Gutzman, and D.T. Burnette. 2018. Muscle-specific stress fibers give rise to sarcomeres in cardiomyocytes. *Elife*. 7.

Fenix, A.M., N. Taneja, C.A. Buttler, J. Lewis, S.B. Van Engelenburg, R. Ohi, and D.T. Burnette. 2016. Expansion and concatenation of non-muscle myosin IIA filaments drive cellular contractile system formation during interphase and mitosis. *Mol Biol Cell*.

Fernandes, T., V.G. Barauna, C.E. Negrao, M.I. Phillips, and E.M. Oliveira. 2015. Aerobic exercise training promotes physiological cardiac remodeling involving a set of microRNAs. *Am J Physiol Heart Circ Physiol*. 309:H543-552.

Fernandez-Gonzalez, R., M. Simoes Sde, J.C. Roper, S. Eaton, and J.A. Zallen. 2009. Myosin II dynamics are regulated by tension in intercalating cells. *Dev Cell*. 17:736-743.

Fessenden, T.B., Y. Beckham, M. Perez-Neut, G. Ramirez-San Juan, A.H. Chourasia, K.F. Macleod, P.W. Oakes, and M.L. Gardel. 2018. Dia1-dependent adhesions are required by epithelial tissues to initiate invasion. *The Journal of cell biology*. 217:1485-1502.

Finer, J.T., R.M. Simmons, and J.A. Spudich. 1994. Single myosin molecule mechanics: piconewton forces and nanometre steps. *Nature*. 368:113-119.

Fink, J., N. Carpi, T. Betz, A. Bétard, M. Chebah, A. Azioune, M. Bornens, C. Sykes, L. Fetler, D. Cuvelier, and M. Piel. 2011. External forces control mitotic spindle positioning. *Nat Cell Biol*. 13:771-778.

Fishkind, D.J., and Y.L. Wang. 1993. Orientation and three-dimensional organization of actin filaments in dividing cultured cells. *The Journal of cell biology*. 123:837-848.

Friedland, J.C., M.H. Lee, and D. Boettiger. 2009. Mechanically activated integrin switch controls alpha5beta1 function. *Science*. 323:642-644.

Friedrich, B.M., A. Buxboim, D.E. Discher, and S.A. Safran. 2011. Striated acto-myosin fibers can reorganize and register in response to elastic interactions with the matrix. *Biophys J*. 100:2706-2715.

Fritzsche, M., C. Erlenkamper, E. Moeendarbary, G. Charras, and K. Kruse. 2016. Actin kinetics shapes cortical network structure and mechanics. *Sci Adv*. 2:e1501337.

Fu, J., I.M. Hagan, and D.M. Glover. 2015. The centrosome and its duplication cycle. *Cold Spring Harb Perspect Biol*. 7:a015800.
Fujiwara, K., and T.D. Pollard. 1976. Fluorescent antibody localization of myosin in the cytoplasm, cleavage furrow, and mitotic spindle of human cells. *J Cell Biol*. 71:848-875.
Fukuda, R., F. Gunawan, R. Ramadass, A. Beisaw, A. Konzer, S.T. Mullapudi, A. Gentile, H.M. Maischein, J. Graumann, and D.Y.R. Stainier. 2019. Mechanical Forces Regulate Cardiomyocyte Myofilament Maturation via the VCL-SSH1-CFL Axis. *Dev Cell*. 51:62-77 e65.
Gardel, M.L., K.E. Kasza, C.P. Brangwynne, J. Liu, and D.A. Weitz. 2008. Chapter 19: Mechanical response of cytoskeletal networks. *Methods Cell Biol*. 89:487-519.
Gardel, M.L., I.C. Schneider, Y. Aratyn-Schaus, and C.M. Waterman. 2010. Mechanical integration of actin and adhesion dynamics in cell migration. *Annu Rev Cell Dev Biol*. 26:315-333.
Geiger, B., J.P. Spatz, and A.D. Bershadsky. 2009. Environmental sensing through focal adhesions. *Nat Rev Mol Cell Biol*. 10:21-33.
Gibbs, C.L., and J.B. Chapman. 1985. Cardiac mechanics and energetics: Chemomechanical transduction in cardiac muscle. *American Journal of Physiology - Heart and Circulatory Physiology*. 18.
Glotzer, M. 2017. Cytokinesis in Metazoa and Fungi. *Cold Spring Harb Perspect Biol*. 9.
Golomb, E., X. Ma, S.S. Jana, Y.A. Preston, S. Kawamoto, N.G. Shoham, E. Goldin, M.A. Conti, J.R. Sellers, and R.S. Adelstein. 2004. Identification and characterization of nonmuscle myosin II-C, a new member of the myosin II family. *J Biol Chem*. 279:2800-2808.
Gordon, A.M., E. Homsher, and M. Regnier. 2000. Regulation of contraction in striated muscle. *Physiol Rev*. 80:853-924.
Goudarzi, M., T.U. Banisch, M.B. Mobin, N. Maghelli, K. Tarbashevich, I. Strate, J. van den Berg, H. Blaser, S. Bandemer, E. Paluch, J. Bakkers, I.M. Tolic-Norrelykke, and E. Raz. 2012. Identification and regulation of a molecular module for bleb-based cell motility. *Dev Cell*. 23:210-218.
Goulas, S., R. Conder, and J.A. Knoblich. 2012. The Par complex and integrins direct asymmetric cell division in adult intestinal stem cells. *Cell Stem Cell*. 11:529-540.
Graham, D.M., and K. Burridge. 2016. Mechanotransduction and nuclear function. *Curr Opin Cell Biol*. 40:98-105.
Granzier, H.L., and T.C. Irving. 1995. Passive tension in cardiac muscle: contribution of collagen, titin, microtubules, and intermediate filaments. *Biophys J*. 68:1027-1044.
Granzier, H.L., and S. Labeit. 2004. The Giant Protein Titin. *Circulation Research*. 94:284-295.
Green, R.A., E. Paluch, and K. Oegema. 2012. Cytokinesis in animal cells. *Annu Rev Cell Dev Biol*. 28:29-58.
Guha, M., M. Zhou, and Y.L. Wang. 2005. Cortical actin turnover during cytokinesis requires myosin II. *Curr Biol*. 15:732-736.
Guillot, C., and T. Lecuit. 2013. Adhesion disengagement uncouples intrinsic and extrinsic forces to drive cytokinesis in epithelial tissues. *Dev Cell*. 24:227-241.
Gupton, S.L., and C.M. Waterman-Storer. 2006. Spatiotemporal feedback between actomyosin and focal-adhesion systems optimizes rapid cell migration. *Cell*. 125:1361-1374.
Gustafsson, M.G. 2005. Nonlinear structured-illumination microscopy: wide-field fluorescence imaging with theoretically unlimited resolution. *Proc Natl Acad Sci U S A*. 102:13081-13086.
Harris, T.J., and U. Tepass. 2010. Adherens junctions: from molecules to morphogenesis. *Nat Rev Mol Cell Biol*. 11:502-514.
He, Z.H., R. Bottinelli, M.A. Pellegrino, M.A. Ferenczi, and C. Reggiani. 2000. ATP consumption and efficiency of human single muscle fibers with different myosin isoform composition. *Biophysical Journal*. 79:945-961.
Heer, N.C., and A.C. Martin. 2017. Tension, contraction and tissue morphogenesis. *Development*. 144:4249-4260.
Hehnly, H., D. Canton, P. Bucko, L.K. Langeberg, L. Ogier, I. Gelman, L.F. Santana, L. Wordeman, and J.D. Scott. 2015. A mitotic kinase scaffold depleted in testicular seminomas impacts spindle orientation in germ line stem cells. *Elife*. 4:e09384.

Hersch, N., B. Wolters, G. Dreissen, R. Springer, N. Kirchgessner, R. Merkel, and B. Hoffmann. 2013. The constant beat: cardiomyocytes adapt their forces by equal contraction upon environmental stiffening. *Biol Open*. 2:351-361.
Hershberger, R.E., D.J. Hedges, and A. Morales. 2013. Dilated cardiomyopathy: the complexity of a diverse genetic architecture. *Nat Rev Cardiol*. 10:531-547.
Hinchcliffe, E.H., E.A. Thompson, F.J. Miller, J. Yang, and G. Sluder. 1999. Nucleo-cytoplasmic interactions that control nuclear envelope breakdown and entry into mitosis in the sea urchin zygote. *J Cell Sci*. 112 (Pt 8):1139-1148.
Horton, E.R., J.D. Humphries, J. James, M.C. Jones, J.A. Askari, and M.J. Humphries. 2016. The integrin adhesome network at a glance. *J Cell Sci*. 129:4159-4163.
Hotulainen, P., and P. Lappalainen. 2006. Stress fibers are generated by two distinct actin assembly mechanisms in motile cells. *The Journal of Cell Biology*. 173:383-394.
Hresko, M.C., B.D. Williams, and R.H. Waterston. 1994. Assembly of body wall muscle and muscle cell attachment structures in Caenorhabditis elegans. *The Journal of cell biology*. 124:491-506.
Huang, D.L., N.A. Bax, C.D. Buckley, W.I. Weis, and A.R. Dunn. 2017. Vinculin forms a directionally asymmetric catch bond with F-actin. *Science*. 357:703-706.
Hung, H.F., H. Hehnly, and S. Doxsey. 2016. The Mother Centriole Appendage Protein Cenexin Modulates Lumen Formation through Spindle Orientation. *Curr Biol*. 26:1248.
Hynes, R.O. 2002. Integrins: bidirectional, allosteric signaling machines. *Cell*. 110:673-687.
Izumi, H., and Y. Kaneko. 2012. Evidence of asymmetric cell division and centrosome inheritance in human neuroblastoma cells. *Proc Natl Acad Sci U S A*. 109:18048-18053.
Jacot, J.G., A.D. McCulloch, and J.H. Omens. 2008. Substrate stiffness affects the functional maturation of neonatal rat ventricular myocytes. *Biophys J*. 95:3479-3487.
Janostiak, R., A.C. Pataki, J. Brabek, and D. Rosel. 2014. Mechanosensors in integrin signaling: the emerging role of p130Cas. *European journal of cell biology*. 93:445-454.
Januschke, J., S. Llamazares, J. Reina, and C. Gonzalez. 2011. Drosophila neuroblasts retain the daughter centrosome. *Nat Commun*. 2:243.
Jefferson, J.J., C.L. Leung, and R.K. Liem. 2004. Plakins: goliaths that link cell junctions and the cytoskeleton. *Nat Rev Mol Cell Biol*. 5:542-553.
Jiang, Y., P. Park, S.M. Hong, and K. Ban. 2018. Maturation of Cardiomyocytes Derived from Human Pluripotent Stem Cells: Current Strategies and Limitations. *Mol Cells*. 41:613-621.
Jinguji, Y., and H. Ishikawa. 1992. Electron microscopic observations on the maintenance of the tight junction during cell division in the epithelium of the mouse small intestine. *Cell Struct Funct*. 17:27-37.
Jonckheere, V., D. Fijalkowska, and P. Van Damme. 2018. Omics Assisted N-terminal Proteoform and Protein Expression Profiling On Methionine Aminopeptidase 1 (MetAP1) Deletion. *Mol Cell Proteomics*. 17:694-708.
Jones, M.C., J.A. Askari, J.D. Humphries, and M.J. Humphries. 2018. Cell adhesion is regulated by CDK1 during the cell cycle. *J Cell Biol*. 217:3203-3218.
Kanada, M., A. Nagasaki, and T.Q. Uyeda. 2005. Adhesion-dependent and contractile ring-independent equatorial furrowing during cytokinesis in mammalian cells. *Mol Biol Cell*. 16:3865-3872.
Kanchanawong, P., G. Shtengel, A.M. Pasapera, E.B. Ramko, M.W. Davidson, H.F. Hess, and C.M. Waterman. 2010. Nanoscale architecture of integrin-based cell adhesions. *Nature*. 468:580-584.
Kang, Y., W. Hu, C. Ivan, H.J. Dalton, T. Miyake, C.V. Pecot, B. Zand, T. Liu, J. Huang, N.B. Jennings, R. Rupaimoole, M. Taylor, S. Pradeep, S.Y. Wu, C. Lu, Y. Wen, J. Huang, J. Liu, and A.K. Sood. 2013. Article role of Focal Adhesion Kinase in regulating YB-1-Mediated Paclitaxel resistance in Ovarian cancer.
Katagiri, K., and T. Kinashi. 2012. Rap1 and integrin inside-out signaling. *Methods Mol Biol*. 757:279-296.
Katsumi, A., T. Naoe, T. Matsushita, K. Kaibuchi, and M.A. Schwartz. 2005. Integrin activation and matrix binding mediate cellular responses to mechanical stretch. *The Journal of biological chemistry*. 280:16546-16549.
Kee, Y.S., and D.N. Robinson. 2013. Micropipette aspiration for studying cellular mechanosensory responses and mechanics. *Methods Mol Biol*. 983:367-382.

Kim, C., F. Ye, and M.H. Ginsberg. 2011. Regulation of integrin activation. *Annu Rev Cell Dev Biol*. 27:321-345.
Kiyomitsu, T., and I.M. Cheeseman. 2012. Chromosome- and spindle-pole-derived signals generate an intrinsic code for spindle position and orientation. *Nature cell biology*. 14:311-317.
Knoll, R., B. Buyandelger, and M. Lab. 2011. The sarcomeric Z-disc and Z-discopathies. *J Biomed Biotechnol*. 2011:569628.
Kosodo, Y., K. Röper, W. Haubensak, A.M. Marzesco, D. Corbeil, and W.B. Huttner. 2004. Asymmetric distribution of the apical plasma membrane during neurogenic divisions of mammalian neuroepithelial cells. *The EMBO Journal*. 23:2314-2324.
Koteliansky, V.E., and G.N. Gneushev. 1983. Vinculin localization in cardiac muscle. *FEBS Lett*. 159:158-160.
Kovacic-Milivojevic, B., F. Roediger, E.A. Almeida, C.H. Damsky, D.G. Gardner, and D. Ilic. 2001. Focal adhesion kinase and p130Cas mediate both sarcomeric organization and activation of genes associated with cardiac myocyte hypertrophy. *Mol Biol Cell*. 12:2290-2307.
Kovacs, M., F. Wang, A. Hu, Y. Zhang, and J.R. Sellers. 2003. Functional divergence of human cytoplasmic myosin II: kinetic characterization of the non-muscle IIA isoform. *J Biol Chem*. 278:38132-38140.
Kulke, M., S. Fujita-Becker, E. Rostkova, C. Neagoe, D. Labeit, D.J. Manstein, M. Gautel, and W.A. Linke. 2001. Interaction betweeen PEVK-titin and actin filaments origin of a viscous force component in cardiac myofibrils. *Circulation Research*. 89:874-881.
Kumar, S., I.Z. Maxwell, A. Heisterkamp, T.R. Polte, T.P. Lele, M. Salanga, E. Mazur, and D.E. Ingber. 2006. Viscoelastic retraction of single living stress fibers and its impact on cell shape, cytoskeletal organization, and extracellular matrix mechanics. *Biophysical Journal*. 90:3762-3773.
Kuo, T.C., C.T. Chen, D. Baron, T.T. Onder, S. Loewer, S. Almeida, C.M. Weismann, P. Xu, J.M. Houghton, F.B. Gao, G.Q. Daley, and S. Doxsey. 2011. Midbody accumulation through evasion of autophagy contributes to cellular reprogramming and tumorigenicity. *Nat Cell Biol*. 13:1214-1223.
Kuppusamy, K.T., D.C. Jones, H. Sperber, A. Madan, K.A. Fischer, M.L. Rodriguez, L. Pabon, W.Z. Zhu, N.L. Tulloch, X. Yang, N.J. Sniadecki, M.A. Laflamme, W.L. Ruzzo, C.E. Murry, and H. Ruohola-Baker. 2015. Let-7 family of microRNA is required for maturation and adult-like metabolism in stem cell-derived cardiomyocytes. *Proceedings of the National Academy of Sciences of the United States of America*. 112:E2785-E2794.
Kwon, M., M. Bagonis, G. Danuser, and D. Pellman. 2015. Direct Microtubule-Binding by Myosin-10 Orients Centrosomes toward Retraction Fibers and Subcortical Actin Clouds. *Dev Cell*. 34:323-337.
Lange, B.M., and K. Gull. 1995. A molecular marker for centriole maturation in the mammalian cell cycle. *J Cell Biol*. 130:919-927.
Lee, G.Y., P.A. Kenny, E.H. Lee, and M.J. Bissell. 2007. Three-dimensional culture models of normal and malignant breast epithelial cells. *Nat Methods*. 4:359-365.
Lee, S., E. Kassianidou, and S. Kumar. 2018. Actomyosin stress fiber subtypes have unique viscoelastic properties and roles in tension generation. *Molecular Biology of the Cell*. 29:1992-2004.
Lehtimäki, J., E. Rajakylä, S. Tojkander, and P. Lappalainen. 2020. Generation of stress fibers through myosin-driven re-organization of the actin cortex. *bioRxiv*:2020.2006.2030.179283.
Lemke, S.B., and F. Schnorrer. 2017. Mechanical forces during muscle development. *Mechanisms of development*. 144:92-101.
Lemke, S.B., T. Weidemann, A.L. Cost, C. Grashoff, and F. Schnorrer. 2019. A small proportion of Talin molecules transmit forces at developing muscle attachments in vivo. *PLoS biology*. 17:e3000057.
Levayer, R., and T. Lecuit. 2012. Biomechanical regulation of contractility: spatial control and dynamics. *Trends Cell Biol*. 22:61-81.

Linke, W.A., and J.M. Fernandez. 2002. Cardiac titin: Molecular basis of elasticity and cellular contribution to elastic and viscous stiffness components in myocardium. *Journal of Muscle Research and Cell Motility*. 23:483-497.
Liu, H., and J.H. Naismith. 2008. An efficient one-step site-directed deletion, insertion, single and multiple-site plasmid mutagenesis protocol. *BMC Biotechnol*. 8:91.
Liu, H., W. Qin, Z. Wang, Y. Shao, J. Wang, T.K. Borg, B.Z. Gao, and M. Xu. 2016. Disassembly of myofibrils and potential imbalanced forces on Z-discs in cultured adult cardiomyocytes. *Cytoskeleton (Hoboken)*. 73:246-257.
Loison, O., M. Weitkunat, A. Kaya-Copur, C. Nascimento Alves, T. Matzat, M.L. Spletter, S. Luschnig, S. Brasselet, P.F. Lenne, and F. Schnorrer. 2018. Polarization-resolved microscopy reveals a muscle myosin motor-independent mechanism of molecular actin ordering during sarcomere maturation. *PLoS biology*. 16:e2004718.
Lordier, L., D. Bluteau, A. Jalil, C. Legrand, J. Pan, P. Rameau, D. Jouni, O. Bluteau, T. Mercher, C. Leon, C. Gachet, N. Debili, W. Vainchenker, H. Raslova, and Y. Chang. 2012. RUNX1-induced silencing of non-muscle myosin heavy chain IIB contributes to megakaryocyte polyploidization. *Nat Commun*. 3:717.
Lu, M.H., C. DiLullo, T. Schultheiss, S. Holtzer, J.M. Murray, J. Choi, D.A. Fischman, and H. Holtzer. 1992. The vinculin/sarcomeric-alpha-actinin/alpha-actin nexus in cultured cardiac myocytes. *The Journal of cell biology*. 117:1007-1022.
Machacek, M., L. Hodgson, C. Welch, H. Elliott, O. Pertz, P. Nalbant, A. Abell, G.L. Johnson, K.M. Hahn, and G. Danuser. 2009. Coordination of Rho GTPase activities during cell protrusion. *Nature*. 461:99-103.
Maddox, A.S., and K. Burridge. 2003. RhoA is required for cortical retraction and rigidity during mitotic cell rounding. *J Cell Biol*. 160:255-265.
Marchesi, S., F. Montani, G. Deflorian, R. D'Antuono, A. Cuomo, S. Bologna, C. Mazzoccoli, T. Bonaldi, P.P. Di Fiore, and F. Nicassio. 2014. DEPDC1B coordinates de-adhesion events and cell-cycle progression at mitosis. *Dev Cell*. 31:420-433.
Martin, A.C., M. Kaschube, and E.F. Wieschaus. 2009. Pulsed contractions of an actin-myosin network drive apical constriction. *Nature*. 457:495-499.
Maruyama, K. 1997. Connectin/titin, giant elastic protein of muscle. *The FASEB Journal*. 11:341-345.
McCain, M.L., H. Lee, Y. Aratyn-Schaus, A.G. Kleber, and K.K. Parker. 2012. Cooperative coupling of cell-matrix and cell-cell adhesions in cardiac muscle. *Proceedings of the National Academy of Sciences of the United States of America*. 109:9881-9886.
Melli, L., N. Billington, S.A. Sun, J.E. Bird, A. Nagy, T.B. Friedman, Y. Takagi, and J.R. Sellers. 2018. Bipolar filaments of human nonmuscle myosin 2-A and 2-B have distinct motile and mechanical properties. *Elife*. 7.
Mentes, A., A. Huehn, X. Liu, A. Zwolak, R. Dominguez, H. Shuman, E.M. Ostap, and C.V. Sindelar. 2018. High-resolution cryo-EM structures of actin-bound myosin states reveal the mechanism of myosin force sensing. *Proc Natl Acad Sci U S A*. 115:1292-1297.
Mierke, C.T., T. Fischer, S. Puder, T. Kunschmann, B. Soetje, and W.H. Ziegler. 2017. Focal adhesion kinase activity is required for actomyosin contractility-based invasion of cells into dense 3D matrices. *Scientific Reports*. 7:1-18.
Milberg, O., A. Shitara, S. Ebrahim, A. Masedunskas, M. Tora, D.T. Tran, Y. Chen, M.A. Conti, R.S. Adelstein, K.G. Ten Hagen, and R. Weigert. 2017. Concerted actions of distinct nonmuscle myosin II isoforms drive intracellular membrane remodeling in live animals. *J Cell Biol*. 216:1925-1936.
Mitchison, T.J. 1992. Actin based motility on retraction fibers in mitotic PtK2 cells. *Cell Motil Cytoskeleton*. 22:135-151.
Murakami, N., P. Mehta, and M. Elzinga. 1991. Studies on the distribution of cellular myosin with antibodies to isoform-specific synthetic peptides. *FEBS Lett*. 288:247.
Murakami, N., S.S. Singh, V.P. Chauhan, and M. Elzinga. 1995. Phospholipid binding, phosphorylation by protein kinase C, and filament assembly of the COOH terminal heavy chain fragments of nonmuscle myosin II isoforms MIIA and MIIB. *Biochemistry*. 34:16046-16055.

Murrell, M., P.W. Oakes, M. Lenz, and M.L. Gardel. 2015. Forcing cells into shape: the mechanics of actomyosin contractility. *Nat Rev Mol Cell Biol*. 16:486-498.
Murrell, M.P., and M.L. Gardel. 2012. F-actin buckling coordinates contractility and severing in a biomimetic actomyosin cortex. *Proc Natl Acad Sci U S A*. 109:20820-20825.
Murugesan, S., J. Hong, J. Yi, D. Li, J.R. Beach, L. Shao, J. Meinhardt, G. Madison, X. Wu, E. Betzig, and J.A. Hammer. 2016. Formin-generated actomyosin arcs propel T cell receptor microcluster movement at the immune synapse. *J Cell Biol*. 215:383-399.
Nakasawa, T., M. Takahashi, F. Matsuzawa, S. Aikawa, Y. Togashi, T. Saitoh, A. Yamagishi, and M. Yazawa. 2005. Critical regions for assembly of vertebrate nonmuscle myosin II. *Biochemistry*. 44:174-183.
Nam, S., and O. Chaudhuri. 2018. Mitotic cells generate protrusive extracellular forces to divide in three-dimensional microenvironments. *Nature Physics*. 14:621-628.
Neujahr, R., C. Heizer, and G. Gerisch. 1997. Myosin II-independent processes in mitotic cells of Dictyostelium discoideum: redistribution of the nuclei, re-arrangement of the actin system and formation of the cleavage furrow. *J Cell Sci*. 110 (Pt 2):123-137.
O'Brien, S., V.M. Golubovskaya, J. Conroy, S. Liu, D. Wang, B. Liu, and W.G. Cance. 2014. FAK inhibition with small molecule inhibitor Y15 decreases viability, clonogenicity, and cell attachment in thyroid cancer cell lines and synergizes with targeted therapeutics. *Oncotarget*. 5:7945-7959.
O'Connell, C.B., M.J. Tyska, and M.S. Mooseker. 2007. Myosin at work: motor adaptations for a variety of cellular functions. *Biochim Biophys Acta*. 1773:615-630.
Palazzo, A.F., C.H. Eng, D.D. Schlaepfer, E.E. Marcantonio, and G.G. Gundersen. 2004. Localized stabilization of microtubules by integrin- and FAK-facilitated Rho signaling. *Science*. 303:836-839.
Paluch, E., M. Piel, J. Prost, M. Bornens, and C. Sykes. 2005. Cortical actomyosin breakage triggers shape oscillations in cells and cell fragments. *Biophys J*. 89:724-733.
Paoli, P., E. Giannoni, and P. Chiarugi. 2013. Anoikis molecular pathways and its role in cancer progression. *Biochim Biophys Acta*. 1833:3481-3498.
Paridaen, J.T.M.L., M. Wilsch-Bräuninger, and W.B. Huttner. 2013. Asymmetric inheritance of centrosome-associated primary cilium membrane directs ciliogenesis after cell division. *Cell*. 155:333-344.
Parsons, J.T., K.H. Martin, J.K. Slack, J.M. Taylor, and S.A. Weed. 2000. Focal adhesion kinase: a regulator of focal adhesion dynamics and cell movement. *Oncogene*. 19:5606-5613.
Pasapera, A.M., I.C. Schneider, E. Rericha, D.D. Schlaepfer, and C.M. Waterman. 2010. Myosin II activity regulates vinculin recruitment to focal adhesions through FAK-mediated paxillin phosphorylation. *The Journal of cell biology*. 188:877-890.
Paszek, M.J., C.C. DuFort, M.G. Rubashkin, M.W. Davidson, K.S. Thorn, J.T. Liphardt, and V.M. Weaver. 2012. Scanning angle interference microscopy reveals cell dynamics at the nanoscale. *Nat Methods*. 9:825-827.
Peng, X., M.S. Kraus, H. Wei, T.L. Shen, R. Pariaut, A. Alcaraz, G. Ji, L. Cheng, Q. Yang, M.I. Kotlikoff, J. Chen, K. Chien, H. Gu, and J.L. Guan. 2006. Inactivation of focal adhesion kinase in cardiomyocytes promotes eccentric cardiac hypertrophy and fibrosis in mice. *J Clin Invest*. 116:217-227.
Petridou, N.I., and P.A. Skourides. 2016. A ligand-independent integrin beta1 mechanosensory complex guides spindle orientation. *Nat Commun*. 7:10899.
Piel, M., P. Meyer, A. Khodjakov, C.L. Rieder, and M. Bornens. 2000. The Respective Contributions of the Mother and Daughter Centrioles to Centrosome Activity and Behavior in Vertebrate Cells. *The Journal of Cell Biology*. 149:317-330.
Pollard, T.D., and J.A. Cooper. 2009. Actin, a central player in cell shape and movement. *Science*. 326:1208-1212.
Prosser, S.L., and L. Pelletier. 2017. Mitotic spindle assembly in animal cells: a fine balancing act. *Nat Rev Mol Cell Biol*. 18:187-201.
Quach, N.L., and T.A. Rando. 2006. Focal adhesion kinase is essential for costamerogenesis in cultured skeletal muscle cells. *Dev Biol*. 293:38-52.

Quyn, A.J., P.L. Appleton, F.A. Carey, R.J. Steele, N. Barker, H. Clevers, R.A. Ridgway, O.J. Sansom, and I.S. Nathke. 2010. Spindle orientation bias in gut epithelial stem cell compartments is lost in precancerous tissue. *Cell Stem Cell*. 6:175-181.
Ramanathan, S.P., J. Helenius, M.P. Stewart, C.J. Cattin, A.A. Hyman, and D.J. Muller. 2015. Cdk1-dependent mitotic enrichment of cortical myosin II promotes cell rounding against confinement. *Nat Cell Biol*. 17:148-159.
Ramkumar, N., and B. Baum. 2016. Coupling changes in cell shape to chromosome segregation. *Nat Rev Mol Cell Biol*. 17:511-521.
Reya, T., S.J. Morrison, M.F. Clarke, and I.L. Weissman. 2001. Stem cells, cancer, and cancer stem cells. *Nature*. 414:105-111.
Rhee, D., J.M. Sanger, and J.W. Sanger. 1994. The premyofibril: evidence for its role in myofibrillogenesis. *Cell Motil Cytoskeleton*. 28:1-24.
Riveline, D., E. Zamir, N.Q. Balaban, U.S. Schwarz, T. Ishizaki, S. Narumiya, Z. Kam, B. Geiger, and A.D. Bershadsky. 2001. Focal contacts as mechanosensors: externally applied local mechanical force induces growth of focal contacts by an mDia1-dependent and ROCK-independent mechanism. *The Journal of cell biology*. 153:1175-1186.
Rosenfeld, S.S., J. Xing, L.Q. Chen, and H.L. Sweeney. 2003. Myosin IIb is unconventionally conventional. *J Biol Chem*. 278:27449-27455.
Roth, M., C. Roubinet, N. Ifflander, A. Ferrand, and C. Cabernard. 2015. Asymmetrically dividing Drosophila neuroblasts utilize two spatially and temporally independent cytokinesis pathways. *Nat Commun*. 6:6551.
Salbreux, G., G. Charras, and E. Paluch. 2012. Actin cortex mechanics and cellular morphogenesis. *Trends Cell Biol*. 22:536-545.
Samarel, A.M. 2005. Costameres, focal adhesions, and cardiomyocyte mechanotransduction. *Am J Physiol Heart Circ Physiol*. 289:H2291-2301.
Sandquist, J.C., and A.R. Means. 2008. The C-terminal tail region of nonmuscle myosin II directs isoform-specific distribution in migrating cells. *Mol Biol Cell*. 19:5156-5167.
Sanger, J.W., S. Kang, C.C. Siebrands, N. Freeman, A. Du, J. Wang, A.L. Stout, and J.M. Sanger. 2005. How to build a myofibril. *J Muscle Res Cell Motil*. 26:343-354.
Sanger, J.W., and J.M. Sanger. 1980. Surface and shape changes during cell division. *Cell Tissue Res*. 209:177-186.
Schaller, M.D., J.D. Hildebrand, J.D. Shannon, J.W. Fox, R.R. Vines, and J.T. Parsons. 1994. Autophosphorylation of the focal adhesion kinase, pp125FAK, directs SH2-dependent binding of pp60src. *Mol Cell Biol*. 14:1680-1688.
Schermelleh, L., P.M. Carlton, S. Haase, L. Shao, L. Winoto, P. Kner, B. Burke, M.C. Cardoso, D.A. Agard, M.G. Gustafsson, H. Leonhardt, and J.W. Sedat. 2008. Subdiffraction multicolor imaging of the nuclear periphery with 3D structured illumination microscopy. *Science*. 320:1332-1336.
Schiffhauer, E.S., Y. Ren, V.A. Iglesias, P. Kothari, P.A. Iglesias, and D.N. Robinson. 2019. Myosin IIB assembly state determines its mechanosensitive dynamics. *J Cell Biol*. 218:895-908.
Schwander, M., M. Leu, M. Stumm, O.M. Dorchies, U.T. Ruegg, J. Schittny, and U. Muller. 2003. Beta1 integrins regulate myoblast fusion and sarcomere assembly. *Dev Cell*. 4:673-685.
Sedzinski, J., M. Biro, A. Oswald, J.Y. Tinevez, G. Salbreux, and E. Paluch. 2011. Polar actomyosin contractility destabilizes the position of the cytokinetic furrow. *Nature*. 476:462-466.
Sezgin, E., I. Levental, S. Mayor, and C. Eggeling. 2017. The mystery of membrane organization: composition, regulation and roles of lipid rafts. *Nat Rev Mol Cell Biol*. 18:361-374.
Sharp, W.W., D.G. Simpson, T.K. Borg, A.M. Samarel, and L. Terracio. 1997. Mechanical forces regulate focal adhesion and costamere assembly in cardiac myocytes. *Am J Physiol*. 273:H546-556.
Shutova, M.S., W.A. Spessott, C.G. Giraudo, and T. Svitkina. 2014. Endogenous species of mammalian nonmuscle myosin IIA and IIB include activated monomers and heteropolymers. *Curr Biol*. 24:1958-1968.
Simpson, D.G., M.L. Decker, W.A. Clark, and R.S. Decker. 1993. Contractile activity and cell-cell contact regulate myofibrillar organization in cultured cardiac myocytes. *The Journal of cell biology*. 123:323-336.

Slack-Davis, J.K., K.H. Martin, R.W. Tilghman, M. Iwanicki, E.J. Ung, C. Autry, M.J. Luzzio, B. Cooper, J.C. Kath, W.G. Roberts, and J.T. Parsons. 2007. Cellular Characterization of a Novel Focal Adhesion Kinase Inhibitor. *Journal of Biological Chemistry*. 282:14845-14852.
So, E.C., K.C. Wu, C.H. Liang, J.Y. Chen, and S.N. Wu. 2011. Evidence for activation of BK Ca channels by a known inhibitor of focal adhesion kinase, PF573228. *Life Sciences*. 89:691-701.
Soung, N.-K., J.-E. Park, L.-R. Yu, K.H. Lee, J.-M. Lee, J.K. Bang, T.D. Veenstra, K. Rhee, and K.S. Lee. 2009. Plk1-dependent and -independent roles of an ODF2 splice variant, hCenexin1, at the centrosome of somatic cells. *Developmental cell*. 16:539-550.
Sparrow, J.C., and F. Schock. 2009. The initial steps of myofibril assembly: integrins pave the way. *Nat Rev Mol Cell Biol*. 10:293-298.
Spira, F., S. Cuylen-Haering, S. Mehta, M. Samwer, A. Reversat, A. Verma, R. Oldenbourg, M. Sixt, and D.W. Gerlich. 2017. Cytokinesis in vertebrate cells initiates by contraction of an equatorial actomyosin network composed of randomly oriented filaments. *Elife*. 6.
Stam, S., J. Alberts, M.L. Gardel, and E. Munro. 2015. Isoforms Confer Characteristic Force Generation and Mechanosensation by Myosin II Filaments. *Biophys J*. 108:1997-2006.
Stepanek, L., and G. Pigino. 2016. Microtubule doublets are double-track railways for intraflagellar transport trains. *Science*. 352:721-724.
Stewart, M.P., J. Helenius, Y. Toyoda, S.P. Ramanathan, D.J. Muller, and A.A. Hyman. 2011. Hydrostatic pressure and the actomyosin cortex drive mitotic cell rounding. *Nature*. 469:226-230.
Straight, A.F., A. Cheung, J. Limouze, I. Chen, N.J. Westwood, J.R. Sellers, and T.J. Mitchison. 2003. Dissecting temporal and spatial control of cytokinesis with a myosin II Inhibitor. *Science*. 299:1743-1747.
Straight, A.F., C.M. Field, and T.J. Mitchison. 2005. Anillin binds nonmuscle myosin II and regulates the contractile ring. *Mol Biol Cell*. 16:193-201.
Sulzmaier, F.J., C. Jean, and D.D. Schlaepfer. 2014. FAK in cancer: mechanistic findings and clinical applications. *Nat Rev Cancer*. 14:598-610.
Surcel, A., Y.S. Kee, T. Luo, and D.N. Robinson. 2010. Cytokinesis through biochemical-mechanical feedback loops. *Semin Cell Dev Biol*. 21:866-873.
Svitkina, T.M. 2020. Actin Cell Cortex: Structure and Molecular Organization. *Trends Cell Biol*. 30:556-565.
Svitkina, T.M., A.B. Verkhovsky, K.M. McQuade, and G.G. Borisy. 1997. Analysis of the actin-myosin II system in fish epidermal keratocytes: mechanism of cell body translocation. *J Cell Biol*. 139:397-415.
Swaminathan, V., J.M. Kalappurakkal, S.B. Mehta, P. Nordenfelt, T.I. Moore, N. Koga, D.A. Baker, R. Oldenbourg, T. Tani, S. Mayor, T.A. Springer, and C.M. Waterman. 2017. Actin retrograde flow actively aligns and orients ligand-engaged integrins in focal adhesions. *Proceedings of the National Academy of Sciences of the United States of America*. 114:10648-10653.
Tan, C.L., J.C. Kwok, J.P. Heller, R. Zhao, R. Eva, and J.W. Fawcett. 2015. Full length talin stimulates integrin activation and axon regeneration. *Mol Cell Neurosci*. 68:1-8.
Taneja, N., M.R. Bersi, S.M. Baillargeon, A.M. Fenix, J.A. Cooper, R. Ohi, V. Gama, W.D. Merryman, and D.T. Burnette. 2020a. Precise Tuning of Cortical Contractility Regulates Cell Shape during Cytokinesis. *Cell Rep*. 31:107477.
Taneja, N., and D.T. Burnette. 2019. Myosin IIA drives membrane bleb retraction. *Mol Biol Cell*. 30:1051-1059.
Taneja, N., A.M. Fenix, L. Rathbun, B.A. Millis, M.J. Tyska, H. Hehnly, and D.T. Burnette. 2016. Focal adhesions control cleavage furrow shape and spindle tilt during mitosis. *Sci Rep*. 6:29846.
Taneja, N., A.C. Neininger, and D.T. Burnette. 2020b. Coupling to substrate adhesions drives the maturation of muscle stress fibers into myofibrils within cardiomyocytes. *Molecular Biology of the Cell*:mbc.E19-11-0652.
Tapia-Rojo, R., A. Alonso-Caballero, and J.M. Fernandez. 2020. Direct observation of a coil-to-helix contraction triggered by vinculin binding to talin. *Sci Adv*. 6:eaaz4707.
Thery, M., V. Racine, A. Pepin, M. Piel, Y. Chen, J.B. Sibarita, and M. Bornens. 2005. The extracellular matrix guides the orientation of the cell division axis. *Nat Cell Biol*. 7:947-953.

Thievessen, I., P.M. Thompson, S. Berlemont, K.M. Plevock, S.V. Plotnikov, A. Zemljic-Harpf, R.S. Ross, M.W. Davidson, G. Danuser, S.L. Campbell, and C.M. Waterman. 2013. Vinculin-actin interaction couples actin retrograde flow to focal adhesions, but is dispensable for focal adhesion growth. *The Journal of cell biology*. 202:163-177.

Tinevez, J.Y., U. Schulze, G. Salbreux, J. Roensch, J.F. Joanny, and E. Paluch. 2009. Role of cortical tension in bleb growth. *Proc Natl Acad Sci U S A*. 106:18581-18586.

Tojkander, S., G. Gateva, A. Husain, R. Krishnan, and P. Lappalainen. 2015. Generation of contractile actomyosin bundles depends on mechanosensitive actin filament assembly and disassembly. *Elife*. 4:e06126.

Tojkander, S., G. Gateva, and P. Lappalainen. 2012. Actin stress fibers--assembly, dynamics and biological roles. *J Cell Sci*. 125:1855-1864.

Toyoshima, F., and E. Nishida. 2007. Integrin-mediated adhesion orients the spindle parallel to the substratum in an EB1- and myosin X-dependent manner. *Embo j*. 26:1487-1498.

Tsankova, A., T.T. Pham, D.S. Garcia, F. Otte, and C. Cabernard. 2017. Cell Polarity Regulates Biased Myosin Activity and Dynamics during Asymmetric Cell Division via Drosophila Rho Kinase and Protein Kinase N. *Dev Cell*. 42:143-155 e145.

Tullio, A.N., D. Accili, V.J. Ferrans, Z.X. Yu, K. Takeda, A. Grinberg, H. Westphal, Y.A. Preston, and R.S. Adelstein. 1997. Nonmuscle myosin II-B is required for normal development of the mouse heart. *Proc Natl Acad Sci U S A*. 94:12407-12412.

Uroz, M., S. Wistorf, X. Serra-Picamal, V. Conte, M. Sales-Pardo, P. Roca-Cusachs, R. Guimera, and X. Trepat. 2018. Regulation of cell cycle progression by cell-cell and cell-matrix forces. *Nat Cell Biol*. 20:646-654.

Vianay, B., F. Senger, S. Alamos, M. Anjur-Dietrich, E. Bearce, B. Cheeseman, L. Lee, and M. Thery. 2018. Variation in traction forces during cell cycle progression. *Biol Cell*. 110:91-96.

Vicente-Manzanares, M., M.A. Koach, L. Whitmore, M.L. Lamers, and A.F. Horwitz. 2008. Segregation and activation of myosin IIB creates a rear in migrating cells. *J Cell Biol*. 183:543-554.

Volk, T., L.I. Fessler, and J.H. Fessler. 1990. A role for integrin in the formation of sarcomeric cytoarchitecture. *Cell*. 63:525-536.

Wang, F., M. Kovacs, A. Hu, J. Limouze, E.V. Harvey, and J.R. Sellers. 2003. Kinetic mechanism of non-muscle myosin IIB: functional adaptations for tension generation and maintenance. *J Biol Chem*. 278:27439-27448.

Wang, K., C. Wloka, and E. Bi. 2019. Non-muscle Myosin-II Is Required for the Generation of a Constriction Site for Subsequent Abscission. *iScience*. 13:69-81.

Wang, S.M., and M.L. Greaser. 1985. Immunocytochemical studies using a monoclonal antibody to bovine cardiac titin on intact and extracted myofibrils. *J Muscle Res Cell Motil*. 6:293-312.

Wang, X., J.W. Tsai, J.H. Imai, W.N. Lian, R.B. Vallee, and S.H. Shi. 2009. Asymmetric centrosome inheritance maintains neural progenitors in the neocortex. *Nature*. 461:947-955.

Wang, Y.L. 1984. Reorganization of actin filament bundles in living fibroblasts. *The Journal of cell biology*. 99:1478-1485.

Webb, D.J., K. Donais, L.A. Whitmore, S.M. Thomas, C.E. Turner, J.T. Parsons, and A.F. Horwitz. 2004. FAK-Src signalling through paxillin, ERK and MLCK regulates adhesion disassembly. *Nat Cell Biol*. 6:154-161.

Wei, W.C., H.H. Lin, M.R. Shen, and M.J. Tang. 2008. Mechanosensing machinery for cells under low substratum rigidity. *Am J Physiol Cell Physiol*. 295:C1579-1589.

Wozniak, M.A., and C.S. Chen. 2009. Mechanotransduction in development: a growing role for contractility. *Nat Rev Mol Cell Biol*. 10:34-43.

Xia, G., B. Huang, Y. Zhang, X. Zhao, C. Wang, C. Jia, J. Zhao, W. Chen, and J. Li. 2019. Nanoscale Insights into Photovoltaic Hysteresis in Triple-Cation Mixed-Halide Perovskite: Resolving the Role of Polarization and Ionic Migration. *Adv Mater*. 31:e1902870.

Xu, K., H.P. Babcock, and X. Zhuang. 2012. Dual-objective STORM reveals three-dimensional filament organization in the actin cytoskeleton. *Nat Methods*. 9:185-188.

Yamaguchi, R., Y. Mazaki, K. Hirota, S. Hashimoto, and H. Sabe. 1997. Mitosis specific serine phosphorylation and downregulation of one of the focal adhesion protein, paxillin. *Oncogene*. 15:1753-1761.

Yamakita, Y., G. Totsukawa, S. Yamashiro, D. Fry, X. Zhang, S.K. Hanks, and F. Matsumura. 1999. Dissociation of FAK/p130(CAS)/c-Src complex during mitosis: role of mitosis-specific serine phosphorylation of FAK. *J Cell Biol*. 144:315-324.

Yamamoto, K., K. Otomo, T. Nemoto, S. Ishihara, H. Haga, A. Nagasaki, Y. Murakami, and M. Takahashi. 2019. Differential contributions of nonmuscle myosin IIA and IIB to cytokinesis in human immortalized fibroblasts. *Exp Cell Res*. 376:67-76.

Yamashita, Y.M., A.P. Mahowald, J.R. Perlin, and M.T. Fuller. 2007. Asymmetric inheritance of mother versus daughter centrosome in stem cell division. *Science*. 315:518-521.

Yang, K.C., A. Breitbart, W.J. De Lange, P. Hofsteen, A. Futakuchi-Tsuchida, J. Xu, C. Schopf, M.V. Razumova, A. Jiao, R. Boucek, L. Pabon, H. Reinecke, D.H. Kim, J.C. Ralphe, M. Regnier, and C.E. Murry. 2018. Novel Adult-Onset Systolic Cardiomyopathy Due to MYH7 E848G Mutation in Patient-Derived Induced Pluripotent Stem Cells. *JACC Basic Transl Sci*. 3:728-740.

Yeatman, T.J. 2004. A renaissance for SRC. *Nat Rev Cancer*. 4:470-480.

Yi, X.P., X. Wang, A.M. Gerdes, and F. Li. 2003. Subcellular redistribution of focal adhesion kinase and its related nonkinase in hypertrophic myocardium. *Hypertension*. 41:1317-1323.

Yuan, H., B. Marzban, and K. Kit Parker. 2017. Myofibrils in Cardiomyocytes Tend to Assemble Along the Maximal Principle Stress Directions. *Journal of biomechanical engineering*. 139.

Zemel, A., F. Rehfeldt, A.E. Brown, D.E. Discher, and S.A. Safran. 2010. Optimal matrix rigidity for stress fiber polarization in stem cells. *Nat Phys*. 6:468-473.

Zhang, X.F., A.W. Schaefer, D.T. Burnette, V.T. Schoonderwoert, and P. Forscher. 2003. Rho-dependent contractile responses in the neuronal growth cone are independent of classical peripheral retrograde actin flow. *Neuron*. 40:931-944.